UNIVERSITÀ DEGLI STUDI DI PARMA

Dipartimento di Scienze Chimiche, della Vita e della Sostenibilità Ambientale

Dottorato di Ricerca in Scienze della Terra

Ciclo XXXI

STRUCTURAL ARCHITECTURE AND PALEOFLUID EVOLUTION IN FAULT ZONES DISSECTING RAMP ANTICLINES: EXAMPLES FROM THE LUNIGIANA REGION (NORTHERN APENNINES) AND THE GRAN SASSO MASSIF (CENTRAL APENNINES), ITALY

Coordinatore:

Chiar.mo Prof. Fulvio Celico

Tutor:

Chiar.mo Prof. Fabrizio Storti

Co-tutor:

Dott. Fabrizio Balsamo

Dottorando: Alessio Lucca

Anni 2015/2018

ABSTRACT

The role of fluids in earthquake mechanics is a topic receiving increasing attention in the last decades due to the detected cause-effect relationships between rapid fluid pressure variations and migration along fault zones, and seismic event occurrences. Their complex interplay depends on the structural and permeability architectures of fault systems, deformation mechanisms and rates, environmental conditions of deformation (lithostatic, pore fluid, and tectonic pressure, and temperature), protolith and fault zone lithology and mechanical stratigraphy, and tectonic setting. Within this context, regional-scale fault systems exert a primary control on the fluid flow pattern, allowing either fluid redistribution and mixing on large scales through highly permeable structural elements, or promoting fluid compartmentalization and sealing when they are characterized by low permeability structural elements, or both.

In the Apennines orogenic wedge, high-angle extensional fault systems dissecting ramp anticlines are associated with intense seismicity or are potential sesismogenetic sources and promote vertical fluid migration from shallow to deep crustal levels and vice versa. For this reason, their study has social, economic and scientific importance. This Ph.D. Thesis investigates on the structural architecture and paleofluid evolution of well exposed fault zones dissecting ramp anticlines in the Northern and Central Apennines. The study was performed with a multidisciplinary approach, to characterize structural and diagenetic processes during fault evolution, with particular attention on the seismological and hydrogeological implications.

In the Northern Lunigiana region, Northern Apennines, we studied extensional deformation structures which progressively formed during the development of a regional-scale extensional fault system in the Tyrrhenian Sea side of the orogenetic belt, where the metamorphic basement was previously affected by multiple thrusting events and supplied hot fluids which migrated upward through the sedimentary cover. The Gran Sasso Massif, in the Central Apennines displays outstanding exposures of a thrust-fold stack that allowed us to investigate on the paleofluid evolution of both extensional and contractional fault systems, which developed in the axial sector of the orogenic belt, where fast uplift rates promoted meteoric fluids infiltration into the shallow crust.

Research activities included in this manuscript have been performed thanks to national and international academic and industrial partners, in the framework of different projects.

The Northern Lunigiana case study was partially funded by ENI S.p.A., in the framework of the SEFRAC project: 3D modeling and fracture characterization of fractured hydrocarbon reservoirs. Anna Laura Cazzola, Alessandro Fattorini, and Claudio Cattaneo of Eni S.p.A. are thanked for providing reflection seismic data and authorizing their publication. Seismic interpretation was done in collaboration with Prof. Andrea Artoni (Università di Parma). Part of the fieldwork was carried out in collaboration with Giancarlo Molli (Università di Pisa). Philippe Muchez (Katholieke Universiteit Leuven) participated in the analysis and interpretation of vein cement petrographic, microthermometric, and geochemical data. Andrea Schito and Sveva Corrado (Università di Roma Tre) provided vitrinite reflectance data and their thermal modelling, and discussed their meaning in the framework of this research.

The Gran Sasso Massif case study was partially funded by Shell Global Solutions International B.V. Noble gases isotopic analyses were performed under the supervision of Prof. Raymond Burgess (University of Manchester). Some of the field work in the Gran Sasso area was performed in collaboration with Prof. Giulio Di Toro, principal investigator of the European Research Council Consolidator Grant Project NOFEAR project (new outlook on seismic faults, from earthquake nucleation to arrest) and his collaborators Michele Fondriest (University of Manchester), Harold Leah (Cardiff University) and Matteo Demurtas (University of Otago).

Chapter 2 is presented in the form of published article thanks to fair use permissions of the *Geological Society of America Bulletin*, which owns the copyright.

Chapter 4 is included in the format of published article on *Journal of Structural Geology*, which owns the copyright and allows to authors its reproduction in Ph.D. Thesis.

Chapter 6 is presented as submitted version to the *Society for Sedimentary Geology (SEPM)*, which owns the copyright.

INDEX

1. INTRODUCTION 1

1.1 Fault zone structural architecture 2
1.2 Fault zone permeability architecture 3
1.3 Structural-diagenetic study of syntectonic cements 3
1.4 Tectonic and structural framework of the selected case studies 4
1.5 Seismological and hydrogeological implications 6
1.6 Bibliography of the introduction chapter 7

2. SEISMICALLY-ENHANCED HYDROTHERMAL PLUME ADVECTION THROUGH THE PROCESS ZONE OF THE COMPIONE EXTENSIONAL FAULT, NORTHERN APENNINES, ITALY 15

ABSTRACT 16

1. INTRODUCTION 16

2. GEOLOGIC SETTING 18

2.1. The Northern Lunigiana Basin 18

3. METHODS 19

3.1. Structural Analysis 19
3.2. Petrography and Cathodoluminescence 19
3.3. Carbon and Oxygen Stable Isotopes 20
3.4. Micro-Raman 21
3.5. Fluid Inclusion Microthermometry 21
3.6. Organic Matter Optical Analysis and Thermal Modelling 21

4. STRUCTURAL ARCHITECTURE OF THE COMPIONE FAULT 21

4.1. Footwall Damage Zone 23
4.2. Hanging Wall Damage Zone 23

5. VEIN CEMENT ANALYSIS 24

5.1. Petrographic Description 24
5.2. Stable Isotopes 25
5.3. Fluid Inclusions 26

6. VITRINITE REFLECTANCE AND THERMAL MODELLING 30

7. DISCUSSION 30

7.1. Process Zone Width 30
7.2. Cyclical Vein Development and Earthquake Cycle 31
7.3. Process Zone Temperature Anomaly 31
7.4. Fluid Sources and Migration Pathways 33
7.5. Evolutionary Model 34

8. CONCLUSION 36

ACKNOWLEDGMENTS 36

REFERENCES CITED 36

SUPPLEMENTARY MATERIAL 41

3. FRACTURE NETWORK ATTRIBUTE DISTRIBUTION IN THICK SANDSTONE STRATA ACROSS THE FOOTWALL DAMAGE ZONE OF THE COMPIONE FAULT, NORTHERN APENNINES, ITALY 53

ABSTRACT 54

1. INTRODUCTION 54

2. GEOLOGICAL FRAMEWORK 55

3. METHODOLOGY 59

4. RESULTS 60

4.1. Fracture dip analysis 60
4.2. Fracture intensity 64
4.3. Fracture density 65
4.4. Fracture connectivity 65
4.5. Fracture network topology 67

5. DISCUSSION 69

5.1. Process zone restoration to the pre-extensional folding stage 69
5.2. Fracture intensity, density and connectivity in the fault process zone 70
5.3. Implications of fracture topology on fault zone evolution 71

6. CONCLUSIONS 73

ACKNOWLEDGMENTS 74

REFERENCES 74

4. COSEISMIC EXTENSION RECORDED WITHIN THE DAMAGE ZONE OF THE VADO DI FERRUCCIO THRUST FAULT, CENTRAL APENNINES, ITALY 79

ABSTRACT 80

1. INTRODUCTION

2. GEOLOGIC SETTING 81

2.1. Gran Sasso Massif 81
2.2. Fornaca Tectonic Window 81
2.3. Lithologies adjacent to the VFTF 82

3. METHODS 83

4. FIELD OBSERVATIONS OF THE VADO DI FERRUCCIO THRUST FAULT

4.1. The Fornaca tectonic window 84
4.2. Hanging wall block 84
4.3. Footwall block 84
4.4. Fault core 87

5. MICROSTRUCTURE AND MINERALOGY OF THE VADO DI FERRUCCIO THRUST FAULT 87

5.1. Microstructure and mineralogy of clay-rich fault core rocks 87
5.2. Microstructure and mineralogy of clay-poor fault core rocks 88

6. DISCUSSION 89

6.1. Thrusting on the VFTF 89
6.1.1. Deformation mechanisms within the thrust fault core 89
6.1.2. Deformation mechanisms and fault kinematics during compression in the fault damage zone 92
6.1.2.1. Hangingwall 92
6.1.2.2. Footwall
6.1.3. Ambient conditions and displacement of the VFTF 93
6.2. Extensional activity recorded in the VFTF core and hangingwall damage zone 93

7. CONCLUSIONS 95

ACKNOWLEDGMENTS 95

REFERENCES 95

5. SUBAERIAL OUT-OF-SEQUENCE THRUSTING AND LATE-STAGE EXTENSION IN THE GRAN SASSO MASSIF, CENTRAL APENNINES, ITALY 99

ABSTRACT 100

1. INTRODUCTION 101

2. GEOLOGICAL FRAMEWORK OF THE CENTRAL APENNINES 103

3. STRUCTURAL SETTING OF THE STUDY AREA 105

4. METHODS 107

4.1. Structural analysis 107
4.2. Petrography 107
4.3. Carbon and oxygen stable isotopes 108
4.4. Strontium isotopes 108
4.5. Noble gases isotopes 109

5. CONTRACTIONAL STRUCTURAL ARCHITECTURE 110

6. EXTENSIONAL STRUCTURAL ARCHITECTURE 114

7. STRUCTURAL DIAGENETIC FEATURES OF THE MONTE CAMICIA AND VADO DI FERRUCCIO THRUST 117

7.1. Monte Camicia thrust zone 117
7.2. Vado di Ferruccio thrust zone 120

8. GEOCHEMICAL DATA 122

8.1. Carbon and oxygen stable isotopes data 122
8.2. Strontium isotopes data 124
8.3. Noble gases isotopes data 126

9. DISCUSSION 126

9.1. Host rock diagenetic framework 126
9.2. Structural diagenesis 128
9.3. Evolutionary model 131

10. CONCLUSIONS 134

ACKNOWLEDGMENTS 135

REFERENCES 136

SUPPLEMENTARY MATERIAL 149

6. PORE TYPE EVOLUTION AND FLOW PROPERTIES OF CARBONATE FAULT ROCKS 153

ABSTRACT 154

1. INTRODUCTION 154

2. GEOLOGICAL SETTING 156

3. METHODS 158

4. RESULTS 159

4.1. Fault Rocks 159
4.2. Fault Core/ Fault Rock Microstructures 159
4.3. Porosity 161
4.4. Permeability 163

5. DISCUSSION 165

5.1. Fault Core Rocks and Fault Displacement 165
5.2. Petrophysical Properties 165
5.3. Implications for Fault Seal 167

6. CONCLUSIONS 169

ACKNOWLEDGMENTS 170

REFERENCES 170

7. GENERAL CONCLUSIONS 177

1

INTRODUCTION

This Ph.D. Thesis is aimed at investigating the structural architecture and paleofluid evolution along fault zones dissecting ramp anticlines, located along the Tyrrhenian side of the Northern Apennines and in the axial zone of the belt, respectively. This because the structural and permeability architectures of fault systems exert a primary control on the fluid flow pattern in the upper crust, allowing either fluid redistribution and mixing on large scales through highly permeable structural elements, or promoting fluid compartmentalization and sealing when they are characterized by low permeability structural elements, or both. Fluid overpressure is well known as a fundamental factor influencing earthquake nucleation and propagation and, consequently, a better understanding of paleofluid evolution in field analogues can provide further constraints on the environmental conditions of earthquake nucleation, particularly in the Apennines. In fact, we studied a segment of the Northern Lunigiana Extensional Fault System in the Northern Apennines, because it cuts through basement rocks and is located close to the Tyrrhenian coast, where the Moho depth is much shallower than underneath the axial zone of the belt, to the East. Accordingly, a significant contribution from deeply-sourced fluids is expected. On the other hand, we selected the Gran Sasso Massif, in the Central Apennines, to address also the case where both contractional and extensional fault zones affect a thick pile of carbonates and deformation occurred at shallow burial conditions. Accordingly, a significant contribution from meteoric fluid infiltration is expected.

An introduction on fluid-rock interaction processes in fault zones is provided to better understand the topics discussed in the following chapters. In this context, the structural and permeability architectures of fault zones, along with the structural-diagenetic study of syntectonic cements, are initially described. Then the tectonic and structural framework of the two selected areas and the hydrogeological and seismological implications of their study are briefly illustrated. After this short introduction, the study of the structural and paleofluid evolution in the selected fault zones is addressed. Our investigations were performed through “case specific” multidisciplinary approaches which include: analysis of large-scale structures in the framework of their regional geologic context supported by

seismic profiles interpretation; detailed structural mapping and structural analysis at the meso- and micro-scale; petrographical, mineralogical, geochemical and microthermometrical characterization of syntectonic cements and fault rocks.

1.1 Fault zone structural architecture

Fault zones are mechanical discontinuities in the upper crust, represented by volumes of rocks characterized by a higher deformation intensity and rate (Van der Pluijm and Marshak, 1997; Davis et al., 2005). Although they occupy a small volume of the crust, they exert a first-order control on its mechanical and fluid flow properties, and their understanding bears fundamental implications for oil and groundwater reservoirs exploitation and seismic hazard assessment. Fault zone structure is the result of the interplay of protolith lithology, mechanical stratigraphy, depth of deformation, tectonic setting and fluid flow. The typical fault zone structure is described as composed of a fault core interposed between two damage zones lying in the hangingwall and footwall, respectively (Chester et al., 1993; Wibberley et al., 2008; Faulkner et al., 2010). The fault core accommodates most of the deformation, does not preserve primary structures, and is generally made by fault rocks composed of fine material, i.e. gouges, cataclasites and/or ultracataclasites. Damage zones are the intensely deformed rock volumes surrounding the fault core and are characterized by subsidiary faults, veins, fractures and other secondary structures whose intensity increases approaching the fault core. However, this simple geometric model of fault zones commonly fails when applied to regional-scale fault systems, which are composed of multiple fault zones comprising, in turn, many fault segments. As a result, processes of linkage and interaction between fault segments give rise to complex three-dimensional fault core and damage zone architectures (Crider and Pollard, 1998; Gupta and Scholz, 2000; Peacock, 2002).

Damage zones have been classified according to their structural position with respect to the master fault plane and within the fault system. Structural position has also been demonstrated to exert a control on mechanics and fluid flow patterns. Wall damage zones are located in the walls along fault traces, tip damage zones are at the end of fault traces and linking damage zones at fault traces intersections and abutments (Kim et al., 2004; Savage and Brodsky, 2011; Choi et al 2016). When an understanding of the geometry of the fault system is not accessible, damage zones are referred to

as cross-fault damage zones. Linking and tip damage zones are located in zones of higher stress concentration compared to wall damage zones which results in higher fracture nucleation. Consequently, zones with higher fracture intensity are more permeable and act as fluid flow preferential pathways (Sibson, 1996; Curewitz and Karson, 1997). Detailed mapping and structural analysis is of primary importance to better understanding the three dimensional geometry of fault systems, which exerts a first order control on fluid flow patterns and, consequently, to unravel fault-related paleofluid evolutions.

1.2 Fault zone permeability architecture

Fault cores and damage zones are characterized by important petrophysical modifications compared to the corresponding protolith rocks. Such deformation-related changes determine the hydrogeological behavior of the major architectural elements of fault zones and depend on deformation mechanisms and conditions, on fault displacement, fault zone thickness and geometry, and fluid-rock interactions (Knipe, 1993; Caine et al., 1996; Caine and Forster, 1999; Rawling et al., 2001; Faulkner et al., 2010). A simple conceptual model characterized by four end-member fault zone permeability architectures, proposed by Caine et al. (1996), is based on the petrophysical properties of fault cores and damage zones with respect to the protolith. These four permeability architectures are the localized conduit, the distributed conduit, the localized barrier and the combined conduit-barrier. Actually, each architectural element can show contrasting hydrogeological behaviors during time as boundary conditions may change. Therefore, when dealing with exhumed fault systems, petrophysical property characterization has to be coupled with that of diagenetic processes, i.e. precipitation, dissolution and mineralogical reactions through the analysis of syntectonic cements, in order to understand the fault hydrogeological behavior through time (Beaudoin et al., 2011; Bense et al., 2013; Laurent et al., 2017; Wüstefeld et al., 2017).

1.3 Structural-diagenetic study of syntectonic cements

At shallow crustal levels, syntectonic cements are the product of crystallization processes from diagenetic fluids during deformation. Fluids at temperatures lower than 200-250 °C (anchizone metamorphism), generally hosted in sedimentary rocks, belong to the diagenetic realm

(Moore, 1990; Morad et al., 2000; Worden and Burley, 2003). As such, chemical saturation is reached in most of the cases only for calcite and quartz, making them the most common diagenetic cements. Peculiar conditions are needed to precipitate different cements, favoured by exotic fluids or mineralogical reactions, making them indicators of specific diagenetic processes (Anderson and Macqueen, 1982; Cathles and Smith, 1983; Machel, 2001). Microtextural analysis of syntectonic cements allows to gain preliminary information on the diagenetic environment of crystallization but only a complete geochemical investigation allows to infer diagenetic fluid sources, migration pathways and fluid-rock interactions (Ferket et al., 2011; Travé et al., 2011; Cantarero et al 2013; Mozafari et al., 2015). Moreover, since cement composition depends both upon fluid composition and temperature of crystallization, independent geothermobarometers or microthermometry are necessary to understand the origin and evolution of the cementing fluids (Mamadou et al., 2016; Honlet et al., 2017). In sedimentary basins, diagenetic fluids are characterized by geochemical patterns and diagenetic processes resulting from lithology, temperature, and the basin scale fluid flow pathways. Conversely, in proximity of regional-scale fault systems, diagenetic processes are interested by further complexity. As discussed in the previous sections, the structural and permeability architectures of fault systems allow fluids belonging to different stratigraphic horizons to migrate upward or downward, mix and equilibrate with other fluids depending on pressure, temperature and chemical gradients (Laurent et al., 2017; Wüstefeld et al., 2017; Lucca et al., in press). Nevertheless, regional-scale fault systems located in the same sectors of orogenic wedges, i.e. outer, axial and inner (moving from the foreland towards the hinterland) are characterized by commonalities in their fluid origin, diagenetic processes and fluid flow patterns. These common features are controlled by the large-scale tectonics and structures in the different sectors of the orogenic wedge (Nesbitt and Muehlenbachs, 1989; Evans and Battles, 1999; Roure et al., 2005).

1.4 Tectonic and structural framework of the selected case studies

The first case study is a fault zone pertaining to the Northern Lunigiana Extensional Fault System, in the Northern Apennines, which constitutes the northern boundary of the Lunigiana graben (Bernini, 1988, 1991). The second study area is located in the thrust-fold stack of the Gran Sasso Massif, in the Central Apennines (Ghisetti and Vezzani, 1986, 1991), and

includes three fault zones, namely Vado di Ferruccio and Monte Camicia out-of-sequence thrust fault zones, and the Campo Imperatore extensional fault system, overprinting and dissecting the first two. The selected study areas share a diachronous but similar sequence of deformation events determined by the tectonic evolution of the Apennines orogenic-wedge and the Tyrrhenian Sea back-arc, which is caused by the Adria microplate westward subduction and related slab rollback below the European plate, and includes northeast directed in-sequence early piggyback thrusting, followed by out-of-sequence thrusting within the thrust wedge, and by late-stage extensional faulting (Boccaletti et al., 1971; Elter et al., 1975; Royden, 1988; Doglioni, 1991; Carmignani et al., 1995).

Both the Northern Lunigiana and the Campo Imperatore regional-scale extensional fault systems are located near the crest to forelimb transition of thrust-related anticlines. Moreover, both extensional fault systems are the youngest and north-easternmost in the Northern and Central Apennines, respectively (Carmignani et al., 1994; Cavinato and De Celles, 1999). Microstructures indicating seismic activity have been documented on both fault systems (Leah et al., 2018; Lucca et al., 2018). Despite these common features, the tectonic framework of the two areas is characterized by first-order differences. The area investigated in the Northern Apennines is located in the inner part of the belt, i.e. Tyrrhenian side, and lies above a "Tyrrhenian Moho", thus implying a higher heat flux (Della Vedova et al., 1995). In upper Miocene times, tectonic thickening in the inner part of the wedge raised its taper up to supercritical conditions that triggered foreland directed low-angle extensional faulting to regain a critical state (Davis et al, 1983; Dahlen et al., 1984; Clemenzi et al., 2015; Molli et al., 2018). Afterwards, contraction resumed involving both the sedimentary cover and the basement in an out-of-sequence fashion (Storti, 1995; Carlini et al., 2013; Clemenzi et al., 2014; Molli et al., 2018). The area studied in the Central Apennines is located in the axial part of the orogenic wedge, where the crust is tectonically thickened and contractional deformation events display a thin-skinned deformation style (Patacca et al., 2008). As a consequence, Quaternary extensional deformations do not directly interact with the Tyrrhenian back-arc opening and the heat flow is lower than that in the Lunigiana region (Ghisetti and Vezzani, 1999; Cosentino et al., 2017). The rapid exhumation rates and the absence of two clearly resolvable Tyrrhenian and Adria crustal discontinuities is interpreted as evidence for delamination of the Adria plate and mantle metasomatism in the Central Apennines (Chiarabba and Chiodini, 2013). Another important difference

between the two study areas is provided by the different burial and thermal histories, resulting in distinct thermo-barometric conditions of deformation (Zattin et al., 2000; Rusciadelli et al., 2005; Carlini et al., 2013).

The purpose of this study is to analyze the effects of the different tectonic settings and environmental conditions of deformation on the paleofluid systems recorded in the two areas

1.5 Seismological and hydrogeological implications

The multidisciplinary approach we adopted to study the selected regional-scale fault systems allowed us to infer fault-related seismological and hydrogeological processes that occurred in the past and likely continue today on the same fault system at depth.

In the case study of the Northern Lunigiana Extensional Fault System, the structural architecture of the fault zone was studied in detail in a cross-section transect, on which the fracture network quantification of the footwall damage zone was also performed. Here, we had the opportunity to study the maximum burial conditions of the host siliciclastic rocks and the syntectonic cements, characterized by outstanding microtextures, using independent geothermometers. The main outcomes of this study indicate that a highly-connected shear fractures network formed in the tip damage zone during upward fault propagation and was cyclically cemented by calc-silicatic mineralizations in thermal disequilibrium with the host rock, triggered by abrupt fluid pressure variations. This testifies for the upward migration of metamorphic fluids into the sedimentary cover, triggered by a *seismic pumping* mechanism (Sibson et al., 1975). Since the Northern Lunigiana Extensional Fault System is rooted in the metamorphic basement, which is still affected by deformation as attested by earthquake occurrence (Giraudi and Frezzotti, 1995; Eva et al., 2014), it is expected that the same processes preserved as fossil evidence at the surface are still active at depth.

In the second study area, which includes the Campo Imperatore and Assergi extensional fault systems, and the Vado di Ferruccio and Monte Camicia out-of-sequence thrusts, outstanding exposures allowed us to reconstruct the three-dimensional geometry through detailed structural analysis. In this case, we approached the study of microstructures and syntectonic cements hosted in carbonatic rocks through compositional and geochemical analyses, namely oxygen and carbon stable isotopes, strontium, and noble gases isotopes. Moreover, fault rocks of the Campo Imperatore

and Assergi extensional fault systems were investigated through petrophysical analyses. The results of this study indicate that out-of-sequence thrusting occurred at very shallow depth to subaerial conditions, associated with marine and meteoric fluids circulation in the thrust fault zones, which promoted local syntectonic dolomitization and late-stage dolomite calcitization, respectively. Quaternary extensional deformation structures, some of which have been shown to be coseismically activated, partially exploited the contractional architecture and allowed increasing infiltration of meteoric fluids into the thrust-fold stack through high-angle faults and fractures. No evidences of mantle and metamorphic fluids were found in the syntectonic cements, coherently with crustal geometries indicating multiple carbonate thrust sheets underneath the study area (e.g. Cosentino et al., 2010). Extensional fault rock fabrics are characterized, with increasing displacements, by an initial permeability increase followed by a permeability drop. This indicates that depending on fault displacement, thickness and structural position, the studied fault zones acted as conduits (breccias) or as dynamic seals (cataclasites). Like in the Lunigiana region, the studied extensional fault zones in the Gran Sasso area are still seismically active and, consequently, inferences obtained from their exhumed parts may be applied to the corresponding segments at depth (Galli et al., 2002).

1.6 *Selected bibliography*

Anderson, G.M., and Macqueen, R.W., 1982. Ore-deposit models - 6. Mississippi Valley-type lead-zinc deposits: Geoscience Canada, v. 9, n. 2, p. 108–117.

Beaudoin, N., Bellahsen, N., Lacombe, O., and Emmanuel, L., 2011. Fracture-controlled paleohydrogeology in a basement-cored, fault-related fold: Sheep Mountain Anticline, Wyoming, United States: Geochemistry, Geophysics, Geosystems, v. 12, n. 6, Q06011.

Bense, V.F., Gleeson, T., Loveless, S.E., Bour, O., and Scibek, J., 2013. Fault zone hydrogeology: Earth Science Reviews, doi:10.1016/j.earscirev. 2013.09.008.

Bernini, M., 1988. Il bacino dell'Alta Val Magra: primi dati mesostrutturali sulla tettonica distensiva: Bollettino della Società Geologica Italiana, v. 107, p. 355-371.

Bernini, M., 1991. Le strutture estensionali della Lunigiana (Appennino Settentrionale): proposta di un modello deformativo: Atti Ticinesi di Scienze della Terra, v. 34, p. 29-38.

Boccaletti, M., Elter, P., and Guazzone, G., 1971. Plate Tectonic Models for the Development of the Western Alps and Northern Apennines: Nature, v. 234, p. 108-111.

Caine, J.S., Evans, J.P., and Forster, J.B., 1996. Fault zone architecture and permeability structure: Geology, v. 24, p. 1025-1028.

Caine, J.S., and Forster, C.B., 1999. Fault zone architecture and fluid flow: Insights from field data and numerical modeling, in Haneberg, W.C., et al., eds., Faults and subsurface fluid flow in the shallow crust: American Geophysical Union Geophysical Monograph, v. 113, p. 101–127.

Cantarero, I., Travé, A., Alías, G., and Baqués, V., 2013. Polyphasic hydrothermal and meteoric fluid regimes during the growth of a segmented fault involving crystalline and carbonate rocks (Barcelona Plain, NE Spain): Geofluids, v. 14, p. 20-44.

Carlini, M., Artoni, A., Aldega, L., Balestrieri, M.L., Corrado, S., Vescovi, P., Bernini, M., and Torelli, L., 2013. Exhumation and reshaping of far-travelled/allochthonous tectonic units in mountain belts. New insights for the relationships between shortening and coeval extension in the western Northern Apennines (Italy): Tectonophysics, v. 608, p. 267–287.

Carmignani, L., Decandia, F.A., Fantozzi, P.L., Lazzarotto, A., Liotta, D., and Meccheri, M., 1994. Tertiary extensional tectonics in Tuscany (Northern Apennines, Italy): Tectonophysics, v. 238, p. 295–315.

Carmignani, L., Decandia, F.A., Disperati, L., Fantozzi, P.L., Lazzarotto, A., Liotta, D., and Oggiano, G., 1995. Relationships between the Tertiary structural evolution of the Sardinia-Corsica-Provençal Domain and the Northern Apennines: Terra Nova, v. 7, no. 2, p. 128–137.

Cathles, L.M., and Smith, A.T., 1983. Thermal constraints on the formation of the Mississippi Valley-type lead-zinc deposits and their implications for episodic basin dewatering and deposit genesis: Economic Geology, v. 78, p. 983-1002.

Cavinato, G.P., and De Celles, P.G., 1999. Extensional basins in the tectonically bimodal central Apennines fold-thrust belt, Italy: Response to

corner flow above a subducting slab in retrograde motion: Geology, v. 27, p. 955-958.

Chester, F.M., Evans, J.P., and Biegel, R.L., 1993. Internal structure and weakening mechanisms of the San Andreas fault: Journal of Geophysical Research, v. 98, p. 771-786.

Chiarabba, C., and Chiodini, G., 2013. Continental delamination and mantle dynamics drive topography, extension and fluid discharge in the Apennines: Geology, v. 41 (6), p. 715-718.

Choi, J.H., Edwards, P., Ko, K., and Kim, Y.S., 2016. Definition and classification of fault damage zones: a review and a new methodological approach: Earth Science Reviews, v. 152, p. 70-87.

Clemenzi, L., Molli, G., Storti, F., Muchez, P., Swennen, R., and Torelli, L., 2014. Extensional deformation structures within a convergent orogen: The Val di Lima low-angle normal fault system (Northern Apennines, Italy): Journal of Structural Geology, v. 66, p. 205-222.

Clemenzi, L., Storti, F., Balsamo, F., Molli, G., Ellam, R., Muchez, P., and Swennen, R., 2015. Fluid pressure cycles, variations in permeability, and weakening mechanisms along low-angle normal faults: the Tellaro detachment, Italy: GSA Bulletin, v. 127 (11-12), p. 1689-1710.

Cosentino, D., Cipollari, P., Marsili, P., and Scrocca, D., 2010. Geology of the Central Apennines: A regional review: in Beltrando, M., Peccerillo, A., Mattei, M., Conticelli, S., & Doglioni, C., eds., The Geology of Italy: Journal of the Virtual Explorer (Electronic Edition), v. 36, paper 11.

Cosentino, D., Asti, R., Nocentini, M., Gliozzi, E., Kotsakis, T., Mattei, M., Esu, D., Spadi, M., Tallini, M., Cifelli, F., Pennacchioni, M., Cavuoto, G., & Di Fiore, V., 2017. New insights into the onset and evolution of the central Apennine extensional intermontane basins based on the tectonically active L'Aquila Basin (central Italy): GSA Bulletin, v. 129 (9/10), p. 1314-1336.

Crider, J.G., and Pollard, D.D., 1998. Fault linkage: three-dimensional mechanical interaction between echelon normal faults: Journal of Geophysical Research, v. 103, p. 24373-24391.

Curewitz, D., and Karson, J.A., 1997. Structural settings of hydrothermal outflow: Fracture permeability maintained by fault propagation and

interaction: Journal of Volcanology and Geothermal Research, v. 79, p. 149-168.

Dahlen, F.A., Suppe, J., and Davis, D., 1984. Mechanics of fold-and-thrust belts and accretionary wedges: Cohesive Coulomb theory: Journal of Geophysical Research, v. 89, p. 10,087-10,101.

Davis, D.M., Suppe, J., and Dahlen, F.A., 1983. Mechanics of foldand-thrust belts and accretionary wedges: Journal of Geophysical Research, v. 88, p. 1153-1172.

Davis, G.H., Reynolds, S.J., and Kluth C.F., 2005. Structural Geology of Rocks and Regions, 3rd Ed. John Wiley & Sons, New York, 839 p.

Della Vedova, B., Lucazeau, F., Pasquale, V., Pellis, G., and Verdoya, M., 1995. Heat flow in the tectonic provinces crossed by the southern segment of the European Geotraverse: Tectonophysics, v. 244, p. 57-74.

Doglioni, C., 1991. A proposal for the kinematic modelling of W-dipping subductions - Possible applications to the Tyrrhenian-Apennines system: Terra Nova, v. 3, n. 4, p. 423–434.

Elter, P., Giglia, G., Tongiorgi, M., and Trevisan, L., 1975. Tensional and compressional areas in recent (Tortonian to present) evolution of Northern Apennines: Bollettino di Geofisica Teorica Applicata, v. 17, p. 13-18.

Eva, E., Solarion, S., and Boncio, P., 2014. HypoDD relocated seismicity in northern Apennines, (Italy) preceding the 2013: seismotectonic implications for the Lunigiana-Garfagnana area: Bollettino di Geofisica Teorica Applicata, v. 55, p. 739-754.

Evans, M. A., and Battles, D.A., 1999. Fluid inclusion and stable isotope analyses of veins from the central Appalachian Valley and Ridge province: Implications for regional synorogenic hydrologic structure and fluid migration: Geological Society of America Bulletin, v. 111, p. 1841-1860.

Faulkner, D., Jackson, C., Lunn, R., Schlische, R., Shipton, Z., Wibberley, C., and Withjack, M., 2010. A review of recent developments concerning the structure, mechanics and fluid flow properties of fault zones: Journal of Structural Geology, v. 32, p. 1557-1575.

Ferket, H., Guilhaumou, N., Roure, F. and Swennen, R., 2011. Insights from fluid inclusions, thermal and PVT modeling for paleo-burial and thermal reconstruction of the Cordoba petroleum system (NE Mexico): Marine and Petroleum Geology, v. 28, p. 936-958.

Galli, P., and Bosi, v., 2002. Paleoseismology along the Cittanova fault: Implications for seismotectonics and earthquake recurrence in Calabria (southern Italy), Journal of Geophysical Research, v. 107 (B3), 2044, doi:10.1029/2001JB000234.

Ghisetti, F., and Vezzani, L., 1986. Assetto geometrico ed evoluzione strutturale della catena del Gran Sasso tra Vado di Siella e Vado di Corno: Bollettino della Società Geologica Italiana, v. 105, p. 131-171.

Ghisetti, F., and Vezzani, L., 1991. Thrust belt development in the Central Apennines (Italy): northward polarity of thrusting and out-of-sequence deformations in the Gran Sasso chain: Tectonics, v. 10, p. 904-919.

Ghisetti, F., and Vezzani, L., 1999. Depths and modes of Pliocene-Pleistocene crustal extension of the Apennines (Italy): Terra Nova, v. 11, p. 67-72.

Giraudi, C., and Frezzotti, F., 1995. Paleoseismicity in the Gran Sasso Massif (Abruzzo, Central Italy): Quaternay International, v. 25, p. 81–93.

Gupta, A., and Scholz, C.H., 2000. A model of normal fault interaction based on observations and theory: Journal of Structural Geology, v. 22, p. 865-879.

Honlet, R., Gasparrini, M., Jager, H., Muchez, P., and Swennen, R., 2017. Precursor and ambient rock paleothermometry to assess the thermicity of burial dolomitization in the southern Cantabrian Zone (northern Spain): International Journal of Earth Sciences, v. 106-7, p. 1-21.

Leah, H., Fondriest, M., Lucca, A., Storti, F., Balsamo, F., and Di Toro, G., 2018. Coseismic extension recorded within the damage zone of the Vado di Ferruccio Thrust Fault, Central Apennines, Italy: Journal of Structural Geology, v. 114, p. 121-138.

Lucca, A., Storti, F., Molli, G., Muchez, P., Schito, A., Artoni, A., Balsamo, F., Corrado, S., and Salvioli Mariani, E., 2018. Seismically enhanced hydrothermal plume advection through the process zone of the Compione extensional Fault, Northern Apennines, Italy: GSA Bulletin, https://doi.org/10.1130/B32029.1.

Kim, Y.S., Peacock, D.C.P., and Sanderson, D.J., 2004. Fault damage zones: Journal of Structural Geology, v. 26 (3), p. 503-517.

Knipe, R.J., 1993. The influence of fault zone processes and diagenesis on fluid flow, in A.D. Horbury and A.D. Robinson, eds., Diagenesis and basin development: AAPG Studies in Geology, v. 36, p. 135-151.

Laurent, D., Lopez, M., Chauvet, A., Sauvage, A.C., Buatier, M., and Spangenberg, J.E., 2017. Sedimentary fluids/fault interaction during syn-rift burial of the Lodève Permian Basin (Hérault, France): An example of seismic-valve mechanism in active extensional faults: Marine and Petroleum Geology, v. 88, p. 303-328.

Machel, H.G., 2001. Bacterial and thermochemical sulphate reduction in diagenetic settings: Sedimentary Geology, v. 140, p. 143-175.

Mamadou, M.M., Chatelineau, M., Bourdelle, F., Boiron, M-C., Elmaleh, A., and Brouand, M., 2016. Hot fluid flows around a major fault identified by paleothermometric studies (Tim Mersoi Basin, Niger): Journal of Sedimentary Research, v. 86, p. 914-928.

Molli, G., Carlini, M., Vescovi, P., Artoni, A., Balsamo, F., Camurri, F., Clemenzi, L., Storti, F., and Torelli, L., 2018. Neogene 3D-structural architecture of the north-west Apennines: the role of the low angle normal faults and basement thrusts: Tectonics, v. 37, p. 2165-2196.

Moore, C.H., 1989. Carbonate Diagenesis and Porosity: Elsevier, Amsterdam, 338 p.

Morad, S., Ketzer, J.M. and De Ros, L.F., 2000. Spatial and temporal distribution of diagenetic alterations in siliciclastic rocks: implications for mass transfer in sedimentary basins: Sedimentology, v. 47 (Millenium Reviews), p. 95-120.

Mozafari, M., Swennen, R., Balsamo, F., Clemenzi, L., Storti, F., El Desouky, H., Vanhaecke, F., Tueckmantel, C., Solum, J., and Taberner, C., 2015. Paleofluid evolution in fault-damage zones: evidence from fault-fold interaction events in the Jabal Qusaybah anticline (Adam Foothills, North Oman): Journal of Sedimentary Research, v. 85, p. 1525-1551.

Nesbitt, B.E., and Muehlenbachs, K., 1989. Origins and movement of fluids during deformation and metamorphism in the Canadian Cordillera: Science, v. 245, p. 733-736.

Patacca, E., Scandone, P., Di Luzio, E., Cavinato, G.P., and Parotto, M., 2008. Structural architecture of the central Apennines: interpretation of the

CROP 11 seismic profile from the Adriatic coast to the orographic divide: Tectonics, v. 27, doi:10.1029/2005TC001917.

Peacock, D.C.P., 2002. Propagation, interaction and linkage in normal fault systems: Earth Science Reviews, v. 58, p. 121-142.

Rawling, G.C., Goodwin, L.B., and Wilson, J.L., 2001. Internal architecture, permeability structure, and hydrologic significance of contrasting fault-zone types: Geology, v. 29 (1), p. 43-46.

Roure, F., Swennen, R., Schneider, F., Faure, J.L., Ferket, H., Guilhaumou, N., Osadetz, K., Robion, P., and Vandeginste, V., 2005. Incidence and importance of tectonics and natural fluid migration on reservoir evolution in foreland fold-and-thrust belts: In: Brosse, E. (Ed.), Oil and Gas Science and Technology, Oil and Gas Science and Technology. Revue de l'IFP 60, pp. 67–106.

Royden, L., 1988. Flexural behaviour of the continental lithosphere in Italy: Constraints imposed by gravity and deflection data: Journal of Geophysical Research, v. 93, p. 7747–7766.

Rusciadelli, G., Viandante, M.G., Calamita, F., and Cook A.C., 2005. Burial-exhumation history of the central Apennines (Italy), from the foreland to the chain building: thermochronological and geological data: Terra Nova, v. 17, p. 560-572.

Savage, H.M., and Brodsky, E.E., 2011. Collateral damage: evolution with displacement of fracture distribution and secondary fault strands in fault damage zones: Journal of Geophysical Research, v. 116, B03405.

Sibson, R.H., Moore, J.McM., and Rankin, A.H., 1975. Seismic pumping-a hydrothermal fluid transport mechanism: Journal of the Geological Society of London, v. 131, p. 653-659.

Sibson, R.H., 1996. Structural Permeability of fluid-driven fault-fracture meshes: Journal of Structural Geology, v. 18, p. 1031-1042.

Storti, F., 1995. Tectonics of the Punta Bianca promontory: Insights for the evolution of the Northern Apennines-Northern Tyrrhenian Sea basin: Tectonics, v. 14, p. 832–847.

Travé, A., and Calvet, F., 2001. Syn-rift geofluids in fractures related to the early–middle Miocene evolution of the Vallés-Penedés half-graben (NE Spain): Tectonophysics, v. 336 (1–4), p. 101-120.

Van der Pluijm, B., and Marshak, S., 1997. Earth Structure. McGrawHill, New York, 495 p.

Wibberley, C.A.J., and Shimamoto, T., 2003. Internal structure and permeability of major strike-slip fault zones: The Median Tectonic Line in Mid Prefecture, southwest Japan: Journal of Structural Geology, v. 25, p. 59-78.

Worden, R.H., and Burley, S.D., 2003. Sandstone diagenesis: the evolution of sand to stone. In: Burley, S.D., Worden, R.H. (Eds.), Sandstone Diagenesis-Recent and Ancient, v. 4. Blackwell, USA, p. 3–47.

Wüstefeld, P., Hilse, U., Lüders, V., Wemmer, K., Koherer, B., and Hilgers, C., 2017. Kilometer-scale fault-related thermal anomalies in tight gas sandstones: Marine and Petroleum Geology, v. 86, p. 288-303.

Zattin, M., Landuzzi, A., Picotti, V., and Zuffa, G.G., 2000. Discriminating between tectonic and sedimentary burial in a foredeep succession, Northern Apennines: Journal of Geological Society of London, v. 157, n. 3, p. 629-633.

2

SEISMICALLY-ENHANCED HYDROTHERMAL PLUME ADVECTION THROUGH THE PROCESS ZONE OF THE COMPIONE EXTENSIONAL FAULT, NORTHERN APENNINES, ITALY

This chapter is presented in the form of a manuscript that was published online by the *Geological Society of America Bulletin*. The manuscript describes the calc-silicatic mineralizations hosted in the damage zone of the Compione Fault, which is a segment of the Northern Lunigiana Extensional Fault System. In this study we show that crystallization occurred cyclically in a mesh of extensional conjugate faults formed at the process zone stage, before upward propagation of the fault tip, and in thermal disequilibrium with the host rock. The Compione Fault allowed, at first, upward migration of hot fluids from the metamorphic basement and, eventually, their mixing with meteoric fluids at shallow crustal levels.

ARTICLE IN PRESS

Lucca A, Storti F., Molli G., Muchez P., Schito A., Artoni A., Balsamo F., Corrado S., Salvioli Mariani E.

Submitted to: *Geological Society of America Bulletin*

Date of Submission: 8 February 2018

Date of Acceptance: 14 August 2018

Published Online: 15 November 2018

DOI: https://doi.org/10.1130/B32029.1

THE GEOLOGICAL SOCIETY OF AMERICA®

Seismically enhanced hydrothermal plume advection through the process zone of the Compione extensional Fault, Northern Apennines, Italy

Alessio Lucca[1,†], Fabrizio Storti[1], Giancarlo Molli[1,2], Philippe Muchez[3], Andrea Schito[4], Andrea Artoni[5], Fabrizio Balsamo[1], Sveva Corrado[4], and Emma Salvioli Mariani[5]

[1]*Department of Chemistry, Life Sciences and Environmental Sustainability, Natural and Experimental Tectonics research group, University of Parma, I-43124 Parma, Italy*

[2]*Department of Earth Sciences, University of Pisa, via S. Maria, 53, I-56126 Pisa, Italy*

[3]*Department of Earth and Environmental Sciences, Katholieke Universiteit Leuven, Celestijnenlaan 200E, B-3001 Heverlee, Belgium*

[4]*Department of Sciences, Geology Section, Roma Tre University, L.go S. Leonardo Murialdo 1, I-00146 Roma, Italy*

[5]*Department of Chemistry, Life Sciences and Environmental Sustainability, University of Parma, I-43124 Parma, Italy*

ABSTRACT

Reconstructing the paleofluid evolution in mature fault zones, which typically have complex structural architectures, is a challenging task because reactivation of pre-existing deformation structures and dissolution-reprecipitation processes are very abundant. Understanding why specific structural elements are preferentially mineralized and what are the factors leading to rapid fluid migration and accumulation, bears geological and economic implications, especially in seismically active fault zones. We studied the Compione Fault on the Tyrrhenian Sea side of the Northern Apennines orogenic wedge, Italy, which is a segment of the 30-km-long Northern Lunigiana high-angle extensional fault system still active today. The Compione Fault propagated from the metamorphic basement and accumulated about 1.5 km of displacement. We used structural, petrographic, isotopic, microthermometric, compositional, and organic matter analyses to constrain fluid and host rock properties during fault zone evolution. This approach allowed us to quantify the thermal anomaly in the fault zone and to infer the processes responsible for such a disequilibrium. Specifically, we show that in the fault process zone ahead of the upper fault tip, which is twice as wide as the damage zone, seismic pumping caused suprahydrostatic fluid pressures and that local dilation promoted the nucleation of a highly permeable mesh of conjugate extensional shear fractures hosting calc-silicate mineralization. The thermal difference between hydrothermal minerals in the conjugate fracture mesh and the host rock is 60–90 °C. The mineralizing fluids were deeply sourced from metamorphic reactions. Propagation of the upper fault tip caused process zone folding and incorporation into the fault damage zones. As the upper fault tip breached through shallower structural levels, it favored mixing between deep and meteoric fluids.

1. INTRODUCTION

Fluid-rock interactions have been widely studied to better understand fluid migration and accumulation and their effects on compositional, petrophysical, and rheological rock modifications during deformation (Nesbitt and Muehlenbachs, 1989; Evans and Battles, 1999; Roure et al., 2005; Vilasi et al., 2009; Vandeginste et al., 2012). Textural, geochemical, and microthermometric analyses of syntectonic vein cements allow constraint of paleofluid properties, such as their origin, migration pathways, temperature and pressure of crystallization, and the local state of stress during deformation (Mullis, 1979, 1987, 1988; Carter and Dworkin, 1990; Fisher et al., 1995; Muchez et al., 1995; Milliken et al., 1998; Montomoli et al., 2001; Montomoli, 2002; Clemenzi et al., 2014; Honlet et al., 2017). In particular, when deformation is thick-skinned, regional-scale fault systems with kilometric offsets are characterized by highly connected fracture networks in their damage zones, which are preferential sites for fluid migration and mixing from the metamorphic basement up to surficial aquifers (Gratier et al., 2002; Beaudoin et al., 2011; Doglioni et al., 2014; Mamadou et al., 2016; Laurent et al., 2017; Wüstefeld et al., 2017). Cements hosted in fault-related fractures commonly record a multi-stage paleofluid and deformational evolution characterized by dissolution-reprecipitation processes and repeated, episodic fracturing (Phillips, 1972; Ramsay, 1980; Parry and Bruhn, 1987; Fisher et al., 1995; Parry, 1998). The latter can be related to the earthquake cycle that, depending on whether seismic pumping or fault-valve occurred (Sibson et al., 1975, 1988), causes high fluid pressures in fault zones after or before earthquake ruptures, respectively (McCaig, 1988; Boullier and Robert, 1992; Cox, 1995; Robert et al., 1995; Cox, 1999). Therefore, cement patterns in seismically active fault damage zones can provide important exhumed analogues to better understand the properties of fluids involved in seismic ruptures at depth. The permeability of fault zones major components, which can act as either conduits, barriers, or mixed conduits-barriers systems, exerts a first-order control on the generation of fluid pressures and fluid flow. Fault zones with kilometric displacement affecting sandstones are typically characterized by low-permeability cores and highly permeable damage zones (Caine et al., 1996; Faulkner and Rutter, 2001; Faulkner et al., 2010). The latter, however, are heterogeneous rock volumes, which can be subdivided in wall damage zones, tip damage zones, and linking damage zones (*sensu* Kim et al., 2004) according to their structural position. Tip damage zones, or process zones (*sensu* Cowie and Shipton, 1998) and linking damage zones, at the tips of propagating faults, have higher permeability due to extensive fracture nucleation with multiple orientations and are preferential sites for fluid flow compared to wall damage zones (Curewitz and Karson, 1997). Accordingly, process zones

[†]alessio.lucca@studenti.unipr.it

GSA Bulletin; https://doi.org/10.1130/B32029.1; 17 figures; 3 tables; Data Repository item 2018298.

For permission to copy, contact editing@geosociety.org
© 2018 Geological Society of America

and linking damage zones can enhance deep fluid advection, producing positive temperature anomalies and chemical and barometric disequilibrium between fluids and host rocks. However, fluid sources and pathways and, consequently, the scales of fault-controlled fluid flow deserve further investigations, as well as the relationships between vein infilling phases and damage zone evolution during fault growth.

In this contribution we present the results of a study of the structural architecture and paleofluid evolution recorded in fault-related veins of the Compione fault zone, a segment of the about 30-km-long Northern Lunigiana high-angle basin-boundary extensional fault system cross-cutting the whole nappe pile in the inner portion of the Northern Apennines (Fig. 1). The Northern Lunigiana Fault started developing since Early Pliocene times during the uplift and exhumation of the Apenninic tectonic wedge and is still active today (Boncio et al., 2000; Eva et al.,

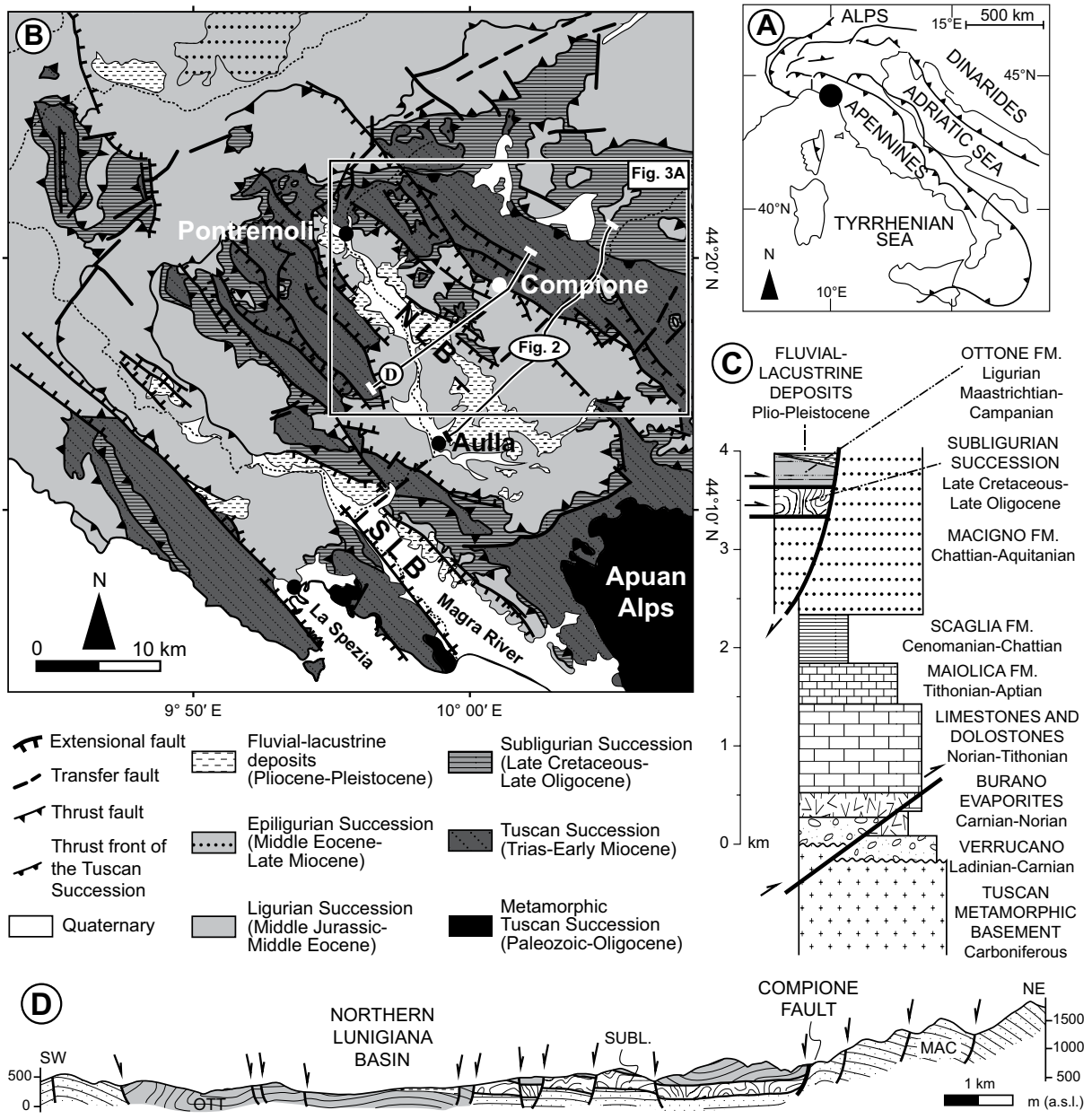


Figure 1. (A) Location of the study area, in the inner part of the Northern Apennines, Italy. (B) Tectonic sketch map of the region where the Lunigiana extensional basin developed (modified from Bernini, 1997); the black and white traces indicate the geologic cross-section represented in (D) and the seismic line in Figure 2, while the black and white rectangle represents the area shown in Figure 3A. NLB—Northern Lunigiana basin; SLB—Southern Lunigiana basin. (C) Schematic column of the inner Northern Apennines stratigraphy. (D) Geological cross-section passing through the studied segment of the Compione extensional fault zone (after Bernini and Papani, 2002). OTT—Ottone Flysch Formation; MAC—Macigno Sandstones Formation; SUBL.–Subligurian Succession; m (a.s.l.)—meters above sea level.

2014; Bonini et al., 2013). The Compione Fault accumulated about 1.5 km of displacement (Bernini and Lasagna, 1988; Bernini, 1991; Bernini and Papani, 2002) and offers suitable exposure conditions for performing a representative structural transect across the fault zone. A multidisciplinary dataset was collected, including independent geothermometers to evaluate thermal anomalies, and geochemical analysis to constrain the fluid sources. Structural analysis was combined with vein cement petrography and optical cold cathodoluminescence (CL), scanning electron microscope-energy dispersive system (SEM-EDS) analysis, carbon and oxygen stable isotope analysis, and microthermometry. Moreover, maximum paleotemperatures recorded in the Macigno Sandstones Formation were constrained by vitrinite reflectance of organic matter and thermal modeling.

Our results show that hydrothermal calc-silicate mineralization occurred in the process zone fracture mesh during upward propagation of the Compione Fault, from fluids at temperatures higher than at the burial peak in the host rock and synchronously with methane migration. Crystallization temperatures of hydrothermal minerals in the footwall damage zone record the progressive cooling/exhumation and folding of the process zone fracture network by extensional fault-propagation folding (Withjack et al., 1990; Schlische, 1995; Hardy and McClay, 1999; Ferrill et al., 2004a; Jin and Groshong, 2006), causing shear reactivation of favorably oriented hydrothermal fractures. We propose a model where mineralization preferentially forms in process zones ahead of propagating fault-tips and fluids responsible for fault-related mineralization are supplied by the metamorphic basement and by the different stratigraphic horizons cut by the fault zone through a seismic pumping mechanism.

2. GEOLOGIC SETTING

The Apennines segments of the Alpine-Himalayan orogenic belt were growing in Cenozoic times due to the southwestward subduction and related slab retreat of the Adria microplate below the overriding European plate (Principi and Treves, 1984; Malinverno and Ryan, 1986; Royden, 1988; Dewey et al., 1989; Patacca et al., 1990; Doglioni, 1991; Jolivet et al., 1998). Two major paleogeographic domains are telescoped in the Apennines: the ocean-derived Jurassic to Paleogene Ligurian succession and the Adria passive margin domain (Boccaletti et al., 1971; Elter and Pertusati, 1973; Elter et al., 1975). The Subligurian domain was originally located in the ocean-continent transition (Plesi, 1975; Montanari and Rossi, 1982; Vescovi, 1998). Building up of the Northern Apennines thrust wedge included underthrusting up to 15–20 km depth and greenschist facies metamorphism (Apuan Alps in Fig. 1; Di Pisa et al., 1985; Franceschelli et al., 1986; Jolivet et al., 1998; Molli et al., 2000a, 2000b, 2002); while the non-metamorphic successions (Tuscan, Subligurian, Ligurian, Epiligurian successions in Fig. 1) were affected by synorogenic extension episodes (Carmignani and Kligfield, 1990; Carmignani et al., 1994; Decandia et al., 1998; Jolivet et al., 1998; Molli, 2008; Clemenzi et al., 2014) and out-of-sequence thrusting (Storti, 1995; Argnani, 2002; Boccaletti et al., 2011; Bonini et al., 2013; Clemenzi et al., 2014). Extensional faulting and magmatism took place since upper Miocene to Pleistocene times and migrated northeastward behind the advancing thrust fronts (Elter et al., 1975; Serri et al., 1993; Bartole, 1995; Carmignani et al., 1995; Barchi et al., 1998; Martini et al., 2001).

Conditions of deformation in the non-metamorphic, dominantly carbonatic thrust sheets of the Northern Apennines have been determined through different methodologies: vitrinite reflectance (Reutter et al., 1981; Corrado et al., 2010; Carlini et al., 2013), illite crystallinity (Cerrina Feroni et al., 1983; Carosi et al., 2003; Carlini et al., 2013), stable isotopes (Carter and Dworkin, 1990; Milliken et al., 1998; Mazzarini et al., 2010; Clemenzi et al., 2014), calcite-dolomite geothermometry (Carosi et al., 2003), fluid inclusion microthermometry (Montomoli et al., 2001; Montomoli, 2002; Mazzarini et al., 2010; Clemenzi et al., 2014), and apatite and zircon fission tracks (Abbate et al., 1994; Zattin et al., 2002; Balestrieri et al., 2003; Bernet et al., 2004; Fellin et al., 2007; Corrado et al., 2010; Thomson et al., 2010; Carlini et al., 2013). The estimated maximum burial is about 7 km at temperatures ranging between 200 and 250 °C. Geothermal gradients calculated with different methodologies span a wide range from 18 to 41 °C/km with a mean value of 31 ± 4 °C/km (Molli et al., 2011).

2.1. The Northern Lunigiana Basin

The Northern Lunigiana Extensional Basin (NLB) is about 25 km long and 10 to 15 km wide. It is the northwesternmost onshore extensional basin in the Northern Apennines and is located to the northwest of the Alpi Apuane metamorphic complex, on the Tyrrhenian Sea side of the orogenic wedge (Fig. 1). The Northern Lunigiana Basin is separated from the Southern Lunigiana Basin by the Secchia transversal line (Fig. 1B; Ghelardoni, 1965). The Northern Lunigiana Basin developed in the hanging wall of a regional-scale out-of-sequence thrust (Storti, 1995; Vescovi, 2005; Clemenzi et al., 2014; Molli et al., 2018) that caused duplexing of the Northern Apennines nappe pile, i.e., subligurian rocks overthrusting the Adria-derived Tuscan succession and overlain by Ligurian thrust sheets (Fig. 1D). As a result of such multiple thrusting events, the basin-boundary fault system juxtaposes the Cretaceous Ligurian Ottone Flysch Formation in the hanging wall, against the Late Oligocene–Early Miocene Macigno Sandstones Formation in the footwall (Figs. 1B and 1D; Elter and Schwab, 1959; Giglia, 1974; Elter et al., 1975; Bernini and Lasagna, 1988). The Campanian to early Maastrichtian Ottone Flysch Formation has a maximum thickness of 300–400 m and is composed of marly calcareous turbiditic and calcarenitic to lithoarenitic strata. The Chattian to Aquitanian Macigno Sandstones Formation is in the studied area about 2300 m thick and is composed of massive sandstone strata in the lower and upper part of the formation, separated by clay- and silt-rich strata (Ghibaudo, 1980). Massive sandstone beds are up to 5 m thick, while the silty and clayey facies beds are a centimeter up to maximum 1.5 m thick. Macigno sandstones are arkoses and contain abundant quartz, feldspars, biotite, muscovite, and chlorite.

The onset of extension in the NLB has been dated using palynology and mammal fauna (Azzaroli, 1950, 1977; Federici, 1978, 1981; Raggi, 1985; Bertoldi, 1988, 1995) in the fluvial-lacustrine deposits that rest on the Ottone Flysch Formation in the depressed central area. These data indicate that two sub-basins developed in response to extensional tectonics: Aulla-Olivola in the SE and Pontremoli in the NW, starting from Early Pliocene and Early Pleistocene times, respectively. The deposits follow a regressive trend from lacustrine to alluvial-fan at the top. In the SE they are characterized by two unconformities, the first Late Pliocene in age and the second dated at Middle Pleistocene times, which occurs also in the Pontremoli depocenter (Boccaletti et al., 1992; Boccaletti and Sani, 1998; Bernini and Papani, 2002). Extension is interpreted to be active during a general uplifting phase of the inner Apenninic belt (Bartolini et al., 1982; Cerrina Feroni et al., 1983; Bernini et al., 1990; Di Naccio et al., 2013).

Both the Northern and the Southern Lunigiana extensional basins are tectonically active, as indicated by extensional earthquakes occurring at depths typically shallower than 15 km, as well as few contractional ones having their hypocenters at about 50 km (Bossolasco et al., 1973; Bossolasco et al., 1974; Augliera et al., 1990; Frepoli and Amato, 1997; Boncio et al., 2000; Eva et al., 2014; Bonini et al., 2013).

This is further supported by morphotectonic evidence (Di Naccio et al., 2013). The NLB formed above a northeastward-dipping low-angle detachment fault (Artoni et al., 1992; Camurri et al., 2001; Argnani et al., 2003; Di Naccio et al., 2013) and it attains a half-graben geometry produced by the activity of the NW-SE–striking, SW-dipping Northern Lunigiana basin-boundary extensional fault system (Bernini, 1988; Bernini and Lasagna, 1988; Bernini, 1991; Bernini and Papani, 2002). The asymmetric topography, with the Apenninic watershed to the NE (Fig. 1D), the northeastward tilt of syn-extensional deposits (Bernini, 1988), and morphotectonic evidence (Di Naccio et al., 2013) support the importance of the Northern Lunigiana extensional fault system in controlling the development of the NLB. In the study area, the NLB is bounded to the NE by the Compione Fault (Figs. 1B, 1D, and 2; Fig. DR1[1]), which can be considered the SE prosecution of the Groppodalosio fault (Fig. 3). Subsurface information provided by a seismic line located in the study area (Figs. 1B and 2) is quite scarce due to the poorly imaged geological complexity of the region (Fig. 2). The proposed geometry shows the Compione Fault cutting through the thrust sheet pile and penetrating into the seismic basement, as previously mapped (Argnani et al., 2003; Camurri et al., 2001), at around 6 to 7 km depth with an almost planar geometry (Fig. 2A and 2B), confirming its role in shaping the NLB. At the surface, the Compione Fault is located at the forelimb-crest transition of the anticline associated with the regional-scale out-of-sequence thrust (Figs. 1D, 3A, and 3B; Vescovi, 2005; Clemenzi et al., 2014; Molli et al., 2018). Synthetic fault zones occur in the footwall, whereas several synthetic and antithetic fault zones dissect the hanging wall (Bernini, 1991; Bernini and Papani, 2002).

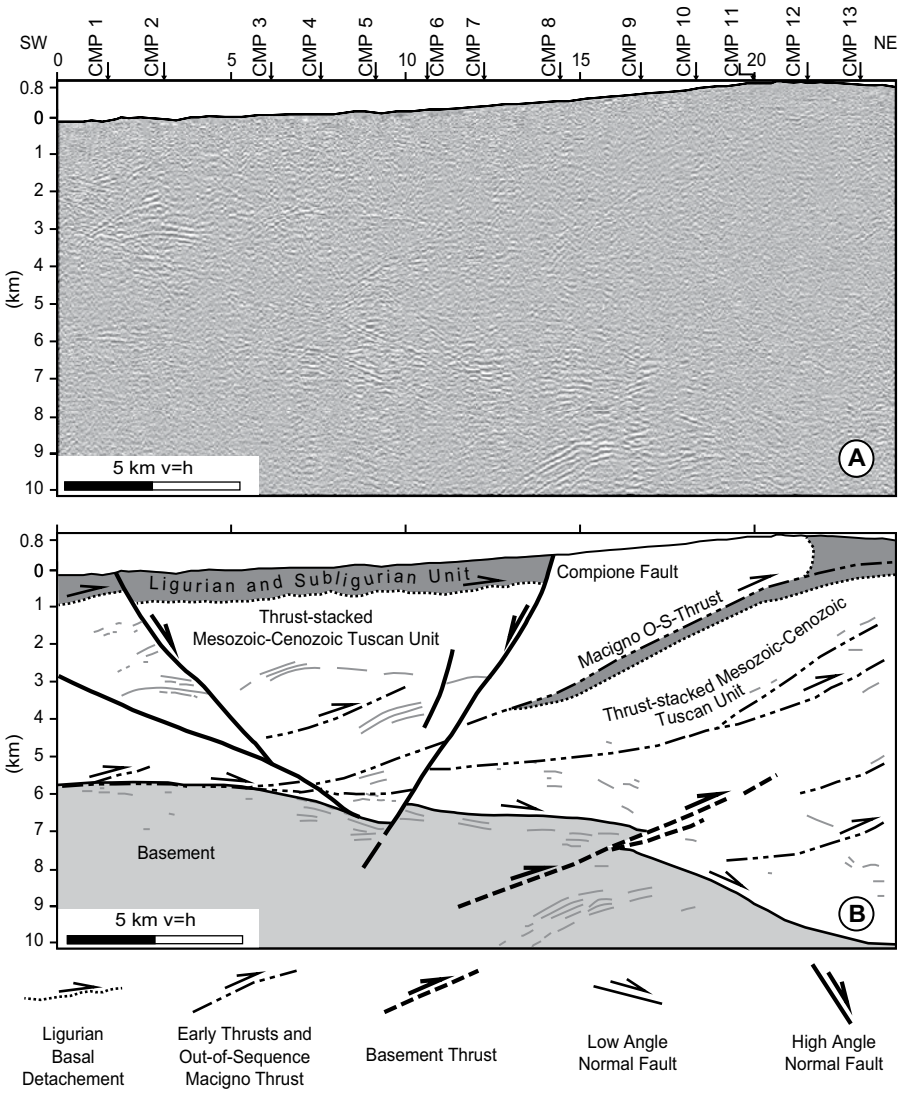


Figure 2. (A) Depth converted seismic line and (B) line drawing highlighting the geometry of the Compione Fault, Northern Apennines, Italy, in the subsurface (segment of a seismic reflection profile acquired from Eni S.p.A.). The seismic reflection profile is depth converted with the Move Software (provided by Midland Valley Exploration Ltd.). By using the "User defined tables/checkshots" method, 13 Time/Interval Velocity tables were defined for the common mid-point (CMP) gathers (CMP1–CMP13 in A). The interval velocities derive by Dix conversion of stacking velocity used for the processing sequence as provided for this seismic profile. The Dix interval velocities are in between 3130 and 7644 m/sec, they had an overall increase down to 5 sec (two-way time) in the seismic reflection profile before depth conversion. v=h—vertical equals horizontal.

3. METHODS

3.1. Structural Analysis

About 600 structural data were collected at six structural sites, five of which located in the fault damage zones and one in the footwall host-rock, for comparative purposes. Structural data are reported according to the right-hand rule (strike/dip), and stereographic projections (lower hemisphere of Schmidt net) are plotted with the Daisy3 software (Salvini, 2017).

[1]GSA Data Repository item 2018298, including structural sites and samples list, and stable isotopic, microthermometric, and SEM-EDS analyses results, is available at http://www.geosociety.org/datarepository/2018 or by request to editing@geosociety.org.

3.2. Petrography and Cathodoluminescence

Fifty veins were sampled in fault damage zones and in the hanging wall host rocks. Moreover, three more sampling sites were identified along strike of the footwall damage zone, to the west of the study transect, at a distance of 0.7, 1.75, and 15 km from it (Figs. 3A and 3C). Each sample was cut in two slabs, one of which was stained with Alizarin Red and potassium ferricyanide to discriminate the different carbonates such as calcite and dolomite and their iron-rich equivalents (Dickson, 1966). Thin sections and wafers were obtained from the other slab. Petrographic and microstructural analyses were carried out on fifty 30-µm-thick thin sections, through standard optical and cold CL microscopy. A Zeiss Axioplan 2 microscope was

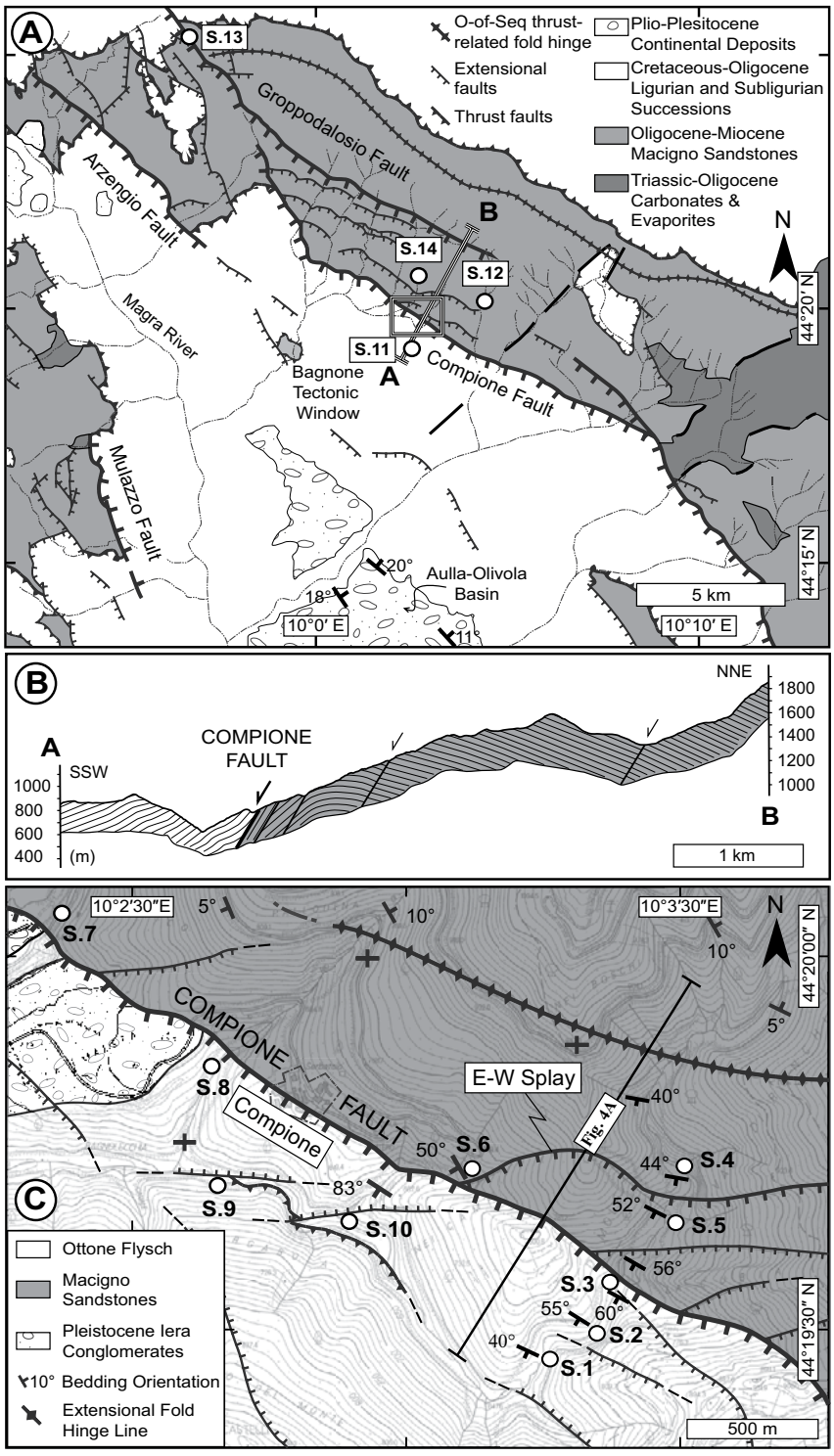


Figure 3. (A) Simplified structural map of the Northern Lunigiana, Northern Apennines, Italy, extensional basin showing the main extensional fault zones that constitute the Northern Lunigiana extensional fault system, bounding the basin to the NE. The black and white trace A–B and the rectangle refer to (B) and (C), respectively. (B) Schematic geological cross-section showing the geometry of the extensional fault propagation fold in the footwall damage zone of the Compione extensional fault zone, overprinting the out-of-sequence (O-of-Seq) thrust-related fold geometry. (C) Structural map of the study area showing structural and sampling sites (S).

used for optical petrography. A Technosyn 8200 Mark II cold CL stage, mounted on a LEICA DM2700P optical microscope, was used at 15 kV and 220–250 µA gun current to perform CL analysis. Compositional analyses were carried out on prehnites with a Jeol 6400 SEM equipped with an Oxford EDS. Operating conditions were 15 kV and 1.2 nA, an electron beam with a diameter of about 1 µm and a counting time of 100 s. Errors are ±2–5% for major elements and ±5–10% for minor components. Standards used to calibrate the EDS include pure elements, simple oxides, and simple silicate compositions (cobalt, anorthoclase, apatite, augite, microcline, and olivine).

3.3. Carbon and Oxygen Stable Isotopes

Stable isotope analyses for oxygen and carbon were performed on host rocks carbonate components and on calcite cements previously identified by petrography and CL. Carbon isotope results are expressed in Vienna Peedee belemnite (VPDB) while oxygen isotope results are expressed both in VPDB and in Vienna standard mean ocean water (VSMOW) for convention purposes. $\delta^{18}O$ values were converted using the equation (Friedman and O'Neil, 1977):

$$\delta^{18}O \text{ SMOW} = 1.03086 \times \delta^{18}O \text{ VPDB} + 30.86 \quad (1)$$

Stable isotope analyses for oxygen and carbon (cf. paragraph 5.2) were carried out on 98 sub-samples of veins and host rocks. Sub-samples were drilled directly from 33 thin sections using an ESI New Wave Research Micromill with a 6.7× to 40× optical zoom, 3.3 mm to 24.5 mm field-of-view, automated 50 mm travel in X, Y, and Z directions stage with sub-micron step resolution and a milling chuck speed ranging from 1200 rpm to 35,000 rpm. 100–150 µg of pure carbonate powder for each sub-sample were loaded into a GasBenchII autosampler interspaced with three isotopically different kinds of reference materials (NBS18, NBS19, and MAB99). After flushing the vessels with ultrapure helium (5.5 grade) in order to replace the air, powders were reacted with 100% orthophosphoric acid at 25 °C for 12 h (McCrea, 1950). Resulting gases were analyzed automatically using a Thermo Finnigan Delta V+ mass spectrometer. For each sample, four reference

gas peaks were measured and the sample gas was introduced ten times into the mass spectrometer. Each sample was analyzed at least in double so the uncertainty on the samples value may be considered ±0.10‰ and ±0.23‰ for $\delta^{13}C$ and $\delta^{18}O$, respectively. Isotope fractionation curves were calculated according to O'Neil et al. (1969).

3.4. Micro-Raman

Micro-Raman measurements were performed using a Jobin-Yvon Horiba LabRam spectrometer equipped with a He-Ne laser (emission line 632.8 nm) and motorized XY stage. The spectral resolution is about 2 cm^{-1}. The confocal hole was adjusted in order to obtain a spatial resolution (lateral and depth) of 1–2 µm. Spectra were obtained using a 50× objective (0.75 N.A. [numerical aperture]). The calibration was made using the 520.7 cm^{-1} Raman line of silicon. The scanned spectral range spans from 1100 to 3300 cm^{-1}. Acquisition time was 120 s. The power on the sample surface is around 1 mW but the power on the analyzed inclusions has to be considered lower due to light reflection and scattering.

3.5. Fluid Inclusion Microthermometry

Fluid inclusions were studied in 44 wafers, i.e., doubly polished sections with a thickness of about 100 µm. Fluid inclusion petrography was carried out on a standard petrographic microscope in order to distinguish assemblages, trails, and isolated inclusions. Fluid inclusion assemblages (FIAs) are groups of inclusions that occur along growth zones or randomly in the minerals and represent the fluid conditions during precipitation or recrystallization (Goldstein and Reynolds, 1994). FIAs were systematically measured. Fluid inclusion trails (FITs) are related to fracturing events after crystallization of at least part of the host mineral and were not considered during microthermometric analysis. Isolated inclusions were measured and were considered reliable if they showed comparable temperatures to the inclusions organized in FIAs in the same sample. After fluid inclusion petrography, the doubly polished wafers were broken in smaller pieces (chips) and analyzed in a Linkam THMSG600 heating-freezing stage. The instrument was calibrated weekly using SynFlinc synthetic standards. Calibration lines were calculated from melting temperature of CO_2, final melting temperature of clathrate, homogenization temperature of CO_2, NaCl eutectic temperature, final ice melting temperature of pure H_2O, and the critical homogenization temperature of pure H_2O. Three temperatures were acquired in aqueous biphase inclusions: (1) homogenization into the liquid phase (Th_{tot}) indicating the minimum temperature of fluid entrapment; (2) first melting temperature (Tfm), related to the fluid composition; (3) ice melting temperature (Tm_{ice}), which is inversely proportional to the amount of solutes in the liquid phase, i.e., the salinity of the fluid. Heating was always performed before freezing runs to avoid artificial stretching of the inclusions during freezing. Monophase gaseous inclusions at room temperature develop a liquid meniscus during cooling in the heating-freezing stage. In these gaseous inclusions, only Th_{tot} was measured and homogenization occurred into the vapor phase. Monophase aqueous inclusions were kept in a freezer for two weeks at –20 °C to nucleate bubbles in metastable inclusions. Inclusions that did not nucleate the vapor phase, were cyclically heated and frozen to induce artificial stretching. In this way, it was possible to measure Tm_{ice} in monophase inclusions. Homogenization temperatures are evidently not measured in artificially stretched aqueous inclusions. Accuracy of measurements is ±2 °C for homogenization temperatures (Th_{tot}) and ±0.2 °C for first melting (Tfm) and ice melting temperatures (Tm_{ice}).

3.6. Organic Matter Optical Analysis and Thermal Modelling

Ten organic-rich laminae were sampled in the footwall damage zone (sites 4 and 5) and in the footwall host rock (Site 14) to constrain the thermal maturity of the Macigno Sandstones Formation through vitrinite reflectance analyses. Vitrinite is the product of thermal maturation of terrestrial plant remnants included in sediments and it is one of the most reliable indicator of peak temperatures at maximum burial depth because it is very sensitive to temperature increase and not affected by retrograde processes (Teichmüller and Teichmüller, 1967; Tissot and Welte, 1984; Teichmüller, 1987). Samples for vitrinite reflectance analyses were crushed and then mounted in epoxy resin and polished, according to the method of Bustin et al. (1990). Samples were analyzed in reflected, non-polarized, monochromatic light (λ = 546 nm) under oil immersion (ν = 1.518) using a Zeiss Axioplan MPM400 microscope equipped with a J&M Analytik Tidas S 800 spectrometer and calibrated with CRAIC vitrinite reflectance standards. Up to 40 Ro% (randomly oriented vitrinite reflectance in oil immersion) measurements per sample were acquired. Thermal modeling was carried out using the BasinMod2 software, based on the Easy%Ro kinetic model of Burnham and Sweeney (1989). The software requires organic maturity indicators, sedimentary successions lithologies, thicknesses, and ages along with paleo-heat flow or paleo-geothermal gradient as basic input data. Sample stratigraphic locations were modelled as a pseudo-well according to Oncken (1982), Di Paolo et al. (2012), Caricchi et al. (2015), and Schito et al. (2018). The main assumptions for the modeling are: (1) decompaction of the burial curves is corrected according to the method of Sclater and Christie (1980); (2) sea-level changes are neglected, as the thermal evolution is influenced more by sediment thickness than water depth (Butler, 1992); (3) thrusting is considered instantaneous when compared with the duration of sedimentation, as generally suggested in theoretical models (Endignoux and Wolf, 1990); (4) geothermal gradient (25–30 °C/km) is calculated from the correlation of vitrinite reflectance data based on the kinetic model of vitrinite maturation of Burnham and Sweeney (1989).

4. STRUCTURAL ARCHITECTURE OF THE COMPIONE FAULT

The area near Compione village was mapped in detail to describe the structural architecture of the Compione Fault, which strikes ~NW-SE and dips to the SW (Fig. 3C). The two different lithologies observed determine different deformation patterns in the footwall and in the hanging wall, respectively (Figs. 4A–4C). In the footwall, Macigno Sandstones Formation strata dip 5°–10° towards the NE in the footwall far from the fault zone. Approaching the footwall damage zone, bedding is progressively tilted towards the SW to become horizontal at around 0.7 km distance from the fault core, then SW-dipping of ~40° at around 0.5 km, and up to 55° at the damage zone-fault core transition. Similarly, the Ottone Flysch Formation in the hanging wall is characterized by strata that dip ~60° SW in proximity of the fault core and become subhorizontal outside the hanging wall damage zone (Figs. 3B, 3C). A major E-W–striking, S-dipping fault zone occurs to the ESE of Compione village (Fig. 4C), abutting the Compione Fault, as well as subsidiary fault segments, to the south (Fig. 3C). The Compione fault zone has a core of up to 50 m wide, consisting of deformed shear lenses of mostly Macigno Sandstones Formation, bounded by anastomosed shear bands of comminuted, incoherent sand and gouge (Bernini and Lasagna, 1988). In the northwestern corner of the map, the Compione Fault affects a Pleistocene conglomerate consisting of boulders and pebbles of Macigno Sandstones Formation, named Iera Conglomerate (Fig. 3C; Bernini and Papani, 2002).

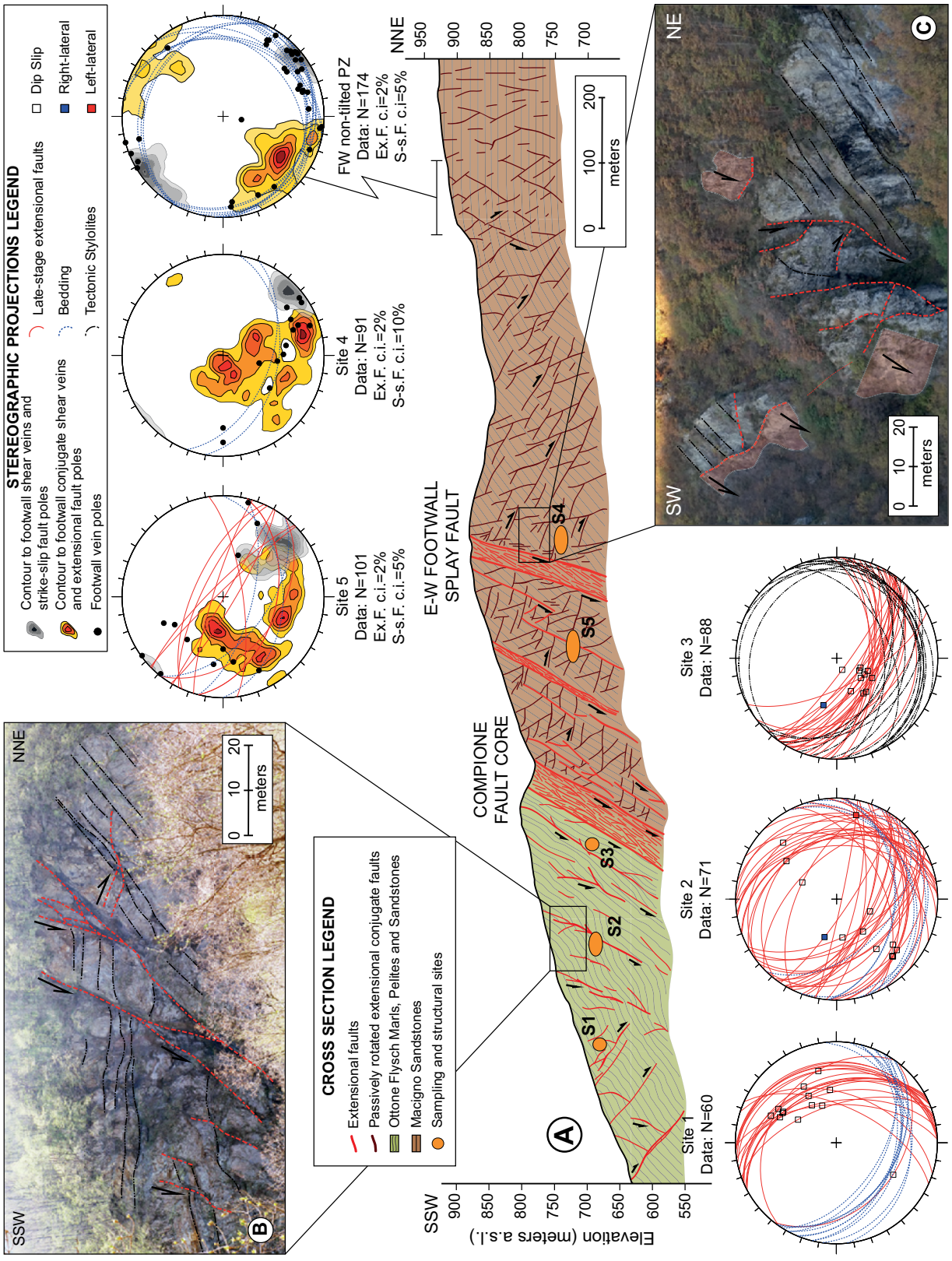


Figure 4. (A) Geologic cross-section across the Compione fault damage zone, Northern Apennines, Italy, and stereographic projections of structural data (Schmidt lower hemisphere). The trace of the section is indicated in Figure 3C. Ex.F. c.i.—Extensional Faults contouring interval; S-s.F. c.i.—Strike-slip Faults contouring interval; FW non-tilted PZ c.i.—Footwall non-tilted Process Zone contouring interval; meters a.s.l.—meters above sea level. (B) Outcrop picture and line drawing of the hanging wall damage zone at Site 2, showing synthetic extensional faults in the Ottone Flysch Formation. (C) Outcrop picture and line drawing of the footwall damage zone at Site 4, showing the major E-W footwall splay extensional fault zone; red areas highlight the master slip surface.

4.1. Footwall Damage Zone

The most abundant deformation structures in the footwall damage zone are conjugate shear vein pairs inclined at ~60° to bedding in both dipping directions and with bisector lines perpendicular to bedding regardless of bedding dip (Figs. 5A, 5B). Outside the damage zone, 900 m to the fault core, veins occur only associated to subsidiary extensional faults with metric offset. In the outer boundary area, where strata are subhorizontal, vein orientation is N306°, 60° for the antithetic set and ~N120°–N140°, 60°–80° for the synthetic (Figs. 4A and 5B). Conjugate shear vein arrays are passively rotated with bedding at decreasing distance from the fault core (Figs. 5C, 5D). Such a rotation and the activity of late subsidiary fault zones causes significant dispersion of vein strike, which varies from NNW-SSE to E-W. This is evident when shear vein data collected in subsidiary fault-bounded blocks to the north and south of the major E-W–striking fault zone are rotated to restore local bedding attitude to horizontal (Fig. 6). The dip direction in non-rotated data varies from north to eastward (Fig. 6A). Rotation systematically produces conjugate arrays striking either NW-SE or E-W, respectively (Fig. 6B). In addition to fault-parallel conjugate shear vein arrays, cross-fault veins striking almost perpendicular to the Compione Fault are also abundant (Fig. 4).

Most fault-related veins are reactivated as strike-slip (cross-fault veins) or conjugate extensional faults (fault-parallel veins; Fig. 5E). Strike-slip faulting in the area is related both to lateral propagation of the Compione fault zone and to the far-field stress of the left-lateral Secchia transversal line, 4 km to the east of the study area. These fault-related shear veins and faults (extensional and strike-slip) are well developed especially in coarse strata, have offsets ranging from centimeters to meters, and are characterized by millimeter to centimeter slickenfibers. Strike-slip and extensional faults mutually crosscut and their slip surfaces frequently show evidence for variable directions of movement (Fig. 5F). In sites 4 and 5, conjugate extensional faults have a more complex pattern that includes two synthetic trends, oriented 255°, 70° and 290°, 56° and two antithetic ones, oriented 350°, 10° and 240°, 30°, respectively. It is important to note that, after bedding restoration to the horizontal, the synthetic sets are 127°, 75° and 75°, 77° and the antithetic sets are 308°, 60° and 257°, 74°, respectively, and that ~E-W–striking conjugate veins show reactivation as strike-slip to oblique-slip subsidiary faults. Reverse kinematics are apparent, indicating that normal to oblique faulting, with top-to-the-WNW shearing, was ongoing during passive bedding rotation in the damage zone sector comprised between the Compione fault core and major E-W footwall splay fault (Fig. 6B). As a result, S- and SW-dipping extensional faults in Figure 6B were re-activated antithetically as soon as they attained a NE-dipping attitude due to bedding rotation. Late-stage faults strike from N110° to N130°, dip 60–80° either to the NE or SW (Fig. 4) and have cores made of cataclastic loose sand and clay smears, bounded by thin slip zones including extremely comminuted material. These late-stage faults occur up to 400 meters from the fault core.

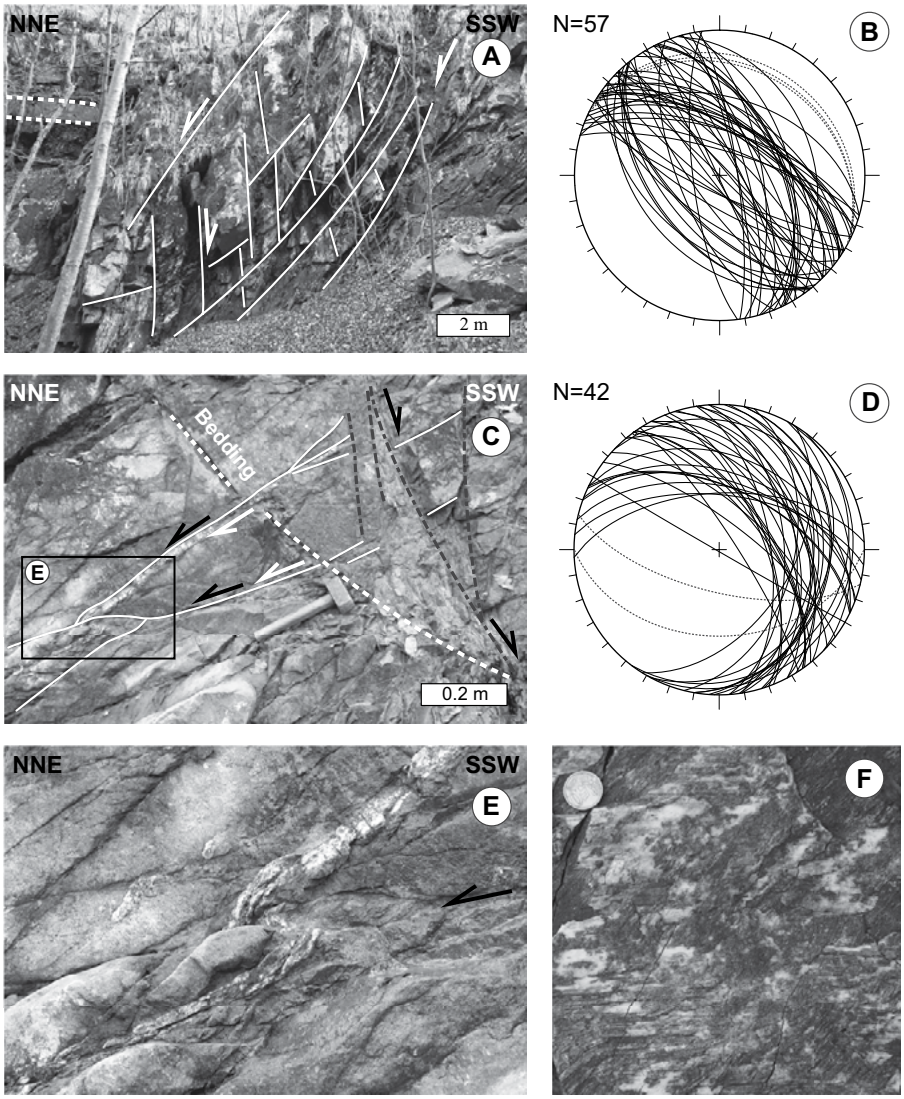


Figure 5. (A) Outcrop picture and line drawing of conjugate shear veins and extensional faults in the footwall damage zone to background transition (44°19′56.65″N 10°3′41.49″E). (B) Stereographic projection of structural data in this area; dashed lines represent bedding. (C) Outcrop picture and line drawing of Site 5; dashed white line corresponds to bedding, white lines highlight conjugate shear veins and faults, and dashed black lines indicate late cataclastic faults; white (black) arrows indicate kinematics before (after) bedding rotation. (D) Stereographic projection of structural data collected at this site. (E) Detail of (C) showing a shear vein reactivated along a synthetic subsidiary fault and later crosscut along an antithetic one. (F) Slickenfibers on a synthetic subsidiary fault showing multiple slip directions; coin for scale.

4.2. Hanging Wall Damage Zone

Subsidiary fault zones mainly arranged in synthetic anastomosed arrays are abundant in the hanging wall damage zone near the fault

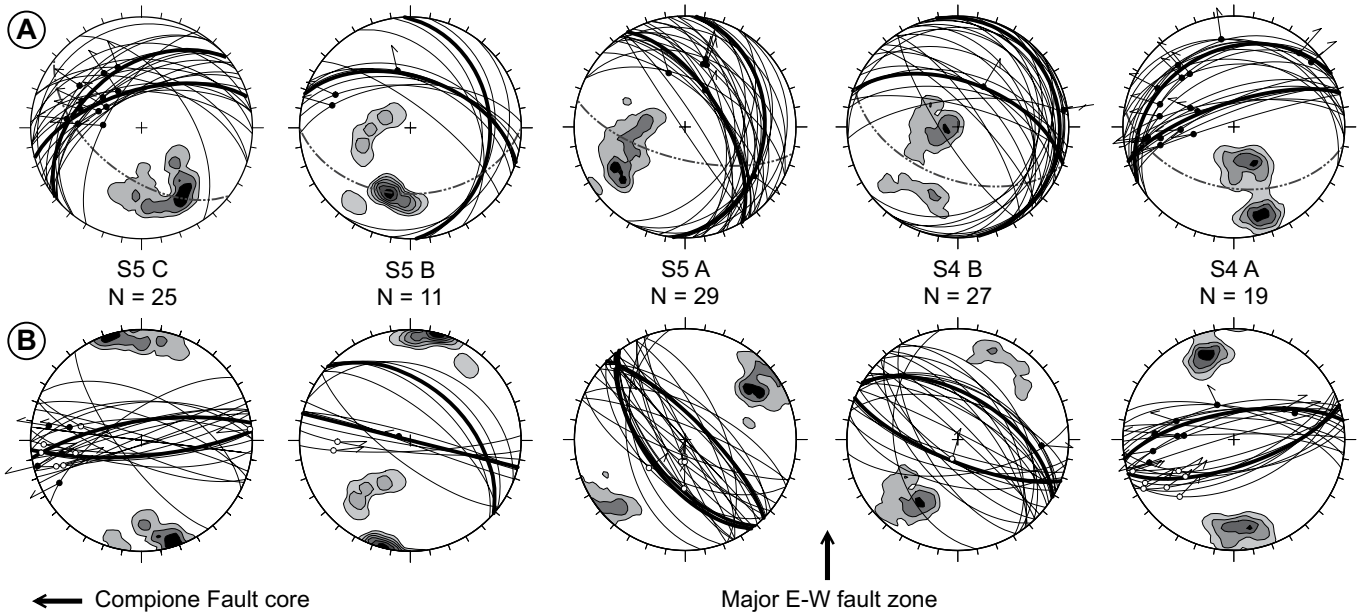


Figure 6. (A) Stereographic projections (Schmidt lower hemisphere) of footwall shear veins and extensional subsidiary conjugate faults, measured at sites 4 and 5, and separated for sectors compartmentalized by late-stage large-scale cataclastic faults. In (B) data are restored to horizontal using the related bedding orientation; black (white) dots indicate normal (reverse) kinematics; reverse kinematics are apparent because of shear reactivation after bedding rotation. S—sampling sites.

core, isolating extensional shear lenses affected by intense pressure solution as indicated by abundant shallow-dipping stylolites (Fig. 4). Moving away from the fault core, both synthetic and antithetic subsidiary faults and fault zones occur, frequently with a ramp-flat geometry. Here very thick beds are cut at high angle and the marly and clayish interlayers are exploited as flat segments, (e.g., Site 2 in Fig. 4) producing significant block tilting about horizontal axes. Eventually, at about 300–400 m away from the fault core of the Compione Fault, the deformation pattern is dominated by high-angle antithetic faults and fault zones (e.g., Site 1 in Fig. 4). Overall, subsidiary faults and fault zones in the hanging wall strike NW-SE, i.e., parallel to the master fault strike, with a subordinate population striking ~E-W and dipping S (e.g., Site 2 in Fig. 4). Abundant veins nearly perpendicular to bedding occur in the hanging wall and crosscut pre-existing bedding-parallel veins. Both populations grew by crack-seal opening (cf. Ramsay, 1980) before the onset of extensional fault-related deformation, during thrusting and stacking of the Ligurian successions. Subvertical veins are passively rotated in the hanging wall blocks of subsidiary fault zones and are commonly reactivated as low-displacement shear surfaces showing slickensides coherent with extensional, almost dip-slip, kinematics.

5. VEIN CEMENT ANALYSIS

5.1. Petrographic Description

Fault-related veins in the footwall damage zone have an aperture varying from 2 to 27 mm and show evidence for antitaxial multiple opening (cf. Durney and Ramsay, 1973; Ramsay and Huber, 1983; Passchier and Trouw, 2005; Bons et al., 2012). Vein cement consists of prehnite, quartz, and three different calcite generations, labelled as MC1A, MC1B, and MC2, respectively (Fig. 7A). Prehnite crystals are generally euhedral to subhedral and their dimension can reach 1500 μm parallel to the *c*-axis and 750 μm orthogonal to it. Prehnite was the first mineral phase to crystallize in columnar-radiating structures that are overgrown by or inter-grown with euhedral to subhedral quartz (Figs. 7A, 7B). When analyzed in cold CL, prehnite luminescence color switches abruptly from "olive green" to "lime green," from the cores towards the rims (Fig. 7B; Huber et al., 2007). Compositional analyses were carried out by SEM-EDS on three prehnite crystals sampled from Site 5. Ten areas were analyzed both along the long and the short axes of the crystals to investigate compositional variations during crystallization. Sixty spectra were acquired and eight of them did evidence calcite contamination, which is often found as isomorphous replacement of prehnite (Figs. 7C, 7D). Analyses results did not evidence any trend in amounts of Fe^{3+}- Al^{3+} along crystal axes from the cores to the rims of crystals. Al_2O_3 ranges between 24.5 and 25.5 wt%, with a mean value of 25.07 ± 0.19 wt%. The mean abundance of SiO_2 is 45.04 ± 0.20 wt%, with values ranging between 44.6 and 45.5 wt%. CaO is comprised between 27.3 and 29 wt% and has a mean value of 27.76 ± 0.23, in agreement with the prehnite formula $Ca_2Al_2Si_3O_{10}(OH)_2$. FeO was detected in 24 spectra and was always below 1 wt%. Quartz sometimes displays bridge structures, growth competition textures, and dissolution embayments (Fig. 7C; Hilgers and Urai, 2002; Bons, 2001; Okamoto and Sekine, 2011). MC1 calcite grew both as isomorphous replacement of prehnite crystals and in the remaining open sites, mostly at the center of fractures. The latter are characterized by poikilotopic rhombohedric crystals up to 1 cm in dimension with abundant Type I and Type II twinning (cf. Burkhard, 1993; Ferrill et al., 2004b) and sweeping extinction (Figs. 7A, 7C, and 7G). Stained MC1 is pink (Fig. 7E), indicating that calcite is non-ferroan (Dickson, 1966). MC1 calcite crystals can be subdivided in MC1A and MC1B: B is mostly characterized by twinning Type I and a "clearer texture" compared to A, which displays abundant twinning Type II. Moreover, MC1A has dark red color in CL while MC1B

is red to orange (Figs. 7B and 7D). Multiple antitaxial opening events (cf. Holland and Urai, 2010; Virgo et al., 2014) caused the cyclic repetition of prehnite + quartz + MC1 calcites bands infilling the veins (Figs. 7E–7G). Shearing of veins caused quartz dynamic recrystallization and formation of straight, micrometric wide mirror surfaces, which truncate vein crystals (Figs. 7E–7G). MC2 is the last cement and is composed of microsparitic to blocky calcite up to maximum 500 μm crystal size, sometimes displaying Type I twinning (cf. Burkhard, 1993). MC2 calcite has bright orange to yellow colors under CL and is hosted in sub-millimetric fracture networks that exploit cleavage surfaces orthogonal and parallel to the *c*-axis of prehnite (Fig. 7A), twinning planes in MC1 calcite and re-opened shear surfaces. Even MC2 calcite, in places, occurs as prehnite isomorphous replacement (Fig. 7H). Veins nearest to the fault core are more intensely affected by shearing, quartz recrystallization, isomorphous replacement of prehnite by MC1 crystals, and by MC2 calcite cementation (Figs. 7G and 7I). In the fault core, in fact, the host rock is disaggregated and cemented by MC2 calcite, which displays an interparticle cement texture (Fig. 7J). Footwall fault-related veins in silt and clay beds have MC1 and MC2 calcite cements (labelled as Macigno host rock calcite cement), but they show a microsparitic texture, whereas prehnite and quartz are absent.

Hanging wall veins, hosted in the Ottone Flysch Formation, are composed of two generations of calcite, labelled as OC1 and OC2, and contain traces of quartz. OC1 calcite veins are considered for comparative purposes only because they formed before the onset of extensional deformation in the studied area. OC2 calcite veins formed by multiple antitaxial fracturing-precipitation events (cf. Holland and Urai, 2010) and crosscut or run parallel to OC1 calcite (Figs. 7K, 7L). OC2 calcites have a blocky texture with a "clear" appearance and dimensions up to 1 mm (Fig. 7K), showing rarely Type I twinning (cf. Burkhard, 1993). Their color under CL is red, slightly brighter than OC1 calcites, but it changes depending on structural position (Fig. 7L). In particular, samples collected less than 50 meters from the fault core have OC2 calcites with the same dull luminescence as the OC1 calcites. Quartz crystals smaller than 100 μm sometimes occur in association with OC2 calcites (Figs. 7M, 7N). A crack-seal bedding parallel vein in the hanging wall damage zone, in proximity of the fault core, shows quartz associated with OC2 calcite, which preserve the prismatic habit of prehnite, similarly to the footwall damage zone cement textures (Fig. 7N). Moreover, close to the fault core, OC2 calcite cement shows a proto-breccia texture in extensional S-C (S—schistosity, C—cisaillement [French for shear]) lithons (Fig. 7O).

Figure 7 (*on following page*). Microphotographs of veins hosted in the footwall and hanging wall damage zones of the Compione extensional fault. (A) Prehnite (Prh) crystals overgrown by quartz (Qz) and MC1 calcite; MC2 calcite grew in dissolution fractures outlined by small dotted white lines (cross-polarized light). (B) Prh growing in columnar-radiating structures, characterized by an abrupt change in luminescence color and MC1A calcite crystals recrystallized in MC1B calcite along crystal fractures,cathodoluminescence (CL) image. (C) Vein composed of euhedral to subhedral Qz rims and MC1 replacive (rep) and rhombohedric (rho) calcite crystals in the center (cross-polarized light). (D) CL detail of (C) showing MC1A and MC1B replacing prismatic Prh crystals. (E) Stained hand sample displaying pink MC1 calcite and composed of five fracturing-sealing increments and/or shear reactivations. (F) Detail of (E) illustrating micrometric wide slip surfaces formed by coseismic slip (cross-polarized light). (G) Shear bands composed of recrystallized Qz subgrains and replacive MC1 calcite crystals (cross-polarized light). (H) Isomorphous replacement of Prh crystals by MC2 calcite (CL). (I) MC1A isomorphous replacements of prehnite crystals cut by late microfractures cemented with MC2 calcite (CL). (J) Sample near the Compione fault core showing disaggregated texture cemented by MC2 calcite. (K) Cross-polarized light image showing OC1 "dirty" and OC2 "clear" calcites textures. (L) CL image highlighting contrast in luminescence colors between OC1 and OC2 calcites from dull red to bright red and pressure solution affecting both OC1 and OC2. (M) Host rock clast in OC1 and late fractures filled by OC2 calcite and quartz (qz). (N) CL image showing detail of a bedding parallel vein where OC2 calcite, associated with qz, isomorphously replaces prehnite crystals. (O) Thin section scan of a breccia-vein composed of OC2 calcite cement collected in extensional S-C (schistosity-cisaillement) structures near the Compione fault core. MC—Macigno Sandstones Formation calcite cements; OC—Ottone Flysch Formation calcite cements.

5.2. Stable Isotopes

Results of carbon and oxygen stable isotopes analyses are summarized in Table 1. MC1 calcites have the most depleted $\delta^{18}O$ values, from +11.8‰ to +14.0 VSMOW while MC2 calcites range from +13.4‰ to +17.9‰ VSMOW. Mean $\delta^{18}O$ is +13.1‰ and +15.8‰ VSMOW for MC1 and MC2 calcites, respectively (Fig. 8A). $\delta^{13}C$ in footwall MC1 and MC2 calcites ranges from –5.8‰ to –0.9‰ and from –7.1‰ to –0.4‰ VPDB, respectively. Plotting $\delta^{18}O$ vs. distance from the Compione fault core for MC1 and MC2 calcites, a slight trend appears (Fig. 8B). In particular, $\delta^{18}O$ values become enriched approaching the fault core. The same plot for $\delta^{13}C$ shows that MC1 and MC2 calcites are characterized by different values depending on structural position (Fig. 8C). Site 5 is located in a different footwall block, compared to other structural sites, and shows depleted $\delta^{13}C$, ranging from –7.1‰ to –3.8‰ VPDB, compared to other sampling sites whose $\delta^{13}C$ is comprised between –2.8‰ and –0.4‰ VPDB (Fig. 8C). MC1 and MC2 calcites from a sample collected near the NW tip of the Compione Fault (Site 13) have $\delta^{18}O$ and $\delta^{13}C$ values that are enriched compared to the bulk of the samples that are located along the studied cross-section of the fault zone (Fig. 8A). The footwall host rock carbonate component is composed of microsparitic calcite crystals, present in silt and clay-sized intervals. It shows $\delta^{18}O$ values between +13.9‰ and +16.0‰ VSMOW and $\delta^{13}C$ from –3.2‰ to –0.7‰ VPDB.

Hanging wall OC1 and OC2 calcites present enriched and more clustered $\delta^{18}O$ and $\delta^{13}C$ values compared to footwall MC1 and MC2 calcite veins. $\delta^{13}C$ values are comparable for hanging wall host rock and both the hanging wall OC1 and OC2 calcite generations. $\delta^{13}C$ in hanging wall carbonates ranges mostly between +1.2‰ and +2.4‰ VPDB, excluding outliers. Mean $\delta^{13}C$ is +1.9‰ VPDB for hanging wall host rock and OC1 calcites, and +1.8‰ VPDB for OC2 calcites. $\delta^{18}O$ values, however, display large variability between hanging wall host rock, OC1, and OC2 calcites, defining a clear horizontally elongated trend in Figure 8A. Host rock $\delta^{18}O$ is between +26.9‰ and +27.5‰ VSMOW; OC1 calcites $\delta^{18}O$ are similar to the host rock, ranging from +23.5‰ to +26.9‰ VSMOW, while OC2 calcites show depleted $\delta^{18}O$ values, comprised between +13.1‰ and +19.7‰ VSMOW (Fig. 8A). Mean $\delta^{18}O$ are +25.7‰ and +16.5‰ VSMOW for OC1 and OC2 calcites, respectively. The OC2 outlier has a $\delta^{13}C$ value of –0.46‰ VPDB, comparable to footwall fault-related veins and corresponds to the replacive calcite shown in Fig. 7N.

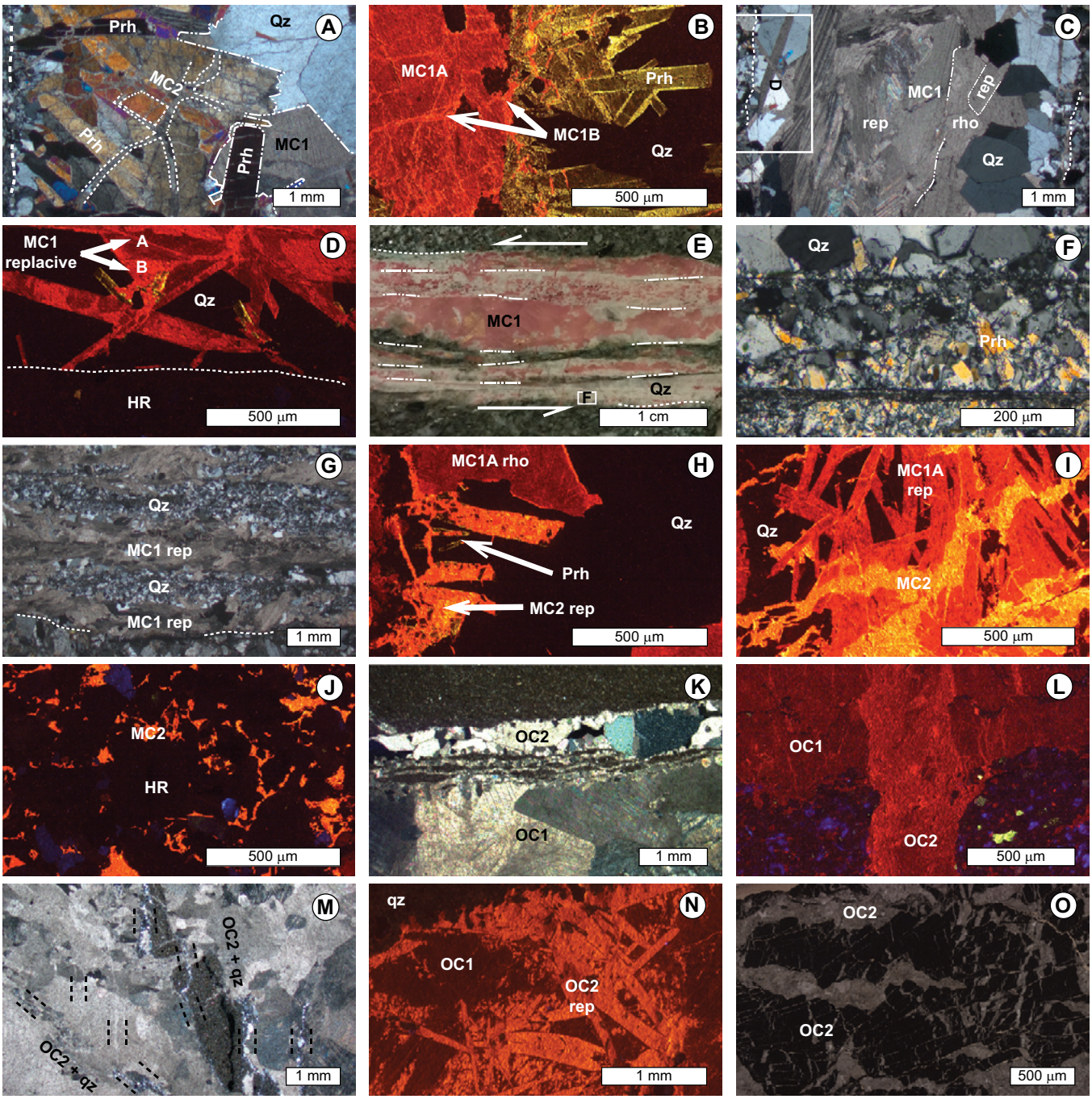


Figure 7.

5.3. Fluid Inclusions

Microthermometry measurements were done on 11 footwall and on 6 hanging wall veins and their results are summarized in Table 2 Quartz in footwall veins shows abundant and clearly visible trails of decrepitated and leaked inclusions. Two types of inclusions have been recognized: biphase aqueous (Q1) and monophase gaseous (Q2). Both of them have a maximum length ranging from 5 to 15 µm and rounded shapes (Figs. 9A and 9C). Only one Q1 primary FIA and two isolated inclusions were large enough to be measured. Vapor to liquid phase ratios are constant and the vapor bubble is less than 15% of the total inclusion volume. Homogenization, always into the liquid phase, occurs between 127 and 215 °C (Fig. 10B) with a mean value of 157 °C. First melting temperatures are in the range of –50 to –45 °C, suggesting a NaCl-$CaCl_2$-H_2O system (Roedder, 1984), and are followed by the hydrohalite melting temperature between –32 and –28 °C. Ice melting temperatures range from –4.8 to –11.4 °C

TABLE 1. SUMMARY OF PETROGRAPHIC OBSERVATIONS AND STABLE ISOTOPES ANALYSIS RESULTS OF THE DIFFERENT CARBONATE CEMENTS

		$\delta^{18}O$ ‰			$\delta^{13}C$ ‰		
Cement	Texture description	Range (VSMOW)	Mean (VSMOW)	st. dev.	Range (VPDB)	Mean (VPDB)	st. dev.
Ottone host rock (n = 4)	Anhedral calcite microcrystals in matrix; non-luminescent in clay-silt size beds; dull luminescent in silt-fine sands beds.	+26.9 to +27.5	+27.2	±0.2	+1.7 to +2.0	+1.9	±0.1
Ottone calcite 1 (n = 26)	Well-developed, rhombohedric "dirty" crystals with abundant twinning Type I, undulose extinction, intercrystalline slip and dissolution surfaces; non- to dull-luminescence.	+23.5 to +26.9	+25.7	±0.7	+1.6 to +2.4	+1.9	±0.2
Ottone calcite 2 (n = 16)	Clean translucent crystals in late fractures with rare twinning Type I; non- to dull-luminescence.	+13.1 to +19.7	+16.5	±1.6	–0.5 to +2.2	+1.8	±0.7
Macigno host rock (n = 3)	Anhedral calcite microcrystals in matrix of fine clay-silt beds; red to orange luminescence.	+13.9 to +16.0	+14.7	±1.1	–3.2 to –0.7	–2.1	±1.3
Macigno calcite 1 (n = 21)	Crystals characterized by twinning Type I and rare Type II, displaying rhombohedric and isomorphously replacing Prh; red (MC1A) to orange (MC1B) luminescence.	+11.8 to +14.0	+13.1	±0.6	–5.8 to –0.9	–3.3	±1.8
Macigno calcite 2 (n = 18)	Crystals in late fractures cross-cutting Prh, Qz, MC1 and locally replacing Prh; orange to yellow bright luminescence.	+13.4 to +17.9	+15.8	±1.2	–7.1 to –0.4	–2.7	±2.0

Note: Data from samples collected in Sites shown in Figures 3A and 3C. VSMOW—Vienna standard mean ocean water; VPDB—Vienna Pee Dee belemnite; st. dev.—standard deviation; Prh—prehnite; Qz—quartz; MC—Macigno Sandstones Formation calcite cements.

(Fig. 10C) with a mean value of –7.2 °C, which corresponds to salinities of 7.6, 15.4, and 10.7 wt% NaCl eq., respectively (Bodnar, 1993). Q2 monophase gaseous inclusions have dimensions similar to Q1 inclusions and a rounded shape. They were measured in three FIAs. Homogenization was into the vapor phase at temperatures ranging from –89 to –83 °C (Fig. 10A). Mean homogenization temperature is –88 °C. No solid was formed in these gaseous inclusions. Q2 inclusions were analyzed through micro-Raman spectroscopy to check their composition. Results of Raman analysis are briefly illustrated in Figure 9B and show a peak at 2914 cm^{-1}, which corresponds to the Raman shift of CH_4. Homogenization temperatures, in agreement with Raman results, indicate that Q2 are monophase CH_4 inclusions.

Fluid inclusions in footwall MC1A calcite are biphase aqueous, with a size from 3 µm to 10–15 µm. They have a negative crystal shape and constant vapor/liquid ratio (Fig. 9D). The vapor phase fills 10 to 15% of the inclusion's volume. Inclusions in MC1A calcite are organized in FIAs and in fluid inclusion (FI) trails that follow twinning planes. FI trails and inclusions near twinning planes were not taken into account during microthermometric measurements. Some inclusions leaked at their homogenization temperatures and some bubbles did not reappear upon cooling. These inclusions were also discarded. A total amount of 22 MC1A inclusions were measured, distributed in six FIAs and three isolated inclusions. MC1A inclusions show homogenization temperatures ranging from 178 to 198 °C. The mean Th_{tot} is 189 °C and the modal peak is between 190 and 195 °C (Fig. 10B). First melting in MC1A inclusions occurred at temperatures between –17 and –21 °C, indicating a H_2O-NaCl composition. The MC1A ice melting temperatures range from –0.8 to –6.2 °C, corresponding to salinities between 1.4 and 9.3 wt% NaCl eq. Mean Tm_{ice}

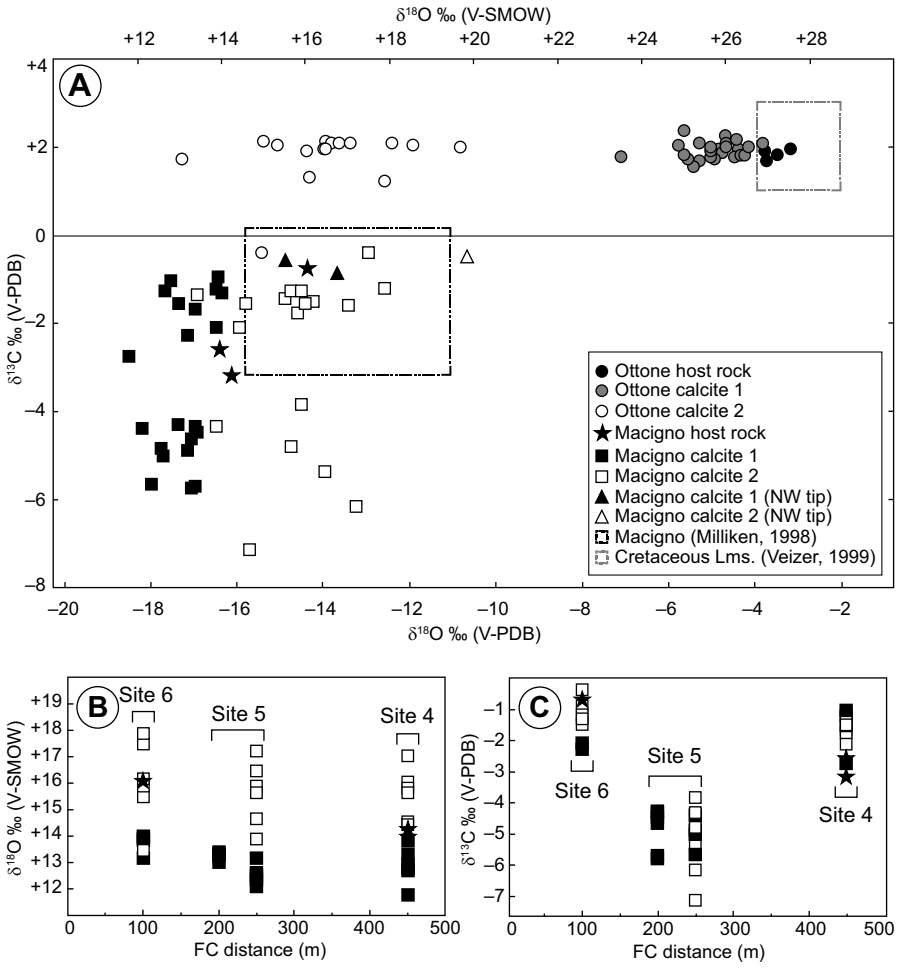


Figure 8. Stable isotope data. (A) $\delta^{18}O$ vs. $\delta^{13}C$ plot of calcite from veins and host rocks; the dashed grey rectangle indicates the range of isotopic values of Cretaceous limestone (Lms.) (after Veizer et al., 1999) and the dashed black rectangle indicates those of Late Oligocene–Early Miocene Macigno Sandstones Formation (after Milliken et al., 1998). (B, C) Plots of $\delta^{18}O$ (B) and $\delta^{13}C$ (C) vs. distance (m) from the Compione fault core, Northern Apennines, Italy. FC—Fault core; VSMOW—Vienna standard mean ocean water; VPDB—Vienna Pee Dee belemnite. In the legend Ottone refers to calcite cements hosted in the Ottone Flysch Formation.

TABLE 2. SUMMARY OF PETROGRAPHIC OBSERVATIONS AND MICROTHERMOMETRY ANALYSIS RESULTS OF QUARTZ AND CARBONATE CEMENTS

Cement	FIA origin and type	Homogenization temperature (°C) range/mean	Ice melting temperature (°C) range/mean	Salinity (eq. wt% NaCl) range/mean
Macigno quartz 1	Primary/pseudosecondary two-phase aqueous	127 to 212/157	–4.8 to –11.4/–7.2	7.6 to 15.4/10.7
Macigno quartz 2	Primary monophase gaseous CH_4	–83 to –89/–88	N.D.	N.D.
Macigno calcite 1A	Primary/pseudosecondary two-phase aqueous	178 to 198/189	–0.8 to –6.2/-2.7	1.4 to 9.3/4.5
Macigno calcite 1B	Primary/pseudosecondary two-phase aqueous	140 to 161/151	–0.8 to –17.2/–5	1.4 to 20.3/7.9
Macigno calcite 2	Primary two-phase aqueous	69 to 115/88	–0.7 to –20.7/-8.7	1.2 to 22.9/12.5
Ottone calcite 1	Reequilibrated two- and one-phase aqueous	<50 to 113	0 to –1.6/–0.8	0 to 2.7/1.4
Ottone calcite 2	Primary two- and one-phase aqueous	<50 to 115	–1.3 to –6.9/–4.4	2.2 to 10.4/7

Note: Data from samples collected in Sites shown in Figures 3A and 3C. FIA—fluid inclusion assemblages; N.D.—no data.

is –2.7 °C, which corresponds to 4.5 wt% NaCl eq. (Bodnar, 1993; Fig. 10C).

Fluid inclusions hosted in impurity-poor MC1B calcite crystals are slightly smaller than MC1A inclusions, ranging from 2 µm to 10 µm. They have rounded to negative crystal shape and constant vapor/liquid ratio where vapor fills around 10% of the inclusion's volume. Nineteen MC1B inclusions were measured, distributed in five FIAs. They show homogenization temperatures between 140 and 161 °C with a mean value of 151 °C and a modal peak at 150–155 °C (Fig. 10B). First melting temperatures of MC1B inclusions range between –8 and –20 °C in three FIAs while they are –31.5 °C in another FIA. Ice melting temperatures for MC1B inclusions range between –0.8 and –17.2 °C, which corresponds to salinities ranging from 1.4 to 20.3 wt% NaCl eq. The mean Tm_{ice} is –5 °C, corresponding to 7.9 wt% NaCl eq. (Bodnar, 1993; Fig. 10C). Only the four MC1B inclusions belonging to the FIA characterized by first melting temperatures of –31.5 °C showed Tm_{ice} lower than –6.2 °C, i.e., ranging from –10. to –17.7 °C.

Footwall MC2 calcite contains biphase aqueous inclusions with the same petrographic characteristics as MC1 inclusions but they were not found aligned in FI trails. Six MC2 FIAs and two isolated inclusions were measured, representing 20 inclusions. They have rounded shapes and dimensions ranging from 2–3 µm up to 10 µm (Fig. 9E). Homogenization tem-

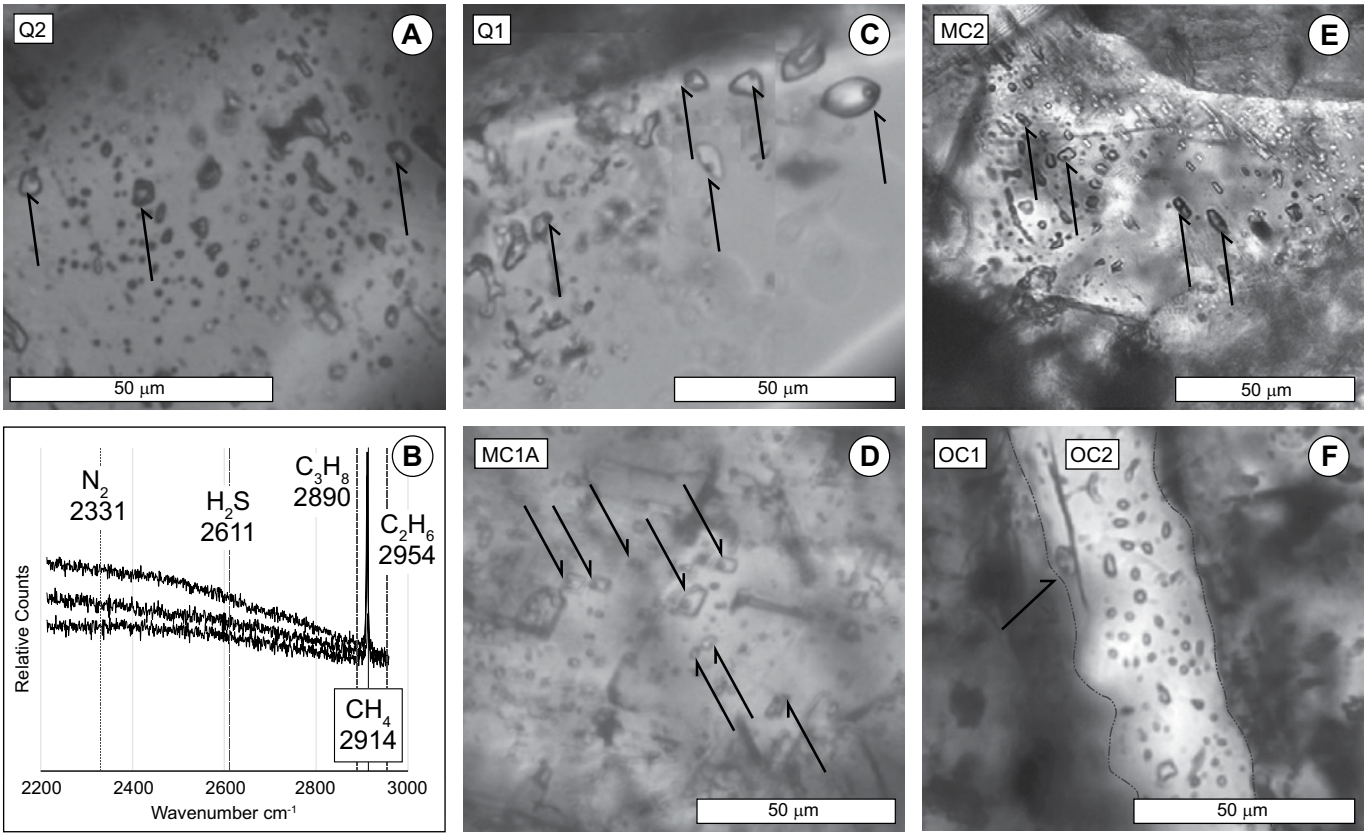


Figure 9. Microphotographs in plane polarized light of fluid inclusion types, in the analyzed veins. (A) Monophase gaseous inclusions Q2 cooled at –100 °C. (B) Raw spectra of Raman analysis performed on Q2 inclusions showing peaks corresponding to CH_4. (C) Fluid inclusion assemblages (FIA) of Q1 aqueous biphase inclusions in quartz from a footwall vein. (D) FIA of aqueous biphase inclusions with a negative crystal shape in MC1. (E) FIA of aqueous biphase inclusions in MC2. (F) FIA of aqueous monophase inclusions in OC2, overprinting a OC1 vein, big inclusions in OC2 are biphase aqueous. MC—Macigno Sandstones Formation calcite cements; OC—Ottone Flysch Formation calcite cements.

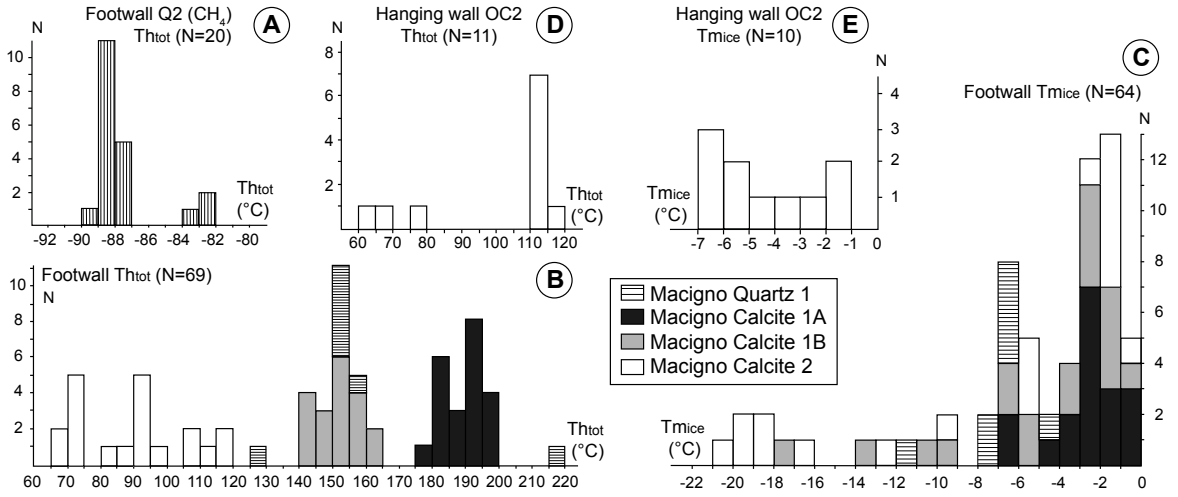


Figure 10. Frequency distribution plots of homogenization (Th_{tot}) and ice melting (Tm_{ice}) temperatures. (A) Th_{tot} of Q2 monophase gaseous inclusions in quartz. (B) Th_{tot} of biphase aqueous inclusions in footwall veins. (C) Tm_{ice} of biphase aqueous inclusions in footwall veins. (D) Th_{tot} of biphase aqueous inclusions in hanging wall veins. (E) Tm_{ice} of monophase and biphase aqueous inclusions in hanging wall veins. Macigno Calcite—Macigno Sandstones Formation calcite cements; OC—Ottone Flysch Formation calcite cements; Footwall veins, hosted in the Macigno Sandstones Formation, from Sites 4, 5, 7, and 13 in Figures 3A and 3C; Hanging wall veins, hosted in the Ottone Flysch Formation, from Sites 2, 3, 8, 9, and 10 in Figure 3C.

peratures range from 69 to 115 °C with a mean value of 88 °C. Ice melting temperatures range from –0.7 to –20.7 °C, corresponding to salinities from 1.2 to 22.9 wt% NaCl eq. The mean Tm_{ice} is –8.7 °C and the mean salinity 12.5 wt% NaCl eq. (Bodnar, 1993) even if the distribution is formed by two clusters, with Tm_{ice} comprised between –16.7 and –20.7 °C, and –0.7 and –5.8 °C, respectively. The modal peak is comprised between –1 and –2 °C (Fig. 10C). MC2 inclusions belonging to the first cluster froze at temperatures lower than –70 °C and showed melting evidence at temperatures comprised between –34 and –27 °C as Q1 inclusions. The first melting temperatures were difficult to evaluate but their similar behavior with Q1 inclusions (this paragraph) suggests a NaCl-$CaCl_2$-H_2O system. Only a first melting temperature of –17.8 °C, indicating a NaCl-H_2O system, was measurable in MC2 inclusions belonging to the second cluster.

Hanging wall OC2 calcite is characterized by fluid inclusions that are monophase and biphase aqueous with rounded shapes and smaller than 10 µm (Fig. 9F). The vapor phase in biphase inclusions fills 5–10% of their volume. Small monophase OC2 inclusions did not nucleate bubbles after two weeks at –20 °C. Two FIAs and an isolated inclusion for a total of 16 were measured. Homogenization temperatures range from 60 to 75 °C in the first FIA and from 110 to 115 °C in the second FIA (Fig. 10D). First melting temperature was never observed. Ice melting temperatures range from –1.3 to –6.9 °C, with a mean value of –4.4 °C (Fig. 10E) and they correspond, respectively, to salinities of 2.2, 10.4, and 7 wt% NaCl eq. (Bodnar, 1993). OC2 inclusions have higher salinities at lower homogenization temperatures.

Homogenization vs. ice melting temperatures of measured inclusions are plotted in Figure 11. Fluid inclusions from quartz in footwall veins show a rather constant salinity, around 10–15 wt% NaCl eq., at different homogenization temperatures. Calcites MC1A, MC1B, and MC2 in

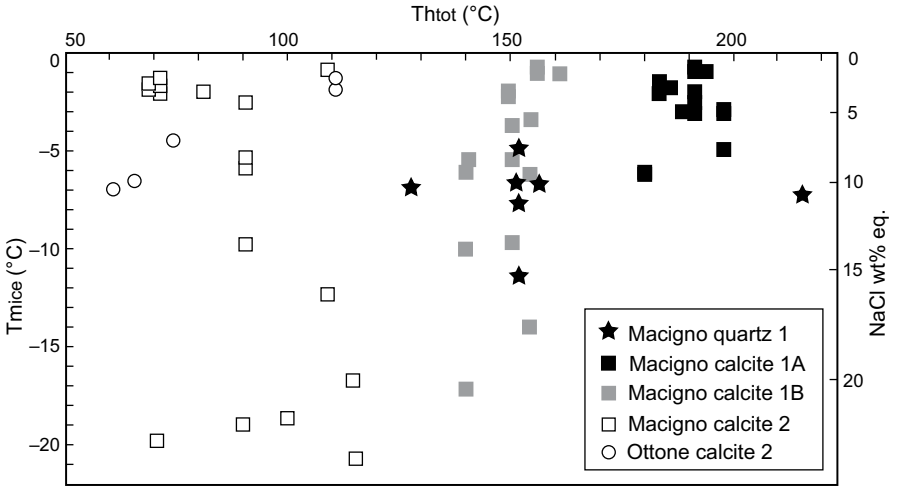


Figure 11. Plot of homogenization temperatures (Th_{tot}) vs. ice melting temperatures (Tm_{ice}) of measured fluid inclusions. Ice melting temperatures are reported along with salinity in NaCl eq. wt%, according to Bodnar (1993). Macigno Calcite—Macigno Sandstones Formation calcite cements; Ottone Calcite—Ottone Flysch Formation calcite cements; Footwall veins, hosted in the Macigno Sandstones Formation, from Sites 4, 5, 7, and 13 in Figures 3A and 3C; Hanging wall veins, hosted in the Ottone Flysch Formation, from Sites 2, 3, 8, 9, and 10 in Figure 3C.

footwall veins are characterized by a different temperature-salinity trend, generally displaying less than 5 wt% NaCl eq. at 180–200 °C (subgroup MC1A) and an increasingly wider range of salinities at decreasing temperatures. Subgroup MC1B with homogenization temperatures between 140 and 160 °C, can have salinities up to 20 wt% NaCl eq. At lower temperatures, between 70 and 110 °C, MC2 inclusions have salinities up to 23 wt% NaCl eq. The data belonging to hanging wall fluid inclusions OC2 show a trend similar to footwall calcites, characterized by higher salinities at lower homogenization temperatures.

6. VITRINITE REFLECTANCE AND THERMAL MODELLING

Results of vitrinite reflectance measurements acquired in footwall Macigno Sandstones Formation are summarized in Table 3. Ten samples were analyzed from sites 14, 4, and 5. Samples from sites 4 and 5 are located in the footwall damage zone while Site 14 is located outside the damage zone. Mean values range between 0.42 and 0.70 Ro% and standard deviations are generally below 0.1 Ro%. More in detail, vitrinite reflectance measured on samples in the footwall damage zone (sites 4 and 5) show very dispersed average values ranging from 0.42 to 0.61 Ro% (Table 3), which were based on the in situ vitrinite. The lowest values were measured on very small and fractured fragments with dark oxidized rims along the irregular micro-fissure in the vitrinite particle, making the reflectance assessment scarcely reliable, while only few sufficiently large and unfractured fragments were found showing generally slightly higher values around 0.65–0.70 Ro%. A further family of vitrinite fragments, excluded from the aforementioned average, was found showing values between 1.0 and 1.30%. These fragments were interpreted as reworked vitrinite.

On the other hand, samples from Site 14, far from the damage zone, indicate average values between 0.66 and 0.70 Ro% (Table 3). In situ vitrinite is here represented by large and unfractured fragments even if averages are based on a small number of measurements (between 8 and 19). Also in these samples reworked vitritine showing higher values (between 1.10 and 1.80 Ro%) was found. Nevertheless, the lowest mean values between 0.42 and 0.61 Ro% are found systematically in the footwall damage zone. These values are always associated with oxidized and pervasively fractured vitrinite fragments and thus were not considered in the calibration of the thermal model. Samples in the footwall sandstones outside the Compione fault damage zone, on the other hand, show consistent Ro% values between 0.66 and 0.70.

TABLE 3. SUMMARY OF RESULTS OF VITRINITE REFLECTANCE MEASUREMENTS

Site no.	Sample no.	Ro (% mean)	Ro (% S.D.)	Data no.
14	1	0.70	0.08	11
14	2	0.66	0.12	8
14	3	0.69	0.10	19
14	4	0.67	0.12	7
4	1	0.61	0.04	8
4	3	0.42	0.06	40
4	4	0.42	0.10	12
5	1	0.46	0.07	29
5	2	0.55	0.05	12
5	3	0.49	0.06	11

Note: Data from samples collected in Sites shown in Figures 3A and 3C. S.D.—standard deviation.

Assumptions about the burial/exhumation history and heat flow in the Macigno Sandstones Formation have to be made, as they are input data necessary for the thermal modelling: (1) stratigraphic location of the samples is comprised between 600 and 1100 m from the top of the Macigno Sandstones Formation, which is 2300 m thick (Ghibaudo, 1980). In detail, samples from Site 14 are located between 600 and 800 m and samples from sites 4 and 5 between 900 and 1100 m; (2) the Macigno Sandstones Formation was rapidly buried below the 4000–6000-m-thick allochtonous Ligurian and Subligurian units (Carlini et al., 2013); (3) syncontractional exhumation took place up to Late Messinian times through low-angle normal faulting in the inner part of the orogenic wedge (Fellin et al., 2007; Carlini et al., 2013; Molli et al., 2018). Moreover, heat flow in the Northern Apennines foredeep has values lower than 30° C/km due to rapid burial and thrusting of foredeep units, whose thermal regime is far from equilibrium (Mongelli et al., 1991; Della Vedova et al., 1995).

Ro% values at maximum burial depth could only be fitted using 3000 m of Ligurian and Subligurian units overburden, lower than the minimum thickness estimates of allochtonous units (according to Carlini et al., 2013) and adopting a geothermal gradient of 25–30° C/km. Thinning of the overburden thickness moving towards the foreland is logical considering the wedge-shaped overall geometry of fold and thrust belts (Davis et al., 1983). The best fit between calculated maturity profile and measured vitrinite reflectance was attained using a geothermal gradient of 25 °C/km up to the end of Miocene that gradually increased up to a present-day value of 30 °C/km. As a consequence, the Macigno Sandstones Formation stratigraphic sector, hosted in the Compione fault footwall damage zone, at 5 km depth, experienced peak temperatures between 140 and 150 °C (Fig. 12).

7. DISCUSSION

7.1. Process Zone Width

An outstanding feature of the Compione Fault is the abundance in the footwall damage zone of veins that, when bedding is rotated to the horizontal, restore to a pattern of conjugate shear fractures with a vertical bisector, i.e., the typical geometry produced in an extensional tectonic regime (Anderson, 1951; Sibson, 1996). This evidence supports vein formation in an early evolutionary stage of the Compione Fault, when bedding in the process zone was still horizontal, before extensional folding and shear localization. Accordingly, the area affected by such extensional shear veins can be interpreted as the process zone sector preserved in the footwall of the Compione Fault, which formed ahead of the upward-propagating master shear zone (cf. Lockner et al., 1992; Reches and Lockner, 1994; Cowie and Shipton, 1998; Vermilye and Scholz, 1998). In the studied across-fault transect, the width of the footwall process zone is about 900 m. The present-day tectonic juxtaposition of the Ottone Flysch Formation in the hanging wall prevents any possibility to quantify the total width of the process zone in the Macigno Sandstones Formation. However, by assuming that the Upper Triassic Burano Evaporites provided a thick plastic layer suitable to enhance initial extensional folding in the

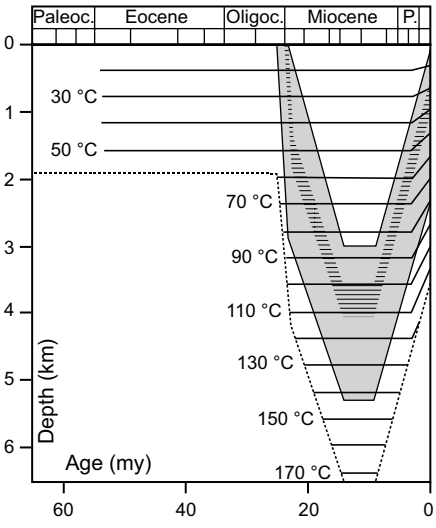


Figure 12. Burial and thermal history of the Macigno Sandstones Formation, Northern Apennines, Italy, shaded in grey, using a geothermal gradient of 25 °C/km up to the end of the Miocene and of 30 °C/km since the Pliocene (P.). Striped areas represent the stratigraphic range of Site 14.

overburden (Schlische, 1995; Withjack and Callaway, 2000), it is possible to hypothesize that the tip of the master shear zone was temporarily arrested at the base of the Burano Evaporites while their top, now at around 6 to 7 km depth, provided the apical point of the extensional fault-propagation fold (Fig. 13). By applying the geometric construction of Jin and Groshong (2006) and assuming a linear velocity field in the trishear zone ahead of the propagating upper fault tip (Hardy and Ford, 1997) it is possible to infer a total process zone width of about 1800 m and an apical angle of ~10° (Fig. 13). Taking into account that the total displacement of the Compione Fault is around 1.5 km (Bernini and Lasagna, 1988), our estimate of the process zone width is out-of-scale compared to displacement (D) to damage zone (DZ) ratios reported in the literature, even though D/DZ is strongly dependent on the criteria used to define damage zone thickness and on lithological properties (Knott et al., 1996; Fossen et al., 2007; Childs et al., 2009; Fossen, 2010; Torabi and Berg, 2011; Solum and Huisman, 2016). In fact, assuming that late-stage extensional fault zones are the structural elements that define the damage zone width, then the D/DZ ratio of the Compione Fault would be comparable to those reported in published datasets.

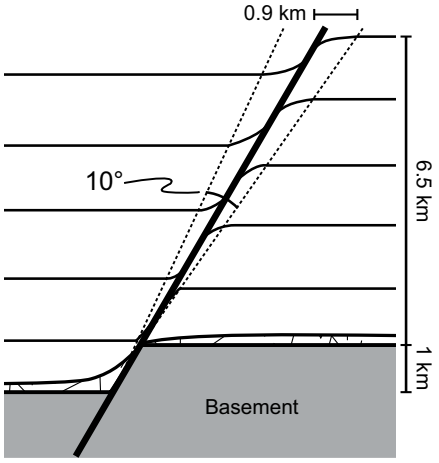


Figure 13. Trishear predicted geometry of the Compione Fault, Northern Apennines, Italy, using the method of Jin and Groshong (2006). Monocline width is around twice the footwall monocline width assuming a linear velocity field in the trishear zone. Striped unit above the basement correspond to Burano Evaporites.

7.2. Cyclical Vein Development and Earthquake Cycle

Footwall damage zone fault-related veins show multiple subparallel fracturing-sealing events indicating that fracturing, cementation, dissolution, and shearing were cyclic (Fig. 14 A–14C; Ramsay, 1980; Boullier and Robert, 1992; Boullier et al., 1994; Sibson, 1996; Renard et al., 2000; Sibson, 2004). The majority of veins is interested by localized shear-reactivation, forming abundant mirror surfaces and, in cases displaying straight micrometric wide slip surfaces truncating crystals, which are interpreted as evidence for coseismic slip (Smith et al., 2011; Fondriest et al., 2013; Smeraglia et al., 2017). Fracturing-sealing cycles caused strain-softening promoting localization of younger fracturing and shearing events at vein-host rock interfaces or in between different openings (Jessell et al., 1994; Virgo et al., 2014). Prehnite exhibits euhedral crystals, organized in columnar-radiating aggregates while quartz shows euhedral to subhedral crystals, in cases also displaying growth competition (Fig. 14A). Both textures require fractures to remain fluid-filled and open during crystal growth (Fisher et al., 1992; Koehn and Passchier, 2000; Oliver and Bons, 2001; Bons et al., 2012), thus implying fluid pressures higher than the local σ_3 for fault-parallel extensional veins. Conversely, blocky rhombohedric calcite texture (Figs. 14A–14C), which occludes completely the remaining fracture space, could be caused by different processes: (a) supersaturation in response to a pressure drop, (b) texture obliteration due to repeated fracturing, and (c) fast crystal nucleation caused by a sudden arrest of an ascending fluid (Oliver and Bons, 2001). Moreover, prehnite dissolution can promote permeability enhancement and, consequently, pressure reduction (Figs. 14B, 14C; Boullier et al., 1994). In the literature, models such as the fault-valve and seismic pumping have been proposed to relate cyclical fracturing-sealing events to the seismic cycle (Sibson et al., 1975, 1988; McCaig, 1988; Boullier and Robert, 1992; Robert et al., 1995; Cox, 1995, 1999).

Our microstructural data support a model of extensional faulting in the upper crust, triggered by shortening and thrusting in a seismically active metamorphic basement (McCaig, 1988). At shallow crustal levels, as in this specific case, fluid pressure is governed by seismic-pumping (Sibson et al., 1975), while the fault-valve mechanism explains supralithostatic pressures at deeper crustal levels (Sibson et al., 1988). In the hypothesis that precipitation of the described prehnite-quartz-calcite assemblages was triggered by seismic activity during upward fault propagation from the basement, silicates (prehnite and quartz) may have crystallized at suprahydrostatic fluid pressure conditions (P_f) after seismically induced fracturing, i.e., in the post-seismic stages (Figs. 14D, 14E). Suprahydrostatic P_f in the extensional process zone may have been generated by ascending fluids that breached a low-permeability layer at depth (Sibson et al., 1988; McCaig, 1988), reasonably provided by the thick evaporitic sequences at the top of the metamorphic basement, which is deformed in a regional scale antiformal stack structure (e.g., Molli et al., 2018). The decrease of P_f to hydrostatic values led to supersaturation of calcite, which precipitated in the remaining voids thus completing vein infilling and favoring a new cycle of pore fluid pressure increase (Figs. 14D, 14E). The causal link between seismic activity and precipitation of the mineralogical assemblage, in rotated shear veins exposed in the footwall damage zone of the Compione Fault, is tentatively proposed as a working hypothesis that deserves further studies specifically designed for acquiring a comprehensive dataset suitable to either support or reject this possibility.

7.3. Process Zone Temperature Anomaly

Paleothermal data obtained from the host Macigno Sandstones Formation and from the shear vein network allow estimating the thermal disequilibrium associated with the upward migrating fluids that infiltrated the process zone in the early stages of faulting and related extensional folding.

An anomalous feature is the maturity difference between sites 4 and 5 with respect to Site 14, which cannot be explained by different burial since low-maturity samples have a lower stratigraphic position. Actually, lower Ro% values from sites 4 and 5 locate into the footwall damage zone and were obtained from very small and fractured fragments with oxidized rims around fractures. This suggests that anomalously low reflectance values are due to oxidation from mixed meteoric and deep fluid weathering occurring probably during the last pulse of fluid circulation around the fault. The increase in permeability during the last stage of the fault's activity created conditions that favored oxidation of the surface of the organic matter which is subsequently degraded during weathering (Petsch et al., 2000).

Accordingly, the thermal model was calibrated using data from Site 14. Thermal modelling of vitrinite reflectance data provided peak temperatures in the footwall damage zone ranging between 140 and 150 °C at maximum depths of about 5 km and geothermal gradients between 25 to 30 °C/km (Fig. 12). In addition, published data from apatite fission tracks in the Macigno Sandstones Formation sampled in the study area

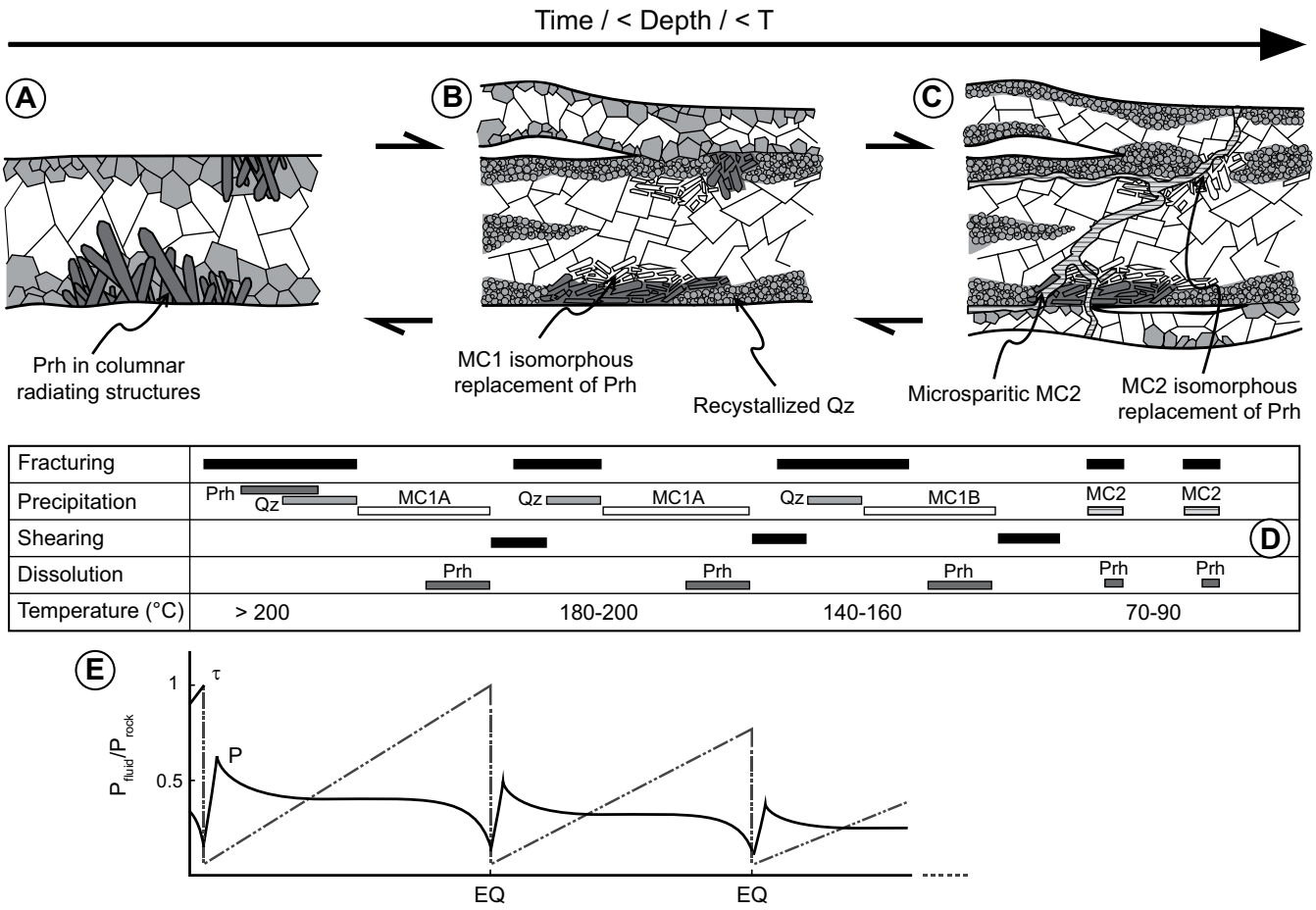


Figure 14. Sketch illustrating the typical paragenetic evolution of conjugate veins in the footwall of the Compione Fault, Northern Apennines, Italy. (A) Pristine crystal textures of the initial infilling event. (B) Microstructural modifications after shear reactivation. (C) After late-stage reactivation. (D) Schematic table showing the cyclic events, indicating the relative chronology of fracturing, precipitation, and dissolution processes, along with their temperature range. (E) Schematic evolution of fluid pressure, reported as ratio to lithostatic pressure, and shear stress in time relative to earthquake rupturing and to shearing, fracturing, precipitation, and dissolution processes (D) in fault-related veins. Prh—prehnite, Qz—quartz; MC—Macigno Sandstones Formation calcite cements; P-pressure; tau-shear stress; EQ-earthquake.

show complete annealing (Thomson et al., 2010; Carlini et al., 2013), which generally indicates temperatures higher than 110 °C (Ketcham et al., 1999). This supports results from our model.

Microthermometric data from quartz Q1 and calcite MC1A cements show homogenization temperatures of 155 and 180 °C, respectively. Accordingly, MC1A calcite in the footwall damage zone fracture network shows homogenization temperatures at least 30 °C higher than the surrounding Macigno Sandstones Formation. If we correct data by pressure, assuming that MC1A crystallized at about 5 km depth in hydrostatic conditions at the onset of exhumation, real fluid trapping temperatures are predicted to be around 210–230 °C (Fig. 15A). Moreover, prehnite in the studied veins, despite the impossibility to provide direct constraints on paleotemperatures may suggest minimum temperature values of about 230 °C based on occurrences in hydrothermal and in geothermal systems in Tuscany, Italy, and other areas showing calc-silicate mineralization (Browne, 1978; Arnason et al., 1993). It is worth noting that uncertainty is associated with this inference because crystallization conditions might depend on fluid chemistry. Hydrothermalism is abundant and ongoing on the Tyrrhenian Sea side of the Apennines and is related to high-temperature–low-pressure contact metamorphism due to the intrusion of igneous bodies into the crust associated with the Tyrrhenian extension (Cavarretta et al., 1982; Boccaletti et al., 1997; Gianelli et al., 1997; Dini et al., 2005; Boiron et al., 2007 and many others). If our assumptions are correct, then the difference in temperature between hydrothermal fluids that circulated through the fracture network in the process zone and the surrounding host Macigno Sandstones Formation was between 60 and 90 °C. Such a high thermal disequilibrium is supported both by the geometry of the process zone, which displays a low apical angle (Fig. 13), and by supra-hydrostatic fluid pressures that promote fast advection of hot fluids from the basement in a channelized, highly fractured, and narrow deformation zone (Sibson et al., 1988, 1996, 2000; Renard et al., 2000; Gratier et al., 2002; Beaudoin et al., 2011). This result highlights the importance of combining different methodologies to constrain host rock and fault-related fluid paleotemperatures (Mamadou et al., 2016; Honlet et al., 2017; Laurent et al., 2017; Wüstefeld et al., 2017).

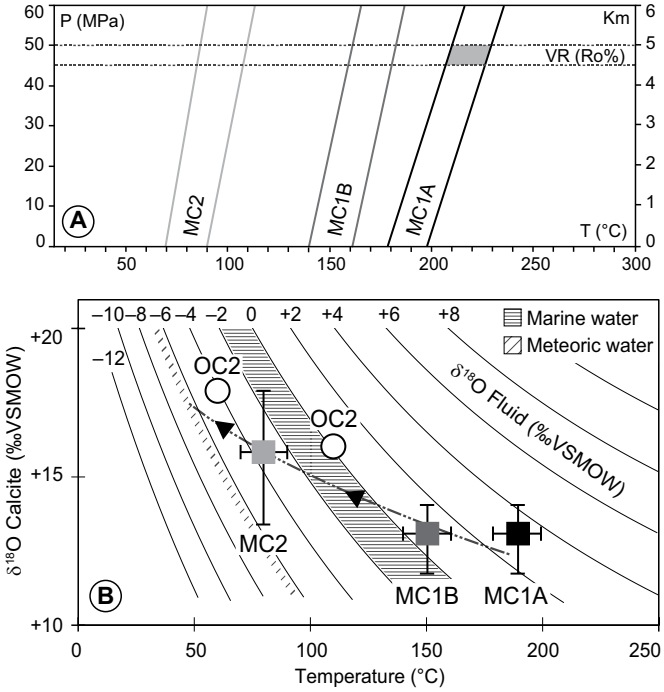


Figure 15. Data are from Sites 4, 5, 7, and 13 in the footwall damage zone (MC) and from Sites 2, 3, 8, 9, and 10 in the hanging wall damage zone (OC); see Figures 3A and 3C. (A) Isochores are plotted for the different fluid inclusion types. Peak burial derived from vitrinite reflectance modelling is used as an independent constraint to calculate a maximum trapping temperature for MC1A (shaded area). (B) Oxygen isotope fractionation during equilibrium calcite precipitation. The fluid oxygen composition is reported as a function of calcite oxygen composition and temperature. Square symbols and error bars represent the mean value and range of footwall calcite MC1A, MC1B, and MC2. OC2 calcite is represented by the white circles. Dashed lines describe the inferred fluid evolution during time. MC—Macigno calcite cements; OC—Ottone Flysch Formation calcite cements; VR (Ro%)—Maximum burial depth estimated from vitrinite reflectance measurements; VSMOW—Vienna standard mean ocean water.

7.4. Fluid Sources and Migration Pathways

Assuming that Q1 and Q2 inclusions are cogenetic, this would imply that the source fluid underwent fluid immiscibility before entrapment. Cogenetic aqueous biphase and CH_4 gaseous monophase inclusions have already been documented in authigenic quartz in sandstones of the Northern Apennines (Mullis, 1979, 1987, 1988; Montomoli et al., 2001; Montomoli, 2002; Mazzarini et al., 2010). This fluid immiscibility is generally caused by decreasing fluid pressure during upward fluid migration in the fault damage zone, (Parry and Bruhn, 1988, 1990; Sibson et al., 1975; Sibson et al., 1988, 2000). MC1B inclusions show the same composition and salinity as MC1A inclusions except for a FIA in Site 5, with higher salinity and lower first melting temperatures, indicating a NaCl-$CaCl_2$-H_2O composition as Q1 inclusions.

Assuming equilibrium precipitation, the calculated $\delta^{18}O_{fluid}$ for MC1 calcites is shown in Figure 15B (Friedman and O'Neil, 1977), and is between +2‰ and +4‰ VSMOW for MC1A calcite and between 0‰ and +2‰ VSMOW for MC1B calcite, indicating ^{18}O enriched waters due to different degrees of water-rock interaction (e.g., Muchez et al., 1995). Taking into account the different lithologies cut by the Compione Fault (Figs. 1C and 2), $\delta^{13}C$ values of MC1 calcites may indicate different degrees of mixing between methane fluid originating from the thermal maturation of organic matter inside the Macigno Sandstones Formation, inorganic marine carbon-rich fluids from the underlying Mesozoic carbonates and, also, a contribution of metamorphic fluids coming from the basement (cf. Hoefs, 1997; Milliken et al., 1998; Mazzarini et al., 2010; Boschetti et al., 2017). The latter is supported by the occurrence of prehnite crystallization in stage 1, which is a typical mineral of anchizone metamorphism (Merriman and Frey, 1999). Moreover, fluid trapped in MC1A inclusions shows low salinity and high temperature, which can be ascribed to devolatilization reactions in the underlying metamorphic basement (Walther and Orville, 1982; Oliver, 1996; Connolly, 2010; Ingebritsen and Manning, 2010), while locally higher salinities in MC1B reflect a decreasing contribution of metamorphic fluids.

Hanging wall calcite OC2 is interpreted to be associated with stage 2 on the basis of structural, microstructural, and isotopic observations: (a) OC2 cements in microfractures that display, locally, quartz crystals along rims; (b) OC2 in Figure 7N occurs, as in the footwall, as isomorphous replacement of prehnite; and (c) isotopic analysis results of OC2 calcite in the same sample shows a $\delta^{13}C$ shift towards MC1 calcites values indicating local mixing between hanging wall and footwall fluids at stage 2 (Fig. 8). Isotopic results of OC2 calcite show that $\delta^{13}C$ values, except the outlier in Figure 7N, are similar to OC1 ones, indicating no external source of carbon in the Ottone Flysch Formation. $\delta^{18}O_{fluid}$ from which OC2 precipitated is characterized by a wide variability (Fig. 15B), ranging from around –6‰ to 0‰ VSMOW. This range could be interpreted as a fluid mix between Ottone Flysch formational waters and meteoric waters ($\delta^{18}O$ around –8‰ to –6‰ VSMOW, cf. Longinelli and Selmo, 2003; Giustini et al., 2016) even this is difficult to prove since we do not have data on the composition of the fluid.

MC2 calcite crystallized in microfractures in the internal footwall damage zone during stage 3. As in stage 1 and 2, even MC2 locally replaces prehnite crystals. The wide range of homogenization temperatures of MC2 inclusions could indicate they were stretched. We, therefore, assume the lower temperatures ranging from 70 to 90 °C as representative for these inclusions. MC2 inclusions with low salinity (<10 wt% NaCl eq.) have a NaCl-H_2O composition while those with high salinity (up to 22.9 wt% NaCl eq.) have a NaCl-$CaCl_2$-H_2O composition. The high salinity could indicate the dissolution of salts in the subsurface (Goldstein and Reynolds, 1994; Boschetti et al., 2017). Carbon forming MC2 calcites was derived from the same sources discussed for MC1 while $\delta^{18}O_{Fluid}$ values, comprised between –6‰ and –2‰ VSMOW, could indicate mixing between MC1 source fluid and meteoric waters (Fig. 15B).

Phase diagrams of log (a Ca^{2+}/a^2 H^+) vs. log a SiO_2 (aq) in Figures 16A and 16B have been plotted for, respectively, temperatures of 200 and 150 °C show the stability fields of the mineral assemblages in stage 1 and stage 2. In this framework, at the beginning of stage 1, the upward migrating fault-related fluid is initially recorded by crystallization of prehnite and quartz, which at 200 °C (Fig. 16A) are stable at lower log (a Ca^{2+}/a^2 H^+) and log a SiO_2 (aq) compared to 150 °C (Fig. 16B; cf. Bird and Helgeson, 1980, 1981; Cavarretta et al., 1982). Then it evolved, at lower temperatures, causing prehnite crystals dissolution and further precipitation of quartz and calcite (MC1 A and B), both in stages 1 and 2. Replacive calcite indicate a dissolution-reprecipitation process, lowering CO_2 content and increasing H_2O, silica, and alumina activity in the fluid. Quartz cementation is coeval with upward methane migration which, in contrast, is not recorded in calcite. It can be inferred that quartz crystallization was inhibited when methane was no longer in the fluid and was oxidized to CO_2, necessary to precipitate calcite. Silicates precipitation from an upward migrating and cooling hot fluid is easily explained by decreasing silica solubility at lower temperatures and pressures, while precipitation of calcite, which solubility increases with decreasing temperature and pressure, is promoted by decreasing fCO_2 (cf. Bird and Helgeson, 1980, 1981; Cavarretta et al., 1982).

MC1 and MC2 calcite cements in Site 5, located in the footwall block between the Compione fault core and the E-W footwall splay, show lighter carbon values compared to other sites (Fig. 8C). This $\delta^{13}C$ variation indicates that the sectors of the process zone were characterized by different quantities of organic matter maturation-derived carbon during upward migration. Stable isotope values of MC1 and MC2 in the sample from Groppodalosio Fault (NW tip area, Site 13) are slightly enriched in ^{18}O (triangles in Fig. 8A) compared to Compione, while minimum temperatures of entrapment were the same. Therefore, the $\delta^{18}O_{Fluid}$ composition in the NW were slightly heavier compared to the Compione area.

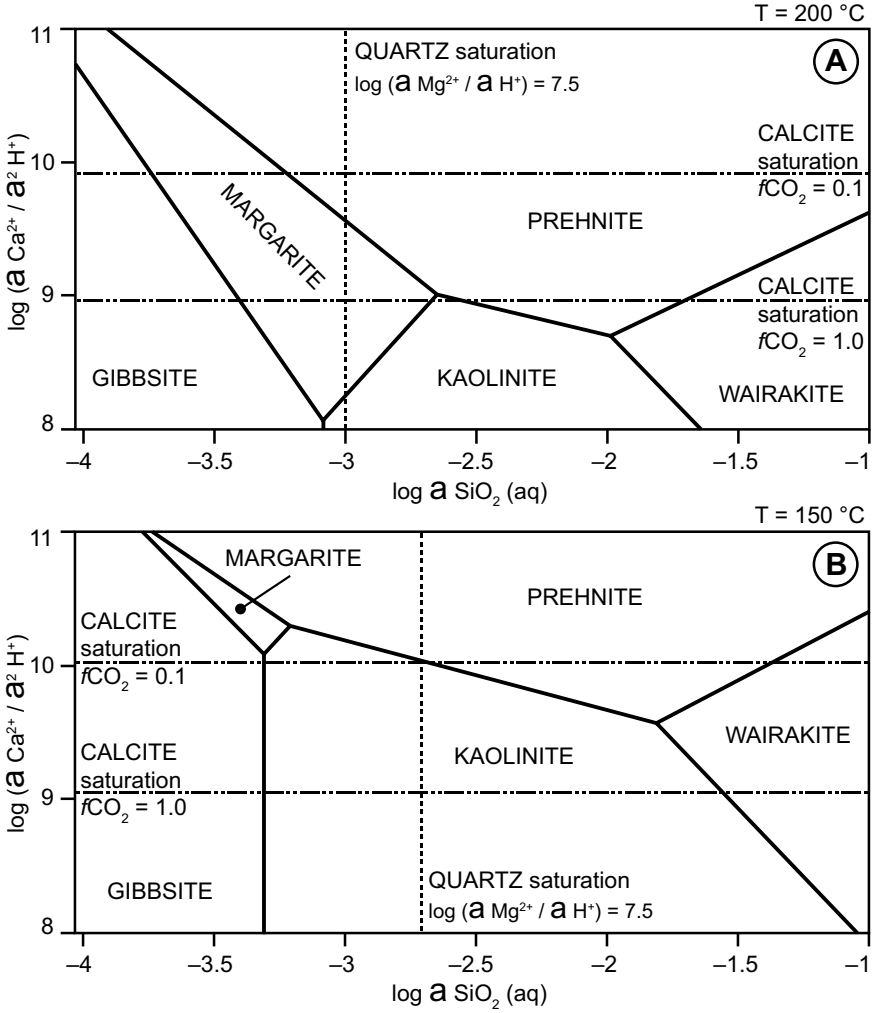


Figure 16. Phase diagrams for calcium and alumina minerals in terms of $Ca^{2+}/(H^+)^2$ activity ratio and of aqueous SiO_2 activity at 200 °C (A) and at 150 °C (B).

7.5. Evolutionary Model

The structural fabric preserved in the footwall of the Compione Fault indicates that fault activity in the Macigno Sandstones Formation started with the formation of a km-scale network of shear fractures in conjugate arrays with vertical σ_1 bisector, as expected in extensional Andersonian faulting (Anderson, 1951; Sibson, 1996). The strike of the fractures was mainly parallel to the main trend of the Compione Fault, but also E-W, i.e., parallel to the major footwall fault splay occurring in the study area. This suggests that linkage within and among the major footwall segments constituting the Northern Lunigiana fault system (Fig. 3) occurred in the very early stages of extensional deformation. Such an early fracture network formed the process zone (Lockner et al., 1992; Reches and Lockner, 1994; Cowie and Shipton, 1998; Vermilye and Scholz, 1998) of the Compione Fault in the Macigno Sandstones Formation, ahead of the upward-propagating master fault surface. The process zone was a preferential site for effective fluid circulation and advection of a hydrothermal plume at minimum temperatures of 210–230 °C, i.e., the trapping temperature of MC1A inclusions assuming hydrostatic conditions at 5 km depth, and possibly exceeding ~230 °C, as suggested by fracture cementation with prehnite (Fig. 17A). Results from microthermometry and stable isotope geochemistry indicate an open system circulation with upward directed and channelized high-temperature and low-salinity fluids coming from the metamorphic basement (Mazzarini et al., 2010; Boschetti et al., 2017) which mixed with carbon derived from the maturation of organic matter in the Macigno host rock. Petrographic evidence supports cross-formational fluid flow up to the base of the Ottone Flysch Formation in this early stage.

With increasing extension, the vein network in the process zone was progressively tilted by extensional fault-propagation folding (Withjack et al., 1990; Schlische, 1995; Hardy and McClay, 1999; Ferrill et al., 2004a; Jin and Groshong, 2006) and bedding attained a synthetic dip attitude. During folding, the fault-parallel extensional conjugate vein arrays was preferentially

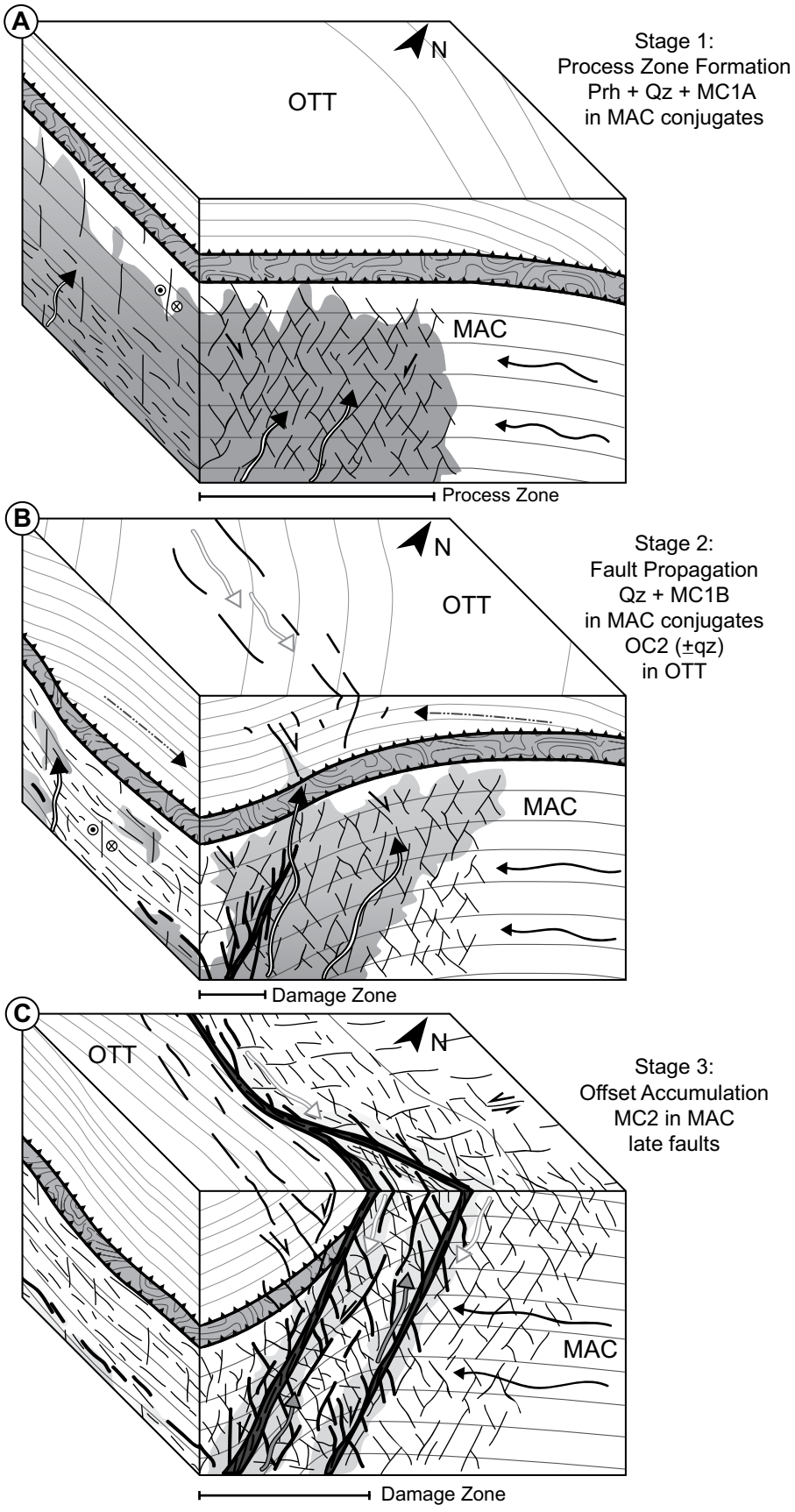


Figure 17. Cartoon showing the proposed evolution of the Compione Fault, Northern Apennines, Italy. (A) Onset of extensional deformations overprinting the previously stacked Sub-Ligurian and Ligurian thrust sheets onto the Macigno foredeep sandstones (MAC). A wide process zone forms, mainly consisting of conjugate shear fractures that enhance the advection of hydrothermal fluids and rapid cementation. (B) Extensional fault-propagation folding during upward fault migration, causing bending of part of the process zone closer to the prospect master shear zone and reactivation of conjugate shear veins as both synthetic and antithetic subsidiary extensional faults. (C) Shear localization, fault breakthrough and accommodation of most of the displacement in the fault core, hanging wall, and footwall subsidiary fault zones. Black arrows are formational fluids, white and black ones are high-temperature low-salinity hydrothermal fluids, white and grey ones are meteoric fluids and black and grey ones are low-temperature high-salinity fluids. OTT—Ottone Flysch Formation; Prh—prehnite, Qz—quartz; MC—Macigno calcite cement; OC—Ottone Flysch Formation calcite cements.

reactivated by antithetic shearing, accompanied by precipitation of quartz and MC1B calcite (Fig. 17B). Mineralization occurred at minimum temperatures between 140 and 160 °C and increasing fluid salinities indicating mixing with a fluid characterized by lower temperature and higher salinity. At this stage there was still stratigraphic continuity across the Compione fault zone, which near surface expression was likely a flexure in the crestal region of the regional-scale anticline deforming the previously stacked thrust sheets of Tuscan and Ligurian rocks. The presence of the clay-rich Subligurian succession at the top of the Macigno Sandstones Formation and the change from siliciclastic to carbonate composition helps explain why conjugate fracture arrays comparable to the underlying ones did not develop in the Ottone Flysch Formation. In the latter, deformation was accommodated through a network of fault segments that partially exploited the pre-existing structural inheritance, accompanied by precipitation of OC2 calcite and rare quartz, at a temperature lower than 110 °C (Fig. 17B).

When bedding dip in the extensional monocline reached values exceeding ~50°, fault propagation and breakthrough was accompanied by formation of a footwall damage zone with

a width of about half that of the corresponding process zone. Many rotated shear veins and subsidiary faults were reactivated and together with newly formed ones, produced a network of high-angle faults with cataclastic cores of disaggregated and gouge layers. MC2 calcite precipitated in fractures of the damage zone, from fluids at temperature between 70° and 90° C, resulting from mixing between deeply sourced fluids and meteoric waters which likely interacted, at different degrees, with the Burano Evaporites in the subsurface (Fig. 17C). This would explain the high salinity of a low-temperature fluid with a stable isotopic composition typical of meteoric fluids. The damage zone in the hanging wall had a comparable width as the footwall but was affected by less intense fracturing, partly replaced by dissolution and discrete subsidiary faulting.

8. CONCLUSION

The Compione Fault is part of the Northern Lunigiana regional-scale extensional fault system, exposed for around 30 km along strike, which accumulated about 1.5 km offset since Early Pliocene times. It is located in the inner portion of the Northern Apennines, at the forelimb-crest transition of a major out-of-sequence thrust-related anticline, that deformed the previously stacked thrust sheet pile. The Compione Fault can be traced in seismic reflection profile down to the seismic basement top at about 6 to 7 km depth and dissects the previously produced contractional architecture. This fault zone offers the possibility to study the interaction between deformation, fluid flow, and fracture cementation that progressed from a depth of ~5 km up to near surface conditions. The following major points can be drawn from this multidisciplinary study of the Compione Fault cross-sectional architecture, resulting from the combination of structural, petrographical, geochemical, microthermometric, and paleothermal analyses.

- The footwall damage zone, affecting thick sandstone strata, is characterized by a network of shear veins with bisectors perpendicular to bedding, which was passively rotated by extensional fault-propagation folding during upward fault growth. Such a fracture mesh testifies for the presence of a wide process zone ahead of the fault tip in the early evolutionary stages. A comparable deformation pattern does not occur in the hanging wall damage zone because of either the carbonate composition of the Ottone Flysch Formation that favored an important role of dissolution, or the presence of clay-rich sediments tectonically juxtaposed at its base, which provided a strong mechanical discontinuity, or both.
- Mineralization of the process zone fracture network by a prehnite-quartz-calcite assemblage from a fluid at a minimum temperature of 210 °C, possibly exceeding 230 °C, indicates that: (*i*) the process zone provided a well-connected fracture mesh that significantly improved porosity and favored effective circulation and upward fluid migration; (*ii*) such a deep fluid volume constituted a hydrothermal plume in strong thermal disequilibrium with the host rock outside the fault zone, which experienced maximum temperatures of less than 140–150 °C.
- Shear vein cementation in the process zone was cyclic and episodic, indicating fluid pressure variations that might relate to the earthquake cycle. According to this hypothesis, seismic pumping may have promoted fast channelized fluid migration from the metamorphic basement, along the fault zone and up to the process zone.
- Synthetic rotation about a horizontal axis of the process zone caused antithetic reactivation of pre-existing shear veins as subsidiary faults and formation of new, non-mineralized high-angle extensional faults. This event of deformation localization represents the formation of the fault damage zones *sensu-stricto*.
- The structural and paleofluid framework exposed in the thick sandstone beds at the footwall of the Compione Fault highlights the importance of the process zone for both fault scaling properties and hydrology. Process zone width is twice that of the damage zone *sensu-stricto*, produced by deformation localization during fault slip. This means that the total volume of footwall fractured rocks, typically included into the damage zone as a whole, is much thicker than what can be expected from statistical scaling laws and has a structural fabric mainly imprinted at the process zone stage. Furthermore, it developed diachronously during fault evolution, with maximum permeability and fluid advection ahead of the upward propagating fault tip, followed by fracture cementation, deformation localization, and porosity and permeability reduction in more mature stages.
- Development of a process zone at the onset of extensional faulting can significantly contribute to creating economically valuable fractured reservoirs ahead of fault tips. Extensional fault-propagation folding favors migration and accumulation of fluids from deeper stratigraphic horizons and the metamorphic basement into the extensional process zone, where high fluid pressures may likely occur. Eventually, fault breakthrough causes reservoir compartmentalization and sealing, preserving favorable conditions for fluid storage in the footwall damage zone and the corresponding process zone sector.
- Depending on the first-order mechanical stratigraphy, development of crustal-scale extensional fault systems can create a strong vertical variability of fractured rock volumes resulting from the interplay among several factors, including: (*i*) the dominant deformation mechanisms, (*ii*) fault-propagation versus slip rates, (*iii*) possible development and width of a vertically compartmentalized process zone ahead of the upward-migrating fault tip, (*iv*) competition between faulting and folding, etc. Such a large variability and vertical compartmentalization of the cross-sectional damage zone width strongly impacts fluid storage potential and partitioning in rift-related fault-bounded blocks, as well as the seismic behavior of fault zones.

ACKNOWLEDGMENTS

Discussions with Mahtab Mozafari and Alessandra Montanini on vein cement analysis are gratefully acknowledged. We are indebted to Andrea Comelli for thin section preparation, Enrico Selmo for providing isotopic data, Luca Barchi for support with scanning electron microscopy, and Zita Kelemen and Steven Bouillon for help with micromilling equipment. Anna Laura Cazzola, Alessandro Fattorini, and Claudio Cattaneo of Eni S.p.A. are thanked for providing reflection seismic data and authorizing their publication, and Midland Valley Exploration Ltd. for the use of MOVE software under the Academic Software Initiative (ASI). Alessio Lucca and Fabrizio Storti ideated the study, collected most of the data, and wrote the manuscript; Giancarlo Molli and Fabrizio Balsamo participated in the fieldwork, data discussion, and tectonic interpretations; Philippe Muchez participated in the analysis and interpretation of vein cement petrographic, microthermometric, and geochemical data; Andrea Schito and Sveva Corrado provided vitrinite reflectance data and their thermal modelling, and discussed their meaning in the framework of this research; Andrea Artoni depth converted and interpreted reflection seismic data; and Emma Salvioli Mariani helped with Raman spectroscopy and fluid inclusion analysis.

REFERENCES CITED

Abbate, E., Balestrieri, M.L., Bigazzi, G., Norelli, P., and Quercioli, C., 1994, Fission-track dating and recent rapid denudation in Northern Apennines, Italy: Memorie della Societa Geologica Italiana, v. 48, p. 579–585.

Anderson, E.M., 1951, The Dynamics of Faulting and Dyke Formation with Application to Britain (2nd edition): Edinburgh, Scotland, Oliver and Boyd, p. 206.

Argnani, A., 2002, The Northern Apennines and the kinematics of Europe-Africa convergence: Bollettino della Società Geologica Italiana, v. 1, p. 47–60.

Argnani, A., Barbacini, G., Bernini, M., Camurri, F., Ghielmi, M., Papani, G., Rizzini, F., Rogledi, S., and Torelli, L., 2003, Gravity tectonics driven by Quaternary uplift in the Northern Apennines: Insights from the La Spezia-Reggio Emilia geo-transect: Quaternary International, v. 101-102, p. 13–26, https://doi.org/10.1016/S1040-6182(02)00088-5.

Arnason, J.G., Bird, D.K., and Liou, J.G., 1993, Variables controlling epidote composition in hydrothermal

and low-pressure regional metamorphic rocks: Abhandlungen der Geologischen Bundesanstalt, v. 49, p. 17–25.
Artoni, A., Bernini, M., Papani, G., Vescovi, P., and Zanzucchi, G., 1992, Sezione geologica schematica Bonassola (SP)-Felino (PR): Studi Geologici Camerti, Volume Speciale 1992/2, CROP 01-1A, p. 61–63.
Augliera, P., Pastore, S., and Tomaselli, A., 1990, Sismicità della Lunigiana-Garfagnana: Primi risultati da una rete mobile: Proc. 9: Gruppo Nazionale di Geofisica della Terra Solida, v. 1, p. 221–232.
Azzaroli, A., 1950, Osservazioni sulla formazione villafranchiana di Olivola in Val di Magra: Atti della Società Toscana di Scienze Naturali Memorie, v. 57, p. 104–111.
Azzaroli, A., 1977, The Villafranchian stage in Italy and the Plio-Pleistocene boundary: Giornale di Geologia, v. 41, p. 61–79.
Balestrieri, M.L., Bernet, M., Brandon, M.T., Picotti, V., Reiners, P., and Zattin, M., 2003, Pliocene and Pleistocene exhumation and uplift of two key areas of the Northern Apennines: Quaternary International, v. 101-102, p. 67–73, https://doi.org/10.1016/S1040-6182(02)00089-7.
Barchi, M.R., Minelli, G., and Pialli, G., 1998, The CROP 03 Profile: A synthesis of results on deep structures of the Northern Apennines: Memorie della Societa Geologica Italiana, v. 52, p. 383–400.
Bartole, R., 1995, The North Tyrrhenian–Northern Apennines post-collisional system: Constraints for a geodynamic model: Terra Nova, v. 7, p. 7–30, https://doi.org/10.1111/j.1365-3121.1995.tb00664.x.
Bartolini, C., Bernini, M., Carloni, G.C., Costantini, A., Federici, P.R., Gasperi, G., Lazzarotto, A., Marchetti, G., Mazzanti, R., Papani, G., Pranzini, G., Rau, A., Sandrelli, F., Vercesi, P.L., Castaldini, D., and Francavilla, F., 1982, Carta Neotettonica dell'Appennino Settentrionale: Note Illustrative: Bolletino della Società Geologica Italiana, v. 101, p. 355–371.
Beaudoin, N., Bellahsen, N., Lacombe, O., and Emmanuel, L., 2011, Fracture-controlled paleohydrogeology in a basement-cored, fault-related fold: Sheep Mountain Anticline, Wyoming, United States: Geochemistry Geophysics Geosystems, v. 12, 6, Q06011, https://doi.org/10.1029/2010GC003494.
Bernet, M., Brandon, M.T., Garver, J.I., and Molitor, B.R., 2004, Fundamentals of detrital zircon fission-track analysis for provenance and exhumation studies with examples from the European Alps, *in* Bernet M., and Spiegel C., eds., Detrital Thermochronology; Provenance Analysis, Exhumation, and Landscape Evolution of Mountain Belts: Geological Society of America Special Paper 378, p. 25–36, https://doi.org/10.1130/0-8137-2378-7.25.
Bernini, M., 1988, Il bacino dell'Alta Val Magra: Primi dati mesostrutturali sulla tettonica distensiva: Bollettino della Società Geologica Italiana, v. 107, p. 355–371.
Bernini, M., 1991, Le strutture estensionali della Lunigiana (Appennino Settentrionale): Proposta di un modello deformativo: Atti Ticinese di Scienze della Terra, v. 34, p. 29–38.
Bernini, M., and Lasagna, S., 1988, Rilevamento geologico e analisi strutturale del bacino dell'Alta Val Magra tra M. Orsaro e Pontremoli (Appennino Settentrionale): Atti della Società Toscana di Scienze Naturali Memorie, Series A, v. 95, p. 139–183.
Bernini, M., and Papani, G., 2002, La distensione della fossa tettonica della Lunigiana nord-occidentale (con carta geologica alla scala 1:50.000): Bollettino della Società Geologica Italiana, v. 121, p. 313–341.
Bernini, M., Boccaletti, M., Moratti, G., Papani, G., Sani, F., and Torelli, L., 1990, Episodi compressivi Neogenico-Quaternari nell'area estensionale tirrenica nord-orientale. Dati in mare e a terra: Memorie della Societa Geologica Italiana, v. 45, p. 577–589.
Bernini, M., Vescovi, P., and Zanzucchi, G., 1997, Schema strutturale dell'Appennino Nord-Occidentale: L'Ateneo Parmense. Acta Naturalia : Organo della Societa di Medicina e Scienze Naturali di Parma, v. 33, p. 43–54.
Bertoldi, R., 1988, Una sequenza palinologica di età ruscciniana nei sedimenti palustri basali del bacino di Aulla-Olivola (Val di Magra): Rivista Italiana di Paleontologia e Stratigrafia, v. 94, p. 105–138.
Bertoldi, R., 1995, Palinostratigrafia dei bacini intramontani dell'Appennino nord-occidentali: Il Quaternario, v. 8, p. 61–70.
Bird, D.K., and Helgeson, H.C., 1980, Chemical interaction of aqueous solutions with epidote-feldspar mineral assemblages in geologic systems. I. Thermodynamic analysis of phase relations in the system CaO-FeO-Fe_2O_3-Al_2O_3-SiO_2-H_2O-CO_2: American Journal of Science, v. 280, p. 907–941, https://doi.org/10.2475/ajs.280.9.907.
Bird, D.K., and Helgeson, H.C., 1981, Chemical interaction of aqueous solutions with epidote-feldspar mineral assemblages in geologic systems. II. Equilibrium constraints in metamorphic/geothermal processes: American Journal of Science, v. 281, p. 576–614, https://doi.org/10.2475/ajs.281.5.576.
Boccaletti, M., and Sani, F., 1998, Cover thrust reactivations related to internal basement involvement during Neogene–Quaternary evolution of the Northern Apennines: Tectonics, v. 17, p. 112–130, https://doi.org/10.1029/97TC02067.
Boccaletti, M., Elter, P., and Guazzone, G., 1971, Plate tectonic models for the development of the Western Alps and Northern Apennines: Nature, v. 234, p. 108–111.
Boccaletti, M., Cerrina Ferroni, A., Martinelli, P., Moratti, G., Plesi, G., and Sani, F., 1992, Late Miocene–Quaternary compressive events in the Tyrrhenian side of the Northern Apennines: Annales Tectonicae, v. 6, p. 214–230.
Boccaletti, M., Gianelli, G., and Sani, F., 1997, Tectonic regime, granite emplacement and crustal structure in the inner zone of the Northern Apennines (Tuscany, Italy): A new hypothesis: Tectonophysics, v. 270, p. 127–143, https://doi.org/10.1016/S0040-1951(96)00177-1.
Boccaletti, M., Corti, G., and Martelli, L., 2011, Recent and active tectonics of the external zone of the Northern Apennines (Italy): International Journal of Earth Sciences, v. 100, p. 1331–1348, https://doi.org/10.1007/s00531-010-0545-y.
Bodnar, R.J., 1993, Revised equation and table to determine the freezing point depression of H_2O-NaCl solutions: Geochimica et Cosmochimica Acta, v. 57, p. 683–684, https://doi.org/10.1016/0016-7037(93)90378-A.
Boiron, M.C., Cathelineau, M., Ruggieri, G., Jeanningros, A., Gianelli, G., and Banks, A., 2007, Active contact metamorphism and CO_2-CH_4 fluid production in the Larderello geothermal field (Italy) at depths between 2.3 and 4 km: Chemical Geology, v. 237, p. 303–327, https://doi.org/10.1016/j.chemgeo.2006.06.028.
Boncio, P., Brozzetti, F., and Lavecchia, G., 2000, Architecture and seismotectonics of a regional low-angle normal fault zone in central Italy: Tectonics, v. 19, p. 1038–1055, https://doi.org/10.1029/2000TC900023.
Bonini, M., Moratti, G., Sani, F., and Balestrieri, M.L., 2013, Compression-to-extension record in the late Pliocene–Pleistocene Upper Valdarno Basin (Northern Apennines, Italy): Structural and thermochronological constraints: Italian Journal of Geosciences, v. 132, p. 54–80, https://doi.org/10.3301/IJG.2011.18.
Bons, P.D., 2001, Development of crystal morphology during unitaxial growth in a progressively widening vein: I. The numerical model: Journal of Structural Geology, v. 23, p. 865–872, https://doi.org/10.1016/S0191-8141(00)00159-0.
Bons, P.D., Elburg, M.A., and Gomez-Rivas, E., 2012, A review of the formation of tectonic veins and their microstructures: Journal of Structural Geology, v. 43, p. 33–62, https://doi.org/10.1016/j.jsg.2012.07.005.
Boschetti, T., Toscani, L., Barbieri, M., Mucchino, C., and Marino, T., 2017, Low enthalpy Na-chloride waters from the Lunigiana and Garfagnana grabens, Northern Apennines, Italy: Tracing fluid connections and basement interactions via chemical and isotopic compositions: Journal of Volcanology and Geothermal Research, v. 348, p. 12–25, https://doi.org/10.1016/j.jvolgeores.2017.10.008.
Bossolasco, M., Eva, C., and Pasquale, C., 1973, Il terremoto del 25 Ottobre in Lunigiana: Rivista Italiana di Geofisica, v. 22, p. 314–322.
Bossolasco, M., Eva, C., and Pasquale, C., 1974, On seismotectonics of the Alps and Northern Apennines: Rivista Italiana di Geofisica, v. 23, 1-2, p. 57–63.
Boullier, A.-M., and Robert, F., 1992, Paleoseismic events recorded in Archean gold-quartz vein networks, Val d'Or, Abitibi, Quebec, Canada: Journal of Structural Geology, v. 14, p. 161–180, https://doi.org/10.1016/0191-8141(92)90054-Z.
Boullier, A.-M., Charoy, B., and Pollard, P.J., 1994, Fluctuation in porosity and fluid pressure during hydrothermal events: Textural evidence in the Emuford District, Australia: Journal of Structural Geology, v. 16, 10, p. 1417–1429, https://doi.org/10.1016/0191-8141(94)90006-X.
Browne, P.R.L., 1978, Hydrothermal alteration in active geothermal fields: Annual Review of Earth and Planetary Sciences, v. 6, p. 229–250, https://doi.org/10.1146/annurev.ea.06.050178.001305.
Burkhard, M., 1993, Calcite twins, their geometry, appearance and significance as stress-strain markers and indicators of tectonic regime: A review: Journal of Structural Geology, v. 15, p. 351–368, https://doi.org/10.1016/0191-8141(93)90132-T.
Burnham, A.K., and Sweeney, J.J., 1989, A chemical kinetic model of vitrinite maturation and reflectance: Geochimica et Cosmochimica Acta, v. 53, p. 2649–2657, https://doi.org/10.1016/0016-7037(89)90136-1.
Bustin, R.M., Barnes, M.A., and Barnes, W.C., 1990, Determining levels of organic diagenesis in sediments and fossil fuels, *in* McIleareath, I.A., and Morrow, D.W., eds., Diagenesis: Geoscience Canada Reprint Series 4, p. 205–226.
Butler, R.W.H., 1992, Hydrocarbon maturation, migration and tectonic loading in the western Alps, *in* England, W.A., and Fleet, A.J., eds., Petroleum Migration: Geological Society of London Special Publication 59, p. 227–244.
Caine, J.S., Evans, J.P., and Forster, J.B., 1996, Fault zone architecture and permeability structure: Geology, v. 24, p. 1025–1028, https://doi.org/10.1130/0091-7613(1996)024<1025:FZAAPS>2.3.CO;2.
Camurri, F., Argnani, A., Bernini, M., Papani, G., Rogledi, S., and Torelli, L., 2001, The basement of the NW Apennines: Interpretation of reflection seismics and geodynamic implications: Final Proceedings, Geoitalia 2001, 3° Forum Italiano di Scienze della Terra (Fist), Chieti, Italy, p. 50–51.
Caricchi, C., Aldega, L., and Corrado, S., 2015, Reconstruction of maximum burial along the Northern Apennines thrust wedge (Italy) by indicators of thermal exposure and modeling: Geological Society of America Bulletin, v. 127, 3-4, p. 428–442, https://doi.org/10.1130/B30947.1.
Carlini, M., Artoni, A., Aldega, L., Balestrieri, M.L., Corrado, S., Vescovi, P., Bernini, M., and Torelli, L., 2013, Exhumation and reshaping of far-travelled/allochthonous tectonic units in mountain belts. New insights for the relationships between shortening and coeval extension in the western Northern Apennines (Italy): Tectonophysics, v. 608, p. 267–287, https://doi.org/10.1016/j.tecto.2013.09.029.
Carmignani, L., and Kligfield, R., 1990, Crustal extension in the Northern Apennines: The transition from compression to extension in the Alpi Apuane core complex: Tectonics, v. 9, p. 1275–1303, https://doi.org/10.1029/TC009i006p01275.
Carmignani, L., Decandia, F.A., Fantozzi, P.L., Lazzarotto, A., Liotta, D., and Meccheri, M., 1994, Tertiary extensional tectonics in Tuscany (Northern Apennines, Italy): Tectonophysics, v. 238, p. 295–315, https://doi.org/10.1016/0040-1951(94)90061-2.
Carmignani, L., Decandia, F.A., Disperati, L., Fantozzi, P.L., Lazzarotto, A., Liotta, D., and Oggiano, G., 1995, Relationships between the Tertiary structural evolution of the Sardinia-Corsica-Provençal Domain and the Northern Apennines: Terra Nova, v. 7, 2, p. 128–137, https://doi.org/10.1111/j.1365-3121.1995.tb00681.x.
Carosi, R., Leoni, L., Montomoli, C., and Sartori, F., 2003, Very low-grade metamorphism in the Tuscan Nappe, Northern Apennines, Italy: Relationships between deformation and metamorphic indicators in the La Spezia mega-fold: Schweizerische Mineralogische und Petrographische Mitteilungen, v. 83, p. 15–32.
Carter, K.E., and Dworkin, S.I., 1990, Channelized fluid flow through shear zones during fluid-enhanced dynamic

recrystallization, Northern Apennines, Italy: Geology, v. 18, p. 720–723, https://doi.org/10.1130/0091-7613(1990)018<0720:CFFTSZ>2.3.CO;2.

Cavarretta, G., Gianelli, G., and Puxeddu, M., 1982, Formation of authigenic minerals and their use as indicators of the physicochemical parameters of the fluid in the Larderello-Travale geothermal field: Economic Geology and the Bulletin of the Society of Economic Geologists, v. 77, p. 1071–1084, https://doi.org/10.2113/gsecongeo.77.5.1071.

Cerrina Feroni, A., Moratti, G., and Plesi, G., 1983, Evidenze di episodi compressivi messiniano-pliocenici alternati alla tettonica di distensione nella Toscana sud-occidentale, emerse dall'analisi mesostrutturale, *in* Atti della riunione su "Meccanismi deformativi nelle catene perimediterranee: Stato di avanzamento delle ricerche e problematiche emerse": Firenze, Italy, 5 dicembre 1983, Centro Stampa Palagi Firenze, p. 35–42.

Childs, C., Manzocchi, T., Walsh, J.J., Bonson, C.G., Nicol, A., and Schopfer, M.P.J., 2009, A geometric model of fault zone and fault rock thickness variations: Journal of Structural Geology, v. 31, 2, p. 117–127, https://doi.org/10.1016/j.jsg.2008.08.009.

Clemenzi, L., Molli, G., Storti, F., Muchez, P., Swennen, R., and Torelli, L., 2014, Extensional deformation structures within a convergent orogen: The Val di Lima low-angle normal fault system (Northern Apennines, Italy): Journal of Structural Geology, v. 66, p. 205–222, https://doi.org/10.1016/j.jsg.2014.05.019.

Connolly, J.A.D., 2010, The mechanics of metamorphic fluid expulsion: Elements, v. 6, p. 165–172, https://doi.org/10.2113/gselements.6.3.165.

Corrado, S., Aldega, L., and Zattin, M., 2010, Sedimentary vs. tectonic burial and exhumation along the Apennines (Italy), *in* Beltrando M., Peccerillo A., Mattei M., Conticelli S., and Doglioni C., eds., The Geology of Italy: Journal of the Virtual Explorer, Electronic Edition, v. 36, paper 15, https://doi.org/10.3809/jvirtex.2010.00232.

Cowie, P.A., and Shipton, Z.K., 1998, Fault tip displacement gradients and process zone dimension: Journal of Structural Geology, v. 20, p. 983–997, https://doi.org/10.1016/S0191-8141(98)00029-7.

Cox, S.F., 1995, Faulting processes at high fluid pressures: An example of fault valve behavior from the Wattle Gully Fault, Victoria, Australia: Journal of Geophysical Research, v. 100, p. 12841–12859, https://doi.org/10.1029/95JB00915.

Cox, S.F., 1999, Deformational controls in the dynamics of fluid flow in mesothermal gold systems, *in* McCaffrey, K., Lonergan, L., and Wilkinson, J., eds., Fractures, Fluid Flow and Mineralization: Geological Society of London Special Publication, v. 155, p. 123–140, https://doi.org/10.1144/GSL.SP.1999.155.01.10.

Curewitz, D., and Karson, J.A., 1997, Structural settings of hydrothermal outflow: Fracture permeability maintained by fault propagation and interaction: Journal of Volcanology and Geothermal Research, v. 79, p. 149–168, https://doi.org/10.1016/S0377-0273(97)00027-9.

Davis, D.M., Suppe, J., and Dahlen, F.A., 1983, Mechanics of fold-and thrust belts and accretionary wedges: Journal of Geophysical Research, v. 88, p. 1153–1172, https://doi.org/10.1029/JB088iB02p01153.

Decandia, F.A., Lazzarotto, A., and Liotta, D., 1998, The CROP 03 traverse: Insights on post-collisional evolution of Northern Apennines: Memorie della Societa Geologica Italiana, v. 52, p. 427–440.

Della Vedova, B., Lucazeau, F., Pasquale, V., Pellis, G., and Verdoya, M., 1995, Heat flow in the tectonic provinces crossed by the southern segment of the European Geotraverse: Tectonophysics, v. 244, p. 57–74, https://doi.org/10.1016/0040-1951(94)00217-W.

Dewey, J.F., Helman, M.L., Knott, S.D., Turco, E., and Hutton, D.H.W., 1989, Kinematics of the western Mediterranean, *in* Coward M.P., Dietrich D., and Park R.G., eds., Alpine Tectonics: Geological Society of London Special Publication, v. 45, p. 265–283.

Dickson, J.A.D., 1966, Carbonate identification and genesis as revealed by staining: Journal of Sedimentary Petrology, v. 32, p. 491–505.

Di Naccio, D., Boncio, P., Brozzetti, F., Pazzaglia, F.J., and Lavecchia, G., 2013, Morphotectonic analysis of the Lunigiana and Garfagnana grabens (northern Apennines, Italy): Implications for active normal faulting: Geomorphology, v. 201, p. 293–311, https://doi.org/10.1016/j.geomorph.2013.07.003.

Dini, A., Gianelli, G., Puxeddu, M., and Ruggieri, G., 2005, Origin and evolution of Pliocene-Pleistocene granites from the Larderello geothermal field (Tuscan Magmatic Province, Italy): Lithos, v. 81, p. 1–31, https://doi.org/10.1016/j.lithos.2004.09.002.

Di Paolo, L., Aldega, L., Corrado, S., and Mastalerz, M., 2012, Maximum burial and unroofing of Mt. Judica recess area in Sicily: Implication for the Apenninic Maghrebian wedge dynamics: Tectonophysics, v. 530-531, p. 193–207, https://doi.org/10.1016/j.tecto.2011.12.020.

Di Pisa, A., Franceschelli, M., Leoni, L., and Meccheri, M., 1985, Regional variation of the metamorphic temperatures across the Tuscanid 1 unit and its implications on the alpine metamorphism (Apuane Alps, N-Tuscany): Neues Jahrbuch für Mineralogie. Abhandlungen, v. 151, p. 197–211.

Doglioni, C., 1991, A proposal for the kinematic modelling of W-dipping subductions: Possible applications to the Tyrrhenian-Apennines system: Terra Nova, v. 3, 4, p. 423–434, https://doi.org/10.1111/j.1365-3121.1991.tb00172.x.

Doglioni, C., Barba, S., Carminati, E., and Riguzzi, F., 2014, Fault on-off versus coseismic fluids reaction: Geoscience Frontiers, v. 5, p. 767–780, https://doi.org/10.1016/j.gsf.2013.08.004.

Durney, D.W., and Ramsay, J.G., 1973, Incremental strains measured by syntectonic crystal growths, *in* De Jong K.A., and Scholten, K., eds., Gravity and Tectonics: New York, USA, Wiley, p. 67–96.

Elter, P., and Pertusati, P., 1973, Considerazioni sul limite Alpi-Appennino e sulle relazioni con l'arco delle Alpi occidentali: Memorie della Societa Geologica Italiana, v. 12, p. 359–375.

Elter, P., and Schwab, K., 1959, Note illustrative della Carta Geologica alla scala 1:50.000 della regione Carro-Zeri-Pontremoli: Bollettino della Società Geologica Italiana, v. 78, p. 157–187.

Elter, P., Giglia, G., Tongiorgi, M., and Trevisan, L., 1975, Tensional and compressional areas in recent (Tortonian to present) evolution of Northern Apennines: Bollettino di Geofisica Teorica ed Applicata, v. 17, p. 13–18.

Endignoux, L., and Wolf, S., 1990, Thermal and kinematic evolution of thrust basins: A 2D numerical model, *in* Letouezy, J., ed., Petroleum and Tectonics in Mobile Belts: Paris, France, Editions Technip, p. 181–192.

Eva, E., Solarion, S., and Boncio, P., 2014, HypoDD relocated seismicity in northern Apennines, (Italy) preceding the 2013: Seismotectonic implications for the Lunigiana-Garfagnana area: Bollettino di Geofisica Teorica ed Applicata, v. 55, p. 739–754.

Evans, M.A., and Battles, D.A., 1999, Fluid inclusion and stable isotope analyses of veins from the central Appalachian Valley and Ridge province: Implications for regional synorogenic hydrologic structure and fluid migration: Geological Society of America Bulletin, v. 111, p. 1841–1860, https://doi.org/10.1130/0016-7606(1999)111<1841:FIASIA>2.3.CO;2.

Faulkner, D.R., and Rutter, E.H., 2001, Can the maintenance of overpressured fluids in large strike-slip fault zones explain their apparent weakness?: Geology, v. 29, 6, p. 503–506, https://doi.org/10.1130/0091-7613(2001)029<0503:CTMOOF>2.0.CO;2.

Faulkner, D., Jackson, C., Lunn, R., Schlische, R., Shipton, Z., Wibberley, C., and Withjack, M., 2010, A review of recent developments concerning the structure, mechanics and fluid flow properties of fault zones: Journal of Structural Geology, v. 32, p. 1557–1575, https://doi.org/10.1016/j.jsg.2010.06.009.

Federici, P.R., 1978, La tettonica recente dell'Appennino 2) Il bacino fluvio-lacustre di Pontremoli (Alta Val di Magra) e sue implicazioni neotettoniche: G.S.Q.P., Quaderno, v. 4, p. 121–131.

Federici, P.R., 1981, Nuovi resti di vertebrato nel bacino fluvio-lacustre villafranchiano di Pontremoli (Val di Magra): Bolletino della Museo di Scienze Naturale della Lunigiana, v. 1, 2, p. 71–74.

Fellin, M.G., Reiners, P.W., Brandon, M.T., Wüthrich, E., Balestrieri, M.L., and Molli, G., 2007, Thermochronologic evidence for the exhumational history of the Alpi Apuane metamorphic core complex, Northern Apennines, Italy: Tectonics, v. 26, TC6015, https://doi.org/10.1029/2006TC002085.

Ferrill, D.A., Morris, A.P., Sims, D.W., Waiting, D.J., and Hasegawa, S., 2004a, Development of synthetic layer dip adjacent to normal faults, *in* Sorkhabi R., and Tsuji Y., eds., Faults, Fluid Flow, and Petroleum Traps: American Association of Petroleum Geologists Memoir: Tulsa, Oklahoma, USA, American Association of Petroleum Geologists, p. 125–138.

Ferrill, D.A., Morris, A.P., Evans, M.A., Burkhard, M., Groshong, R.H., and Onasch, C.M., 2004b, Calcite twin morphology: A low-temperature deformation geothermometer: Journal of Structural Geology, v. 26, p. 1521–1529, https://doi.org/10.1016/j.jsg.2003.11.028.

Fisher, D.M., Brantley, S.L., Everett, M., and Dzvonik, J., 1995, Cyclic fluid-flow through a regionally extensive fracture network within the Kodiak accretionary prism: Journal of Geophysical Research. Solid Earth, v. 100, p. 12881–12894, https://doi.org/10.1029/94JB02816.

Fondriest, M., Smith, S.A.F., Candela, T., Nielsen, S.B., Mair, K., and Di Toro, G., 2013, Mirror-like faults and power dissipation during earthquakes: Geology, v. 41, 11, p. 1175–1178, https://doi.org/10.1130/G34641.1.

Fossen, H., 2010, Structural Geology: Cambridge, UK, Cambridge University Press, 463 p., https://doi.org/10.1017/CBO9780511777806.

Fossen, H., Schultz, R.A., Shipton, Z.K., and Mair, K., 2007, Deformation bands in sandstone: A review: Journal of the Geological Society, v. 164, p. 755–769, https://doi.org/10.1144/0016-76492006-036.

Franceschelli, M., Leoni, L., Memmi, I., and Puxeddu, M., 1986, Regional distribution of Al-silicates and metamorphic zonation in the low-grade Verrucano metasediments from the Northern Apennines, Italy: Journal of Metamorphic Geology, v. 4, p. 309–321, https://doi.org/10.1111/j.1525-1314.1986.tb00353.x.

Frepoli, A., and Amato, A., 1997, Contemporaneous extension and compression in the Northern Apennines from earthquake fault-plane solutions: Geophysical Journal International, v. 129, p. 368–388, https://doi.org/10.1111/j.1365-246X.1997.tb01589.x.

Friedman, I., and O'Neil, J.R., 1977, Compilation of stable isotope fractionation factors of geochemical interest, *in* Fleisher, M., ed., Data of Geochemistry (6th edition): U.S. Geological Survey Professional Paper 440-KK, 117 p.

Ghelardoni, R., 1965, Osservazioni sulla tettonica trasversale dell'Appennino settentrionale: Bollettino della Società Geologica Italiana, v. 84, p. 276–290.

Ghibaudo, G., 1980, Deep-sea fan deposits in the Macigno Formation (middle-upper Oligocene) of the Gordana Valley, northern Apennines, Italy: Journal of Sedimentary Research, v. 50, p. 723–741.

Gianelli, G., Ruggieri, G., and Mussi, M., 1997, Isotopic and fluid inclusion study of hydrothermal and metamorphic carbonates in the Larderello geothermal field and surrounding areas, Italy: Geothermics, v. 26, p. 393–417, https://doi.org/10.1016/S0375-6505(97)00001-1.

Giglia, G., 1974, L'insieme Corsica-Sardegna e I suoi rapport con l'Appenino settentrionale: rassegna di dati cronologici e strutturali, *in* Maxia, C., and Pomesano A., eds., Paleogeografia del Terziario sardo nell'ambito del Mediterraneo occidentale: Cagliari, Italy, Rendiconti Semestrali della Facoltà di Scienze, Università di Cagliari, 43, p. 245–275.

Giustini, F., Brilli, M., and Patera, A., 2016, Mapping oxygen stable isotopes of precipitation in Italy: Journal of Hydrology: Regional Studies, v. 8, p. 162–181.

Goldstein, R.H., and Reynolds, J., 1994, Systematics of Fluid Inclusions in Diagenetic Minerals: Short Course Notes: Tulsa, Oklahoma, USA, The Society for Sedimentary Geology, v. 31, https://doi.org/10.2110/scn.94.31.

Gratier, J.P., Favreau, P., Renard, F., and Pili, E., 2002, Fluid pressure evolution during the earthquake cycle controlled by fluid flow and pressure-solution crack sealing: Earth, Planets, and Space, v. 54, p. 1139–1146, https://doi.org/10.1186/BF03353315.

Hardy, S., and Ford, M., 1997, Numerical modelling of trishear fault propagation folding: Tectonics, v. 16, 5, p. 841–854, https://doi.org/10.1029/97TC01171.

Hardy, S., and McClay, K., 1999, Kinematic modeling of extensional fault propagation folding: Journal of Structural Geology, v. 21, p. 695–702, https://doi.org/10.1016/S0191-8141(99)00072-3.

Hilgers, C., and Urai, J.L., 2002, Experimental study of syntaxial vein growth during lateral fluid flow in transmitted light: First results: Journal of Structural Geology, v. 24, p. 1029–1043, https://doi.org/10.1016/S0191-8141(01)00089-X.

Hoefs, J., 1997, Stable Isotope Geochemistry: Berlin, Germany, Springer Verlag, 200 p, https://doi.org/10.1007/978-3-662-03377-7.

Holland, M., and Urai, J.L., 2010, Evolution of anastomosing crack-seal vein networks in limestones: Insights from an exhumed high pressure cell, Jabal Shams, Oman Mountains: Journal of Structural Geology, v. 32, p. 1279–1290, https://doi.org/10.1016/j.jsg.2009.04.011.

Honlet, R., Gasparrini, M., Jager, H., Muchez, P., and Swennen, R., 2017, Precursor and ambient rock paleothermometry to assess the thermicity of burial dolomitization in the southern Cantabrian Zone (northern Spain): International Journal of Earth Sciences, v. 106-107, p. 1–21.

Huber, M., Halas, S., and Sikorska, M., 2007, Evolution of prehnite-albite-calcite veins in metamorphic rocks from the Lapland Granulite Belt (Kandalaksha region of Kola Peninsula): Geologija, v. 57, p. 1–7.

Ingebritsen, S.E., and Manning, C.E., 2010, Permeability of the continental crust: Dynamic variations inferred from seismicity and metamorphism: Geofluids, v. 10, p. 193–205.

Jessell, M.W., Willman, C.E., and Gray, D.R., 1994, Bedding parallel veins and their relationship to folding: Journal of Structural Geology, v. 16, p. 753–767, https://doi.org/10.1016/0191-8141(94)90143-0.

Jin, G., and Groshong, R.H., Jr., 2006, Trishear kinematic modelling of extensional fault-propagation folding: Journal of Structural Geology, v. 28, p. 170–183, https://doi.org/10.1016/j.jsg.2005.09.003.

Jolivet, L., Faccenna, C., Goffé, B., Mattei, M., Rossetti, F., Brunet, C., Storti, F., Funiciello, R., Cadet, J.P., D'Agostino, N., and Parra, T., 1998, Midcrustal shear zones in postorogenic extension: Example from the northern Tyrrhenian Sea: Journal of Geophysical Research, v. 103, p. 12123–12160, https://doi.org/10.1029/97JB03616.

Ketcham, R.A., Donelick, R.A., and Carlson, W.D., 1999, Variability of apatite fission-track annealing kinetics: III. Extrapolation to geological time scales: The American Mineralogist, v. 84, p. 1235–1255, https://doi.org/10.2138/am-1999-0903.

Kim, Y.S., Peacock, D.C.P., and Sanderson, D.J., 2004, Fault damage zones: Journal of Structural Geology, v. 26, 3, p. 503–517, https://doi.org/10.1016/j.jsg.2003.08.002.

Knott, S.D., Beach, A., Brockbank, P.J., Brown, J.L., McCallum, J.E., and Welbon, A.I., 1996, Spatial and mechanical controls on normal fault population: Journal of Structural Geology, v. 18, p. 359–372, https://doi.org/10.1016/S0191-8141(96)80056-3.

Koehn, D., and Passchier, C.W., 2000, Shear sense indicators in striped bedding-veins: Journal of Structural Geology, v. 22, p. 1141–1151, https://doi.org/10.1016/S0191-8141(00)00028-6.

Laurent, D., Lopez, M., Chauvet, A., Sauvage, A.C., Buatier, M., and Spangenberg, J.E., 2017, Sedimentary fluids/fault interaction during syn-rift burial of the Lodève Permian Basin (Hérault, France): An example of seismic-valve mechanism in active extensional faults: Marine and Petroleum Geology, v. 88, p. 303–328, https://doi.org/10.1016/j.marpetgeo.2017.08.021.

Lockner, D.A., Byerlee, J.D., Kuksenk, V., Ponomarev, A., and Sidorin, A., 1992, Observation of quasistatic fault growth from acoustic emissions, *in* Evans, B., and Wong, T.F., eds., Fault Mechanics and Transport Properties of Rocks: San Diego, California, USA, Academic, p. 3–32.

Longinelli, A., and Selmo, E., 2003, Isotopic composition of precipitation in Italy: A first overall map: Journal of Hydrology (Amsterdam), v. 270, p. 75–88, https://doi.org/10.1016/S0022-1694(02)00281-0.

Malinverno, A., and Ryan, W.B.F., 1986, Extension in the Tyrrhenian Sea and shortening in the Apennines as result of arc migration driven by sinking of the lithosphere: Tectonics, v. 5, p. 227–245, https://doi.org/10.1029/TC005i002p00227.

Mamadou, M.M., Chatelineau, M., Bourdelle, F., Boiron, M.-C., Elmaleh, A., and Brouand, M., 2016, Hot fluid flows around a major fault identified by paleothermometric studies (Tim Mersoi Basin, Niger): Journal of Sedimentary Research, v. 86, p. 914–928, https://doi.org/10.2110/jsr.2016.62.

Martini, I.P., Sagri, M., and Colella, A., 2001, Neogene-Quaternary basins of the inner Apennines and Calabrian arc, *in* Vai G.B., and Martini I.P., eds., Anatomy of an orogeny: The Apennines and adjacent Mediterranean Basins: Dordrecht, Netherlands, Kluwer Academic, p. 375–400, https://doi.org/10.1007/978-94-015-9829-3_22.

Mazzarini, F., Isola, I., Ruggieri, G., and Boschi, C., 2010, Fluid circulation in the upper brittle crust: Thickness distribution, hydraulic transmissivity fluid inclusion and isotopic data of veins hosted in the Oligocene sandstones of the Macigno Formation in southern Tuscany, Italy: Tectonophysics, v. 493, p. 118–138, https://doi.org/10.1016/j.tecto.2010.07.012.

McCaig, A.M., 1988, Deep fluid circulation in fault zones: Geology, v. 16, p. 867–870, https://doi.org/10.1130/0091-7613(1988)016<0867:DFCIFZ>2.3.CO;2.

McCrea, J.M., 1950, On the isotopic chemistry of carbonates and a paleotemperature scale: The Journal of Chemical Physics, v. 18, p. 849–857, https://doi.org/10.1063/1.1747785.

Merriman, R.J., and Frey, M., 1999, Patterns of very low-grade metamorphism in metapelitic rocks, *in* Frey, M., and Robinson, D., eds., Low-grade Metamorphism: Oxford, UK, Blackwell Science, p. 61–107.

Milliken, K.L., McBride, E.F., Cavazza, W., Cibin, U., Fontana, D., Picard, M.D., and Zuffa, G.G., 1998, Geochemical history of calcite precipitation in Tertiary sandstones, Northern Apennines, Italy, *in* Morad, S., ed., Carbonate Cementation in Sandstones: International Association of Sedimentologists Special Publications, v. 26, p. 213–240.

Molli, G., 2008, Northern Apennine-Corsica orogenic system: An updated review, *in* Siegesmund S., Fugenschuh B., and Froitzheim N., eds., Tectonic Aspects of the Alpine-Dinaride-Carpathian System: Geological Society of London Special Publication, v. 298, p. 413–442.

Molli, G., Conti, P., Giorgetti, G., Meccheri, M., and Oesterling, N., 2000a, Microfabric study on the deformational and thermal history of the Alpi Apuane marbles (Carrara marbles), Italy: Journal of Structural Geology, v. 22, p. 1809–1825, https://doi.org/10.1016/S0191-8141(00)00086-9.

Molli, G., Giorgetti, G., and Meccheri, M., 2000b, Structural and petrological constraints on the tectono-metamorphic evolution of the Massa unit (Alpi Apuane, NW Tuscany, Italy): Geological Journal, v. 35, p. 251–264, https://doi.org/10.1002/gj.860.

Molli, G., Giorgetti, G., and Meccheri, M., 2002, Tectono-metamorphic evolution of the Alpi Apuane metamorphic complex. New data and constraints for geodynamic models: Bollettino della Società Geologica Italiana, v. 1, p. 801–817.

Molli, G., White, J.C., Kennedy, L., and Taini, V., 2011, Low-temperature deformation of limestone, Isola Palmaria, northern Apennine, Italy—the role of primary textures, precursory veins and intracrystalline deformation in localization: Journal of Structural Geology, v. 33, p. 255–270, https://doi.org/10.1016/j.jsg.2010.11.015.

Molli, G., Carlini, M., Vescovi, P., Artoni, A., Balsamo, F., Camurri, F., Clemenzi, L., Storti, F., and Torelli, L., 2018, Neogene 3-D structural architecture of the northwest Apennines: The role of the low-angle normal faults and basement thrusts: Tectonics, https://doi.org/10.1029/2018TC005057, (in press).

Mongelli, F., Zito, G., Della Vedova, B., Pellis, G., Squarci, P., and Taffi, L., 1991, Geothermal regime of Italy and surrounding areas, *in* Cermàk, V., and Rybach, L., eds., Terrestrial Heat Flow and the Lithosphere structure: Berlin, Germany, Springer, p. 381–394, https://doi.org/10.1007/978-3-642-75582-8_18.

Montanari, L., and Rossi, M., 1982, Evoluzione delle unità stratigrafico-strutturali terziarie del nordappennino; 1. L'unità di Canetolo: Bollettino della Società Geologica Italiana, v. 101, p. 275–289.

Montomoli, C., 2002, Vein development and fluid inclusion data: Insight on the evolution of the Tuscan Nappe in the Northern Apennine: Bollettino della Società Geologica Italiana, v. 1, p. 801–817.

Montomoli, C., Ruggieri, G., Boiron, M.C., and Cathelineau, M., 2001, Pressure fluctuation during uplift of the Northern Apennines (Italy): A fluid inclusions study: Tectonophysics, v. 341, p. 121–139, https://doi.org/10.1016/S0040-1951(01)00197-4.

Muchez, P., Slobodnik, M., Viaene, W.A., and Keppens, E., 1995, Geochemical constraints on the origin and migration of palaeofluids at the northern margin of the Variscan foreland, southern Belgium: Sedimentary Geology, v. 96, p. 191–200, https://doi.org/10.1016/0037-0738(94)00118-E.

Mullis, J., 1979, The system methane-water as a geological thermometer and barometer from the external part of the Central Alps: Bulletin de Mineralogie, v. 102, p. 526–536.

Mullis, J., 1987, Fluid inclusion studies during very low-grade metamorphism, *in* Frey, M., ed., Low Temperature Metamorphism: Glasgow, Scotland, Blackie, p. 162–199.

Mullis, J., 1988, Rapid subsidence and upthrusting in the Northern Apennines, deduced by fluid inclusion studies in quartz crystals from Porretta Terme: Schweizerische Mineralogische und Petrographische Mitteilungen, v. 68, p. 157–170.

Nesbitt, B.E., and Muehlenbachs, K., 1989, Origins and movement of fluids during deformation and metamorphism in the Canadian Cordillera: Science, v. 245, p. 733–736, https://doi.org/10.1126/science.245.4919.733.

Okamoto, A., and Sekine, K., 2011, Textures of syntaxial quartz veins synthesized by hydrothermal experiments: Journal of Structural Geology, v. 33, p. 1764–1775, https://doi.org/10.1016/j.jsg.2011.10.004.

Oliver, N.H.S., 1996, Review and classification of structural controls on fluid flow during regional metamorphism: Journal of Metamorphic Geology, v. 14, p. 477–492, https://doi.org/10.1046/j.1525-1314.1996.00347.x.

Oliver, N.H.S., and Bons, P.D., 2001, Mechanisms of fluid flow and fluid-rock interaction in fossil metamorphic hydrothermal systems inferred from vein-wallrock patterns, geometry and microstructure: Geofluids, v. 1, p. 137–162, https://doi.org/10.1046/j.1468-8123.2001.00013.x.

Oncken, O., 1982, Basin reconstruction by coalification studies: Geologische Rundschau, v. 71, p. 579–602, https://doi.org/10.1007/BF01822384.

O'Neil, J.R., Clayton, R.N., and Mayeda, T.K., 1969, Oxygen isotope fractionation in divalent metal carbonates: The Journal of Chemical Physics, v. 51, p. 5547–5558, https://doi.org/10.1063/1.1671982.

Parry, W.T., 1998, Fault-fluid compositions from fluid inclusion observations and solubilities of fracture-sealing minerals: Tectonophysics, v. 290, p. 1–26, https://doi.org/10.1016/S0040-1951(98)00013-4.

Parry, W.T., and Bruhn, R.L., 1987, Fluid inclusion evidence for a minimum 11 km vertical offset on the Wasatch fault, Utah: Geology, v. 15, p. 67–70, https://doi.org/10.1130/0091-7613(1987)15<67:FIEFMK>2.0.CO;2.

Parry, W.T., and Bruhn, R.L., 1990, Fluid pressure transients on seismogenic normal faults: Tectonophysics, v. 179, p. 335–344, https://doi.org/10.1016/0040-1951(90)90299-N.

Passchier, C.W., and Trouw, R.A.J., 2005, Microtectonics, second edition: Berlin, Germany, Springer Verlag, 371 p.

Patacca, E., Sartori, R., and Scandone, P., 1990, Tyrrhenian Basin and Apenninic arc: Kinematic relations since late Tortonian times: Memorie della Societa Geologica Italiana, v. 45, p. 425–451.

Petsch, S.T., Berner, R.A., and Eglinton, T.I., 2000, A field study of the chemical weathering of ancient sedimentary organic matter: Organic Geochemistry, v. 31, p. 475–487, https://doi.org/10.1016/S0146-6380(00)00014-0.

Phillips, W.J., 1972, Hydraulic fracturing and mineralization: Journal of the Geological Society, v. 128, p. 337–359, https://doi.org/10.1144/gsjgs.128.4.0337.

Plesi, G., 1975, La nappe de Canetolo: Bulletin de la Société Géologique de France, v. S7-XVII, 6, p. 979–983, https://doi.org/10.2113/gssgfbull.S7-XVII.6.979.

Principi, G., and Treves, B., 1984, Il sistema corso-appennino come prisma d'accrezione. Riflessi sul problema generale del limite Alpi-Appennino: Memorie della Societa Geologica Italiana, v. 28, p. 529–576.

Raggi, G., 1985, Neotettonica ed evoluzione paleogeografica Plio-Pleistocenica del Bacino de fiume Magra: Memorie della Societa Geologica Italiana, v. 30, p. 35–62.

Ramsay, J.G., 1980, The crack-seal mechanism of rock deformation: Nature, v. 284, p. 135–139, https://doi.org/10.1038/284135a0.

Ramsay, J.G., and Huber, M.I., 1983, The Techniques of Modern Structural Geology: Volume I: Strain Analysis: London, UK, Academic Press, 307 p.

Reches, Z., and Lockner, D.A., 1994, Nucleation and growth of faults in brittle rocks: Journal of Geophysical Research, v. 99, B9, p. 18159–18173, https://doi.org/10.1029/94JB00115.

Renard, F., Gratier, J.P., and Jamtveit, B., 2000, Kinetics of crack-sealing, intergranular pressure solution, and compaction around active faults: Journal of Structural Geology, v. 22, 10, p. 1395–1407, https://doi.org/10.1016/S0191-8141(00)00064-X.

Reutter, K.J., Teichmüller, M., Teichmüller, R., and Zanzucchi, G., 1981, Le ricerche sulla carbonificazione dei frustoli vegetali nelle rocce clastiche, come contributo ai problemi di paleogeotermia e tettonica nell'Appenino settentrionale: Memorie della Societa Geologica Italiana, v. 21, p. 111–126.

Robert, F., Boullier, A.-M., and Firdaous, K., 1995, Gold-quartz veins in metamorphic terranes and their bearing on the role of fluids in faulting: Journal of Geophysical Research, v. 100, p. 12861–12879, https://doi.org/10.1029/95JB00190.

Roedder, E., 1984, Fluid inclusions, *in* Ribbe, P.H., ed., Reviews in Mineralogy: Washington, D.C., USA, Mineralogical Society of America, v. 12, 644 p.

Roure, F., Swennen, R., Schneider, F., Faure, J.L., Ferket, H., Guilhaumou, N., Osadetz, K., Robion, P., and Vandeginste, V., 2005, Incidence and importance of tectonics and natural fluid migration on reservoir evolution in foreland fold-and-thrust belts, *in* Brosse, E., ed., Oil and Gas Science and Technology: Revue de l'IFP 60, p. 67–106, https://doi.org/10.2516/ogst:2005006.

Royden, L., 1988, Flexural behaviour of the continental lithosphere in Italy: Constraints imposed by gravity and deflection data: Journal of Geophysical Research, v. 93, p. 7747–7766, https://doi.org/10.1029/JB093iB07p07747.

Salvini, F., 2017, Daisy 3: The Structural Data Integrated System Analyzer. Software: Rome, Italy, Roma Tre University, GeoQuTe Lab, http://host.uniroma3.it/progetti/fralab/.

Schito, A., Andreucci, B., Aldega, L., Corrado, S., Di Paolo, L., Zattin, M., Szaniawski, R., Jankowski, L., and Mazzoli, S., 2018, Burial and exhumation of the western border of the Ukrainian Shield (Podolia): A multidisciplinary approach: Basin Research, v. 30, supplement 1, p. 532–549, https://doi.org/10.1111/bre.12235.

Schlische, R.W., 1995, Geometry and origin of fault-related folds in extensional settings: The American Association of Petroleum Geologists Bulletin, v. 79, p. 1661–1678.

Sclater, J.G., and Christie, P., 1980, Continental stretching: An explanation of the post-mid Cretaceous subsidence of the central North Sea basin: Journal of Geophysical Research. Solid Earth, v. 85, B7, p. 3711–3739.

Serri, G., Innocenti, F., and Manetti, P., 1993, Geochemical and petrological evidence of the subduction of delaminated Adriatic continental lithosphere in the genesis of the Neogene-Quaternary magmatism of central Italy: Tectonophysics, v. 223, p. 117–147, https://doi.org/10.1016/0040-1951(93)90161-C.

Sibson, R.H., 1996, Structural Permeability of fluid-driven fault-fracture meshes: Journal of Structural Geology, v. 18, p. 1031–1042, https://doi.org/10.1016/0191-8141(96)00032-6.

Sibson, R.H., 2000, Fluid involvement in normal faulting: Journal of Geodynamics, v. 29, p. 469–499, https://doi.org/10.1016/S0264-3707(99)00042-3.

Sibson, R.H., 2004, Controls on maximum fluid overpressure defining conditions for mesozonal mineralization: Journal of Structural Geology, v. 26, p. 1127–1136, https://doi.org/10.1016/j.jsg.2003.11.003.

Sibson, R.H., Moore, J.McM., and Rankin, A.H., 1975, Seismic pumping: A hydrothermal fluid transport mechanism: Journal of the Geological Society, v. 131, p. 653–659, https://doi.org/10.1144/gsjgs.131.6.0653.

Sibson, R.H., Robert, F., and Poulsen, K.H., 1988, High-angle reverse faults, fluid-pressure cycling, and mesothermal gold-quartz deposits: Geology, v. 16, p. 551–555, https://doi.org/10.1130/0091-7613(1988)016<0551:HARFFP>2.3.CO;2.

Smeraglia, L., Billi, A., Carminati, E., Cavallo, A., and Doglioni, C., 2017, Field- to nano-scale evidence for weakening mechanisms along the fault of the 2016 Amatrice and Norcia earthquakes, Italy: Tectonophysics, v. 712-713, p. 156–169, https://doi.org/10.1016/j.tecto.2017.05.014.

Smith, S.A.F., Billi, A., Di Toro, G., and Spiess, R., 2011, Principal slip zones in limestone: Microstructural characterization and implications for the seismic cycle (Tre Monti fault, Central Apennines, Italy): Pure and Applied Geophysics, v. 168, p. 2365–2393, https://doi.org/10.1007/s00024-011-0267-5.

Solum, J.G., and Huisman, B.A.H., 2016, Toward the creation of models to predict static and dynamic fault-seal potential in carbonates: Petroleum Geoscience, v. 23, 1, p. 70–91, https://doi.org/10.1144/petgeo2016-044.

Storti, F., 1995, Tectonics of the Punta Bianca promontory: Insights for the evolution of the Northern Apennines-Northern Tyrrhenian Sea basin: Tectonics, v. 14, p. 832–847, https://doi.org/10.1029/95TC01203.

Teichmüller, M., 1987, Organic material and very low grade metamorphism, *in* Frey M., ed., Low-temperature Metamorphism: Glasgow, Scotland, Chapman and Hall, p. 114–161.

Teichmüller, M., and Teichmüller, R., 1967, Diagenesis of Coal (Coalification), *in* Larsen G., and Chilingar G.V., eds., Diagenesis in Sediments: Elsevier, Developments in Sedimentology, v. 8, p. 391–415.

Thomson, S.N., Brandon, M.T., Reiners, P.W., Zattin, M., Isaacson, P.J., and Balestrieri, M.L., 2010, Thermochronologic evidence for orogeny-parallel variability in wedge kinematics during extending convergent orogenesis of the Northern Apennines, Italy: Geological Society of America Bulletin, v. 122, p. 1160–1179, https://doi.org/10.1130/B26573.1.

Tissot, B.P., and Welte, D.H., 1984, From Kerogen to Petroleum, *in* Tissot, B.P., and Welte, D.H., eds., Petroleum Formation and Occurrence: Berlin, Heidelberg, Germany, Springer-Verlag, p. 160–198, https://doi.org/10.1007/978-3-642-87813-8_10.

Torabi, A., and Berg, S.S., 2011, Scaling of fault attributes: A review: Marine and Petroleum Geology, v. 28, p. 1444–1460, https://doi.org/10.1016/j.marpetgeo.2011.04.003.

Vandeginste, V., Swennen, R., Allaeys, M., Ellam, R.M., Osadetz, K., and Roure, F., 2012, Challenges of structural diagenesis in foreland fold-and-thrust belts: A case study on paleofluid flow in the Canadian Rocky Mountains west of Calgary: Marine and Petroleum Geology, v. 35, p. 235–251, https://doi.org/10.1016/j.marpetgeo.2012.02.014.

Veizer, J., Ala, D., Azmy, K., Bruckschen, P., Buhl, D., Bruhn, F., Carden, G.A.F., Diener, A., Ebneth, S., Godderis, Y., Jasper, T., Korte, C., Pawellek, F., Podlaha, O.G., and Strauss, H., 1999, $^{87}Sr/^{86}Sr$, $\delta^{13}C$ and $\delta^{18}O$ evolution of Phanerozoic seawater: Chemical Geology, v. 161, p. 59–88, https://doi.org/10.1016/S0009-2541(99)00081-9.

Vermilye, J.M., and Scholz, C.H., 1998, The process zone: A microstructural view of fault growth: Journal of Geophysical Research, v. 103, B6, p. 12223–12237, https://doi.org/10.1029/98JB00957.

Vescovi, P., 1998, Le Unità Subliguri dell'alta Val Parma (Provincia di Parma): Atti Ticinesi di Scienze Terra, v. 40, p. 215–231.

Vescovi, P., 2005, The Middle Miocene Mt. Ventasso: Mt. Cimone arcuate structure of the Emilia Apennines: Bollettino della Società Geologica Italiana, v. 124, p. 53–67.

Vilasi, N., Malandain, J., Barrier, L., Callot, J.-P., Amrouch, K., Guilhaumou, N., Lacombe, O., Muska, K., Roure, F., and Swennen, R., 2009, From outcrop and petrographic studies to basin-scale fluid flow modelling: The use of the Albanian natural laboratory for carbonate reservoir characterisation: Tectonophysics, v. 474, 1-2, p. 367–392, https://doi.org/10.1016/j.tecto.2009.01.033.

Virgo, S., Abe, S., and Urai, J.L., 2014, The evolution of crack seal vein and fracture networks in an evolving stress field: Insights from Discrete Element Models of fracture sealing: Journal of Geophysical Research. Solid Earth, v. 119, p. 8708–8727, https://doi.org/10.1002/2014JB011520.

Walther, J.V., and Orville, P.M., 1982, Volatile production and transport in regional metamorphism: Contributions to Mineralogy and Petrology, v. 79, p. 252–257, https://doi.org/10.1007/BF00371516.

Withjack, M.O., and Callaway, S., 2000, Active normal faulting beneath a salt layer: An experimental study of deformation patterns in the cover sequence: The American Association of Petroleum Geologists Bulletin, v. 84, 5, p. 627–651.

Withjack, M.O., Olson, J., and Peterson, E., 1990, Experimental models of extensional forced folds: The American Association of Petroleum Geologists Bulletin, v. 74, p. 1038–1054.

Wüstefeld, P., Hilse, U., Lüders, V., Wemmer, K., Koherer, B., and Hilgers, C., 2017, Kilometer-scale fault-related thermal anomalies in tight gas sandstones: Marine and Petroleum Geology, v. 86, p. 288–303, https://doi.org/10.1016/j.marpetgeo.2017.05.015.

Zattin, M., Picotti, V., and Zuffa, G.G., 2002, Fission-track reconstruction of the front of the Northern Apennine thrust wedge and overlying Ligurian unit: American Journal of Science, v. 302, p. 346–379, https://doi.org/10.2475/ajs.302.4.346.

Science Editor: Rob Strachan
Associate Editor: Stephano Mazzoli

Manuscript Received 9 February 2018
Revised Manuscript Received 10 July 2018
Manuscript Accepted 14 August 2018

Printed in the USA

Structural sites and samples list

Coordinates	Site N.	Sample N.	Description	Domain	Strike	Dip	Pitch
			Vein & Fault Samples				
44°19'27.39"N 10° 3'14.29"E	1	1	Longitudinal antithetic vein-stylolites	HW_DZ	355	32	
	1	2	Longitudinal synthetic vein-stylolites	HW_DZ	307	65	
44°19'27.77"N 10° 3'19.43"E	2	1	Longitudinal synthetic vein-stylolites	HW_DZ	320	80	
	2	2	Fault core calcite concretion	HW_DZ			
	2	3	Obliquely sheared vein	HW_DZ	290	50	
	2	4	Bed parallel vein-stylolites	HW_DZ	76	16	
	2	5	Longitudinal synthetic shear vein	HW_DZ	60	23	120
44°19'30.72"N 10° 3'21.57"E	3	1A	Fault core Breccia	HW_FC			
	3	1B	Fault core Breccia	HW_FC			
	3	1C	Fault core Breccia	HW_FC			
	3	2	Bed parallel vein-stylolites	HW_DZ-FC transition	118	60	
	3	3	Transversal vein-stylolites	HW_DZ-FC transition	196	67	
	3	4	Fault core calcite concretion	HW_DZ-FC transition	126	65	
	3	5	Transversal vein-stylolites	HW_DZ-FC transition	196	67	
	3	6	Longitudinal antithetic shear vein	HW_DZ-FC transition	309	64	100
44°19'40.65"N 10° 3'30.93"E	4	1	Transversal shear vein	FW_DZ	230	85	
	4	2	Transversal vein	FW_DZ	0	75	
	4	3	Longitudinal shear vein	FW_DZ	305	47	
	4	4	Transversal slip surface	FW_DZ	236	83	25
	4	5	Transversal shear vein	FW_DZ	0	61	
	4	6	Vein in clay bed	FW_DZ	276	45	
44°19'37.98"N 10° 3'28.42"E	5	1	Antithetic slip surface	FW_DZ	299	51	130
	5	2	Transversal shear vein	FW_DZ	195	86	
	5	3	Transversal vein	FW_DZ	205	69	
	5	4	Antithetic slip surface	FW_DZ	200	36	
	5	5	Longitudinal synthetic vein	FW_DZ	334	70	
	5	6	Longitudinal synthetic vein	FW_DZ	334	70	
	5	7	Oblique shear vein	FW_DZ	351	55	
	5	8	Oblique shear vein	FW_DZ	40	46	
	5	9	Oblique shear vein	FW_DZ	66	54	

44°19'42.06"N 10° 3'4.34"E	6	1	Fault core synthetic slip surface	FW_DZ-FC transition	150	60	
	6	2	Vein in clay bed	FW_DZ-FC transition	330	45	
	6	3	Vein in silt bed	FW_DZ-FC transition	330	45	
	6	4	Synthetic shear vein	FW_DZ-FC transition	80	50	120
	6	5	Transversal shear vein	FW_DZ-FC transition	233	84	10
44°20'4.01"N 10° 2'20.67"E	7	1	Transversal vein	FW_DZ	230	80	
	7	2	Transversal shear vein	FW_DZ	230	80	
	7	3	Transversal vein	FW_DZ	230	80	
	7	4	Transversal shear vein	FW_DZ	230	80	
44°19'50.13"N 10° 2'38.41"E	8	1	Fault core calcite concretion	HW_DZ-FC transition	135	76	
	8	2	Longitudinal antithetic breccia-vein	HW_DZ-FC transition	336	86	
	8	3	Fault core S-C	HW_DZ-FC transition	156	23	
	8	4	Fault core S-C	HW_DZ-FC transition	156	23	
44°19'42.26"N 10° 2'38.35"E	9	1	Thrust R' vein	HW_DZ	323	40	
	9	2	Transversal vein	HW_DZ	238	76	
	9	3	Bed parallel vein-stylolites	HW_DZ	127	56	
44°19'38.33"N 10° 2'54.02"E	10	1	Thrust footwall vein-stylolites	HW_DZ	134	70	
	10	2	Thrust hangingwall vein-stylolites	HW_DZ	332	64	
44°19'0.16"N 10° 3'13.04"E	11	1	Longitudinal synthetic vein	HW_BG	280	50	
44°19'33.34"N 10° 4'43.09"E	12	1	Transversal vein	FW_BG	254	72	
44°24'51.31"N 9°57'4.64"E	13	1	Fault Core Breccia	FW_DZ NW tip			

Oxygen and carbon stable isotopes contents

Calcite Type	Site/ Sample	$\delta^{13}C$ (V-PDB)	$\delta^{18}O$ (V-PDB)	$\delta^{18}O$ (V-SMOW)
Macigno Host Rock				
	4/6	-3,1	-16,1	14,2
	4/6	-2,6	-16,4	13,9
	6/2	-0,7	-14,4	16,0
MC1 (A & B) Calcite				

	4/1		-1,0	-17,6	12,8
	4/2		-2,7	-18,5	11,8
	4/3		-1,2	-16,5	13,8
	4/3	Replacive	-1,6	-17,0	13,4
	4/5		-1,5	-17,4	12,9
	4/6		-1,3	-17,7	12,7
	5/2	Replacive	-4,4	-16,9	13,4
	5/2	Replacive	-4,3	-17,0	13,3
	5/3		-4,3	-17,3	13,0
	5/3	Replacive	-4,6	-17,1	13,3
	5/4		-5,7	-17,0	13,4
	5/4	Replacive	-5,7	-17,1	13,3
	5/6		-4,9	-17,1	13,2
	5/7		-4,8	-17,8	12,5
	5/7	Replacive	-4,4	-18,2	12,1
	5/8		-5,6	-18,0	12,3
	5/9		-5,0	-17,7	12,6
	6/2		-2,3	-17,2	13,2
	6/2	Replacive	-2,1	-16,5	13,9
	6/3		-0,9	-16,4	13,9
	7/1		-1,3	-16,4	14,0
	NWtip		-0,6	-14,9	15,5
	NWtip	Replacive	-0,8	-13,7	16,7
MC2 Calcite					
	4/1		-1,5	-14,4	16,0
	4/2		-2,1	-15,9	14,4
	4/2	Replacive	-1,8	-14,6	15,8
	4/3		-1,2	-14,8	15,7
	4/5		-1,5	-15,8	14,5
	4/6		-1,6	-13,4	17,0
	5/6		-4,8	-14,8	15,6
	5/7		-3,8	-14,5	15,9
	5/8		-6,1	-13,2	17,2
	5/8		-7,1	-15,7	14,6
	5/9		-4,3	-16,5	13,9
	5/9	Replacive	-5,3	-14,0	16,5
	6/1		-1,2	-12,6	17,9
	6/1		-0,4	-13,0	17,5
	6/2		-1,4	-14,9	15,5
	6/2		-1,2	-14,5	15,9
	6/3		-1,3	-16,9	13,4
	7/1		-1,5	-14,3	16,2
	NWtip		-0,5	-10,7	19,8
Ottone					

HR					
	10/2		1,8	-3,5	27,2
	9/2		1,9	-3,2	27,5
	1/2		1,7	-3,8	27,0
	3/5		2,0	-3,8	26,9
OC1 Calcite					
	10/1		1,9	-4,8	25,9
	10/1		2,1	-4,7	26,0
	10/2		2,0	-4,8	25,9
	9/2		1,9	-5,1	25,6
	9/2		1,8	-4,5	26,2
	9/3		1,8	-5,0	25,7
	9/3		1,6	-5,5	25,2
	1/1		2,2	-4,5	26,2
	1/1		2,3	-4,7	26,0
	1/2		2,4	-5,7	25,0
	1/2		1,9	-4,4	26,3
	1/2		2,1	-3,9	26,9
	2/1		2,0	-5,1	25,6
	2/1		1,8	-5,0	25,7
	2/3		1,8	-4,3	26,4
	2/4		1,7	-5,4	25,3
	2/4		1,9	-5,7	25,0
	2/4		1,8	-5,0	25,7
	2/5		1,9	-5,0	25,7
	2/5		1,7	-5,6	25,1
	2/5		2,0	-4,4	26,3
	3/3		1,8	-7,1	23,5
	3/3		2,0	-5,8	24,9
	3/4		2,0	-4,2	26,6
	3/5		2,1	-5,3	25,4
	3/6		2,0	-4,7	26,0
OC2 Calcite					
	10/1		1,3	-12,6	17,9
	10/2		1,4	-14,3	16,1
	9/3	Replacive	-0,5	-15,3	15,0
	8/1		2,1	-15,4	15,0
	8/1		1,9	-14,4	16,0
	1/1		2,1	-13,6	16,8
	2/1		2,0	-14,0	16,5
	2/3		2,0	-14,0	16,4
	3/2		1,7	-17,3	13,1
	3/2		2,1	-15,1	15,3

3/3	2,1	-13,4	17,1
3/3	2,1	-14,0	16,5
3/4	2,1	-13,8	16,6
3/5	2,1	-12,4	18,1
3/5	2,1	-11,9	18,6
3/6	2,0	-10,9	19,7

Fluid inclusions microthermometry

Inclusion Type	Site/ Sample	FIA	Thtot	Tfm	Tmice
Quartz 1					
Biphase	4/3	A	151		-6.5
Acqueous	4/3	A	151		-7.8
	4/3	A	151	-49.8	-6.5
	4/3	A	151	-49.8	-11.4
	4/3	A	151	-49.8	-4.8
	4/3	A	156	-50.1	-6.6
	4/3	I	215	-45.5	-7.2
	4/3	I	127		-6.9
Quartz 2					
Monophase	4/3	A	-83		
CH_4	4/3	A	-83		
	4/3	A	-84		
	13/1	A	-88		
	13/1	A	-88		
	13/1	A	-88		
	13/1	A	-88		
	13/1	A	-88		
	13/1	A	-88		
	13/1	A	-87		
	13/1	B	-89		
	13/1	B	-89		
	13/1	B	-89		
	13/1	B	-88		
	13/1	B	-89		
	13/1	B	-88		
	13/1	B	-88		
	13/1	B	-89		
	13/1	B	-88		
	13/1	B	-88		
MC1A					
Calcite	4/2	A	183		-2

	4/2	A	198		-2.8
	4/5	A	190		-2.6
	4/5	A	190		-3
	4/5	A	190		-1.9
	5/2	A	188	-18.4	-2.9
	5/2	A	198	-21.4	-3
	5/2	A	198	-21.4	-2.7
	5/2	A	198	-17.4	-4.9
	5/3	A	183		-2
	5/3	A	183		-2
	5/3	A	178		
	5/6	I	183		-1.5
	5/9	I	194		-0.8
	7/1	A	180		-6
	7/1	A	180		-6.2
	13/1	A	186		
	13/1	A	191		
	13/1	A	186		-1.8
	13/1	A	191		-0.9
	13/1	A	191		
	13/1	I	191		-0.8
MC1B					
Calcite	4/1	A	140		-5.5
	4/1	A	155	-19.9	-3.4
	5/2	A	149	-8.2	-2.1
	5/2	A	149	-8.6	-2
	5/2	A	149	-8	-2
	5/9	A	140	-11.9	-6
	5/9	A	155	-12.1	-6.2
	5/9	A	150		-3.7
	5/9	A	150		-5.4
	5/9	B	150		-2
	5/9	B	150	-31.5	-9.7
	5/9	B	140	-31.5	-10
	5/9	B	140	-31.5	-17.2
	5/9	B	155	-31.5	-14
	13/1	A	156		-1
	13/1	A	156		-1
	13/1	A	156		-0.8
	13/1	A	161		-1
	13/1	A	161		-1
MC2					
Calcite	4/1	A	115	-27.3	-20.7
	4/1	A	115		
	4/5	A	69		-1.7
	4/5	A	69		-1.5
	5/8	A	70	-27.9	-19.8

	5/8	A	70	-27.8	-19.8
	5/8	B	89	-34.5	-18.9
	5/8	B	99	-34.4	-18.6
	5/8	B	114	-34.1	-16.7
	5/9	A	80		-1.8
	5/9	A	70		-1.9
	5/9	A	70		-1.5
	5/9	A	70		-1.3
	7/1	A	90	-17.8	-5.3
	7/1	A	90		-5.3
	7/1	A	90		-5.8
	7/1	A	90		-9.7
	7/1	A	90		-2.5
	13/1	I	108		-12.3
	13/1	I	108		-0.7
OC1 Calcite	10/1	A	90		
	10/1	A	90		
	10/1	I	90		
	10/1	I	90		-0.5
	10/1	I	100		
	10/1	I	100		-0.1
	10/2	A	90		-1.5
	10/2	A	100		
	10/2	I	100		
	9/1	A	100		
	9/1	A	100		
	9/1	A	100		
	9/1	A	105		
	8/2	A	78		
	8/2	A	78		
	8/2	A	113		
	8/2	A	113		
	2/4	A	100		-0.2
	2/4	A			-0.1
	3/4	A	95		
	3/4	A	105		-1.6
	3/4	I	100		-1.5
OC2 Calcite	10/1	A	60		-6.9
	10/1	A	65		-6.5
	10/1	A			-6.3
	10/1	A			-5.9
	10/1	A			-5.2
	10/1	A			-3.4
	10/1	A			-2
	10/2	A	110		-1.9

10/2	A	110	-1.3
10/2	A	110	
10/2	A	110	
10/2	A	110	
10/2	A	110	
10/2	A	110	
10/2	A	115	
8/2	I	74	-4.4

SEM-EDS prehnite major elements contents

Al_2O_3	SiO_2	CaO	FeO
25.32	45.40	27.67	-
25.17	45.30	27.78	-
25.14	44.86	27.90	-
24.95	45.23	27.78	0.46
25.27	45.24	27.96	-
25.32	45.44	27.72	-
25.31	45.21	27.89	-
25.14	45.21	27.41	-
24.80	44.74	28.10	-
24.75	45.02	27.66	0.37
24.81	44.91	27.73	0.29
24.79	44.77	28.94	-
25.33	44.76	27.77	-
25.02	45.29	28.09	-
24.91	45.20	27.98	0.44
24.77	44.74	27.45	0.57
25.00	44.68	27.93	0.39
25.33	45.00	27.84	-
24.99	44.80	27.76	0.35
25.10	45.22	27.72	-
25.11	45.34	27.96	-
24.97	45.27	27.60	0.48
25.02	44.92	27.86	-
25.03	44.81	27.90	-
24.56	44.90	27.60	0.52
24.98	44.94	27.72	-
25.00	45.24	27.71	0.33
25.05	45.08	27.49	0.40
25.15	44.98	27.62	-
25.06	44.83	27.75	-
25.01	45.07	27.78	0.52
24.89	45.28	27.78	-
24.98	44.88	27.67	-
25.00	45.13	27.75	0.50
25.03	44.84	27.83	0.28

25.19	44.99	28.05	-
25.22	44.97	27.69	0.35
25.27	45.19	27.76	0.33
25.13	45.01	27.38	-
24.83	45.20	27.79	0.42
24.92	45.26	27.70	-
25.31	45.01	27.85	-
25.48	45.24	27.69	-
25.11	45.09	27.76	0.31
24.94	44.94	27.66	0.35
25.28	44.87	27.59	-
25.04	45.34	27.42	-
25.30	45.02	27.64	-
25.02	44.73	27.59	0.43
25.41	44.82	27.47	-
25.22	45.16	27.76	-
25.02	44.94	27.80	-

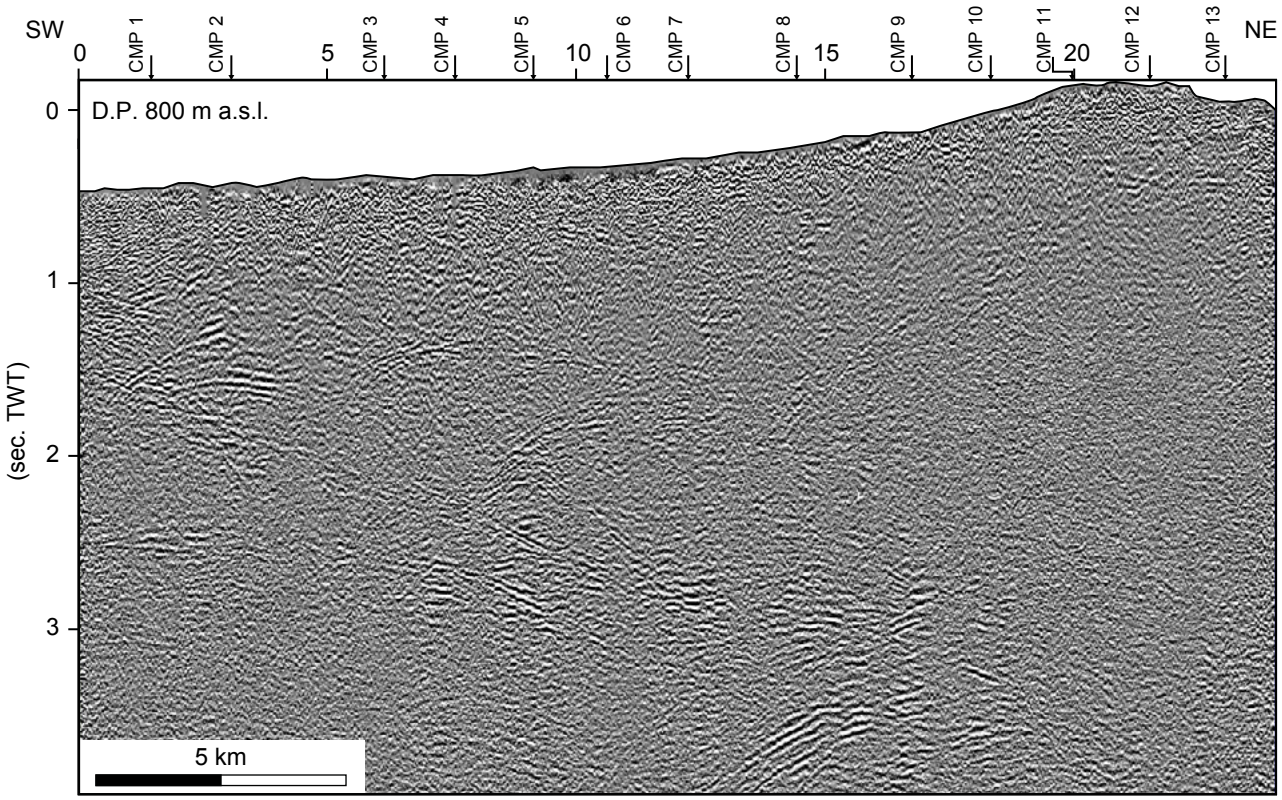


Figure S1. Seismic reflection profile of Fig. 2 before being depth-converted

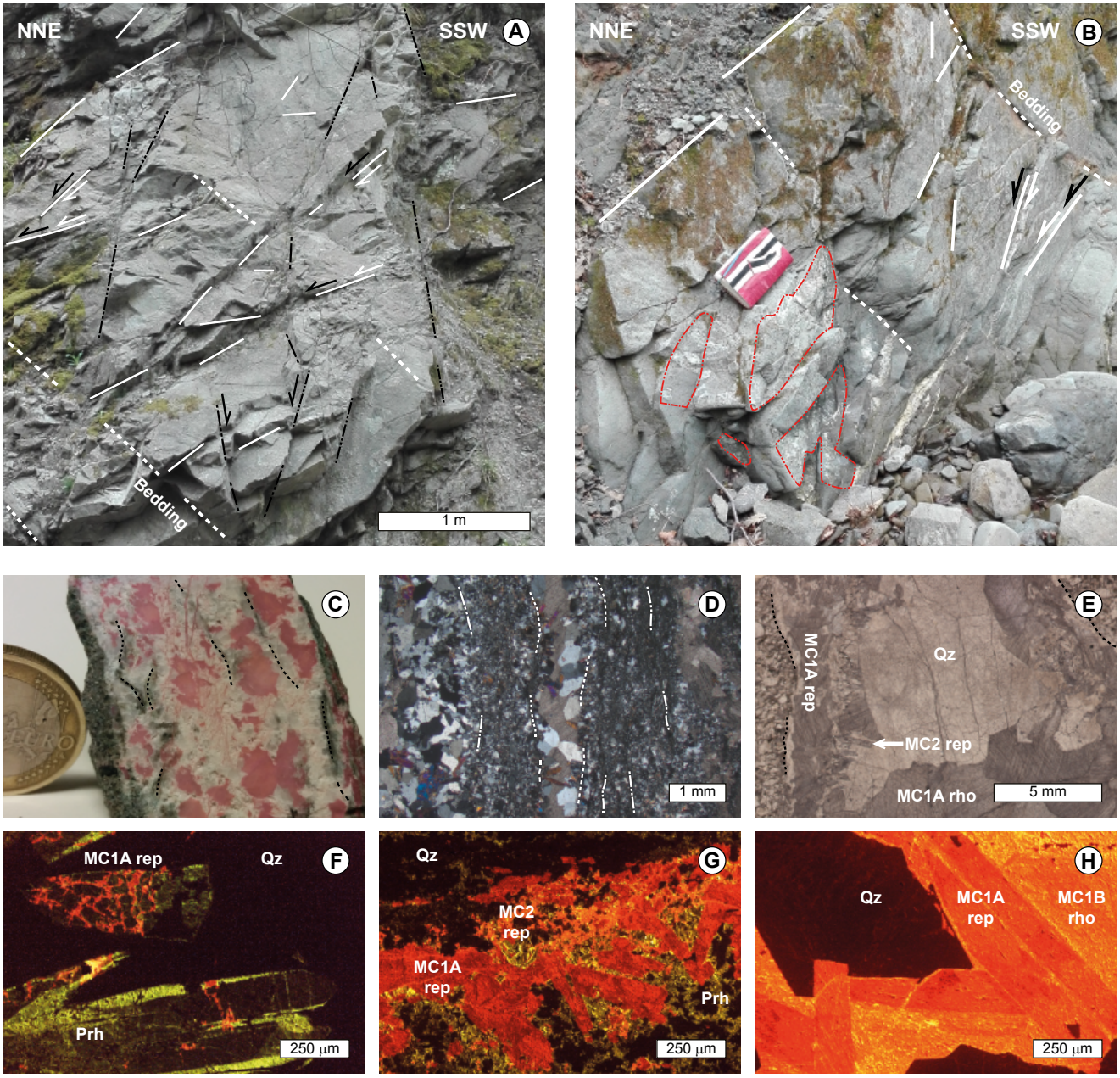


Figure S2. (A-B) Outcrop pictures of coarse sandstones strata in footwall damage zone Site 5. White dotted lines represent bedding, white lines are conjugate extensional shear veins and fractures with σ_1 orthogonal to bedding, black dashed lines are late-stage extensional shear fractures and red dashed lines indicate strike-slip shear veins and fractures. White arrows indicate pre-bedding rotation kinematics while black arrows indicate kinematics after bedding rotation. (C) Stained hand specimen of footwall fault-related shear vein; black dotted lines separate different opening events. (D) XPL image showing, as in C, multiple openings (separated by white dotted lines), of which some interested by shearing and quartz recrystallization. (E) PPL image of vein showing both MC1A and MC2 replacive calcite crystals along with quartz and rhombohedric MC1A. (F-G-H) CL images showing progressive Prehnite dissolution and replacement by MC calcites.

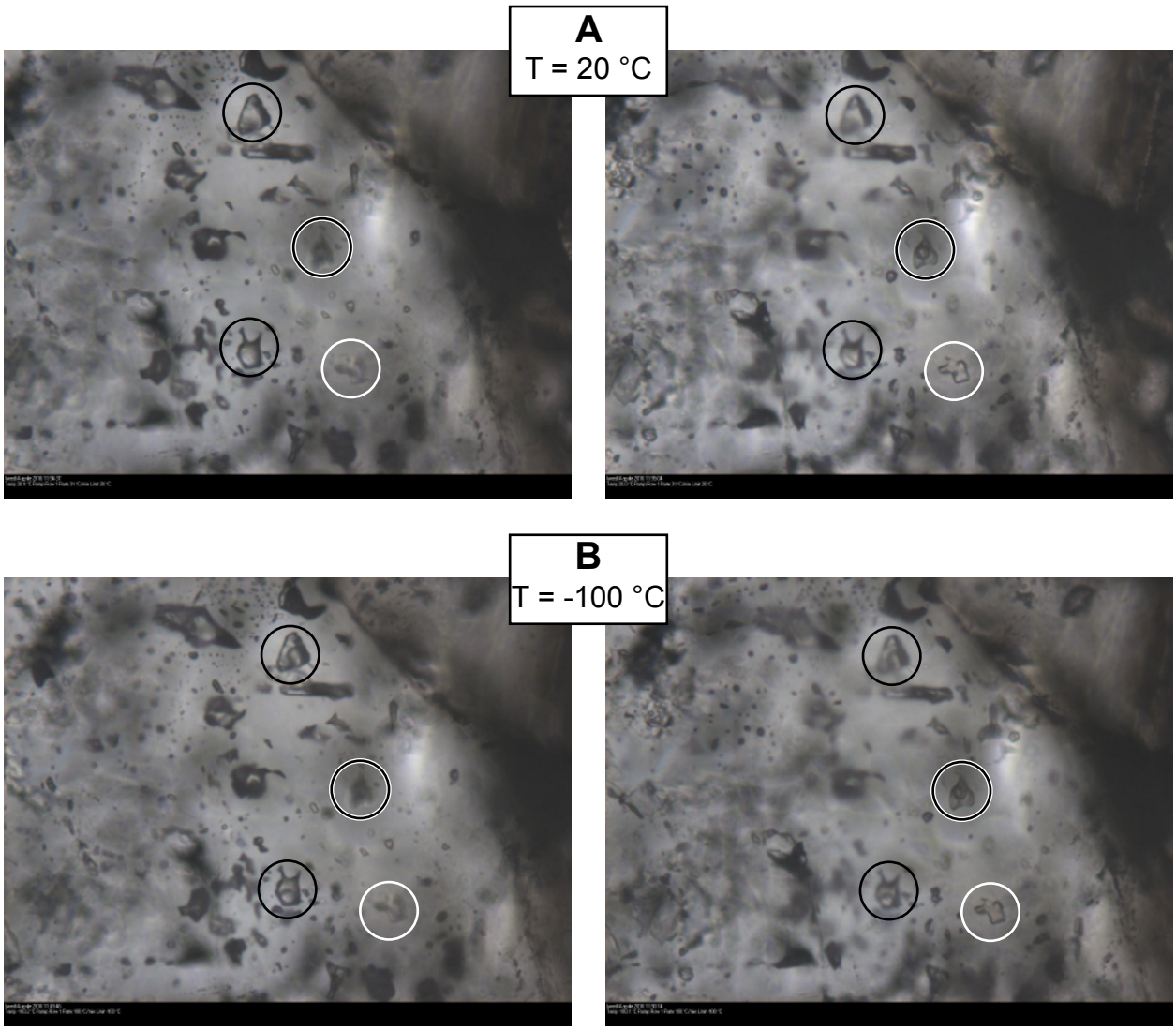


Figure S3. Fluid inclusion assemblage in quartz of footwall damage zone fault-related shear veins showing aqueous inclusion (white), gaseous CH_4 inclusions (black) and an inclusion containing liquid H_2O and gaseous CH_4 (black and white). In (A) at 20 °C and in (B) at -100 °C.

3

FRACTURE NETWORK ATTRIBUTE DISTRIBUTION IN THICK SANDSTONE STRATA ACROSS THE FOOTWALL DAMAGE ZONE OF THE COMPIONE FAULT, NORTHERN APENNINES, ITALY

This chapter is presented in the form of a manuscript that is currently in preparation for submission to *Journal of Structural Geology*. This manuscript deals with the quantification of the fault-related fracture pattern formed at the process zone stage of the Compione Fault, which is a segment of the Northern Lunigiana Extensional Fault System. In this study we adopted a new fracture analysis methodology, proposed by Sanderson and Nixon (2015). We describe fracture orientation, topology, intensity, density and connectivity, which indicate that the fault-related fracture network acts as an effective conduit for fluid migration already at the process zone stage.

ARTICLE IN PREPARATION

Lucca A, Storti F., and Molli G.

Article in preparation for submission to *Journal of Structural Geology*

Fracture network attribute distribution in thick sandstone strata across the footwall damage zone of the Compione Fault, Northern Apennines, Italy

Alessio Lucca[1], Fabrizio Storti[1], Giancarlo Molli[1,2]

[1]*NEXT - Natural and Experimental Tectonics research group, Department of Chemistry, Life Sciences and Environmental Sustainability, University of Parma, I-43124 Parma, Italy*

[2]*Department of Earth Sciences, University of Pisa, via S. Maria, 53, I-56126 Pisa, Italy*

*Corresponding Author Details

E-mail: alessio.lucca@studenti.unipr.it

Telephone number: +39 393 1323420

Abstract

Regional-scale fault zones represent important barrier, conduits or mixed barrier-conduits to fluid flow, depending on their complex structural and permeability architectures that, in turn, are imprinted by the mechanical stratigraphy of faulted rocks. Intensely fractured rock volumes characterize fault damage zones in cohesive rocks, typically developed from multiple deformation stages associated with fault propagation and linkage. In this paper, we report on the results of a study performed to quantify the fracture pattern in the footwall of the Compione extensional fault, where thick to very thick sandstone strata preserve the deformation signatures of the entire evolutionary pathway, from early blind faulting and tip damage zone development, to late-stage wall damage zone fracture reworking and localization. Fracture network attributes were studied in cross-sectional exposures by acquiring circular scan windows moving away from the fault core, up to the undamaged rocks. Our data indicate that fracture network topologies are dominated by Y-nodes despite being mainly composed by antithetic subsidiary extensional faults.

1. Introduction

Regional-scale fault damage zones in cohesive rocks are typically characterized by complex fracture networks resulting from (i) long lasting deformation histories including fault nucleation, propagation, slip accumulation, and linkage of adjacent segments (ii) the mechanical stratigraphy of faulted rocks, and (iii) the environmental conditions of deformation (Chester et al., 1993; Caine et al., 1996; Faulkner et al., 2010). Understanding the evolution of fracture networks in damage zones

and quantifying their main attributes bears fundamental implications for making reliable predictions of fluid flow and storage in aquifers and hydrocarbon reservoirs, and for improved models of the mechanical behavior of fault slip, including earthquake nucleation and slip rates (Nelson, 1985; Tinti et al., 2005; Maerten and Maerten, 2006; Jenkins et al., 2009; Perrin et al., 2016). Results from many studies on fault damage zones are available in the literature, particularly in well bedded rocks where linear scan lines are the most common tool for quantifying typically strata-bound fracture attributes in cross-sectional exposures (Wennberg et al., 2006; Barbier et al., 2012; Lamarche et al., 2012; Reyer et al., 2012; Sonntag et al., 2014). Thick strata, however, are commonly characterized by more complex fracture networks, which in many cases can be better studied by areal methods (e.g. Mauldon, 1998; Watkins et al., 2015). Adding topological analysis to areal methods provides an effective tool for fracture network characterization and connectivity assessment (Sanderson and Nixon, 2015).

In this contribution, we present the results of the study of fracture network attributes across the footwall damage zone of the Compione Fault, an extensional fault in the Northern Apennines, which accumulated about 1.5 km offset in the study area since Early Pliocene times (Lucca et al., 2018). The exposed footwall damage zone of the Compione Fault developed in turbiditic sandstones characterized by strata up to about 6 meter thick. They are affected by complex arrays of conjugate shear veins that prevent the use of linear scan lines to quantify fracture network attributes in cross-sectional exposures. We performed circular scan windows in cross-sectional exposures of strata thicker than 2 meters, moving away from the fault core, along a structural transect perpendicular to the fault zone strike. Results indicate that the fracture network in the footwall damage zone is dominated by Y-nodes and is hydraulically connected both in the vertical and across-fault directions.

2. Geological framework

The Compione Fault belongs to the northeastern basin-boundary fault system of the Northern Lunigiana Basin, which is the northernmost onshore tectonic depression in the Northern Apennines (Fig. 1A). The Lunigiana Basin has developed in the hanging wall of a major NE-verging out-of-sequence thrust the in the Northern Apennines, bringing the Adria passive margin Tuscan Succession onto the allochtonous, ocean-derived Ligurian Succession in Tortonian times (Fig. 1B; Boccaletti et al., 1971; Elter and Pertusati, 1973, Elter, 1975; Vescovi et al., 2005; Molli et al., 2018). Such an out-of-sequence thrusting episode overprinted initial in sequence thrusting of the Ligurian Succession onto the Tuscan one and wedge thickening (e.g. Elter and Schwab, 1959; Principi and Treves, 1984), and in turn was followed by synorogenic extension, now recorded by

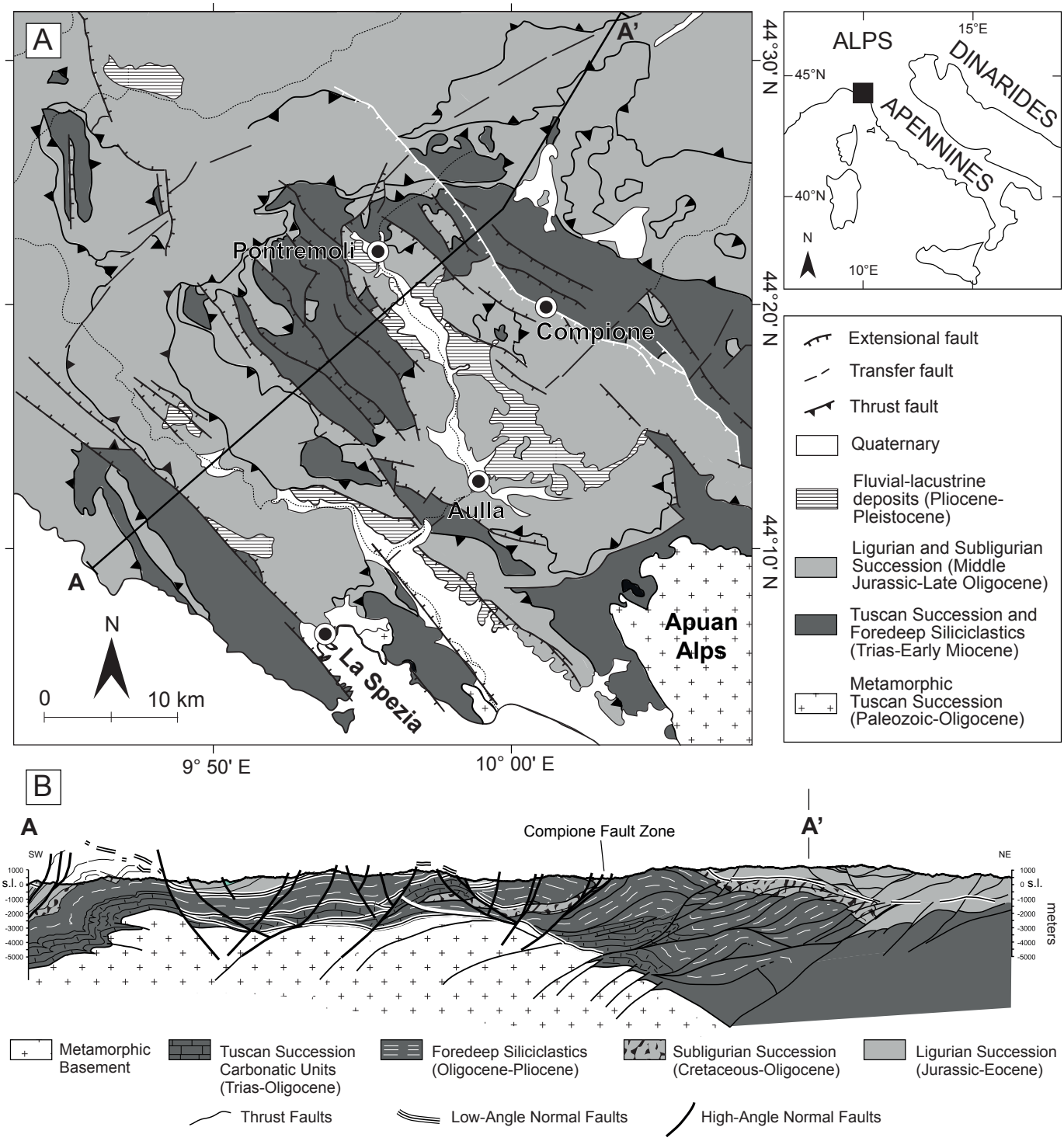


Figure 1: (A) Simplified structural geologic map of the Tyrrhenian Sea side of the Northern Apennines (modified from Bernini et al., 1997). The Compione Fault belongs to the Northern Lunigiana Fault System, indicated in white. Inset indicates location of A. (B) Regional geologic-cross section (A-A') showing the Northern Apennines orogenic wedge architecture, modified from Molli et al., 2018.

NE-dipping low-angle detachments (Carmignani and Kligfield, 1990; Storti, 1995; Decandia et al., 1998; Jolivet et al., 1998; Clemenzi et al., 2014: Molli et al., 2018). This Cenozoic polyphasic tectonic pathway affected the Apennines orogenic belt as a consequence of both the complex evolution of the plate boundary setting between Eurasia and Europa plates, and the internal dynamics of the growing thrust wedge (Malinverno and Ryan, 1986; Royden, 1988; Dewey et al., 1989; Doglioni, 1991; Molli et al., 2018). In such a long lasting evolution, Plio-Quaternary extension in the Lunigiana Basin, as well as in the other basins developed along the Tyrrhenian side of the Apenninic belt, has been classically associated with the eastward propagation of crustal thinning in the back-arc basin, overprinting orogenic contraction (Elter et al., 1975; Carmignani et al., 1995; Barchi et al., 1998; Jolivet et al., 1998; Martini et al., 2001).

In more detail, the Northern Lunigiana Basin developed since Early Pliocene times in its SE part, and since Early Pliostecene times in its NW area (Azzaroli, 1977; Federici, 1978; Raggi, 1985, Boccaletti et al., 1992). It is bounded to the NE by the NW-SE striking, SW dipping Northern Lunigiana Extensional Fault System, which is longer than 30 km and juxtaposes the Upper Cretaceous Ottone Flysch of the Ligurian Succession in the hanging wall, against the Chattian to Aquitanian Macigno Sandstone Formation in the footwall, (Fig. 1A; Elter et al., 1975; Bernini and Lasagna, 1988). The Compione fault is about 15 km long, major segment of the Northern Lunigiana Extensional Fault System (Fig. 1A) and is located at the crest to forelimb transition of the regional-scale anticline associated with major out-of-sequence thrusting (Fig. 1B). It penetrates into the metamorphic basement at 6 to 7 km depth (Camurri et al., 2001; Argnani et al.; 2003; Lucca et al., 2018) and accumulated more than 1.5 km of maximum extensional displacement (Bernini and Lasagna, 1998).

We studied the fracture network attribute distribution along a structural transect in the footwall of the Compione Fault, normal to its strike (Fig. 2A). Outside the fault zone, Macigno Fm. sandstone strata dip 5°-10° towards the NE and the fracture network includes a fracture set near perpendicular to bedding and another one parallel to primary depositional structures, likely produced by de-compaction during exhumation. Approaching the fault core, bedding is tilted towards the SSW and acquires dip values up to 60° at the damage zone-fault core transition. Within the fault zone, Macigno Fm. sandstone strata, up to 5-6 m thick, are affected by conjugate shear fracture arrays striking parallel to the Compione Fault trend and having acute bisectors orthogonal to bedding, regardless of bedding dip (Fig. 2B; Lucca et al., 2018). Cumulative fracture orientation analysis indicates that most of the fault-related fractures shows apparent dip values comprised between 10° and 50° to the NNE, which assume, after bedding rotation to horizontal, values between 60° and 90° to the NNE (Figs. 2C, D). A major E-W striking, S dipping fault splay of the

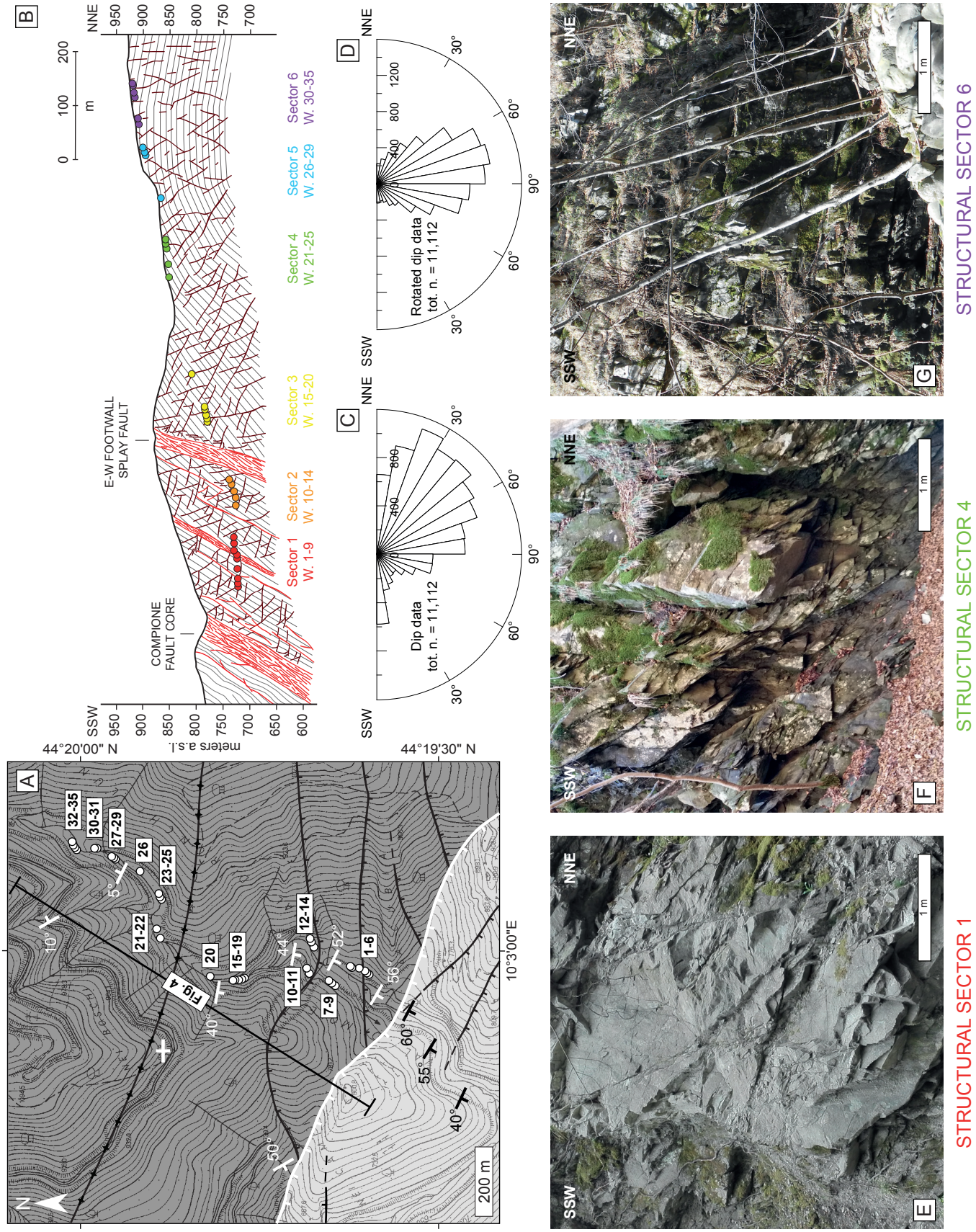


Figure 2: (A) Geologic map of the study area showing locations of circular windows in the footwall of the Compione Fault, which is indicated in white, along with bedding attitudes and secondary faults. Black line with rhombs is the hinge of the extensional fault propagation fold. (B) Cross-section illustrating the

structural architecture of the Compione footwall damage zone with projected locations of circular windows, grouped in structural sectors. (C) Cumulative apparent dip data plotted in half-rose diagram. (D) Data in C after bedding restoration to horizontal. (E-F-G) Outcrop pictures showing the fault-related fracture patterns in structural sectors 1, 4 and 6, respectively.

Compione Fault intersects the structural transect at a distance of about 250-280 m away from the fault core (Fig. 2B). Fracture network patterns in different structural sectors are shown in Figs. 2E, F, G. In the sector comprised between the Compione fault core and the E-W footwall splay fault, discrete fault zones, dipping 60-80° to the SW and to the NE developed after bedding rotation, which was commonly exploited as slip surfaces.

3. Methodology

Thirty-five circular scan windows (Mauldon, 1998) located on SSW-NNE striking vertical exposures of meters-thick Macigno Fm. sandstone strata, were performed at increasing distance between 80 and 1030 meters from the Compione fault core, to analyze fracture apparent dip, density, intensity and connectivity of the footwall damage zone. Deterioration of outcrop quality and increasing debris cover prevented data collection closer to the fault core. A scan window diameter of 0.5 m was selected as the best compromise between the size of clean exposures and the need of including at least 30 nodes per window (Fig. 3; Mauldon, 1998). Scan windows were performed on photographs acquired with a Sony Alpha 6500 camera, equipped with a Sony Sonnar FE 55 mm lens. To minimize any possible distortion, the camera was mounted on a tripod and the lens was oriented perpendicularly to the outcrop surface (Fig. 3A). The FracPaQ2D tool for MATLAB (Healy et al., 2017) was used to extract fracture apparent dip directions and total fracture lengths from digitized fracture maps (Fig. 3B). Apparent dip of each fracture segment was plotted on half-rose diagrams in a SSW-NNE oriented vertical plane (Fig. 3D).

Fracture network topology and connectivity were quantified following the node counting approach of Sanderson and Nixon (2015). Nodes are subdivided in three types (Manzocchi, 2002), namely isolated tips (I nodes), splays and abutments (Y nodes) and crossing fractures (X nodes; Fig. 3C). Number of nodes (N_I, N_Y, N_X), circular window areas (πr^2), and total fracture length (ΣL) were used to calculate the following parameters (Sanderson and Nixon 2015):

(1) Number of fractures $N_L = (N_I + N_Y)/2$

(2) Number of branches $N_B = (N_I + 3N_Y + 4N_X)/2$

(3) Areal fracture density $P_{20} = N_L/\pi r^2$ (m^{-2})

(4) Areal branch density $B_{20} = N_B/\pi r^2$ (m^{-2})

(5) Areal fracture intensity (S&N) $P_{21} = \Sigma L/\pi r^2$ (m^{-1})

(6) Connections per fracture $C_L = 2(N_Y + N_X)/N_L$

(7) Connections per branch $C_B = (3N_Y + 4N_X)/N_B$

For comparison, areal fracture intensity was also calculated by counting the number of fracture intersections (n) with the circular window circumference (Mauldon, 1998):

(8) Areal fracture intensity (M) $P_{21} = n/4r$ (m^{-1})

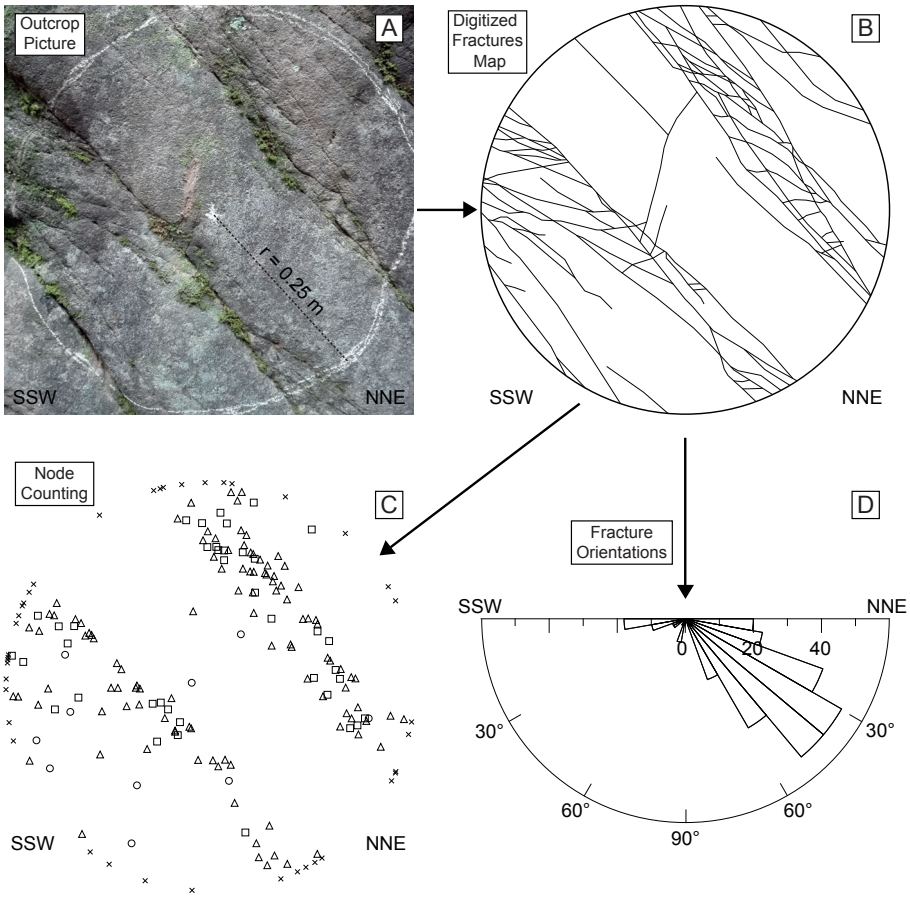


Figure 3: Workflow of the study. (A) Selecting SSW-N-NE oriented wall exposures of thick-bedded Macigno Sandstones Formation strata, draw a circle of 25 cm radius and acquire the outcrop picture. (B) Digitize fracture traces inside the circle using straight segments. (C) Count I (circles), X (squares) and Y (triangles) nodes inside the circular window and fracture intersections with the circumference (crosses). (D) Fracture orientations and lengths can be calculated from the digitized fracture trace map using FracPaQ2D (Healy et al., 2017).

4. Results

4.1 Fracture dip analysis

More than ten thousand (10,857) data were extracted from the digitized fracture maps (Fig. 4). Qualitative analysis of fracture patterns clearly illustrates an overall decreasing fracture density and variable orientations moving away from the fault core, despite a regular trend cannot be

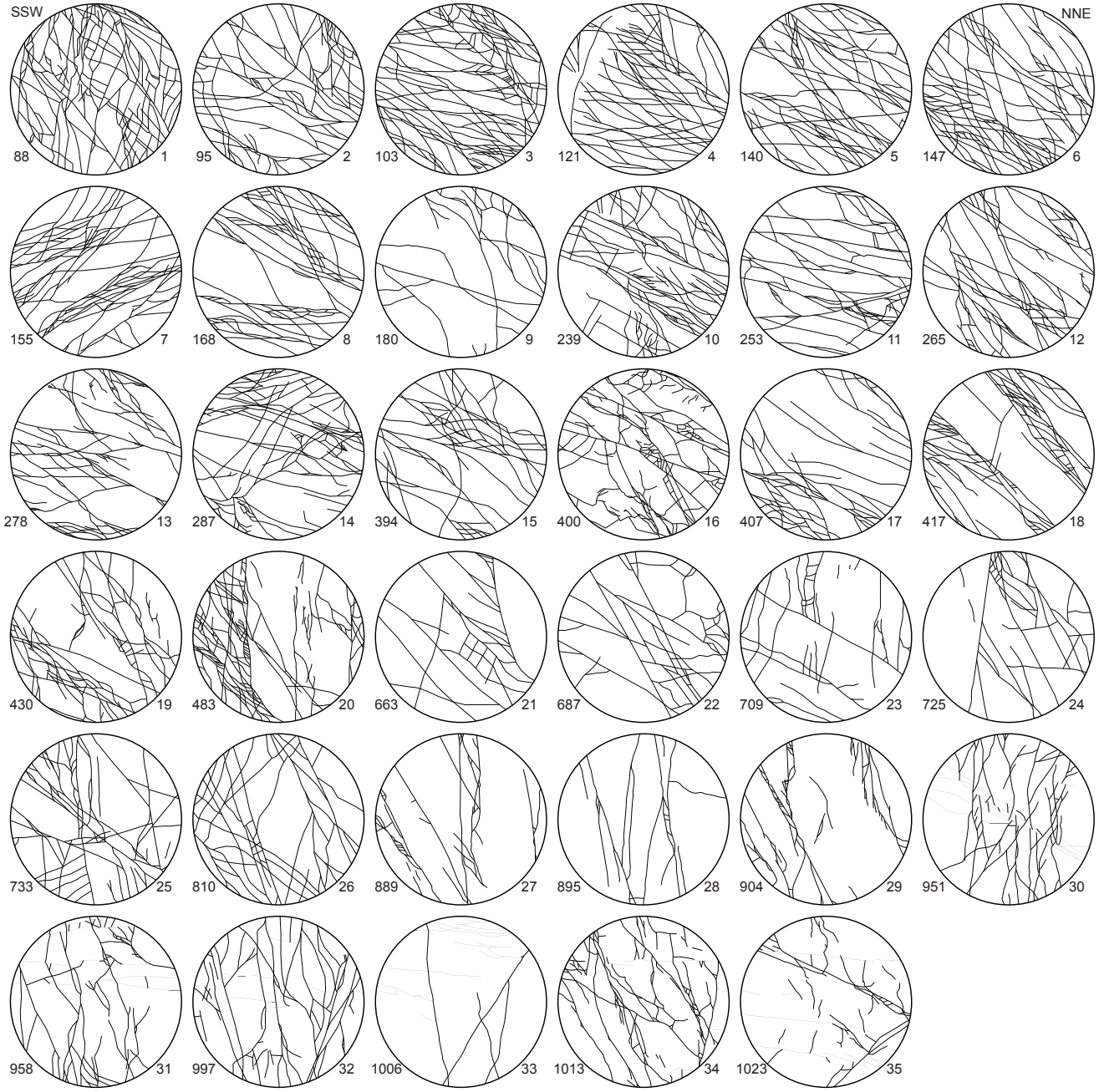


Figure 4: Digitized fracture traces inside circular windows of photographs acquired on vertical, SSW-NNE oriented, outcrops of Macigno Sandstones Formation thick strata. Dashed lines in windows from 30 to 35 represent fractures which opened along primary sedimentary bedding anisotropies. Window number to the right and distance from the fault core to the left of each circular window.

identified. Data in structural sector 1 are located at a distance between 88 and 180 meters from the fault core (windows W1 to W9), where bedding dips 50° to 60° towards SSW, and show mainly and eastward dip values (Fig. 5). More in detail, W1 is characterized by two fracture dip maxima, 70°-90° to the SSW, and 40°-60° to the NNE, respectively. Circular windows W2 to W4 and W8 and W9 include fractures dipping mostly 10° to 30° towards the NNE, while dip increase to 30° to 50°

in W5 and W6. Conversely, in window W7 fractures mostly dip 20° to 30° towards the SSW. Cumulative data analysis for structural sector 1 shows dip values ranging from 10° to 50° to the NNE, with a maximum at 20° to 30° (Fig. 6A). Restoring data to the horizontal bedding stage results in fracture dip values ranging from 60° to 90° towards the NNE, and from 70° to 90° to the SSW respectively, with a maximum between 70° and 80° to the NNE (Fig. 6B).

Circular scan windows W10 to W14, in structural sector 2, are located at a distance between 239 to 287 meters from the fault core, in the hanging wall block of the E-W trending master splay fault, where bedding dips 45° to 50° towards the SSW (Fig. 5). In this sector, four out of the five windows display fractures mostly dipping 10° to 30° towards the NNE, whereas in W12 dip value are more scattered from 20° to 70° towards NNE, with a maximum at 30°-40°. Cumulated data analysis shows that fractures mostly dip from 10° to 50° to the NNE, with a maximum between 20° and 30°, similarly to data from structural sector 1. When bedding dip is restored to the horizontal, fractures display dip values ranging from 50° to 90° to the NNE, with a maximum between 60° and 70° (Fig. 6).

Circular scan windows W15 to W20, in structural sector 3, are located at a distance between 394 and 483 meters from the Compione Fault core, in the footwall block of the E-W major footwall splay fault, where bedding dips 35° to 45° towards the SSW (Fig. 5). In windows W15 to W17, fractures mostly dip from 10° to 40° towards the NNE. Conversely, fracture dip switches to 30°-50° towards the SSW at W18 and then come back to 50°-70° to the NNE at W19 up to subvertical at W20. Cumulative data analysis indicates that most fractures dip 20°-50° to the NNE. Restoring bedding to the horizontal results in dip values between 60° and 90° to the NNE (Fig. 6).

Scan windows W21 to W25, in structural sector 4, are located at a distance between 663 and 733 meters from the Compione fault core, where bedding dip is around 10°-20° to the SSW (Fig. 5). In this sector, fracture dip is more variable than in the previous sites. In particular, at W21 the most frequent dip values occur between 30° to 50° towards NNE; at W22 it slightly shallows to 20° to 40°. Windows W23 and W25 are characterized by mostly near vertical fractures, whereas at site W24 fracture dip mostly 50° to 70° towards the NNE. Cumulative data analysis shows that fracture dip values are clustered in two maxima, between 30° and 50°, and 70° to 90° to the NNE, respectively. When bedding is restored to the horizontal, fractures acquire dip values comprised between 50° and 70° to the NNE, and 70° to 90° to the SSW, respectively (Fig. 6).

Scan windows W26 to W29 are located at a distance between 810 and 904 meters from the Compione fault core, in structural sector 5, where bedding dip is comprised between horizontal and 5° to the NNE. Dip values at W26 are clustered in two maxima, between 30° and 70° to the NNE,

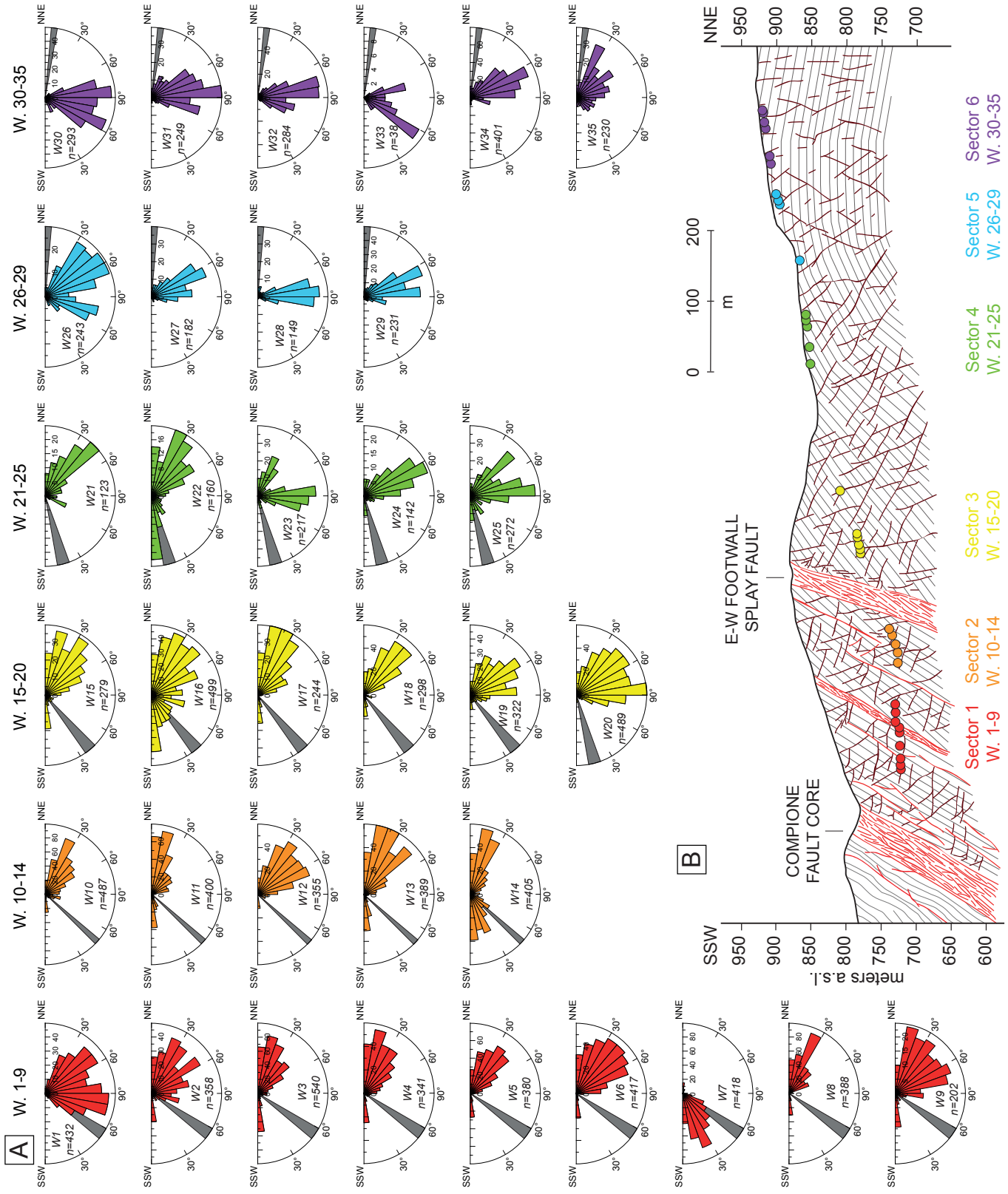


Figure 5: (A) Dip values of fractures in each circular window are plotted in half-rose diagrams, which pass through a SSW-NNE striking vertical plane. Grey bar indicates mean bedding attitude for each structural sector. Half-rose diagrams in the same column belong to the same structural sector. (B) Corss-section of Fig. 2B.

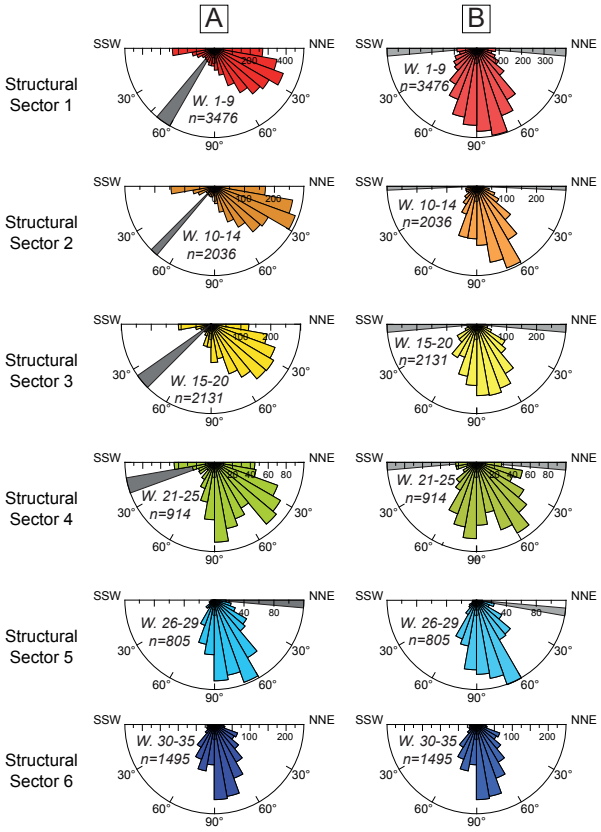


Figure 6: (A) Dip values of fractures are plotted in half-rose diagrams passing through a SSW-NNE striking vertical plane and grouped by structural sector. (B) Fracture dip data shown in A are rotated restoring bedding attitude to horizontal. Data belonging to structural sector 6 are not restored since they are assumed not to be affected by rotation.

and 60° to 80° to the SSW, respectively (Fig 5). Windows W27 and W29 are characterized by dip values spanning from 50° to 90° to the NNE, with a maximum between 60° and 70°, whereas fractures are near vertical (from 80° SSW to 80° NNE) at site W28. Cumulative data analysis indicates that the majority of fractures dip 50° to 90° towards the NNE, with a maximum at 60°-70°. When bedding is restored to a dip of 10° to the NNE, i.e. the expected pre-faulting forelimb dip in this sector, most fractures acquire dip values between 60° to 90° to the NNE, and 80° to 90° to the SSW, respectively, with a maximum between 60° and 70° to the NNE (Fig. 6).

Scan windows from W30 to W35 are located at a distance between 951 and 1023 meters from the Compione fault core, in structural sector 6, where bedding dip ranges between 5° and 10° to the NNE (Fig. 5). At scan windows W30, W31, W32, and W34, most fractures are sub-vertical to 60° to the NNE dipping. Sites W33 and W35 are characterized by dip maxima at 60° to 70° to the SSW and 20° to 30° to the NNE, respectively. Cumulative data analysis indicates that fractures are mostly sub-vertical, with most dip values spanning from 70° to 90° to the NNE. This sector is assumed to be not affected by fault-related folding (Fig. 6).

4.2. Fracture intensity

Areal fracture intensity P_{21} values calculated by equation (5) range from 71.87 m^{-1} in W3 to 15.89 m^{-1} in W28, with an outlier value of 3.14 m^{-1} at W33. Fracture intensity values calculated by equation (8) range from 58 m^{-1} at W3 to 12 m^{-1} at W28, the outlier value of 6 m^{-1} at site W33 (Fig. 7A). Overall, P_{21} values decrease with increasing distance from the Compione fault core despite in the first case data are best fit by a lognormal function, whereas in the second one they are best fit by a linear function. In both cases, data scattering is quite high. The decreasing trend of fracture

density away from the fault core is better described by data grouped by structural sector (Fig. 7B). Sector 1 shows the highest fracture intensity, with P_{21} values of 54.79 ± 13.61 m^{-1} and of 44.89 ± 9.69 m^{-1}, using equations (5) and (8), respectively. Structural sectors 5 and 6 are characterized by the lowest fracture intensity values, corresponding to 23.16 ± 7.95 m^{-1} and 25.13 ± 11.47 m^{-1} using equation (5), and to 23.00 ± 9.14 m^{-1} and 21.33 ± 8.20 m^{-1} using equation (8), respectively. Overall, P_{21} values obtained by the two different equations are quite comparable for structural sectors 4, 5 and 6. Approaching the fault core, equation (8) systematically provides lower values than those obtained from equation (5) (Fig. 7B).

4.3. Fracture density

Areal fracture and branch density were obtained by equations (3) and (4), respectively. Fracture density P_{20} spans from 478.74 m^{-2} at window W1 to 71.30 m^{-2} at W28, excluding outliers at W9, W16, W20, W33, and W34. Branch density B_{20} values follow a similar trend, characterized by decreasing values moving away the fault core and shows outlier values at the same sites as before (Fig. 7C). The maximum branch density value of 2352.95 m^{-2} occurs at site W3, while the minimum one is 203.72 m^{-2} and occurs at W28. Fracture density P_{20} density trend is poorly fitted by a lognormal function and branch density B_{20} is fitted by a linear function, both showing extremely small coefficients of determination. Grouping B_{20} density values for structural sectors indicates an overall decrease with increasing distance from the Compione fault core, and decreasing bedding dip (Fig. 7D). Values are very similar at sectors 1 to 3, and 4 to 6, respectively. The largest standard deviations occur in sectors 1 and 3, due to outlier values. Grouping P_{20} density values for structural sectors show comparable values for sectors 1-3 and 4-6, respectively. The largest standard deviation occurs in sector 3 due to the outlier value at site W16.

4.4. Fracture connectivity

2-D connectivity is expressed as number of connections per fracture and branch, i.e. dimensionless numbers derived from the topological analysis of fracture networks. Fracture connectivity C_L values are generally lower than 3.57 from sites W27 to W35, while acquires higher values up to 6.32 in W4. Outliers occur at sites W15 (8.06) and W26 (7.27), respectively. Overall, there is a decreasing trend moving away from the fault core (Fig. 7E). Such a trend is well illustrated when data are cumulated by structural sector (Fig. 7F). Large standard deviations in structural sectors 3 and 5 are caused by the outlier values at W15 and W26, respectively.

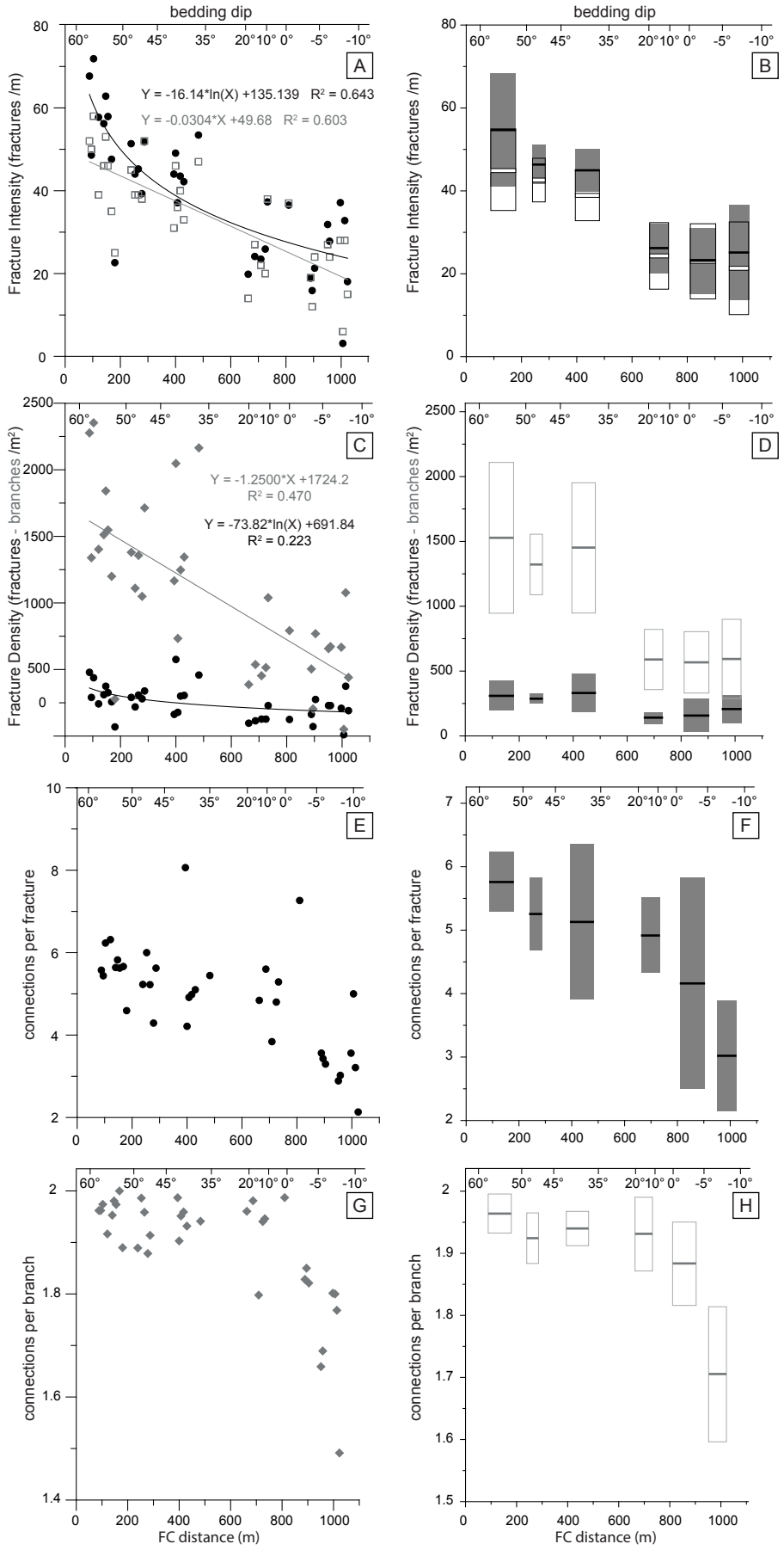


Figure 7: (A-B) Plot of fracture intensity vs. distance from the fault core and boxplots showing mean values and standard deviations grouped by structural sector; black dots and filled boxplots for fracture intensity calculated with equation (5) and white squares and empty boxplots when calculated with equation (8). (C-D) Plot and boxplots of fracture (black dots and filled boxplots) and branch density (grey rhombs and empty boxplots) vs. distance from the fault core. (E-F) Plot and boxplots of number of connections per fracture vs. distance from the fault core. (G-H) Plot and boxplots of number of connections per branch vs. distance from the fault core.

Branch connectivity C_B values are always higher than 1.87 from W1 to W26, i.e. up to about 800 m away from the Compione fault core, with the exception of site W23. Farther to the NE, C_B values suddenly decrease up to a value of 1.49 at site W35 (Fig. 7G). Such a parabolic trend is well illustrated by cumulative data analysis in structural sectors (Fig. 7H).

4.5. Fracture network topology

The total number of nodes per scan window shows quite a large variability when plotted versus the distance from the Compione fault core (Fig. 8A). Maximum values of 280 occur at sites W1 and W3, while values lower than 100 were obtained at distances higher than about 600 m from the fault core. Overall, a decreasing trend with decreasing bedding dip can be envisaged, described by a quite poor linear best fit. I nodes are mostly lower than 30 per scan window and do not show any trend with increasing distance from the fault core (Fig. 8B). Conversely, such a trend occurs for X nodes, which are more than 60 per window in structural sector 1 and decrease down to less than 20 per scan window from W27 to W35 (Fig. 8C). The number of Y nodes also decreases with distance from the fault core, from 171 at site W1, down to less than 60 from W21 to W35. Data are more scattered and, consequently, a quite poor linear best fit was obtained (Fig. 8D). The number of total nodes per circular window shows a quite good positive correlation with the corresponding fracture intensity values P_{21} (Fig. 9A). The same cannot be said when only I nodes are analyzed because a trend cannot be identified (Fig. 9B). On the other hand, good positive linear correlations occur for X and Y nodes plotted versus P_{21} values (Figs. 9C, D).

Network topology can be classified by the relative proportion of I, X, and Y nodes in both singular scan windows and in structural sectors (Fig. 10). The relative abundance of I nodes is 0 % at site W8 and then typically remains lower than 20 % in structural sectors 1 to 4 (scan windows W1 to W26). It increases to 20-25 % in sector 5 (sites W27 to W29) and, eventually, up to about 52% in scan window W35. The relative abundance of X nodes varies from 20 to 40 % in structural sectors 1 to 4 and then lowers down to about 7 to 17 % in sectors 5 and 6. Scan windows W26 and W33 make exception to this trend and show percentages of 46.15 and 42.86 %, respectively. The relative abundance of Y nodes does not show a systematic trend with structural sectors. Percentages typically vary between 40 and 70 %, in most scan windows, with higher values at sites W8, W21 and W28, and lower ones at W33 and W35 (Fig. 10).

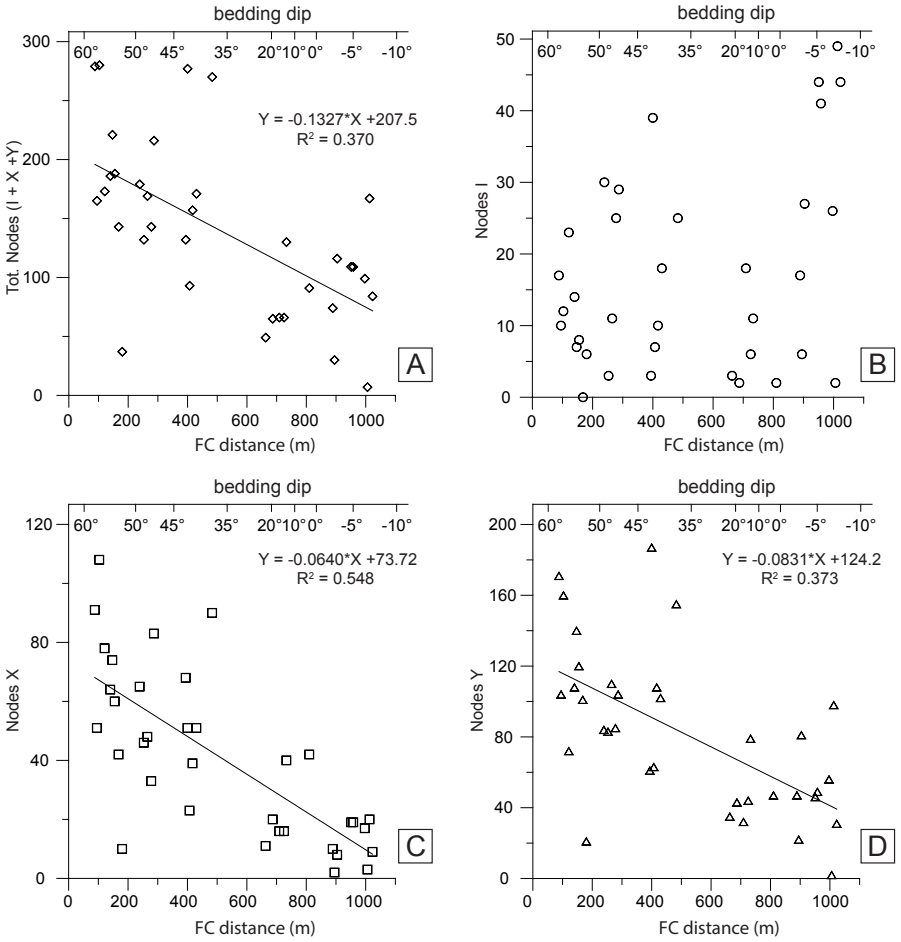


Figure 8: Plots showing number of nodes vs. distance from the fault core. (A) Total number of nodes (I + X + Y) vs. distance from the fault core. (B) Number of I nodes vs. distance from the fault core. (C) Number of X nodes vs. distance from the fault core. (D) Number of Y nodes vs. distance from the fault core.

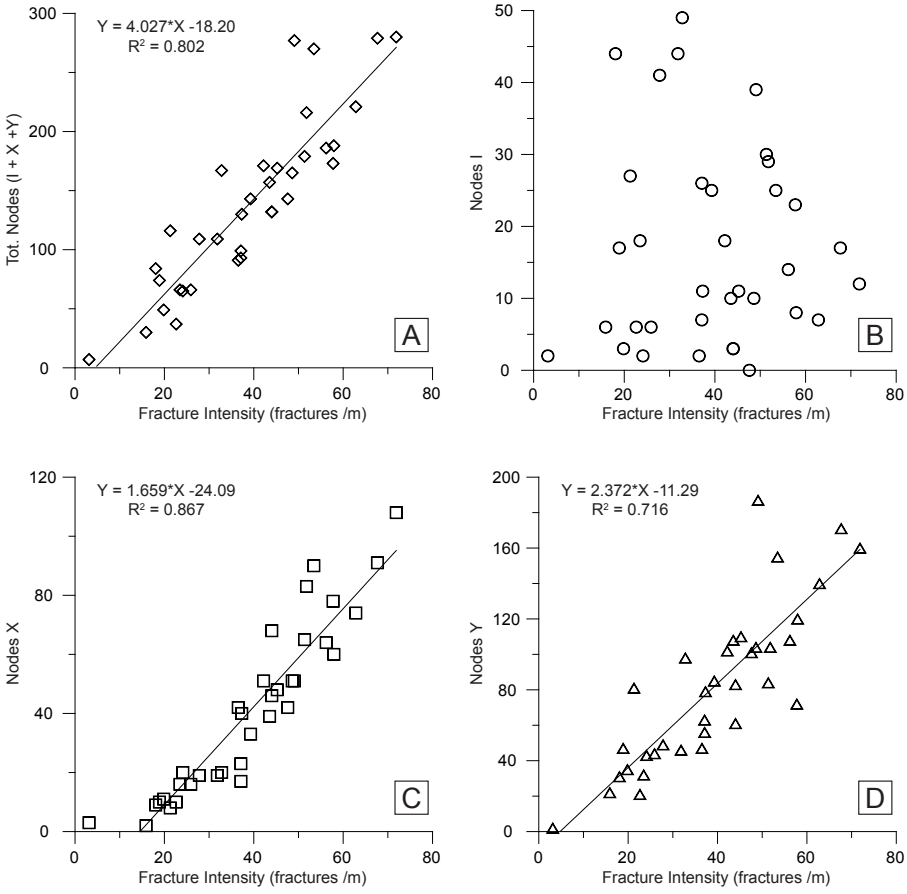


Figure 9: Plots of number of nodes vs. fracture intensity (equation 5). (A) Total number of nodes (I + X + Y) vs. fracture intensity. (B) Number of I nodes vs. fracture intensity. (C) Number of X nodes vs. fracture intensity. (D) Number of Y nodes vs. fracture intensity.

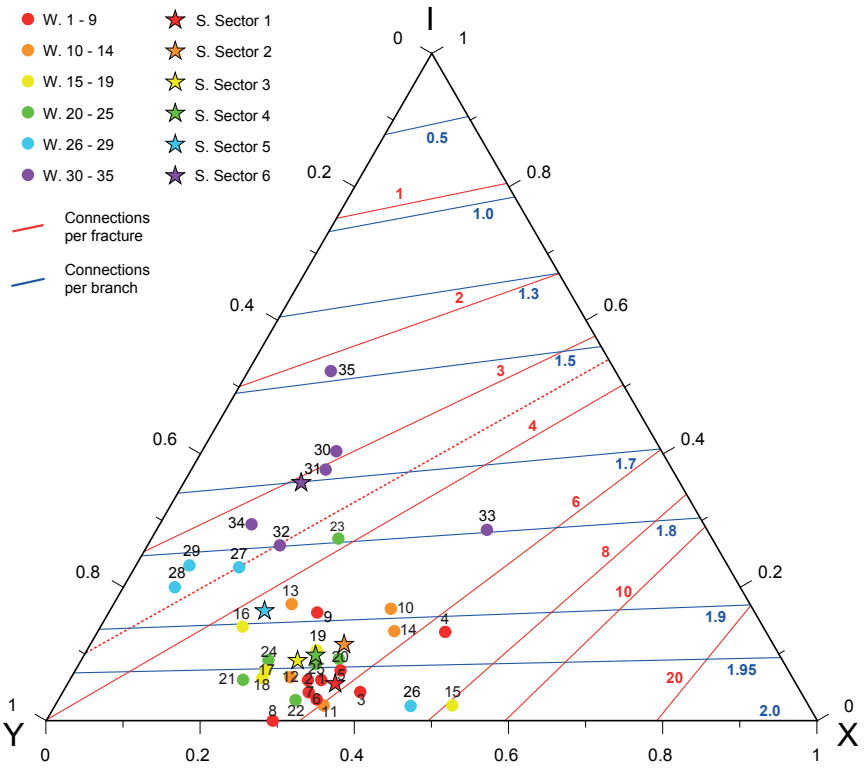


Figure 10: Triangular plot showing relative percentage of I, X and Y nodes per circular window (circles) and per structural sector (stars). Number of connections per fracture (red) and per branch (blue) are also shown. Dashed red line corresponds to 3.57 connections per fracture, which is the percolation threshold value of 2D fracture networks.

5. Discussion

Results from this study indicate that application of scan area and window techniques, which were typically designed for quantifying fracture attributes in map view (e.g. Mauldon, 1998; Sanderson and Nixon, 2015), can be effectively applied to cross-sectional exposures of thick to very thick strata, i.e. within single mechanical layers. A typical limitation of studies in map view (e.g. Watkins et al., 2015) is that collection of 2D datasets in thick strata is expected to imply a significant uncertainty when trying to build 3D discrete fracture networks because of the lack of reliable information on the third dimension. In our case, unavailability of suitable exposures in map view prevented any attempt to combine 2D datasets in mutually orthogonal surfaces and produce 3D discrete fracture network geometry. Accordingly, we rely on 2D exposures to speculate on fault zone evolution.

5.1 Footwall damage zone restoration to the pre-extensional folding stage

Angular relationships between fracture cross-sectional geometry and bedding dip (Fig. 11A) support early formation of conjugate shear vein arrays in the tip damage zone (*sensu* Kim et al., 2004) of the blind Compione Fault, before extensional fault-propagation folding and breakthrough in the Macigno Fm. sandstones (Lucca et al., 2018). Assuming that the crest to forelimb transition of the out-of-sequence thrust-related anticline was located between structural sectors 5 and 6,

restoration of fracture geometry at the pre fault-related folding stage results in southwestward tilted conjugate vein arrays in sectors 2 to 5, with their bisectors inclined to the NE (Fig. 11B). This is not expected in extension-related deformation, where conjugate fault arrays typically have vertical bisectors representing the orientation of the principal axis of the stress ellipse (e.g. Anderson, 1951). A possibility for explaining such a discrepancy relies on the very poor constraints that are available on the pre-extensional, cross-sectional shape of the regional anticline. In particular, the conservative solution of locating the crest-to-forelimb hinge area between structural sectors 5 and 6 can be released and the transition from flat-lying to eastward dipping strata can be moved to the southwest, in between structural sectors 1 and 2. This hypothesis implies an additional clockwise (towards NNE) rotation of fracture sets to match bedding attitude from sectors 2 to 5 with that of the forelimb in sector 6. The result of such a rotation is the restoration of conjugate fracture bisectors to a vertical attitude (Fig. 11C). Formation of conjugate shear fracture arrays with vertical bisectors in gently northeastward bedding strata, can mechanically help explaining the higher abundance of northeast-dipping fractures if stress channeling (Mandl, 2005) is assumed to have occurred in thick and strong beds.

Only in scan window W1 and, to a certain degree W2, the distribution of fracture dip differs from the other sites within structural sector 1 because there occurs a steeply-dipping to near vertical set of fractures and overprints the rotated conjugate shear fracture pattern. Such a fracture pattern is associated with high-angle subsidiary fault zones which occur up to 400 m from the fault core and mark the boundary of the wall damage zone (*sensu* Kim et al., 2004). The intensity of the damage zone fracture pattern in the area close to the fault core (about 100 m) was likely produced by fault slip after breakthrough and deformation localization. Implications for the evolution of the cross-sectional permeability structure of the Compione fault are straightforward: initially, the tip damage zone likely acted as a large and effective conduit ahead of the fault tip, facilitating hot fluid advection from the basement (Lucca et al., 2018); with increasing fault propagation and slip, fracture cementation and shear localization in the wall damage zone strongly reduced the area where effective fluid flow was possible.

5.2 Fracture intensity, density and connectivity in the tip damage zone

Fracture intensity values in the tip damage zone are characterized by an increasing trend approaching the fault core (Fig. 12A). It is interesting to note that values calculated with the method of Mauldon (1998) are always lower than those obtained by applying the method of Sanderson and Nixon (2015). Such a difference can be interpreted as resulting from the faster increase of total

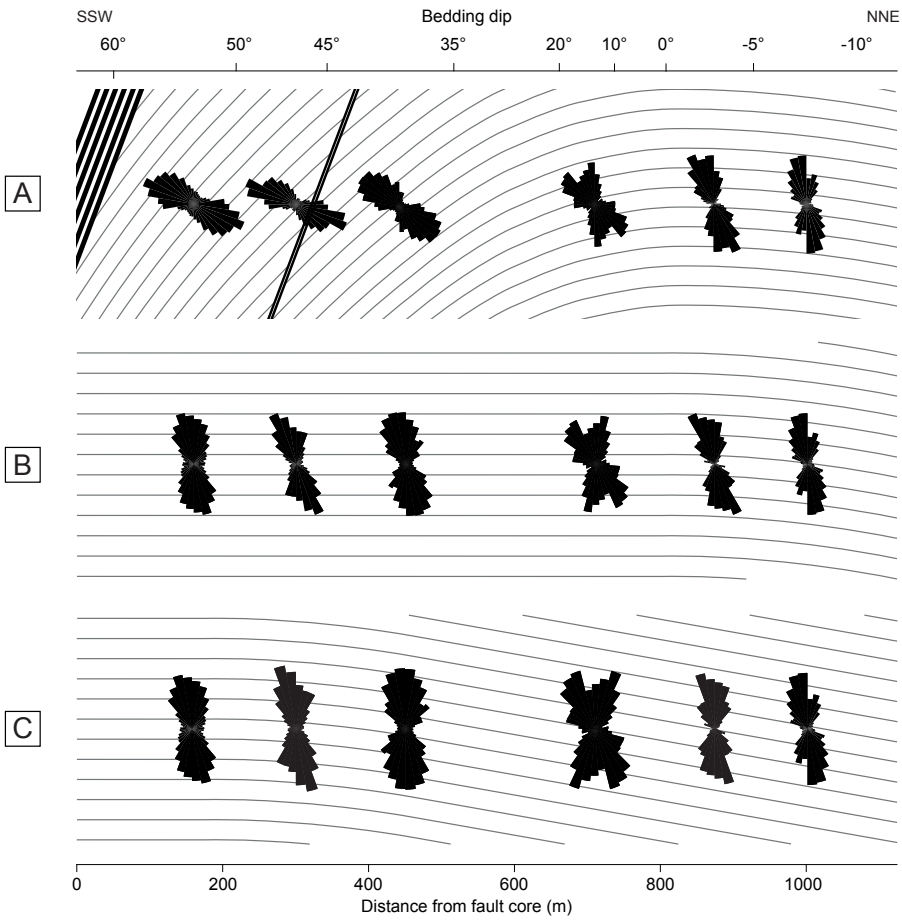


Figure 11: Synoptic scheme of the Compione fault footwall damage zone. (A) Schematic cross-section with projected rose diagrams showing fracture apparent dip directions grouped by structural sector; black lines in the left corner represent the Compione fault core while the other two black lines schematically indicate the major E-W footwall splay fault. (B) After bedding restoration to horizontal. (C) After an additional 10° of clockwise rotation (towards the NNE) compared to B.

fracture length inside scan windows compared to the number of fracture intersections with scan circumferences. Accordingly, also the number of branches and nodes increases at a higher rate than the number of fractures, i.e. N_B/N_L ratio is higher closer to the fault core (Fig. 12). As a consequence, fracture connectivity increases towards the fault core and shows values higher than 3.57 connections per fracture in all structural sectors apart from sector 6. This number corresponds to the percolation threshold for a two-dimensional fracture network, i.e. it is the value above which fractures are connected in a single cluster spanning over the entire area of observation (Balberg et al., 1984). Such an evidence provides further support to the evidence that thick coarse sandstone beds in the footwall of the Compione Fault provided effective pathways for fluid migration since the tip damage zone fracture network had developed (Lucca et al., 2018).

5.3 Implications of fracture topology on fault zone evolution

The evidence that the tip damage zone of the Compione Fault is characterized by increasing amounts of X and Y nodes approaching the fault core, and that the latter are systematically more abundant (Fig. 12C), could be explained by noting that even small amounts of slip on two conjugate

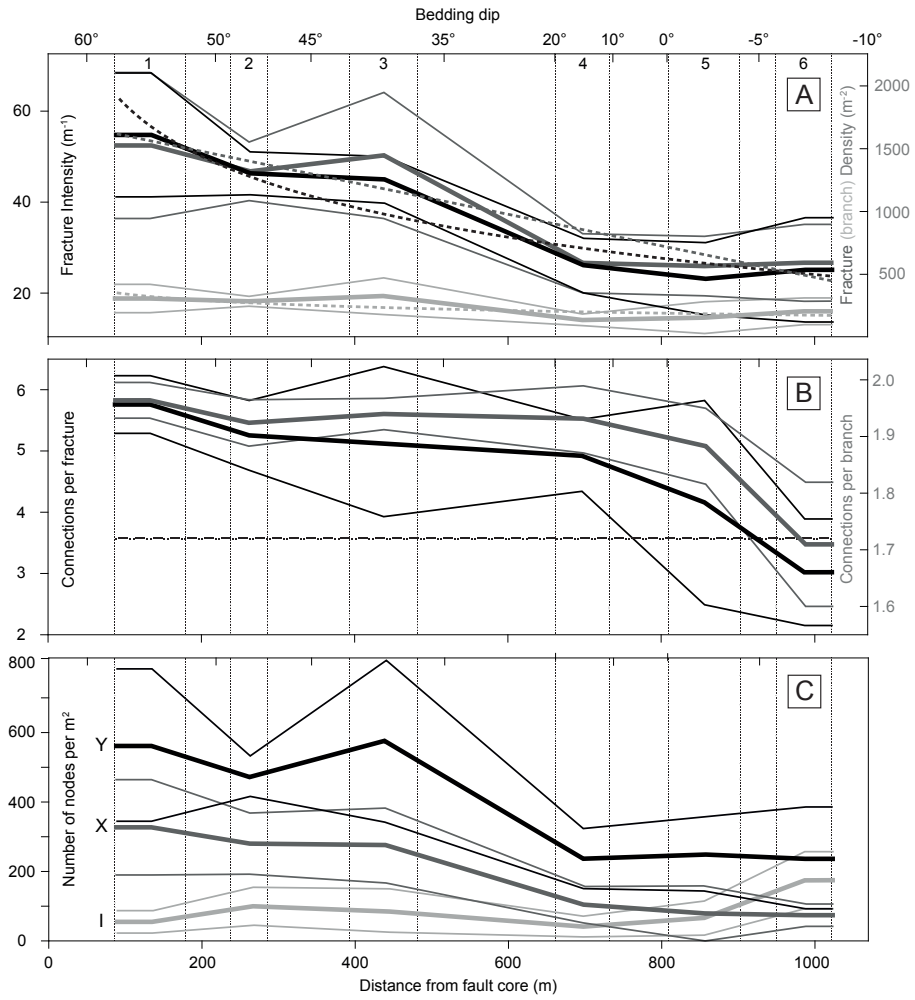


Figure 12: (A) Plot showing mean values (thick lines), ± 1□□(thin lines) and best fits (dashed-dotted lines) of fracture intensity (black), fracture density (light grey) and branch density (dark grey) vs. distance from the fault core grouped by structural sector; bedding dip values are also represented on the horizontal axis. (B) Same plot of A showing number of connections per fracture (black) and number of connections per branch (dark grey). (C) Same plot of A and B showing number Y nodes (black), X nodes (dark grey) and I nodes (light grey) per square meter.

shear fractures forming a X node, produces two Y nodes. Further slip on the same shear fracture doesn't produce any other topological change. The almost linear increase of X nodes might relate to the formation of the tip damage zone, where a positive gradient of conjugate shear fracture abundancy towards the prospect master slip zone was imprinted in the very early evolutionary stages. The increase of Y nodes at an overall comparable rate might relate to the same phenomenon, i.e. an increase of displacement associated with shear fracturing. The only deviation from this behavior occurs at about 350 to 550 meters from the fault core, where some major splay fault zones occur and may have caused additional shearing of X nodes (Fig. 5). In this view, overprinting of the tip damage zone fracture pattern by wall damage zone-related fracturing is negligible. However, it has to be recalled that suitable exposures for fracture pattern analysis are available starting from about 80 m away from the fault core. Outcrop degradation may relate to such overprinting, which is particularly intense near the fault core even at the scale of the scan window, as seen from W1 and W2.

The higher number of I nodes in structural sector 6 compared to the other ones, may indicate

that it lies at the outer boundary of the fault tip damage zone, because fault-related fracture networks are typically dominated by Y nodes (Nixon et al., 2012; Morley and Nixon, 2016). This inference is supported by the corresponding lower connectivity values and by the dominantly bed-perpendicular attitude of fractures (Fig. 6).

6. Conclusions

The Compione Fault is a segment of the Northern Lunigiana, regional-scale extensional fault system, on the Tyrrhenian Sea side of the Northern Apennines orogenic wedge. It accumulated about 1.5 km of maximum displacement since Early Pliocene times, offsetting the forelimb to crest transition of regional-scale out-of-sequence thrust-related anticline. In the footwall it exposes thick to very thick sandstone strata, where we acquired circular scan windows on vertical outcrops along a transect oriented perpendicular to the fault strike, to quantify fracture network attributes. Their variability allowed us to highlight the following main points:

- Fault-related damaging evolved from initial formation of an about 900 m wide footwall tip damage zone ahead of the upward propagating blind fault tip, which was overprinted only for 400 m away from the fault core, by fracturing produced by slip after fault breakthrough;
- Topological analysis supports this inference by showing a progressive and almost linear increase of X and Y nodes towards the fault core, which we interpret as mostly imprinted from the onset of the tip damage zone formation, when the prospect master slip zone was not yet formed;
- Y nodes are more abundant than X nodes because shearing a conjugate pair of shear fractures without visible displacement (X node) systematically produces two Y nodes;
- Restoration of fracture dip in the tip damage zone indicates that the hinge zone of the extensional fault-propagation fold associated with the Compione Fault locates about 0.6 km into the forelimb of the out-of-sequence thrust-related anticline, whereas the fault core locates close to the crest-to-forelimb transition of the anticline;
- Connectivity is above the percolation threshold value in all structural sectors within the tip damage zone and this indicates efficient fault-controlled fluid circulation in the very early evolutionary stages of the Compione Fault;
- Progressive cementation of the tip damage zone fracture network dramatically reduced the conduit behavior of the Compione Fault footwall after fault breakthrough and localization of deformation in the wall damage zone which is half wide as the tip damage zone; at this mature stage the fault zone was characterized by a typical conduit-barrier hydraulic

behavior;

- Fracture intensity values calculated with the methods of Sanderson and Nixon (2015) and Mauldon (1998) well agree in the outer tip damage zone whereas the latter systematically underestimates fracture intensity in more intensely deformed sectors, approaching the fault core, where the branch to fracture ratio increases.

7. Acknowledgements

We are grateful to F. Balsamo for fruitful discussions on the structure and evolution of the Compione Fault. This work was partly funded by ENI S.p.A., grants to F. Storti. Author's contribution: A. Lucca carried out field work, collected and analyzed data, and wrote the manuscript; F. Storti conceived the research, participated to some field work, and critically reviewed the manuscript; G. Molli participated to some field work and critically reviewed the manuscript.

References

Anderson, E.M., 1951. The Dynamics of Faulting and Dyke Formation with Application to Britain (2nd edn). Oliver and Boyd, Edinburgh.

Argnani, A., 2002. The Northern Apennines and the kinematics of Europe-Africa convergence: Bollettino della Società Geologica Italiana. vol. 1, p. 47–60.

Azzaroli, A., 1977. The Villafranchian stage in Italy and the Plio-Pleistocene boundary. Giornale di Geologia, v. 41, p. 61-79.

Balberg, I., Anderson, C.H., Alexander, S., and Wagner, N., 1984. Excluded volume and its relation to the onset of percolation. Phys. Rev., 30 (7), p. 3933-3943.

Barbier, M., Hamon, Y., Callot, J., Floquet, M., and Daniel, J., 2012. Sedimentary and diagenetic controls on the multiscale fracturing pattern of a carbonate reservoir: the Madison Formation (Sheep Mountain, Wyoming, USA). Mar. Petrol. Geol., vol. 29, p. 50-67.

Barchi, M.R., Minelli, G., and Pialli, G., 1998. The CROP 03 Profile: A synthesis of results on deep structures of the Northern Apennines. Memorie della Società Geologica Italiana, vol. 52, p. 383–400.

Bernini, M., and Lasagna, S., 1988. Rilevamento geologico e analisi strutturale del bacino dell'Alta Val Magra tra M. Orsaro e Pontremoli (Appennino Settentrionale): Atti della Società Toscana di

Scienze Naturali, Memorie, Serie A, 95, p. 139-183.

Bernini, M., Vescovi, P., and Zanzucchi, G., 1997, Schema strutturale dell'Appennino Nord-Occidentale: L'Ateneo Parmense Acta Naturalia, v. 33, p. 43-54.

Boccaletti, M., Elter, P., and Guazzone, G., 1971. Plate Tectonic Models for the Development of the Western Alps and Northern Apennines. Nature, vol. 234, p. 108-111.

Boccaletti, M., Corti, G., and Martelli, L., 2011. Recent and active tectonics of the external zone of the Northern Apennines (Italy). Int. J. Earth Sci., vol. 100, p. 1331-1348.

Caine, J.S., Evans, J.P., and Forster, J.B., 1996. Fault zone architecture and permeability structure. Geology, vol. 24, p. 1025-1028.

Camurri, F., Argnani, A., Bernini, M., Papani, G., Rogledi, S., and Torelli, L., 2001. The basement of the NW Apennines: interpretation of reflection seismics and geodynamic implications. Final Proceedings, Geoitalia 2001, 3° Forum Italiano di Scienze della Terra (Fist), Chieti, Italy, p. 50-51.

Carmignani, L., and Kligfield, R., 1990. Crustal extension in the Northern Apennines: The transition from compression to extension in the Alpi Apuane core complex. Tectonics, vol. 9, p. 1275–1303.

Carmignani, L., Decandia, F.A., Disperati, L., Fantozzi, P.L., Lazzarotto, A., Liotta, D., and Oggiano, G., 1995. Relationships between the Tertiary structural evolution of the Sardinia-Corsica-Provençal Domain and the Northern Apennines. Terra Nova, vol. 7, no. 2, p. 128–137.

Chester, F.M., Evans, J.P., and Biegel, R.L., 1993. Internal structure and weakening mechanisms of the San Andreas fault. Journal of Geophysical Research, vol. 98, p. 771-786.

Clemenzi, L., Molli, G., Storti, F., Muchez, P., Swennen, R., and Torelli, L., 2014. Extensional deformation structures within a convergent orogen: The Val di Lima low-angle normal fault system (Northern Apennines, Italy). Journal of Structural Geology, vol. 66, p. 205-222.

Decandia, F.A., Lazzarotto, A., and Liotta, D., 1998. The CROP 03 traverse: insights on post-collisional evolution of Northern Apennines. Memorie della Società Geologica Italiana, vol. 52, p. 427–440.

Dewey, J.F., Helman, M.L., Knott, S.D., Turco, E., and Hutton, D.H.W., 1989. Kinematics of the western Mediterranean, In: Coward M.P., Dietrich D., and Park R.G., eds., Alpine Tectonics. Geological Society of London Special Publication, vol. 45, p. 265–283.

Doglioni, C., 1991. A proposal for the kinematic modelling of W-dipping subductions - Possible applications to the Tyrrhenian-Apennines system. Terra Nova, vol. 3, n. 4, p. 423–434.

Elter, P., and Schwab, K., 1959. Note illustrative della Carta Geologica alla scala 1:50.000 della regione Carro-Zeri-Pontremoli. Boll. Soc. Geol. It., vol. 78, p. 157-187.

Elter, P., and Pertusati, P., 1973. Considerazioni sul limite Alpi-Appennino e sulle relazioni con l'arco delle Alpi occidentali. Mem. Soc. Geol. It., vol. 12, p. 359-375.

Elter, P., Giglia, G., Tongiorgi, M., and Trevisan, L., 1975. Tensional and compressional areas in recent (Tortonian to present) evolution of Northern Apennines. Boll. Geofis. Teor. Appl, vol. 17, p. 13-18.

Faulkner, D., Jackson, C., Lunn, R., Schlische, R., Shipton, Z., Wibberley, C., and Withjack, M., 2010. A review of recent developments concerning the structure, mechanics and fluid flow properties of fault zones. Journal of Structural Geology, vol. 32, p. 1557-1575.

Federici, P.R., 1978. La tettonica recente dell'appennino; 2) Il bacino fluvio-lacustre di Pontremoli (Alta Val di Magra) e sue implicazioni neotettoniche. G.S.Q.P., Quaderno n. 4, p. 121-131.

Healy, D., Rizzo, R.E., Cornwell, D.G., Farrell, N.J., Watkins, H., Timms, N.G., Gomez-Rivas, E., and Smith, M., 2016. FracPaQ: a MATLAB toolbox for the quantification of fracture patterns. Journal of Structural Geology, vol. 95, p. 1-16.

Jenkins, C., Ouenes, A., Zellou, A., and Wingard, J., 2009. Quantifying and predicting naturally fractured reservoir behavior with continuous fracture models. AAPG Bulletin, vol. 93 (11), p. 1597-1608.

Jolivet, L., Faccenna, C., Goffé, B., Mattei, M., Rossetti, F., Brunet, C., Storti, F., Funiciello, R., Cadet, J.P., D'Agostino, N., and Parra, T., 1998. Midcrustal shear zones in postorogenic extension: Example from the northern Tyrrhenian Sea. Journal of Geophysical Research, vol. 103, p. 12,123–12,160.

Lamarche, J., Lavenu, A., Gauthier, B., Guglielmi, Y., and Jayet, O., 2012. Relationships between fracture patterns, geodynamics and mechanical stratigraphy in carbonates (SouthEast Basin, France). Tectonophysics, vol. 581, p. 231–245.

Lucca, A., Storti, F., Molli, G., Muchez, P., Schito, A., Artoni, A., Balsamo, F., Corrado, S., and Salvioli Mariani, E., 2018. Seismically-enhanced hydrothermal plume advection through the process zone of the Compione extensional Fault, Northern Apennines, Italy. Geological Society of

America Bulletin, accepted for publication 14/08/2018, https://doi.org/10.1130/B32029.1.

Maerten, L., and Maerten, F., 2006. Chronologic modeling of faulted and fractured reservoirs using geomechanically based restoration: Technique and industry applications. AAPG Bulletin, vol. 90, p. 1201-1226.

Malinverno, A., and Ryan, W.B.F., 1986. Extension in the Tyrrhenian Sea and shortening in the Apennines as result of arc migration driven by sinking of the lithosphere. Tectonics, vol. 5, p. 227-245.

Mandl, G., 2005. Rock Joints. The Mechanical Genesis. Springer, Berlin/Heidelberg/New York.

Manzocchi, T., 2002. The connectivity of two dimensional networks of spatially correlated fractures. Water Resources, Res. 38, http://dx.doi.org/10.1029/2000WR000180.

Martini, I.P., Sagri, M., and Colella, A., 2001. Neogene-Quaternary basins of the inner Apennines and Calabrian arc. In: Anatomy of an orogeny: The Apennines and adjacent Mediterranean Basins, edited by Vai G.B. and Martini I.P., p. 375-400, Kluwer Acad., Dordrecht, Netherlands.

Mauldon, M., 1998. Estimating mean fracture trace length and density from observations in convex windows. Rock Mechanics and Rock Engineering, vol. 31, p. 201-216.

Molli, G., Carlini, M., Vescovi, P., Artoni, A., Balsamo, F., Camurri, F., Clemenzi, L., Storti, F., and Torelli, L., 2018. Neogene 3D-structural architecture of the north-west Apennines: the role of the low angle normal faults and basement thrusts. Tectonics, vol. 37, p. 2165-2196.

Morley, C.K., and Nixon, C.W., 2016. Topological characteristics of simple and complex normal fault networks. J. Struct. Geol., vol. 84, p. 68-84.

Nelson, R.A., 1985. Geologic Analysis of Naturally Fractured Reservoirs, Gulf, Houston, Tex., 320 p.

Nixon, C.W., Sanderson, D.J., and Bull, J.M., 2012. Analysis of a strike-slip fault network using high resolution multibeam bathymetry, offshore NW Devon U.K. Tectonophysics, vol. 541-543, p. 69-80.

Perrin, C., Manighetti, I., Ampuero, J.P., Cappa, F., and Gaudemer, Y., 2016. Location of largest earthquake slip and fast rupture controlled by along-strike change in fault structural maturity due to fault growth. J. Geophys. Res. Solid Earth, vol. 121, p. 3666-3685.

Principi, G., and Treves, B., 1984. Il sistema corso-appennino come prisma d'accrezione. Riflessi sul problema generale del limite Alpi-Appennino. Memorie della Società Geologica ltaliana, vol.

28, p. 529-576.

Raggi, G., 1985. Neotettonica ed evoluzione paleogeografica plio-pleistocenica del Bacino de fiume Magra. Memorie della Società Geologica Italiana, vol. 30, p. 35-62.

Reyer, D., Bauer, J.F., and Philipp, S.L., 2012. Fracture systems in normal fault zones crosscutting sedimentary rocks, Northwest German Basin. J. Struct. Geol., vol. 45, p. 38-51.

Royden, L., 1988. Flexural behaviour of the continental lithosphere in Italy: Constraints imposed by gravity and deflection data. Journal of Geophysical Research, vol. 93, p. 7747–7766.

Sanderson, D.J., and Nixon, C.W., 2015. The use of topology in fracture network characterization. Journal of Structural Geology, vol. 72, p. 55-66.

Sonntag, R., Evans, J.P., La Pointe, P., Deraps, M., Sisley, H. and Richey, D., 2012. Sedimentological controls on the fracture distribution and network development in Mesaverde Group sandstone lithofacies, Uinta Basin, Utah, USA. In: Spence, G.H., Redfern, J., Aguilera, R., Bevan, T.G., Cosgrove, J.W., Couples, G.D. & Daniel, J.-M. (eds) Advances in the Study of Fractured Reservoirs. Geological Society, London, Special Publications, vol. 374, 23-50. First published online September 10, 2012, http://dx. doi.org/10.1144/SP374.4.

Storti, F., 1995. Tectonics of the Punta Bianca promontory: Insights for the evolution of the Northern Apennines-Northern Tyrrhenian Sea basin. Tectonics, vol. 14, p. 832–847.

Tinti, E., Spudich, P., and Cocco, M., 2005. Earthquake fracture energy inferred from kinematic rupture models on extended faults. J. Geophys. Res., vol. 110, B12303, doi:10.1029/2005JB003644.

Vescovi, P., 2005. The Middle Miocene Mt. Ventasso – Mt. Cimone arcuate structure of the Emilia Apeninnes. Bollettino della Società Geologica Italiana, vol. 124, p. 53-67.

Watkins, H., Bond, C.E., Healy, D., and Butler, R.W., 2015. Appraisal of fracture sampling methods and a new workflow to characterise heterogeneous fracture networks at outcrop. J. Struct. Geol., vol. 72, p. 67-82.

4

COSEISMIC EXTENSION RECORDED WITHIN THE DAMAGE ZONE OF THE VADO DI FERRUCCIO THRUST FAULT, CENTRAL APENNINES, ITALY

This chapter is presented in the form of a manuscript published in *Journal of Structural Geology*. This manuscript describes the structural architecture of the Vado di Ferruccio out-of-sequence Thrust Fault. Specifically, in this study, we show that high-angle extensional subsidiary faults with mirror-like surfaces occurring in the hanging wall damage zone of the thrust can represent exhumed analogues of high-angle structures rupturing during foreshocks and aftershocks sequences above low-angle shallow detachments in the Apennines, recently illuminated through seismological methods.

PUBLISHED ARTICLE

Leah H., Fondriest M., Lucca A., Storti F., Balsamo F., and Di Toro G.

Published in: *Journal of Structural Geology, Volume 114, September 2018, Pages 121-138*

Date of Submission: 8 March 2018

Date of Acceptance: 18 June 2018

Journal of Structural Geology 114 (2018) 121–138

Contents lists available at ScienceDirect

Journal of Structural Geology

journal homepage: www.elsevier.com/locate/jsg

Coseismic extension recorded within the damage zone of the Vado di Ferruccio Thrust Fault, Central Apennines, Italy

Harold Leah[a,e,*], Michele Fondriest[a], Alessio Lucca[b], Fabrizio Storti[b], Fabrizio Balsamo[b], Giulio Di Toro[a,c,d]

[a] School of Earth and Environmental Sciences, The University of Manchester, M13 9PL, UK
[b] NEXT – Natural and Experimental Tectonics Research Group, Università degli Studi di Parma, Dipartimento di Scienze Chimiche, della Vita e della Sostenibilità Ambientale, 43124 Parma, Italy
[c] Istituto Nazionale di Geofisica e Vulcanologia (INGV), Via di Vigna Murata 605, 00143 Roma, Italy
[d] Dipartimento di Geoscienze, Università degli Studi di Padova, Via G. Gradenigo 6, 35131, Padua, Italy
[e] School of Earth and Ocean Sciences, Cardiff University, Main Building, Cardiff, CF10 3AT, UK

A B S T R A C T

Recent high resolution hypocentral localisation along active fault systems in the Central Apennines illuminates the activation of seismogenic volumes dipping at low angle (< 30°) in extensional settings overprinting contractional deformations affecting the continental crust of the Adria microplate. Individuation of the geological structures and of the fault processes associated with these seismic patterns will contribute to the interpretation of seismic sequence evolution, and seismic hazard studies.

Here we report field and microstructural evidence of seismogenic extensional faults localized within pre-existing thrust fault zones. The Vado di Ferruccio Thrust Fault (VFTF) is a narrow fault zone (< 2.5 m thick fault core) in the Central Apennines of Italy, accommodating ~1 km of shortening during Miocene-Pliocene and exhumed from < 3.5 km depth. In the thrust zone, exposures throughout the Fornaca Tectonic Window show Late Triassic bituminous dolostones thrust over Middle Jurassic interlayered carbonates upon a SSW-dipping fault. Isoclinal folds are dragged and sheared by thrust-parallel reverse faults in the footwall block whereas NW-striking faults occur within the hanging wall. Fault core observations are consistent with stable pressure solution-mediated aseismic sliding towards N024° during thrusting, with cyclic veining and faulting. Later extension has been accommodated at the regional scale by major normal faults cutting through the VFTF, while veins and pressure-solution seams crosscut the microstructures associated with thrusting and record the extensional stress regime within the thrust fault core. Lenses of shattered rocks (up to 10 s m thick), cut by a dense network of small displacement (< 1.2 m) mirror-like normal faults, are reported in the hangingwall of the VFTF. These minor faults, related to a sharp principal slipping surface on the upper margin of the VFTF fault core, are interpreted as fossil evidence of microseismicity compartmentalized within the hanging wall of the VFTF. Synthetic and antithetic normal faults within the VFTF hangingwall damage zone are geometrically and kinematically similar to small earthquake ruptures (M_w < 2) in the hangingwall of low angle structures such as the thrust flats illuminated during the 2009 M_w 6.1 L'Aquila seismic sequence.

1. Introduction

Activation of extensional faults in the Central Apennines is associated with significant seismicity (Galli, 2002), including the 2009 M_w 6.1 L'Aquila (Chiaraluce et al., 2011; Valoroso et al., 2013) and 2016 M_w 6.5 Amatrice-Norcia (Michele et al., 2016; Chiaraluce et al., 2017) seismic sequences, both of which led to significant loss of life, infrastructure collapse and significant economic losses (Dolce and Di Bucci, 2017). These earthquakes typically occur on normal faults which cut through thick (4–8 km) sequences of carbonate rocks in the upper crust (Vezzani et al., 2010; Dolce and Di Bucci, 2017). Comprehensive and high-resolution monitoring and hypocentral relocation of seismicity in the region has provided important insights into the geometry of activated fault systems (Chiaraluce et al., 2011, 2017; Valoroso et al., 2013). For example, the 2009 L'Aquila seismic sequence was characterised by foreshocks which ruptured "high-angle" (i.e., dipping 50–60°) normal faults, and aftershocks which ruptured both high-angle and "low-angle" (i.e., dipping 15–25°) rock volumes (Chiaraluce et al.,

* Corresponding author. School of Earth and Ocean Sciences, Cardiff University, Main Building, Cardiff, CF10 3AT, UK.
E-mail address: LeahHR@Cardiff.ac.uk (H. Leah).

https://doi.org/10.1016/j.jsg.2018.06.015
Received 8 March 2018; Received in revised form 15 June 2018; Accepted 18 June 2018
Available online 23 June 2018
0191-8141/ © 2018 Elsevier Ltd. All rights reserved.

2011; Valoroso et al., 2013), suggested to represent re-activated thrust faults (Falcucci et al., 2015). Normal faulting associated with low-angle structures has been studied in the field in the Alps (e.g. Cardello and Mancktelow, 2015), Northern Apennines (e.g. Clemenzi et al., 2015), and Gran Sasso Massif (e.g. Demurtas et al., 2016) where normal faults were shown to be exhumed analogues of seismically-active normal faults at depth. Investigation of the Vado di Corno Fault Zone showed in-situ shattering, formation of mirror-like slip surfaces, and highly-localised sheared calcite veins within a cataclastic unit resulting from multiple seismic ruptures on a high-angle normal fault (Demurtas et al., 2016). Intersecting the normal fault, an extensionally-reactivated low-angle thrust was inherited from earlier Pliocene compression and partially reactivated during later extension (Demurtas et al., 2016). This geometry is coherent with associated high-angle normal faults and low-angle volumes at depth seismically-activated during the 2009 M_w 6.1 L'Aquila earthquake (Chiaraluce et al., 2011; Valoroso et al., 2013). To better understand the processes occurring in seismically-activated low-angle fault zones in the Central Apennines we investigate the Vado di Ferruccio Thrust Fault (VFTF), a thrust fault exposed further east in the Gran Sasso Massif, and document localised coseismic extension compartmentalised within the hangingwall block of the thrust.

Coseismic extension is used here to describe extensional slip occurring on a fault or a fault network during a seismic event (earthquake). Coseismic extension on a thrust fault can imply the reactivation of the low angle surface (i.e., negative inversion) formed during initial compression or, as is documented here, localised extensional secondary faulting within the damage zone of the thrust. This paper documents a case of coseismic extension within the hangingwall damage zone of the VFTF in the Central Apennines, and shows how it is distinct from compressional features formed during thrusting.

The VFTF was first described alongside the entire thrust stack exposed in the Gran Sasso chain in the seminal paper of Ghisetti (1987) and mapped by Ghisetti and Vezzani (1986), with the name “thrust 7” (φ7 or T_7). The current study consists of an integrated field-microstructural reappraisal of the VFTF architecture based upon this previous work. The studied fault likely corresponds, at the regional scale, to the “Upper thrust” described by Pace and Calamita (2015) on the north side of the Corno Grande and the Gran Sasso Massif (Adamoli et al., 2012). Here, we prefer to use the name Vado di Ferruccio Thrust Fault (VFTF) which strictly relates the studied thrust to its outcropping area. New techniques are used here to discern the structure of the Vado di Ferruccio thrust zone from meso-to micro-scale; detailed field investigation at selected localities is accompanied by microstructural description of fault core samples using optical microscopy, field-emission scanning electron microscopy, and micro-Raman spectroscopy. The resulting data is used to describe observed microstructures, minerals, and previously undescribed amorphous materials. These observations are then used to (i) determine mesoscale processes accommodating strain throughout the fault zone during compression and extension, (ii) establish kinematics of thrusting and normal faulting, (iii) infer deformation processes for compression and extension from microstructures and relate this to fault core lithology, and (iv) discuss whether there is evidence of seismic activation of the VFTF hanging wall, and if so, compare with microseismicity distributions of seismic sequences in the Central Apennines.

2. Geological setting

2.1. Gran Sasso Massif

The Gran Sasso Massif is a fault-bounded area in the Central Apennines (Fig. 1b) containing the highest peaks of the mountain range. It was formed by Miocene-Pliocene thrusting of Triassic to Pliocene age rocks during the westward subduction of the Adriatic slab beneath the European Plate (e.g. Devoti et al., 2008; Cardello and Doglioni, 2015). The massif axis trends N-S in the eastern part and WNW-ESE in the central and western parts, reflecting inherited Jurassic palaeogeography and faulting (Speranza, 2003; Adamoli et al., 2012; Cardello and Doglioni, 2015). The range is bounded on its south side by a 30 km long segmented normal fault system (the Campo Imperatore fault system; Galadini and Messina, 2004). The north side of the massif consists of approximately 2000 m high cliffs, exposing multiple stacked folds and thrusts in thick carbonate successions (Ghisetti, 1987; Ghisetti and Vezzani, 1991; Vezzani et al., 2010). Thrusting in the Gran Sasso area propagated from west to east from the Miocene-Pliocene, with increased deformation intensity on deeper thrusts (Ghisetti, 1987). Transport was towards the north-east (Ghisetti and Vezzani, 1991), accommodated by slip along the E-W trending thrusts on the north side of the range and increasing towards the east (Ghisetti and Vezzani, 1991; Adamoli et al., 2012). Thrusting may have rotated pre-existing Mesozoic normal faults to younger-on-older low-angle summit faults (Pace et al., 2014; Pace and Calamita, 2015).

Thrusting at ~7 Ma was followed by back-arc extension, which propagated eastward from the Early to Middle Pleistocene onward (Ghisetti and Vezzani, 2002). The frontal margin of active extension is demarcated by the Gran Sasso range (D'Agostino et al., 1998; Ghisetti and Vezzani, 1999; Galadini and Messina, 2004).

2.2. Fornaca Tectonic Window

The study area is localized in the Gran Sasso Range and encompasses the “Fornaca Tectonic Window” (FTW), situated in the Fornaca Valley on the northern border of Campo Imperatore plain (Fig. 1a). Campo Imperatore is an intra-mountain basin (1700–1900 m) bordered by Quaternary active seismogenic faults (Galli, 2002; Demurtas et al., 2016). WNW-ESE trending ridges, bounded by these normal faults, contain the peaks of the eastern Gran Sasso Massif; including Mt. Prena, Mt. Camicia, and Mt. Brancastello on the north side (Fig. 1a).

The Fornaca Valley is a lightly-vegetated valley between Monte Prena and Monte Camicia with two thrust faults exposed within it. On the upper east side of the valley, an upper out-of-sequence thrust fault (Fig. 1c) is noted for its emplacement of younger rocks upon older (Ghisetti, 1987; D'Agostino et al., 1998). At the base of the valley, the Vado di Ferruccio Thrust Fault (VFTF) has been exposed by erosion to form the FTW (Fig. 1a and c). The VFTF places Upper Triassic bituminous dolostone (*Dolomie Bituminose*) upon Middle Jurassic carbonate grainstones (*Corniola*) and marls (*Verde Ammonitico*) (Fig. 1c and d). Several normal faults cut the VFTF in the tectonic window (Fig. 2), offsetting it by 10–30 m in places (Ghisetti and Vezzani, 1986).

Most work in the Fornaca Valley has been focused on the kinematics of the out-of-sequence thrust (T_1 *sensu* Ghisetti, 1987, Fig. 1c) near the summit of Monte Camicia (Ghisetti and Vezzani, 1991; D'Agostino et al., 1998; Adamoli et al., 2012; Pace et al., 2014; Pace and Calamita, 2015). The footwall of this thrust is composed of crystalline and bituminous dolostone (Fig. 1d) sitting in large-scale recumbent chevron folds trending E-W and verging north (Ghisetti and Vezzani, 1986, 1991; Ghisetti, 1987). These folded dolostones represent the hanging wall of the VFTF (T_7 in Ghisetti, 1987, Fig. 1c) within a large duplex structure; similar folding has also affected the footwall Jurassic carbonates (Fig. 1c), attributed to the exploitation of bedding and mechanically weaker layers during thrusting (Ghisetti and Vezzani, 1986, 1991). The overriding thrust fault (T_1 in Ghisetti, 1987) is steeper than the VFTF and truncates it near the base of the valley (Fig. 1c). Thrust plane-bedding cut-offs indicate a transport direction of N020, temporally constrained by synorogenic sedimentation in the Laga and Cellino basins and the Adriatic foredeep as Messinian-early Pliocene (Ghisetti and Vezzani, 1991).

Detailed field description of the fabrics and structures of the thrust stack, the VFTF in particular, was undertaken by Ghisetti (1987). The VFTF principal slip surface was characterised as having large-scale undulations (10s–100 s m) associated with thrust duplexes, upon an

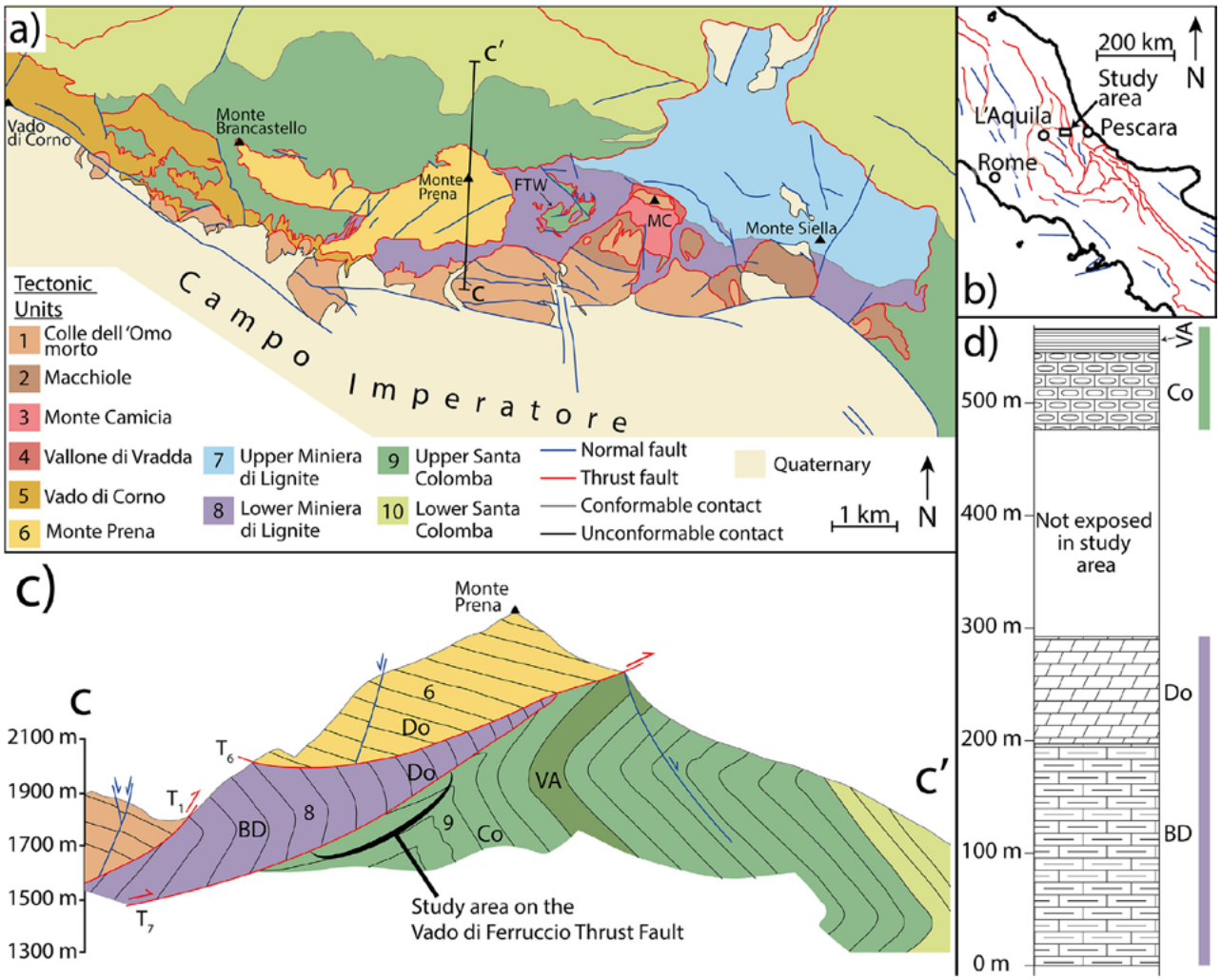


Fig. 1. Maps, cross section, and stratigraphic column of the study area. (a) Map showing the tectonic units and structural setting of the eastern Gran Sasso range; FTW = Fornaca Tectonic Window, MC = Monte Camicia. Modified after Ghisetti and Vezzani (1986). (b) Map of central Italy showing main faults (red = thrust, blue = normal) and location of study area and map (a) (black rectangle). Adapted from Vezzani et al. (2010). (c) Cross section c-c' (see figure section a) highlighting the structural setting at Monte Prena, adjacent to the Fornaca Tectonic Window. Line of section shown in (a), adapted from Ghisetti and Vezzani (1986). (d) Stratigraphic column showing lithological units present in thrust sheets adjacent to the Vado di Ferruccio thrust (VA = Verde Ammonitico, Co = Corniola, Do = Dolomia Principale, BD = Dolomie Bituminose). Coloured bars indicate the lithologies present within the Miniera di Lignite (purple) and Santa Colomba (green) thrust sheets. After (Ghisetti, 1987; Adamoli et al., 1990). (For interpretation of the references to colour in this figure legend, the reader is referred to the Web version of this article.)

overall convex-up geometry. Within duplexes, dolomitic lenses from the hanging wall show abundant cataclastic textures, whereas pure to marly limestone lenses from the footwall show evidence of both cataclasis and pressure solution. Deformation structures observed within these duplexes are stated to be the result of localized shear between contrasting lithologies. Foliated fault rocks, mainly developed within marly limestones, contain S-C fabrics (e.g. Koopman, 1983) and Riedel shear surfaces (e.g. Tchalenko, 1970; Davis et al., 2000; Katz et al., 2004) associated with cataclasite microlithons. The S surfaces rotate and converge into thrust-parallel microshears, intersecting with C microshear surfaces at angles of 30–40°. Microshears are thought to accommodate slip of microlithons, which acted as a rigid obstruction during deformation in the core of the VFTF. Deformation was concentrated in the marly portions of the core of the VFTF, where pressure solution and grain crushing were dominant (e.g. Fig. 11 of Ghisetti, 1987). At the thin section scale, the occurrence of fine grained brown material is attributed to organic carbon within the *Dolomie Bituminose*. Pull-apart regions show syn-tectonic fibrous calcite growth and veins, which contain sparry calcite, are deformed where they intersect microshears at a high angle. Such features suggest early vein formation prior to deformation along with the host rock. This study builds on this previous work by Ghisetti (1987); deformation mechanisms in the thrust are discerned and greater consideration is given to the later extensional deformation phase in the area.

2.3. Lithologies adjacent to the VFTF

Deposition of the units lying in the hanging wall of the VFTF began in the Late Triassic with widespread transgression due to rifting associated with the opening of the Neotethys ocean (Adamoli et al., 1990; Ciarapica, 2007). Approximately 180 m of organic-rich, planar-laminated dolostones (*Dolomie Bituminose*) containing anhydrite and chert nodules are exposed in the Fornaca Valley (Adamoli et al., 1990) (Fig. 1d). Up to 1.5 km total thickness of dolostones formed within

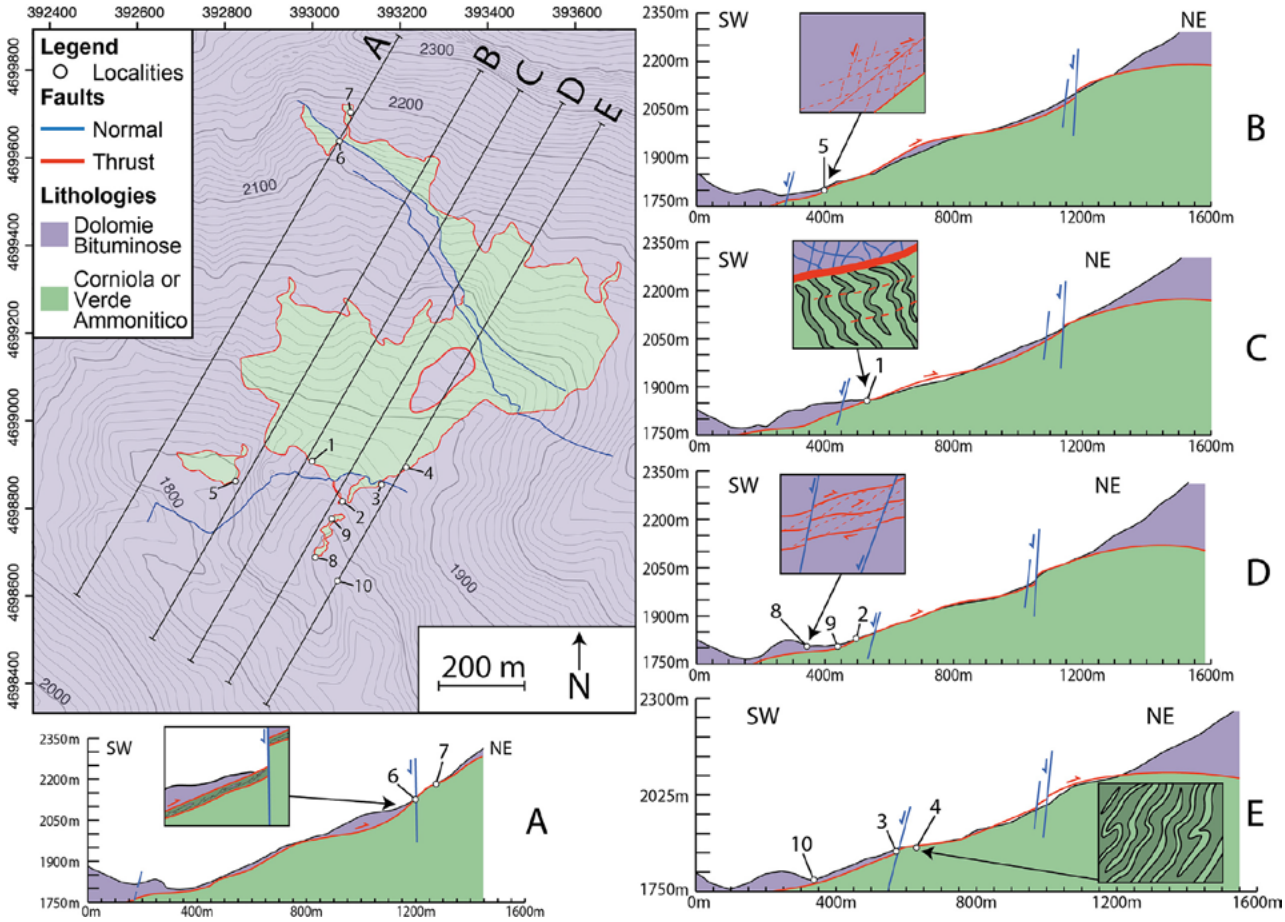


Fig. 2. Local geometry of the VFTF. Map, modified after Ghisetti and Vezzani (1986), showing the outcrop of the Fornaca Tectonic Window, and associated cross-sections (A–E) showing topography and orientation of thrust and normal faulting across the area. Schematic local sketches illustrate textural variations seen at different localities across the area. For each section the schematic sketch shows; (A) normal faulting of the thrust core by large later normal faults, (B) YPR localised shear surfaces in the hangingwall associated with compressional thrusting, (C) shear folding of S-verging isoclinal folding in the footwall beneath the fault core and extensional shattering of the hangingwall adjacent to the thrust, (D) normal faulting cutting mesoscopic S-C fabrics formed in the hangingwall, (E) N-verging isoclinal folding of marl-rich lithologies. Within local schematic sketches, darker colour shades illustrate more marl-rich lithologies, red lines represent compressional structures, and blue lines represent extensional structures. Map grid is in UTM 33T. (For interpretation of the references to colour in this figure legend, the reader is referred to the Web version of this article.)

localised, shallow basins during the early stages of the Late Triassic marine transgression (Centamore et al., 2002; Cardello and Doglioni, 2015). The basins were poorly interconnected and consequently euxinic (Adamoli et al., 1990; Barattolo and Bigozzi, 1996; Cardello and Doglioni, 2015). This preserved organic matter and limited faunal bioturbation, forming an organic carbon-rich planar carbonate in the lower thickness (Adamoli et al., 1990; Ciarapica, 2007).

The *Dolomie Bituminose* grades up into a more massive Early Jurassic dolostone (*Dolomia Principale*) (Fig. 1d), associated with shallow-water marginal facies before lagoonal facies form poorly bedded grainstone lenses in the upper third of the sequence (Adamoli et al., 1990; Barattolo and Bigozzi, 1996). The *Dolomia Principale* formation is at least 600 m thick (Fig. 1c) at Monte Prena (Barattolo and Bigozzi, 1996) and contains very low organic content (Ciarapica, 2007). The gradual transition between the *Dolomie Bituminose* and the *Dolomia Principale* is visible in the hanging wall as one moves north along the thrust fault in the FTW.

Formations in the footwall of the thrust are described as pelagic with varying degrees of input from a strongly detrital supply. Micritic cherty limestones are interbedded with marly layers 0.5–1 m thick in the Middle Jurassic-age *Corniola*, where brachiopods and ammonites are reported (Ghisetti and Vezzani, 1986; Bertinelli et al., 2004). Lithologies gradually become more marl-rich in the overlying Middle-Late Jurassic *Verde Ammonitico* (Ghisetti, 1987) (Fig. 1d). The Cretaceous to Oligocene age carbonates in the succession correspond to the base of the slope connected to the adjacent Lazio-Abruzzi carbonate platform (Van Konijnenburg et al., 1999).

3. Methods

Orthorectified photographs from the 2009 20 cm resolution aerial survey (available at www.regione.abruzzo.it/xcartografia) were used, in conjunction with elevation data, field photographs, field sketches, and previously published geological maps (Ghisetti and Vezzani, 1986), to trace major tectonic surface outcrops in the area using ArcGIS 10.3 software. Elevation data was used from the 10 m cell grid size TINITALY/01 digital elevation model (Tarquini et al., 2007, 2012).

Ten localities within the FTW were selected for the systematic measurement of orientations and lineations (where present) of faults, veins, fractures, and folds. Orientation measurements of features associated with exposures of normal faults in the hanging wall of the VFTF (fault plane and lineation, exposure orientation, marker orientation)

were used to calculate absolute displacement in the lineation orientation. Localities were mostly situated in the southern half of the tectonic window since previous work showed abundant structural data collection in the northern part of the area (Ghisetti and Vezzani, 1986) and because outcrop exposure was better due to stream incisions. Measurements were plotted onto stereonets using Stereonet 9 (Allmendinger et al., 2011; Cardozo and Allmendinger, 2013).

Thirty oriented samples of fault rocks were collected of structurally significant features within the core of the VFTF. To investigate the effect of fault geometry, sampling of the fault core was performed at localities where the VFTF showed different dip angle. Ten polished thin sections, cut parallel to the slip direction and orthogonal to the foliation of each sample, were produced at the School of Earth and Environmental Science, The University of Manchester. Some delicate samples were set in thermosetting resin to maintain the internal structure during sample preparation. Thin sections were scanned at high resolution to provide a reference image prior to any micro-analytical work.

Optical microscopy, using both transmitted and reflected light, was used to determine the cross-cutting relationships visible at the thin section scale, and to identify areas suitable for further analysis using scanning electron microscopy and micro-Raman spectroscopy. Transmitted light photomicrographs were, when necessary, stitched together using Microsoft ICE (http://research.microsoft.com/enus/um/redmond/groups/ivm/ICE/). Micro-Raman spectroscopy was performed with a 532-nm green laser on untreated thin sections using a Horiba XploRA Microscope Raman System at the Nanoscale Imaging and Analysis Facility for Environmental Materials (NIAFEM) at the University of Manchester. Spectra obtained from this operation were adaptively baseline-corrected using Spectragryph software (www.effemm2.de/spectragryph/) and the resultant data was compared to spectra of known minerals from multiple databases (including the Bio-Rad Raman Spectral Database and the Romanian Database of Raman Spectroscopy) to qualitatively determine mineralogy and nature of any amorphous material in the samples. Thin sections of two samples from each thrust fault core locality and three from the hanging wall adjacent to the fault core were selected for analysis using electron microscopy. Backscattered electron images and energy-dispersed spectra were collected with either a FEI Quanta 650 Electron Microscope or Philips/FEI XL30 Field Emission Gun Environmental Scanning Electron Microscope, both at NIAFEM, in the School of Earth and Environmental Science at The University of Manchester. Backscattered electron images and energy-dispersed spectra were acquired at 15 KeV and standard spot size.

4. Field observations of the Vado di Ferruccio Thrust Fault

Thrust zone features vary throughout the study area but are dominantly associated with faulting in the dolomitic hanging wall and folding with minor faulting in the mixed carbonate footwall. The main features are presented here prior to description and data relating to structural features in the hanging wall (HW), footwall (FW) and fault core throughout the FTW. Field descriptions and structural data from more than ten localities are presented to illustrate the variation in structure within the tectonic window (Figs. 2 and 3).

4.1. The Fornaca tectonic window

The VFTF dip angle varies over tens of metres throughout the FTW from 11° to 50°, significantly steepening in the north-west of the area despite a generally convex-up geometry elsewhere in the tectonic window (Fig. 2). Strike also varies locally between 090 and 140 (strike and dip data are given from N azimuth), trending E-W in the north and NW-SE in the south (Fig. 3). Near vertical normal faults offsetting the core of the VFTF by 5–15 m strike NW-SE (Fig. 2). Normal fault surfaces are sharp with clay-smear defining sub-vertical lineations (Fig. 3, locality 6).

4.2. Hanging wall block

Fault slip surfaces are abundant in the hangingwall with variable orientation, shear sense, and surface texture (Figs. 3, 4a and 4b). Reverse faults, subsidiary to the principal thrust slip surface, typically form at low angle and rarely form lineations on slip surfaces (Figs. 2 and 3, localities 2, 4, 5, 8a, 8b, 9, 10). Normal faults form at high angle, often with well-defined lineations on surfaces cutting low-angle slip surfaces (Figs. 2 and 3). Folding in the hangingwall is rarely exposed, though where it is, heavily-faulted beds of *Dolomie Bituminose* form metre-scale open (interlimb angle ~100°) folds with gently west-plunging axes and N-S striking profile planes (Fig. 3, locality 10).

Faults in the dolomitic hangingwall often form in systematic orientations with similarly-oriented surfaces showing consistent shear sense (Fig. 3, localities 2, 6, 8b, 10). Thrust-parallel surfaces are common throughout the area (Fig. 3, localities 2, 8a, 10), often coexisting alongside synthetic P and R surfaces. These surfaces often form mesoscopic fabrics whereby bitumen-poor dolostone is faulted into lenticular blocks by a shallow (< 20°) and steeper (45–80°) set of S-dipping shear surfaces, often acute towards the NE (Fig. 3, locality 8–1 & 5). Steeply-dipping (60–80°) normal shear surfaces cut both synthetic reverse and thrust parallel shear surfaces (Fig. 5). Lineations on these SW-dipping normal surfaces plunge steeply (60–80°) to the south (Fig. 5), indicating dip-slip movement. Where the hangingwall is more bituminous, slip has occurred along the bedding in both normal and reverse senses (Fig. 3, localities 4, 8b).

Bitumen-poor dolostones in the hanging wall are pervasively shattered up to ten meters from the thrust fault (Fig. 4a and b). These heavily fractured dolostones are cut by a dense network of highly-reflective mirror fault surfaces with dominant dip-slip kinematics (Fig. 3, locality 1). Bed-parallel slip was not observed. Fault orientations are widely scattered, though more SE-dipping surfaces were measured (Fig. 3, locality 1). Lineations on mirror surface faults are defined by smeared bitumen streaks and aligned truncated clasts parallel to slip direction (Fig. 6c and d). Lineations are oriented within a high-angle SW-striking band (Fig. 3, locality 1). Fault displacements up to a maximum of 1.2 m were constrained, exploiting the occurrence of displaced markers (e.g. rock laminations) and fault cross-cutting relations. These normal faults have a lateral continuity of few meters, are compartmentalized within the hangingwall block of the VFTF, and terminate upon a sharp principal slipping surface (PSS) bordering the top of the thrust fault core (Fig. 6a and b).

4.3. Footwall block

Steeply-dipping isoclinal folding in the FW is continuous along strike across the tectonic window. Exposures of folds, grouped by lithology, are described here in terms of geometry and association with faulting.

Folding in marl-rich lithologies is defined by thin (< 15 cm) beds of grainstone within a more abundant marl (Fig. 7a). Folding is isoclinal, N-verging, and cut by a handful of small-offset (< 15 cm) minor faults. Due to the isoclinal nature of the folding, bedding dips predominantly south at approximately 50°. The fold axes plunge gently west, defining (together with poles to bedding) a N-S profile plane across E-striking folds (Fig. 7a).

Isoclinal folding of more thickly-bedded (~1 m) grainstone-rich lithologies with less marl is cut by low-angle south-dipping reverse faults, sub-perpendicular to bedding (Fig. 7b). Isoclinal folding is defined by steeply north-dipping bedding and verges to the south. Where minor faults have no visible offset, minor recumbent shear folding of the isoclinal folds has occurred adjacent to thrust-parallel reverse faults, producing sinuously-undulating isoclinal folds of interbedded grainstones and marls near localised reverse fault surfaces (Fig. 7b). Recumbent folds have axial planes subparallel to minor fault surfaces. In the upper part of the exposure, low-angle reverse faults have offsets up

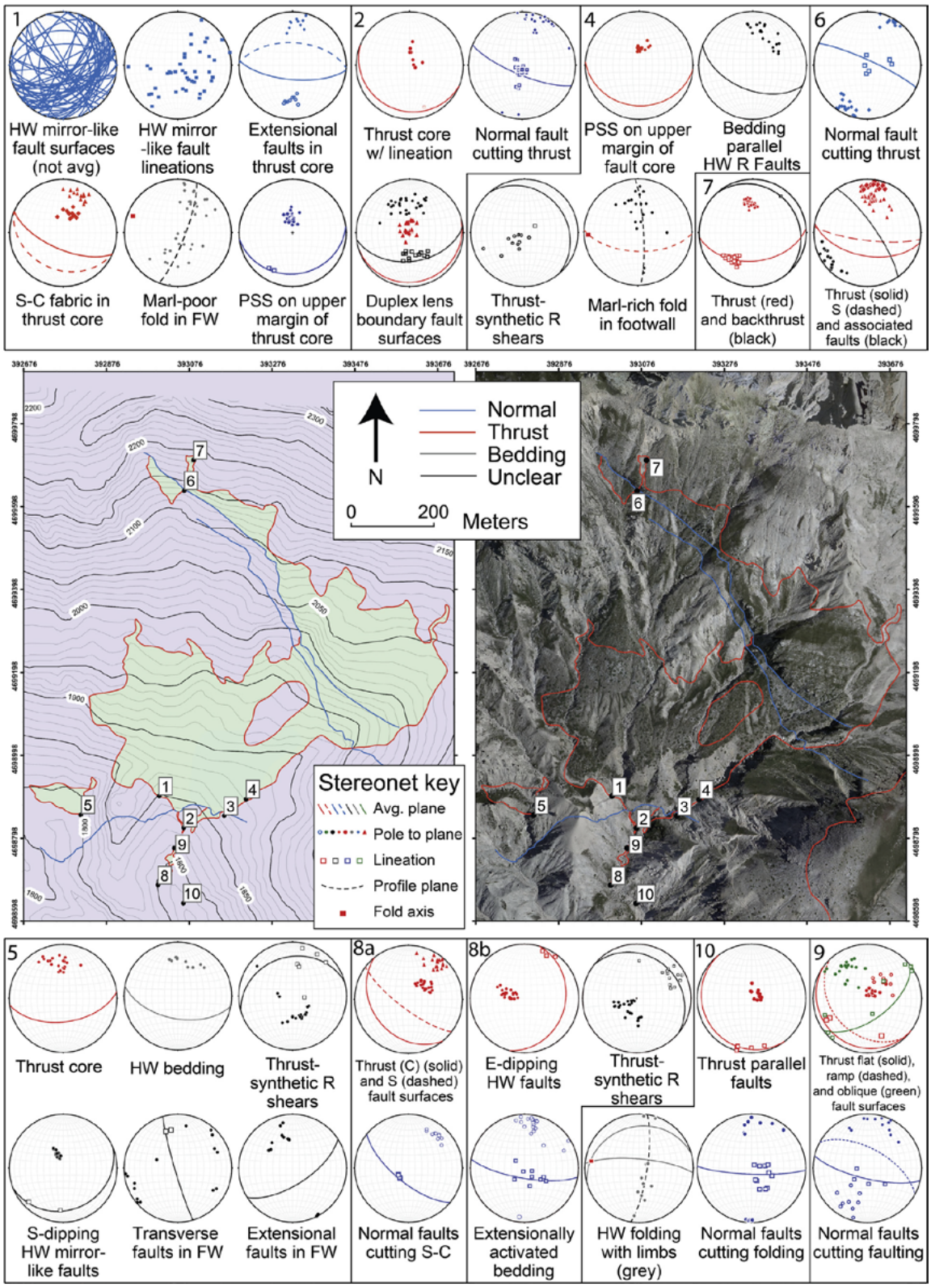


Fig. 3. Structural data summary. Maps and accompanying stereonets showing all of the 763 structural data systematically collected around the Fornaca tectonic window at each locality. HW = hangingwall, FW = footwall, PSS = principal slip surface, R faults = Riedel faults. Measurements are presented as poles, average planes and lineations. Red data correspond to compressional structures, blue data correspond to extensional structures, grey data correspond to bedding, black dashed lines represent profile planes of folds while black solid data represent data with no obvious shear sense, green data represent oblique structures. (For interpretation of the references to colour in this figure legend, the reader is referred to the Web version of this article.)

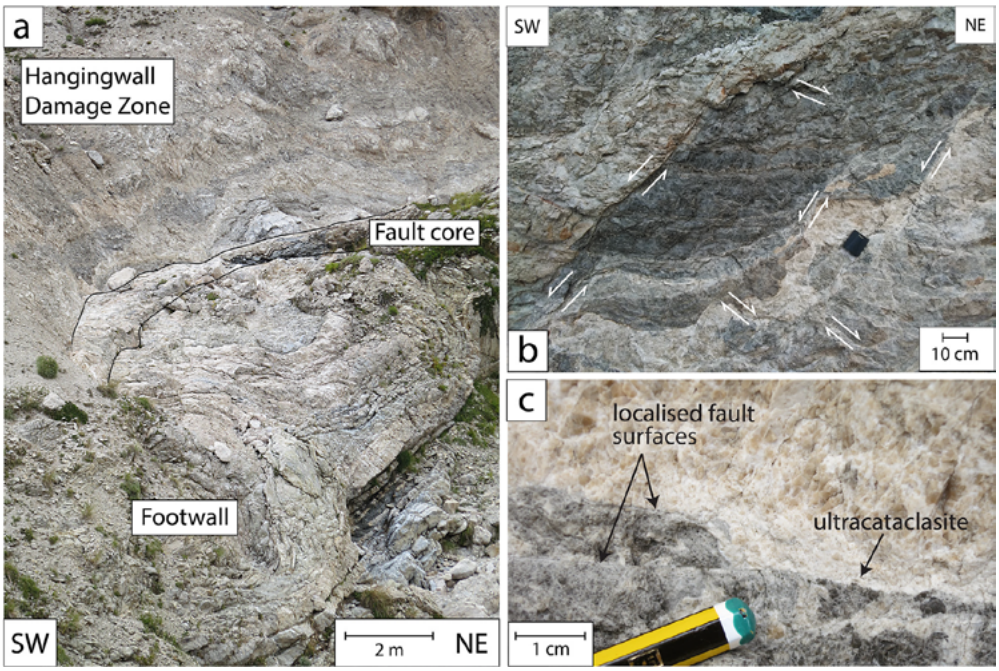


Fig. 4. Fault zone exposure and hangingwall damage zone character. Individual photos show: (a) exposure of the VFTF at the main locality mirror-like surfaces were observed, black lines mark the upper and lower boundary of the thrust core, (b) nature of damage in the hangingwall, with traces of hangingwall mirror-like fault surfaces (black) on a face oriented 145/65 (azimuth/dip), (c) sub-centimetre detail of a mirror-surface bordered by ultracataclasite. All photos were taken at locality 1 (0393004, 4698901).

to 3 m and form well-developed (~20 cm thick) fault cores.

Strongly refolded isoclinal folding is exposed just beneath the thrust surface (Fig. 7c). Limbs of the recumbent fold dip moderately (~45°) to the SW and gently (20–30°) to the NE, the hinge plunges to the NW. The core of the main thrust fault, which dips 25° to the S, truncates the fold limbs (Fig. 7c). Marl-rich beds within refolded folds have been incorporated into marl-rich fault core above. The profile surface of the fold trends on average NE-SW, though poles to bedding are spread as

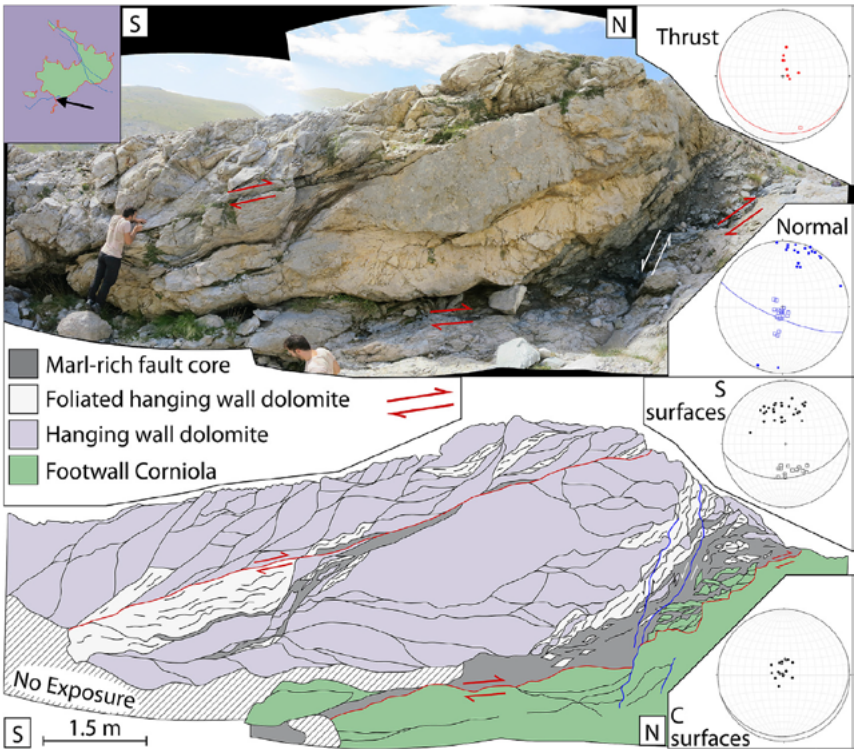


Fig. 5. Photograph with accompanying sketch of a meso-scale thrust duplex cut hosting an S-C fabric cut by a normal fault. The normal fault cuts hangingwall dolomite and the fault core at locality 2 (0393063, 4698824). Stereonets show: poles to thrust surface (n = 8, red circles), average thrust surface (red great circle), lineation found upon thrust surface (n = 1, hollow red square); poles to normal fault surfaces (n = 20, blue circles), average normal fault surface (blue great circle), lineations upon normal fault surfaces (n = 18, hollow blue squares); poles to S surfaces (n = 29, black circles), average S surface fault (black great circle), lineations on S surfaces (n = 13, hollow black squares); poles to C surfaces (n = 19, black circles), average C surface (black great circle). Arrow on inset map shows location photograph was taken (see Fig. 2). (For interpretation of the references to colour in this figure legend, the reader is referred to the Web version of this article.)

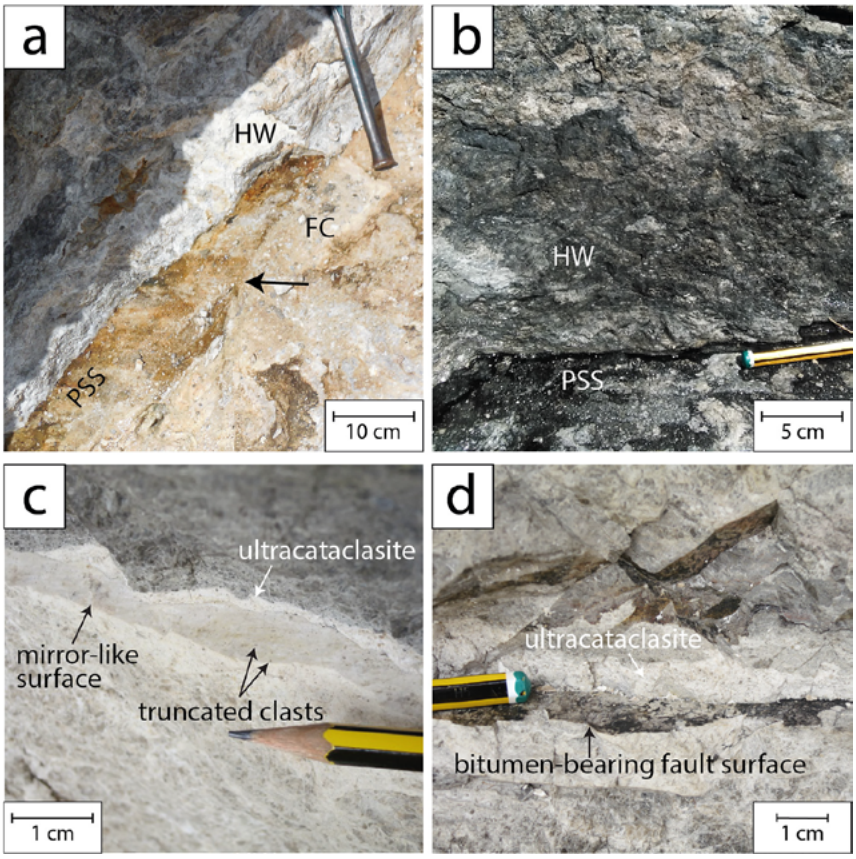


Fig. 6. Morphology of slip surfaces. Photos show the principal slip surface in bitumen-poor (a) and bitumen-rich dolomite (b) and mirror surfaces in the hanging wall in bitumen-poor (c) and bitumen-rich dolomite (d). Hanging wall (HW), fault core (FC), and principal slip surface (PSS) are labelled on photographs. Black arrow in (a) is parallel to the on-plane lineation, a lineation is not present in (b). Pencil is parallel to lineation on HW mirror surface in (c). Photos were taken at localities 1 (a & c; 0393004, 4698901), 4 (b; 0393214, 4698893), and 5 (d; 0392815, 4698855).

the fold hinge varies locally in orientation (Fig. 7c).

4.4. Fault core

The fault core of the VFTF is well developed throughout a variety of lithologies, maintaining a thickness of 0.5–2 m throughout the area (Fig. 8). Occasionally, a sharp ultracataclasite-bearing PSS on the upper surface of the fault core forms a measurable lineation, with clay smearing or alignment of grains (Fig. 6a and b). Structure within the fault core varies throughout the area but generally consists of foliated cataclasite with lenticular sheared lithons within a phyllosilicate-defined S-C fabric. Larger lithons often contain subvertical veins perpendicular to thrust plane orientation. Angles between S and C planes are around 30° (Fig. 3, locality 1). Some minor extensional surfaces cut the fabric at high angles, oblique to the thrust (Fig. 3, locality 1), these surfaces do not cut the PSS.

Fault core lithology and fabric varies significantly throughout the area (Fig. 8); bitumen is more common in the south of the area and fabrics become increasingly clast-dominated in the north of the area (Locality locations indicated in Figs. 2 and 3). Foliated cataclasites are categorised as marly lithologies (blue on Fig. 8) , S-C fabrics within these encompass sheared clasts up to 20 cm long. Relative proportions of marl and clasts varies from marl-dominated to clast-dominated unsystematically between localities. Locally marl-enriched (up to 100%; Fig. 8) areas are associated with m-scale duplexes which occur at localised irregularities in thrust orientation, often associated with later normal faults (Fig. 5).

Fractured lithologies (green on Fig. 8) do not contain calcite veins characteristic of the veined lithologies also described below. Fractures occur commonly as part of the hangingwall damage zone above the PSS but are more common in the fault core where *Dolomie Bituminose* is present in moderate to significant amounts (< 80%). Veined fault rocks (yellow on Fig. 8) appear brown in the field, with voids filled in with calcite. Veined fault rocks occur in abundance in the upper part of the fault core (< 90%), often adjacent to the PSS and hanging wall dolomite. Bituminous fault rocks (purple on Fig. 8) are so called due to the dark material present within. This material is attributed to amorphous carbon within the *Dolomie Bituminose*. Dark material is often associated with marl or cataclasite in the upper part of the fault core in small to moderate amounts (< 35%).

5. Microstructure and mineralogy of the Vado di Ferruccio Thrust Fault

Microstructural observations from the thrust fault core are presented for clay-rich and clay-poor samples. Within each group of samples, features are often similar. The structure and mineralogy of each type of fault core “lithology” are described. A summary table of observations and interpretations is provided at the end of the section (Table 1).

5.1. Microstructure and mineralogy of clay-rich fault core rocks

Clay-rich fault rocks are characterized by a heterogeneous assemblage with domains strongly affected by pressure solution and local clay enrichment embedding other more cataclastic domains (Fig. 9a–d). R-type shears consistent with thrusting are widespread within these fault rocks and normally dissect both domains (Fig. 9b–d).

Cataclasite-dominated regions are composed of either homogeneous calcite or dolomite (Fig. 9f and g), with occasional quartz grains. Sparse, immature, sub-horizontal pressure solution seams cut a very fine ultracataclastic (grain size < 100 μm) dolomitic matrix with gently

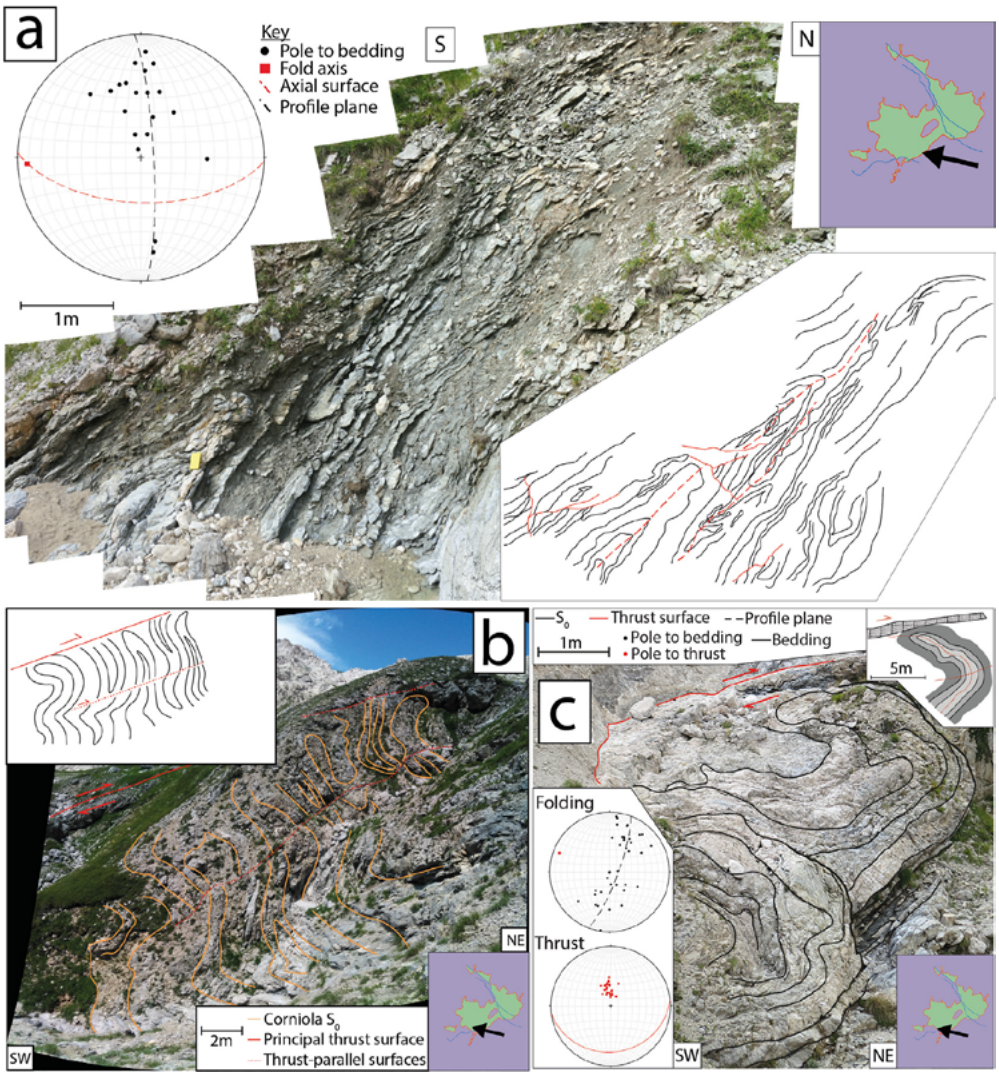


Fig. 7. Character of folding of the interbedded marl-grainstone Corniola in the footwall. Marl rich lithologies in the east (a) form isoclinal folds with S-dipping grainstone bed limbs within a marl-rich matrix. Beneath the fault core (b) isoclinally-folded grainstone beds are cut by thrust parallel reverse faults with minor folding adjacent to fault surfaces. Adjacent to the fault core (c) isoclinal folds in grainstone-rich beds are refolded around an axial plane oriented subparallel to the main thrust. Photos were taken at localities 1 (b & c; 0393004, 4698901), and 4 (a; 0393214, 4698893).

(15°) south-dipping surfaces (Fig. 9d). Grains within fine cataclastic lenses are angular and affected by intense fracturing. Sub-vertical calcite veins up to 150 μm wide cut through the cataclastic lenses (Fig. 9d, g, h & i) perpendicular to pressure solution seams, which often truncate them (Fig. 9h and i).

Pressure solution-rich regions are up to 5 mm thick and mainly consist of foliated clays with sheared clasts of cataclastic material up to 1 mm in size. Pressure solution seams contain a mixture of iron oxides, amorphous carbon (Fig. 9e), and clays. Clays occur in localised seams along mineralogical contrasts adjacent to grains and veins. Two sets of veins can be discerned within pressure solution-rich regions dipping NE and SW, respectively. NE-dipping veins are up to 80 μm wide and are truncated by thrust parallel shear surfaces, SW-dipping veins are up to 30 μm wide and are continuous through these microshear surfaces (Fig. 9h).

R-type shear surfaces dip north at 40–60°, offsetting cataclastic and pressure solution-dominated domains by up to 1 mm (Fig. 9b and c). These shear surfaces are most dominant at the top of the fault core, within five centimetres of the PSS on the fault core's upper boundary (Fig. 9a). Further down into the core they are generally less developed. Significant amounts of clay and oxide rich material have developed upon the R-type shear surfaces, truncating south-dipping veins (Fig. 9h and i). R-type shear surfaces converge with well-developed sub-horizontal pressure solution seams which cut across the whole fabric (Fig. 9b–d).

5.2. Microstructure and mineralogy of clay-poor fault core rocks

Clay-poor lithologies, sampled from sheared lithons within the thrust core, exhibit a diverse range of matrix types and deformation features. These features include veins, pull-apart structures, cataclastic fabrics, microfaults, and minor localised pressure solution (Table 1).

The mineralogy of clay-poor lithons is mostly homogenous calcite (Fig. 10a), though some dolomitic lithons are present. Matrix textures vary throughout clay-poor lithons; intact textures include crystalline twinned calcite encompassing recrystallised fossils (Fig. 10b) and peloidal grainstones, while some samples display significant cataclasis and microfaulting. At least three vein sets are present within the

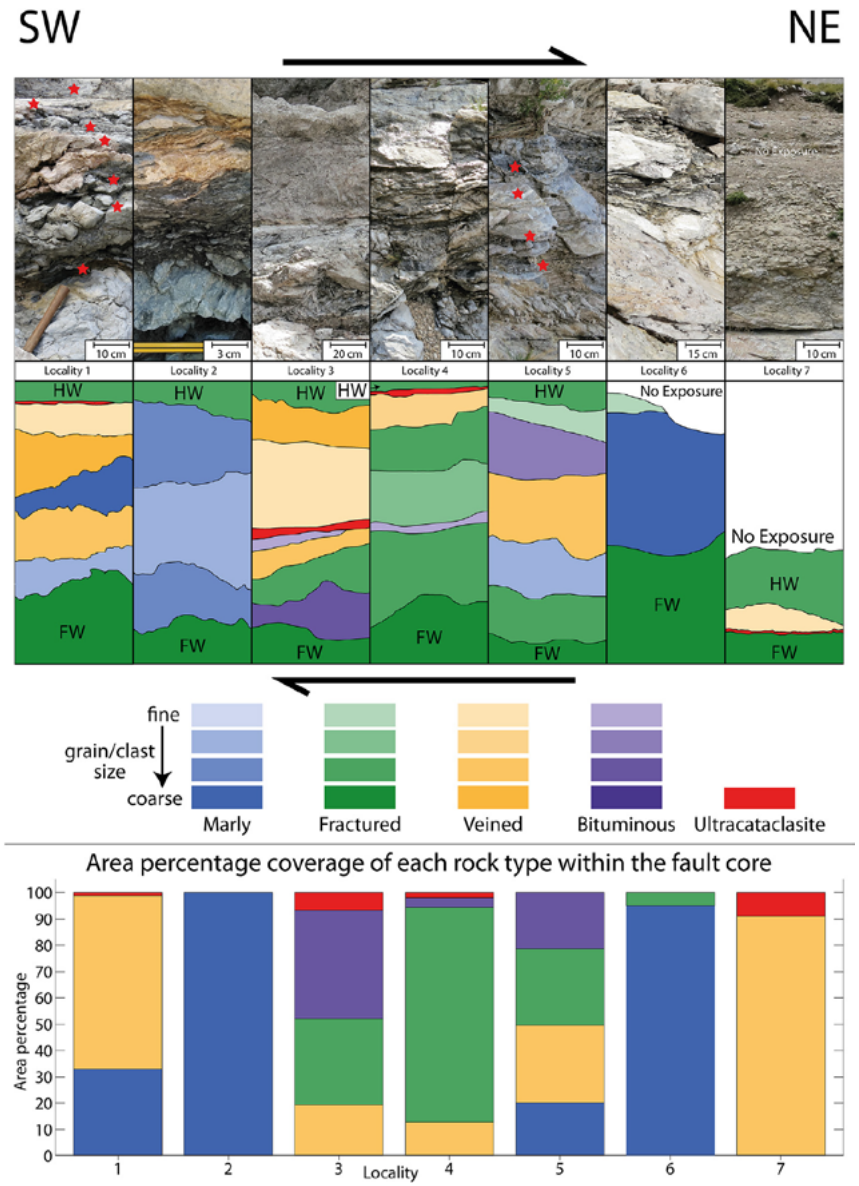


Fig. 8. Variation of fault core lithologies across the area. Red stars show locations samples were collected for microanalysis. Stacked bar graphs show percentage area coverage of thrust core lithologies derived from the sketches above without accounting for clast/grain size. Thrust shear sense is indicated by red arrows. Locations of localities can be seen in Fig. 2 and 3. (For interpretation of the references to colour in this figure legend, the reader is referred to the Web version of this article.)

lithons: a fine-grained low angle NE-dipping set up to 100 μm wide; a sub-vertical set up to 50 μm wide with a sub-horizontal opening direction and fine-grained crystals near the margins; and a coarse-grained vein set enveloping locally clay-rich pressure solution material within both sub-vertical and sub-horizontal veins (Fig. 10a). Within intact calcitic matrices, pull-apart structures up to 300 μm long and 100 μm wide are present.

Cataclastic textures are also present within clay-poor lithons. Sub-horizontal and ~30° north-dipping bands of finer (< 10 μm) material lie between heavily fractured grains of calcite and minor quartz up to 1 mm in size. Rarely, partially-intact cataclastic grains show wavy and complex twinning. Larger twins up to 15 μm wide contain smaller high angle twins (< 2 μm in size) and cross-cut thinner (< 3 μm in size), more numerous sub-horizontal twins. Some recrystallization of twins and the matrix is visible as fine grains. Calcite veins within cataclastic fabrics do not show twinning and tend to form normal to the PSS. Pressure solution seams up to 100 μm thick follow irregular paths through homogeneous clay-poor lithons, often coinciding with dolomitic bands or quartz grains and truncating some veins (Fig. 10a, c & d). Some veining has exploited these pressure solution seams; these veins correlate with dark sub-vertical veins visible in clay-poor lithons in the field (Fig. 10c and d).

6. Discussion

6.1. Thrusting on the VFTF

6.1.1. Deformation mechanisms within the thrust fault core

Dominant deformation mechanisms accommodating strain within the fault core are cataclasis, diffusive mass transfer in the form of pressure solution, and veining. The prevalent deformation mechanism varies throughout the thrust core between more localized fracturing

Table 1
Table of dominant microstructures, inferred deformation processes, and kinematics.

Fault rock type	Dominant microstructures	Inferred deformation processes	Inferred kinematics
Clay-enriched (Fig. 9)	Lenses of angular fractured grains of variable size	Initial cataclastic grain size reduction	Compressional thrusting
	Clay-rich pressure solution seams containing oxides	Diffusion-controlled pressure solution-mediated stable sliding aided by the presence of clays and fluids	Compressional thrusting
	Calcite veins with varying orientation and opening directions	Veining episodes due to cyclic fluid overpressure	Compressional thrusting and extensional stress regime
	Smaller sharp microfault surfaces cutting veins of certain orientation	Failure between veining episodes due to cyclic fluid overpressure	Compressional thrusting
	Larger north-dipping microfaults with clays and oxides upon fault surface offsetting clay-rich and cataclastic regions and cutting veins	Major rock failure prior to pressure solution upon fine-grained fault surfaces then reactivation of microfault surfaces as pressure solution seams by extensional stress	Failure during compressional thrusting, pressure solution during extensional stress regime
	Well-developed sub-horizontal pressure solution seams, cutting texture and intruding into most recent vein generations	Recent pressure solution, locally developed horizontal response to sub-vertical principal stresses	Extensional stress regime
Clay-poor (Fig. 10)	Multiple sets of cross-cutting veins offsetting each other (Fig. 10a)	Veining episodes due to fluid overpressure in variable strain environments forming veins of different orientations	Compressional thrusting and extensional reactivation
	Isolated pressure solution seams, often concurrent with quartz or dolomite grains within calcitic matrix (Fig. 10a,c)	Diffusion-controlled pressure solution, aided by diffusion upon polymineralic grain boundaries	Compressional thrusting and extensional stress regime
	Curved complex calcite twinning of variable degrees of intensity (Fig. 10b)	Irregular twinning due to texture-dependent stress within the fault core	Compressional thrusting and extensional stress regime
	Angular fractured grains of varied size cut by microfaults	Cataclastic grain size reduction and flow	Compressional thrusting
Hanging wall	Heavily fractured angular grains	Cataclasis in the hanging wall adjacent to the thrust surface	Compressional thrusting and hangingwall activation
	Clay-bearing microfault surfaces	Failure and possible minor pressure solution localised in dolomite over a prolonged period	Compressional thrusting and hangingwall activation
	Mirror fault surfaces (Fig. 6)	Velocity-weakening slip and thermal decomposition at high slip rate	Hangingwall activation

and veining in clay-poor crystalline carbonate lithons and more diffuse deformation within clay-dominated foliated cataclasites (cf. Ghisetti, 1987). This complexity arises from the mixing of hangingwall and footwall lithologies, highlighted by small-scale duplexes and sharp boundaries between distinctly-deforming domains and noted by Ghisetti (1987; Fig. 5). Fault rock microstructures are grouped and discussed based upon clay content, their microstructural attributes, and inferred active deformation mechanisms (see also Table 1).

The S-C fabrics within the fault core are defined by foliated cataclasites around sheared lithons. The S and C surfaces are acute towards the NNE, perpendicular to a vertical plane striking 024, implying thrust transport towards the NNE. This is similar to that discerned by Ghisetti (1987) from similar S-C fabrics on the VFTF. Within clay-poor fault core lithons, the dominant deformation mechanisms are cataclasis and veining. Lithons with homogenous fine-grained calcite preserve three vein generations cross-cutting the matrix (Fig. 10a). Multiple generations of veins with distinct orientations suggest multiple veining events under variable stress conditions occurred on the VFTF. Vertical veins (V2 on Fig. 10) cut NE-dipping veins (V1 on Fig. 10) and could be associated with either extensional (Sibson, 2000) or compressional deformation. Compression would cause vertical vein formation by increasing overburden as thrust sheets are emplaced on overlying thrust faults within the Gran Sasso thrust stack. Both sets of veins (NE-dipping and vertical) are cut by larger, more continuous veins with no distinct orientation (V3 on Fig. 10). Here, both NE-dipping and vertical veins (V1 and V2) are attributed to compression and larger, more continuous veins (V3) are attributed to extension due to their dissimilar structure and cross-cutting nature indicating more recent formation. Regardless of associated stress conditions, vein textures in clay-poor lithons suggest fluid circulation during discrete deformation phases formed distinct sets of veins.

In foliated fault core samples incorporating clays in moderate to rich amounts, strain accommodation is partitioned between cataclasis, frictional sliding upon clays or carbon-coated surfaces, and pressure solution. Enrichment of insoluble species within pressure solution seams (Figs. 9i and 10c) suggest diffusion-mediated pressure solution was prevalent (Bos and Spiers, 2001; Gratier et al., 2013b), aided by initial grain-size reduction by cataclasis. Incorporated and authigenic clays may have aided aseismic stable sliding, which accommodated the majority of slip. The R surfaces offsetting regions of pressure solution (Fig. 9b–d) are consistent with northward thrusting, suggesting cyclic pressure solution and cataclasis with veining during compression. Veining events are better preserved within the monomineralic matrix of clay-poor lithons (Fig. 10a) than in the clay-rich areas where heterogeneous mineralogy aided pressure-solution mediated slip within the fault core. Furthermore, recrystallized fossils alongside preserved vein sets (Fig. 10b) within lithons show that some lithons stayed intact during thrusting and cataclasis was not pervasive throughout the core.

Cataclasis during early deformation on the VFTF, overprinted throughout the fault core (Figs. 9 and 10), decreased porosity and would have trapped upwelling fluids (Storti et al., 2003; Billi, 2010). Incorporation of clays from the footwall marl into the fluid-rich fault core during subsequent frictional sliding would have accelerated the onset of pressure solution (Hadizadeh, 1994; Gratier et al., 2013a). Abundant pressure solution within the core (Fig. 9) led to the production of authigenic clays by diffusive mass transfer (Rutter, 1983; Viti et al., 2014) and aided frictional sliding on clays and carbon. This is one way in which regions of high strain positively feedback to concentrate deformation within the same regions of the fault core. Diffusive mass transfer could also achieve further porosity reduction within the fault core by the growth of authigenic clays perpendicular to fluid transport direction and decreased pore volume by grain tip removal (Rutter, 1983; Yasuhara et al., 2005). Reduced porosity may lead to overpressuring of fluids ($P_f > P_c$) forming north-dipping veins, though the localised and discontinuous nature of veining (Fig. 9h and i) suggests it is probably the result of extension perpendicular to the orientation of maximum compression defined by adjacent pressure solution seams (Hadizadeh, 1994).

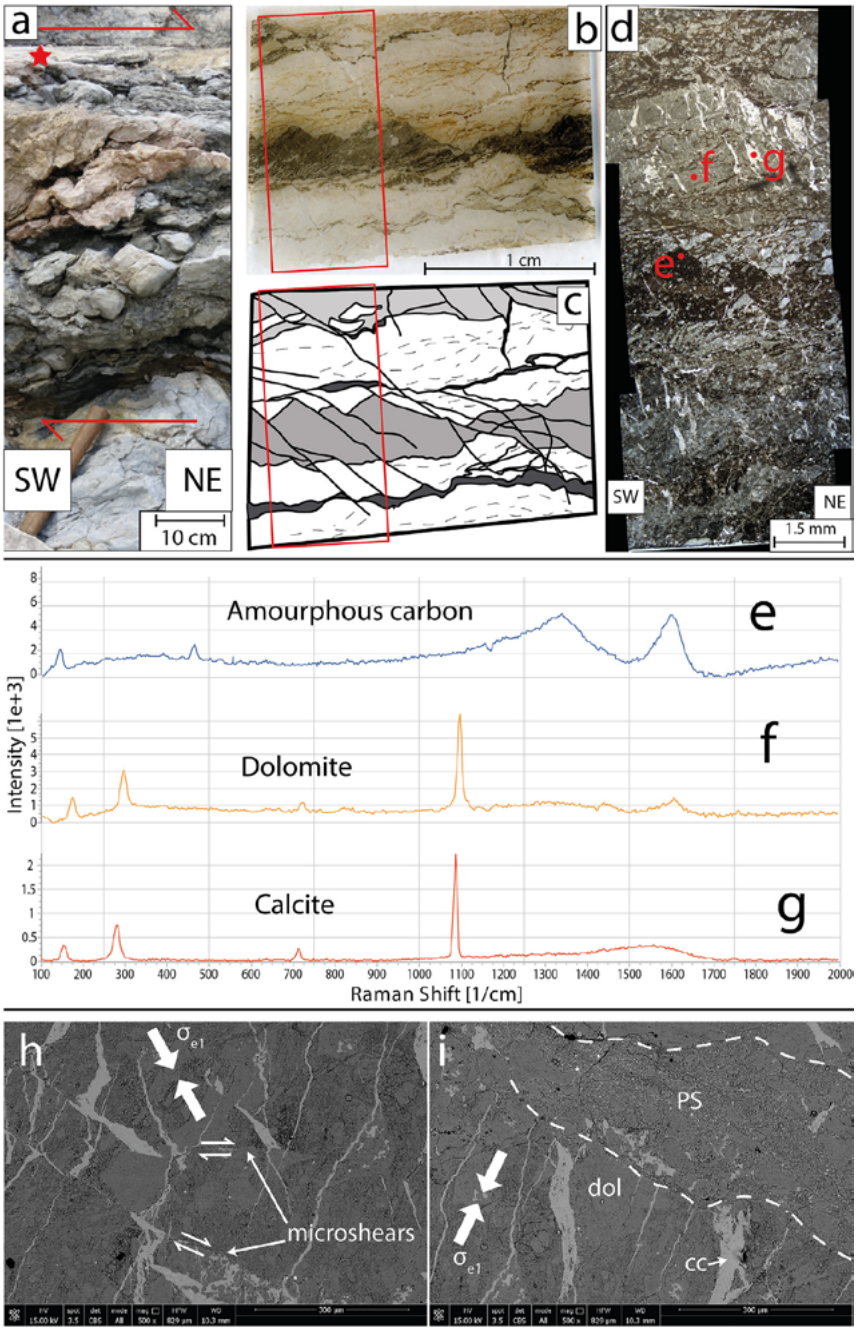


Fig. 9. Microstructural summary of clay-enriched fault core rocks. Sample location is shown as a red star upon a field photo of S-C tectonites in (a). Sense of shear in (a) is consistent throughout all images. High resolution scan (b) and associated sketch (c) show the location of stitched plane-polarised light optical photomicrograph (d) as red rectangle. Points (e,f,g) in (d) indicate locations of point raman spectroscopic analyses, the spectra for which are indicated below, labelled with the dominant species visible from raman shift peaks; amorphous carbon (e), dolomite (f), and calcite (g). SEM-BSE images (h & i) show interactions of calcite (cc) veining through a dolomite matrix (dol) hosting pressure solution seams (PS). Microshears in (h) almost always cut NE-dipping veins rather than SW dipping veins. SW-dipping veins in (i) are truncated by an R-shear, offsetting PS-rich areas of the matrix. This shear surface has been reactivated as a PS seam due to stress inversion. Sub-vertical arrows labelled σ_{e1} in parts (h) & (i) indicate orientation of effective maximum compressive stress within the fault core, assuming parallel vein orientation and perpendicular pressure solution seam formation. Sample was collected at Locality 1 (0393004, 4698901). (For interpretation of the references to colour in this figure legend, the reader is referred to the Web version of this article.)

Vein formation and sealing, possibly accompanied by healing at grain tips by mass transfer (e.g. Yasuhara et al., 2005), would strengthen the fault core. Shear of this re-strengthened fault core could cause a reversion to cataclastic deformation, forming the observed R surfaces which offset areas of pressure solution (Fig. 9b–d; Hadizadeh, 1994) and truncate north-dipping veins (Fig. 9i). Cataclasis of these regions of the fault core after veining could also result from localisation of strain away from sealed veins or by smearing and incorporation of weak phyllosilicate or carbon horizons during frictional sliding. Shear surfaces occur in orientations corresponding to steepened YPR shear planes (Tchalenko, 1970) and incorporate layers enriched in carbon liberated from carbonate by dissolution during pressure solution (Fig. 9e). Shearing on R surfaces was therefore aided by pressure solution (Gratier et al., 2013a) which continued to accommodate lesser amounts of slip. Microstructures upon shear surfaces appear consistent with weak-phase frictional sliding (Rutter et al., 2013; Tesei et al., 2013), perhaps of clays or carbon concentrated there during sliding.

Deformation of clay-enriched core lithologies represents a complex interaction of mechanisms, each altering fault core rheology based upon the properties of its products. This feedback is not seen within clay-poor fault core lithons, perhaps due to higher strain rates than be accommodated by pressure solution or more homogenous lithology limiting grain-boundary diffusion (Gratier et al., 2013b; Tesei et al., 2013). The abundance of weak clays and pressure solution seams within clay-enriched domains (Fig. 9d) implies that the thrust, at some stage probably early in its history, accommodated diffuse strain and gradual

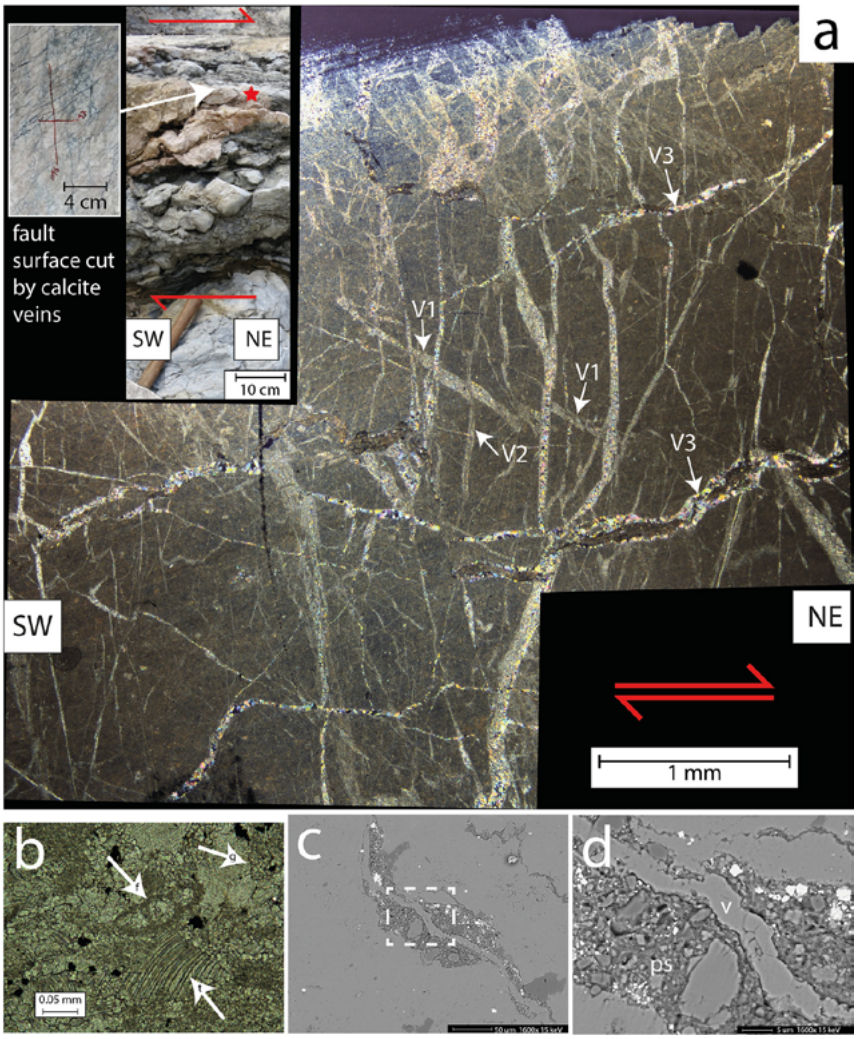


Fig. 10. Microstructural summary of clay-poor fault core lithologies. Stitched cross-polarised optical photomicrographs (a) show multiple mutually-offsetting filled hybrid fracture vein sets (V1-V3). Inset photographs show location of sample within fault core (red star) and field view of dark-coloured veins in (a). Optical photomicrograph (b) of the matrix of separate clay-poor fault core rocks shows recrystallised fossils (arrow labelled f), lobate grain boundaries (arrow labelled g), and curved twinning within calcite crystals (arrow labelled t). SEM-BSE images show isolated pressure solution (PS) seams within the homogenous calcite matrix (c), within which calcite veins occur (d). Samples were collected at Locality 1 (0393004, 4698901). (For interpretation of the references to colour in this figure legend, the reader is referred to the Web version of this article.)

slip by stable sliding (Gratier et al., 2011, 2013b; Tesei et al., 2014). The heterogeneity of structures associated with the VFTF indicates this likely changed during slip on the thrust, with transient periods of diffuse shear transitioning to slip on more localised surfaces seen throughout the fault core (Fig. 8). Cyclic veining and cataclasis indicate the build-up of fluid overpressures and fracturing followed by fault core re-strengthening (Fig. 11g and h); Caine et al., 1996; Yasuhara et al., 2005; Woodcock et al., 2007; Cardello and Mancktelow, 2015; Clemenzi et al., 2015).

6.1.2. Deformation mechanisms and fault kinematics during compression in the fault damage zone

6.1.2.1. Hangingwall. Compressional hangingwall faults corresponding to Y, R, P and rotated Riedel surfaces indicate a NE-ward thrust transport direction (Fig. 3, locality 4), though lineations upon planes to corroborate this are sparse. Riedel surfaces intersect at a line oriented 9.3/117.6 (plunge/trend), perpendicular to the transport direction. Mesoscopic S-C structures within HW dolomite are often acute to within ten degrees of the core-derived transport direction (034; Fig. 3, locality 8–1), but there is significant variability in this throughout the area (Fig. 3). Planes and lineations on faults forming the borders of dolomitic lenses within thrust duplexing indicate local variability in transport direction over tens of metres (Fig. 5). The rotation of strike of the principal thrust surface in the upper part of the Fornaca valley (Fig. 3, localities 6 & 7) is perhaps an indicator of more northward thrusting or local adjustment to accommodate more competent footwall lithologies (Ghisetti, 1987; Ghisetti and Vezzani, 1991).

6.1.2.2. Footwall. Complex refolded isoclinal folding in the footwall reflects lithological response to diffuse, then localised, shear. Initial compression led to the folding of footwall units to isoclinal geometry, with limbs dipping steeply to the S, implying significant shortening. As the VFTF developed, different lithologies within the footwall *Corniola* adjacent to the thrust responded in distinct styles (e.g. Lena et al., 2015). Marl-rich lithologies were subject to more diffuse shear strain, with dragging of the isoclinal fold limbs to the north and minor faulting. The axial planes of marl-rich folds have then progressively rotated towards the thrust fault orientation in relation to the gradual accommodation of shear strain within the fault core (Ramsay, 1980; Ghisetti, 1987).

Bouma sequences preserved within the *Corniola* beds comprise depositional clay-rich bands in their upper parts, which favoured bed-parallel slip (Bullock et al., 2014). Refolding of isoclinal folding is perpendicular to inferred transport direction and the fold axes varies locally, characteristic of shear folding (Ramsay, 1980; Ghisetti, 1987). Low-angle reverse shear surfaces emanate from the thrust and are less well-developed away from the thrust, indicating the main thrust core was the site of the majority of shear strain. Minor reverse faults may

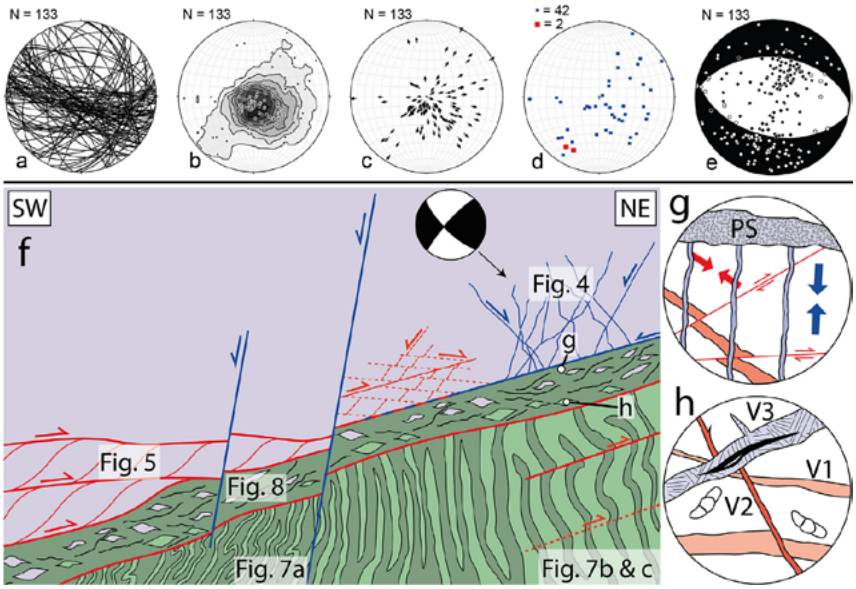


Fig. 11. Kinematics of mirror-like hangingwall normal faults and schematics of structures found in the thrust zone. Stereonets show the distribution of (a) mirror-like fault surfaces, (b) slip lineations on mirror-like fault surfaces (contoured after Kamb (1959), intervals of 2 and significance level of 3), (c) hanging wall transport directions, (d) mirror-surface fault lineations at locality one (blue) and fault core principal slip surface lineations at locality one (red), (e) focal mechanism derived from kinematic inversion of 133 mirror-like faults in the hangingwall damage zone of the VFTF (sensu Marrett and Allmendinger, 1990). All Stereonets are lower hemisphere equal area projections. Schematic sketches show mesoscale structures in the thrust zone (f) with reference to figure where feature is shown, and microscale features in clay-enriched (g) and clay-poor (h) fault rocks. In mesoscale sketch (f), kinematic mechanism is Fig. 11e viewed parallel to thrust strike. Micro-scale sketches show microstructural features rotated based on average thrust core dip, compressional structures are coloured red and extensional features coloured blue. Red and blue arrows show the effective principal compressive stress orientation derived from microstructures for compressional and extensional stress regimes, respectively. Pressure solution is labelled PS and successive vein sets labelled V1-V3 (V3 is the most recent). (For interpretation of the references to colour in this figure legend, the reader is referred to the Web version of this article.)

represent periods of main thrust core strengthening causing propagation of minor thrusting into footwall lithologies in a small-scale 'piggyback' thrusting episodes (Ori and Friend, 1984) to accommodate compressional strain by de-localisation away from the thrust core (Wojtal and Mitra, 1986; Lena et al., 2015). Is it possible each of these surfaces locked before forming the surface beneath, or, conversely, these surfaces developed contemporaneously, accommodating lesser strain upon each. The orientation of the well-developed shear folds sits perpendicular to N021, coherent with other results from kinematic analysis of compression in both the work presented here and of Ghisetti (1987).

6.1.3. Ambient conditions and displacement of the VFTF

Analysis of kinematic indicators throughout the hangingwall, footwall, and fault core indicate thrusting on the Vado di Ferruccio was towards N024, with local variability over tens of metres between N000 and N034. Distance of transport from stratigraphic offset is difficult to accurately calculate due to: (1) the locally variable nature of units involved in thrusting (Cardello and Doglioni, 2015), (2) variable thrust orientation and possible reactivation in extension (Ghisetti and Vezzani, 1986; Ghisetti, 1987; Pace et al., 2014; this paper), (3) the scarcity of literature describing the *Dolomie Bituminose* and its stratigraphic relationships within the carbonate sequence present in the Central Apennines (Adamoli et al., 1990; Barattolo and Bigozzi, 1996; Bertinelli et al., 2004), (4) folding complicating estimates of stratigraphic offset. Nevertheless, assuming an average thrust dip angle of 25° perpendicular to transport direction and a stratigraphic gap of 550 m (between the top of *Dolomie Bituminose* and the base of the *Verde Ammonitico*), the resulting transport distance on the thrust plane is ca. 1.3 km ($h = o/\sin\theta$; h = distance of transport along thrust surface, o = stratigraphic gap due to thrusting, θ = dip of thrust fault). This is likely a conservative estimate due to the intensity of folding, pressure solution in the fault core, and subsidiary fault structures, all of which could have increased the accommodated displacement.

Within the FTW, areas with steeper thrust orientations are associated with more competent grainstone lithology in the footwall while shallower thrust orientations correspond to regions overlying interbedded marls-grainstones in the footwall. Local variation in thrust fault geometry therefore records the effect of variable lithology adjacent to the VFTF on strain localisation during thrust fault propagation. The evolution of the principal thrust fault, from shallow SW-ward dipping in the south of the study area to steeper southward dip in the north of the area, defines a variable geometry for the VFTF of concave-up in the north-west of the study area and convex-up elsewhere. This has previously been attributed to a lenticular geometry of the Santa Colomba Thrust Sheet (Ghisetti, 1987), though the more competent lithology within the core of large-scale footwall folding is raised here as a potential source of ramping.

Ambient conditions (confining pressure and temperature) during thrusting can be constrained by combining various sources of data. Apatite fission track and vitrinite reflectance data from the *Dolomie Bituminose* samples in the Gran Sasso yielded maximum burial temperatures of 100–105 °C between 35 and 15 Ma, maintaining up to 108 °C at 10 Ma (Rusciadelli et al., 2005). Assuming no anomalous geotherm due to thermal subduction-related degassing, a standard geothermal gradient of 30 °C km^{-1} yields a depth estimate of 3.33–3.60 km. Indeed, estimated the maximum stratigraphic thickness of formations overlying the *Dolomia Principale* in the Gran Sasso is 3.48 km (Cardello and Doglioni, 2015). This is highly variable between relative paleogeographic highs and lows (where it is significantly thinned) in the basin of deposition of these units (Cardello and Doglioni, 2015). Nevertheless, this may represent the maximum depth of thrusting, and perhaps peak ambient conditions during Miocene compression.

6.2. Extensional activity recorded in the VFTF core and hangingwall damage zone

Dominant normal faults in the study area clearly indicate that extension was the most recent deformation mode active, overprinting compressional structures (Figs. 2 and 11f). Microstructures within the fault core indicate a change, after compression, to an inverted stress orientation containing a sub-vertical principal stress (Fig. 9h and i, 11g). High angle compressional R shears within upper fault core samples have well-developed pressure solution upon them, cutting the most recent veins. These surfaces would be low-angle due to the dip of the fault core, optimally oriented for activation as pressure solution seams perpendicular to a vertical σ_1, consistent with extensional stresses (Fig. 11g; Ghisetti and Vezzani, 1999; D'Agostino et al., 2014). The least deformed veins within pressure solution-rich regions are orthogonal to

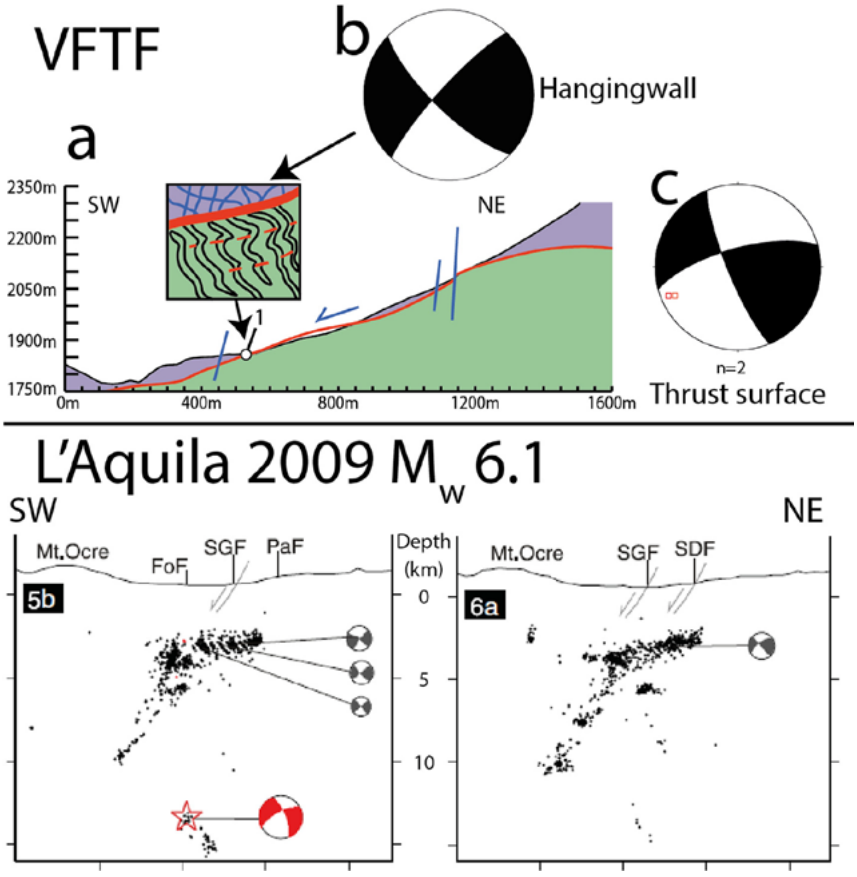


Fig. 12. Comparison of kinematics and geometry of hanging wall volumes activated on the VFTF and in the L'Aquila 2009 M_w 6.1 seismic sequence. **VFTF**: (a) cross section indicating the location of the measured kinematics used to construct focal mechanisms (locality 1; see Fig. 2 for further detail of location). Focal mechanisms are derived from (b) 133 mirror-surfaced faults in the hangingwall of the VFTF, and (c) 2 lineations and 30 fault plane measurements collected on the principal slip surface on the boundary between the thrust core and hangingwall on the VFTF. **L'Aquila**: Cross sections (after Valoroso et al., 2013) indicating the distribution and typical focal mechanisms of fore and aftershocks during the 2009 M_w 6.1 L'Aquila seismic sequence.

the dominant pressure solution seam orientation (Fig. 9h and i, 11g). These veins would also be subparallel to a vertical σ_1 and corroborate the existence of extensional stresses, likely associated with the collapse of the thrust stack. Aside from millimetre-scale veins, meso-scale structures within the VFTF core show no evidence of measurable extensional reactivation (Fig. 8), indeed major normal faults accommodating regional extension cut through the VFTF core (Fig. 11f). Rather, a sharp surface upon the upper margin of the thrust fault core delineates a boundary of extensional faulting between the core and hanging wall damage zone (Figs. 6 and 8).

Lenses up to 10 m (measuring perpendicular to the average thrust plane) thick of shattered dolostones are locally observed in the hangingwall damage zone just above the thrust fault core. These heavily fractured dolostones (Fig. 4b) are cut by a dense network of mirror-like fault surfaces (Fig. 6c) characterized by a wide distribution of plane orientations and lineations (Fig. 3, locality 1 & 11a). Movement lineations on fault planes are distributed around a NE-SW striking plane, with a clustering around steeply SSW-plunging dip-slip (Fig. 11b–d). The scattering in orientation of normally-faulted mirror surfaces and their lineations is consistent with an extensional, possibly dynamic, collapse of the hangingwall block associated with small seismic ruptures. Determined offsets of sampled extensional faults in the hanging wall are up to 1.2 m, though many show offset of a few centimetres or less. The length of these faults is difficult to assess precisely, due to the limited outcrop exposure, but is in the range of tens to a few hundred meters. These are therefore structures which could have hosted small earthquake ruptures ($M_w < 2$) (Wells and Coppersmith, 1994). The range of fault lineations indicates a NE-SW normal dip-slip trend within the faulting scheme, consistent with kinematic inversion of measured faults (Fig. 11e) and more general extensional trends in the Gran Sasso (D'Agostino et al., 2009; Cardello and Doglioni, 2015). The intensive shattering of the hangingwall is a localised phenomenon, most-strongly visible in the SW part of the FTW directly adjacent to the fault core (Fig. 3, localities 1 & 5). Elsewhere, low-angle north-dipping fault surfaces are present in the hangingwall adjacent to the thrust core (Figs. 2 and 3, localities 4, 5 & 8b) which are probably R-shears formed during compression (Fig. 11f). These fault surfaces could have been reactivated in extension alongside the intensive localised hangingwall faulting but are far more systematic in orientation and continuously-recognisable in exposure.

Lineations upon the highly-localised thrust principal slip surface are consistent with the lineation distribution of extensional hangingwall faults (Fig. 11d), suggesting they may be related. The principal slip surface could therefore represent a potential decoupling boundary between the hangingwall block, associated with shattering and compartmentalized extensional faulting (each mirror-like fault is associated with extremely localized shear strain), and the thrust core (Fig. 11f). The mechanical basis for this interpretation rests upon the contrast in materials between the dolomitic hangingwall and the marl-rich fault core and footwall preventing fault propagation downward across the detachment. Fault propagation across mechanically-heterogeneous layers has been numerically modelled by Welch et al. (2009) who show that faults which nucleate in the layer with a higher coefficient of sliding friction (the dolomitic hangingwall) upon microshears will not propagate into an adjacent weak ductile layer (such as the marl-rich VFTF core) if the ratio of horizontal to vertical stresses in the weak layer is high (< 0.4). We suggest the contrast in frictional and mechanical properties (e.g. stiffness) across the principal slipping surface is sufficiently different, perhaps in concert with a high vertical-horizontal stress ratio, to inhibit the propagation of localised mirror-like fault

surfaces into the fault core or hangingwall, instead forming a layer-bound fault set (Welch et al., 2009).

Abundant mirror surfaces within dolostones, such as those seen in the hanging wall adjacent to the thrust (Figs. 4b, 6 and 11), possibly represent evidence of coseismic shear strain localization at high slip rates (0.1–1 m/s) (Fondriest et al., 2013, 2015; Siman-Tov et al., 2015; Kuo et al., 2016). The association of shattered dolostones and small-displacement mirror-like faults with variable orientations have been previously interpreted at a potential record of earthquake rupture propagation through carbonates at shallow depth (< 3 km; Fondriest et al., 2015, 2017). Mirror surfaces seem to be less frequent within more bitumen-rich HW lithologies in the south of the tectonic window. Within bitumen-rich dolostones, weak phase smearing of amorphous carbon on fault surfaces is observed (Fig. 6d); this might represent a mechanism to stably reduce friction coefficient (Oohashi et al., 2011; Rutter et al., 2013). Smearing of dark material on mirror surfaces within moderately bituminous lithologies (Fig. 6d) could be further investigated to better determine controls on graphitisation of amorphous carbonaceous material (Oohashi et al., 2011; Kuo et al., 2014), associated controls on fault friction, and promotion of seismic slip by carbonaceous material.

Monitoring of seismicity during the 2009 L'Aquila earthquake sequence (main shock M_w 6.1) highlighted the potential activation of inherited compressional structures at hypocentral depths of < 3–4 km (Valoroso et al., 2013, Fig. 12), similar to the exhumation depth of the VFTF. Indeed, minor earthquakes (mainly aftershocks with M_w < 3) were illuminating low angle regional structures compatible with Miocene-Pliocene thrust flats. Focal mechanisms of these events (Fig. 12) may be irregularly consistent with normal activation of low-angle thrust flats, but mainly correspond to high-angle antithetic faults (Chiaraluce et al., 2011; Valoroso et al., 2013). In the case of the VFTF, the negative inversion of the pre-existing thrust flat (*sensu* Bigi, 2006) was not documented: the fault core preserves evidence of stress inversion at the microscale (Fig. 11f) but it is cut by regional normal faults. Conversely, shattering, and diffuse microfaulting (mostly high angle synthetic and antithetic normal faults; Fig. 11e and f) registered the local extensional collapse of the hanging wall damage zone, possibly during dynamic seismic activity.

7. Conclusions

Field and microstructural study of the structure and lithology throughout the Fornaca Tectonic Window has shown the Vado di Ferruccio Thrust Fault accommodated at least 1.3 km of displacement towards N024. A combination of cataclastic and pressure solution-dominated deformation took place within the marl-rich fault core where the compression was most likely accommodated by stable aseismic creep. Intermittent fluid pressure build-ups within the creeping fault core caused cyclic vein generations and cataclasis. The hanging wall damage zone accommodated compression by sliding on minor, systematically-oriented faults. Deformation in the interlayered carbonate footwall damage zone was dominated by isoclinal folds, which were refolded by dragging in marl-rich areas or shearing on thrust-parallel reverse faults in more competent grainstone-rich areas.

Subsequent extensional stress is recorded at the micro-scale on the VFTF, but no measurable displacement is recorded. Microstructures within the clay-rich thrust fault core register a late rotation of the applied stress field consistent with southward normal inversion. Asymmetric strain across the fault core formed a sharp localized principal slip surface on the upper margin which acted as a decoupling surface between the fault core and the hangingwall damage zone and possibly accommodated a small extensional strain component. Extensional activity is instead well registered in the hangingwall damage zone where, locally, lenses up to 10 m thick of shattered dolostones are cut by a dense network of normal faults with mirror-like finish. These mirror faults display scattered orientations and are suggested to have formed by dynamic processes during rapid coseismic slip. In particular, the association of local bodies of intensely fractured wall rocks cut by small displacement highly localized fault surfaces has been interpreted as the result of microseismicity (M_w < 2) occurring in the hangingwall block of a low angle extensional fault.

Small synthetic and antithetic normal faults surfaces within the VFTF hangingwall damage zone are shown to be kinematically similar to structures rupturing during small (microseismic) earthquakes (M_w < 2) in the hangingwall of low angle shallow detachments illuminated during the 2009 M_w 6.1 L'Aquila seismic sequence. The structural setting of the VFTF can therefore be considered as an analogue of seismically-activated low-angle volumes recently illuminated in the Apennines through seismological methods. Further work to determine the influence of this extension on other thrust faults in the Gran Sasso massif may shed further light on the processes which occur on low-angle faults within extensional regimes.

Acknowledgements

Staff at Rifugio Campo Imperatore, Paolo in particular, are thanked for accommodation and friendly support during field seasons. Microstructural data discussed within this work would not have been carried out effectively but for the patient help of H. Bagshaw and J. Fellows, whose assistance is greatly appreciated. The “Ente Parco Nazionale del Gran Sasso e Monti della Laga” are also thanked for permission to conduct fieldwork in the Fornaca Valley. Aerial photographs are from the Regione Abruzzo, the use of which is greatly appreciated. Stereonets were produced using Stereonet and Faultkin software by Rick Allmendinger (Marrett and Allmendinger, 1990; Allmendinger et al., 2011; Cardozo and Allmendinger, 2013). This research was funded by the European Research Council Consolidator Grant Project (NOFEAR) No 614705 (principal investigator: Giulio Di Toro). Luca Cardello and Telemaco Tesei are thanked for constructive reviews which improved this manuscript.

References

Adamoli, L., Bigozzi, A., Ciarapica, G., Cirilli, S., Passeri, L., Romano, A., Duranti, F., Venturi, F., 1990. Upper triassic bituminous facies and hettangian pelagic facies in the gran sasso range. Boll. Soc. Geol. Ital. 109, 219–230.

Adamoli, L., Calamita, F., Pizzi, A., 2012. Note Illustrative Della Carta Geologica D'Italia Alla Scala 1:50,000, Foglio 349. Gran Sasso d'Italia.

Allmendinger, R.W., Cardozo, N., Fisher, D.M., 2011. Structural Geology Algorithms, Structural Geology Algorithms. Cambridge University Press, Cambridge. https://doi.org/10.1017/CBO9780511920202.

Barattolo, F., Bigozzi, A., 1996. Dasycladaleans and depositional environments of the upper Triassic-Liaasic carbonate platform of the Gran Sasso (central Apennines, Italy). Facies 35, 163–208.

Bertinelli, A., Nannarone, C., Passeri, L., Venturi, F., 2004. Hettangian ammonites and radiolarians in the Mt. Camicia (gran sasso, central apennines). Riv. Ital. Paleontol. Stratigr. 110, 87–95. https://doi.org/https://doi.org/10.13130/2039-4942/6270.

Bigi, S., 2006. An example of inversion in a brittle shear zone. J. Struct. Geol. 28, 431–443. https://doi.org/10.1016/j.jsg.2005.12.012.

Billi, A., 2010. Microtectonics of low-P low-T carbonate fault rocks. J. Struct. Geol. 32, 1392–1402. https://doi.org/10.1016/j.jsg.2009.05.007.

Bos, B., Spiers, C.J., 2001. Experimental investigation into the microstructural and mechanical evolution of phyllosilicate-bearing fault rock under conditions favouring pressure solution. J. Struct. Geol. 23, 1187–1202. https://doi.org/10.1016/S0191-8141(00)00184-X.

Bullock, R.J., De Paola, N., Holdsworth, R.E., Trabucho-Alexandre, J.J., 2014. Lithological controls on the deformation mechanisms operating within carbonate-hosted faults during the seismic cycle. J. Struct. Geol. 58, 22–42. https://doi.org/10.1016/j.jsg.2013.10.008.

Caine, J.S., Evans, J.P., Forster, C.B., 1996. Fault zone architecture and permeability structure. Geology 24, 1025–1028 https://doi.org/10.1130/0091-7613(1996)024 < 1025.

Cardello, G.L., Doglioni, C., 2015. From mesozoic rifting to apennine orogeny: the gran sasso range (Italy). Gondwana Res. 27, 1307–1334. https://doi.org/10.1016/j.gr.2014.09.009.

Cardello, G.L., Mancktelow, N.S., 2015. Veining and post-nappe transtensional faulting in the SW Helvetic Alps (Switzerland). Swiss J. Geosci. 108, 379–400. https://doi.org/10.1007/s00015-015-0199-7.

Cardozo, N., Allmendinger, R.W., 2013. Spherical projection with OSXStereonet. Comput. Geosci. 51, 193–205.

Centamore, E., Fumanti, F., Nisio, S., 2002. The central-northern apennines geological evolution from triassic to neogene time. Boll. Soc. Geol. Ital. 1, 181–197 Volume Speciale.
Chiaraluce, L., Di Stefano, R., Tinti, E., Scognamiglio, L., Michele, M., Casarotti, E., Cattaneo, M., De Gori, P., Chiarabba, C., Monachesi, G., Lombardi, A., Valoroso, L., Latorre, D., Marzorati, S., 2017. The 2016 Central Italy seismic sequence: a first look at the mainshocks, aftershocks, and source models. Seismol Res. Lett. 88, 757–771. https://doi.org/10.1785/0220160221.
Chiaraluce, L., Valoroso, L., Piccinini, D., Di Stefano, R., De Gori, P., 2011. The anatomy of the 2009 L'Aquila normal fault system (central Italy) imaged by high resolution foreshock and aftershock locations. J. Geophys. Res. 116, B12311. https://doi.org/10.1029/2011JB008352.
Ciarapica, G., 2007. Regional and global changes around the Triassic-Jurassic boundary reflected in the late Norian-Hettangian history of the Apennine basins. Palaeogeogr. Palaeoclimatol. Palaeoecol. 244, 34–51. https://doi.org/10.1016/j.palaeo.2006.06.022.
Clemenzi, L., Storti, F., Balsamo, F., Molli, G., Ellam, R., Muchez, P., Swennen, R., 2015. Fluid pressure cycles, variations in permeability, and weakening mechanisms along low-angle normal faults: the Tellaro detachment, Italy. Geol. Soc. Am. Bull. 127, 1689–1710. https://doi.org/10.1130/B31203.1.
D'Agostino, N., Chamot-Rooke, N., Funiciello, R., Jolivet, L., Speranza, F., 1998. The role of pre-existing thrust faults and topography on the styles of extension in the Gran Sasso range (central Italy). Tectonophysics 292, 229–254. https://doi.org/10.1016/S0040-1951(98)00070-5.
D'Agostino, N., England, P., Hunstad, I., Selvaggi, G., 2014. Gravitational potential energy and active deformation in the Apennines. Earth Planet Sci. Lett. 397, 121–132. https://doi.org/10.1016/j.epsl.2014.04.013.
D'Agostino, N., Mantenuto, S., D'Anastasio, E., Avallone, A., Barchi, M., Collettini, C., Radicioni, F., Stoppini, A., Fastellini, G., 2009. Contemporary crustal extension in the Umbria-Marche Apennines from regional CGPS networks and comparison between geodetic and seismic deformation. Tectonophysics 476, 3–12. https://doi.org/10.1016/j.tecto.2008.09.033.
Davis, G.H., Bump, A.P., García, P.E., Ahlgren, S.G., 2000. Conjugate Riedel deformation band shear zones. J. Struct. Geol. 22, 169–190. https://doi.org/10.1016/S0191-8141(99)00140-6.
Demurtas, M., Fondriest, M., Balsamo, F., Clemenzi, L., Storti, F., Bistacchi, A., Di Toro, G., 2016. Structure of a normal seismogenic fault zone in carbonates: the Vado di Corno Fault, Campo Imperatore, Central Apennines (Italy). J. Struct. Geol. 90, 185–206. https://doi.org/10.1016/j.jsg.2016.08.004.
Devoti, R., Riguzzi, F., Cuffaro, M., Doglioni, C., 2008. New GPS constraints on the kinematics of the Apennines subduction. Earth Planet Sci. Lett. 273, 163–174. https://doi.org/10.1016/j.epsl.2008.06.031.
Dolce, M., Di Bucci, D., 2017. Comparing recent Italian earthquakes. Bull. Earthq. Eng. 15, 497–533. https://doi.org/10.1007/s10518-015-9773-7.
Falcucci, E., Gori, S., Moro, M., Fubelli, G., Saroli, M., Chiarabba, C., Galadini, F., 2015. Deep reaching versus vertically restricted Quaternary normal faults: implications on seismic potential assessment in tectonically active regions: lessons from the middle Aterno valley fault system, central Italy. Tectonophysics 651, 186–198. https://doi.org/10.1016/j.tecto.2015.03.021.
Fondriest, M., Aretusini, S., Di Toro, G., Smith, S.A.F., 2015. Fracturing and rock pulverization along an exhumed seismogenic fault zone in dolostones: the Foiana Fault Zone (Southern Alps, Italy). Tectonophysics 654, 56–74. https://doi.org/10.1016/j.tecto.2015.04.015.
Fondriest, M., Doan, M.-L., Aben, F., Fusseis, F., Mitchell, T.M., Voorn, M., Secco, M., Di Toro, G., 2017. Static versus dynamic fracturing in shallow carbonate fault zones. Earth Planet Sci. Lett. 461, 8–19. https://doi.org/10.1016/j.epsl.2016.12.024.
Fondriest, M., Smith, S.A.F., Candela, T., Nielsen, S.B., Mair, K., Di Toro, G., 2013. Mirror-like faults and power dissipation during earthquakes. Geology 41, 1175–1178. https://doi.org/10.1130/G34641.1.
Galadini, F., Messina, P., 2004. Early–Middle Pleistocene eastward migration of the abruzzi apennine (central Italy) extensional domain. J. Geodyn. 37, 57–81. https://doi.org/10.1016/j.jog.2003.10.002.
Galli, P., 2002. New paleoseismological data from the Gran Sasso d'Italia area (central Apennines). Geophys. Res. Lett. 29, 1134. https://doi.org/10.1029/2001GL013292.
Ghisetti, F., 1987. Mechanisms of thrust faulting in the gran sasso chain, central apennines, Italy. J. Struct. Geol. 9, 955–967. https://doi.org/10.1016/0191-8141(87)90004-6.
Ghisetti, F., Vezzani, L., 2002. Normal faulting, transcrustal permeability and seismogenesis in the Apennines (Italy). Tectonophysics 348, 155–168. https://doi.org/10.1016/S0040-1951(01)00254-2.
Ghisetti, F., Vezzani, L., 1999. Depth and modes of Pliocene-Pleistocene crustal extension of the Apennines (Italy). Terra. Nova 11, 67–72. https://doi.org/10.1046/j.1365-3121.1999.00227.x.
Ghisetti, F., Vezzani, L., 1991. Thrust belt development in the central Apennines (Italy): northward polarity of thrusting and out-of-sequence deformations in the Gran Sasso Chain. Tectonics 10, 904–919. https://doi.org/10.1029/91TC00902.
Ghisetti, F.C., Vezzani, L., 1986. Carta Geologica del Gruppo M.Siella-M.Camicia-M.Prena-M.Brancastello (Gran Sasso d'Italia, Abruzzo). Scale 1:15.000. https://doi.org/10.13140/RG.2.1.5022.1683.
Gratier, J.P., Richard, J., Renard, F., Mittempergher, S., Doan, M.L., Di Toro, G., Hadizadeh, J., Boullier, A.M., 2011. Aseismic sliding of active faults by pressure solution creep: evidence from the san andreas fault observatory at depth. Geology 39, 1131–1134. https://doi.org/10.1130/G32073.1.
Gratier, Dysthe, D.K., Renard, F., 2013a. The role of pressure solution creep in the ductility of the Earth's upper crust. Adv. Geophys. 47–179. https://doi.org/10.1016/B978-0-12-380940-7.00002-0.
Gratier, Thouvenot, F., Jenatton, L., Tourette, A., Doan, M.L., Renard, F., 2013b. Geological control of the partitioning between seismic and aseismic sliding behaviours in active faults: evidence from the Western Alps, France. Tectonophysics 600, 226–242. https://doi.org/10.1016/j.tecto.2013.02.013.
Hadizadeh, J., 1994. Interaction of cataclasis and pressure solution in a low-temperature carbonate shear zone. Pure Appl. Geophys. PAGEOPH 143, 255–280. https://doi.org/10.1007/BF00874331.
Kamb, W.B., 1959. Ice petrofabric observations from Blue Glacier, Washington, in relation to theory and experiment. J. Geophys. Res. 64, 1891. https://doi.org/10.1029/JZ064i011p01891.
Katz, Y., Weinberger, R., Aydin, A., 2004. Geometry and kinematic evolution of Riedel shear structures, capitol reef national Park, Utah. J. Struct. Geol. 26, 491–501. https://doi.org/10.1016/j.jsg.2003.08.003.
Koopman, A., 1983. Detachment Tectonics in the central Apennines, Italy. Instituut voor Aardwetenschappen RUU.
Kuo, L.-W., Song, S.-R., Suppe, J., Yeh, E.-C., 2016. Fault mirrors in seismically active fault zones: a fossil of small earthquakes at shallow depths. Geophys. Res. Lett. 43, 1950–1959. https://doi.org/10.1002/2015GL066882.
Kuo, L., Li, H., Smith, S.A.F., Di Toro, G., Suppe, J., Song, S.S.-R., Nielsen, S., Sheu, H.-S.H., Si, J., Wenchuan, M., Kuo, L., Li, H., Smith, S.A.F., Toro, G., Di Suppe, J., Song, S.S.-R., Nielsen, S., Sheu, H.-S.H., Si, J., 2014. Gouge graphitization and dynamic fault weakening during the 2008 Mw 7.9 Wenchuan earthquake. Geology 42, 47–50. https://doi.org/10.1130/G34862.1.
Lena, G., Barchi, M.R., Alvarez, W., Felici, F., Minelli, G., 2015. Mesostructural analysis of S-C fabrics in a shallow shear zone of the Umbria–Marche Apennines (Central Italy). Geol. Soc. Lond. Spec. Publ. 409, 149–166. https://doi.org/10.1144/SP409.10.
Marrett, R., Allmendinger, R.W., 1990. Kinematic analysis of fault-slip data. J. Struct. Geol. 12, 973–986. https://doi.org/10.1016/0191-8141(90)90093-E.
Michele, M., Di Stefano, R., Chiaraluce, L., Cattaneo, M., De Gori, P., Monachesi, G., Latorre, D., Marzorati, S., Valoroso, L., Ladina, C., Chiarabba, C., Lauciani, V., Fares, M., 2016. The Amatrice 2016 seismic sequence: a preliminary look at the mainshock and aftershocks distribution. Ann. Geophys. 59. https://doi.org/10.4401/ag-7227.
Oohashi, K., Hirose, T., Shimamoto, T., 2011. Shear-induced graphitization of carbonaceous materials during seismic fault motion: experiments and possible implications for fault mechanics. J. Struct. Geol. 33, 1122–1134. https://doi.org/10.1016/j.jsg.2011.01.007.
Ori, G.G., Friend, P.F., 1984. Sedimentary basins formed and carried piggyback on active thrust sheets. Geology. https://doi.org/10.1130/0091-7613(1984)12<475:SBFACP>2.0.CO;2.
Pace, P., Calamita, F., 2015. Coalescence of fault-bend and fault-propagation folding in curved thrust systems: an insight from the Central Apennines, Italy. Terra. Nova 27, 175–183. https://doi.org/10.1111/ter.12146.
Pace, P., Domenica, A., Di Calamita, F., 2014. Summit low-angle faults in the Central Apennines of Italy: younger-on-older thrusts or rotated normal faults? Constraints for defining the tectonic style of thrust belts. Tectonics 33, 756–785. https://doi.org/10.1002/2013TC003385.
Ramsay, J.G., 1980. Shear zone geometry: a review. J. Struct. Geol. 2, 83–99. https://doi.org/10.1016/0191-8141(80)90038-3.
Rusciadelli, G., Viandante, M.G., Calamita, F., Cook, A.C., 2005. Burial-exhumation history of the central Apennines (Italy), from the foreland to the chain building: thermochronological and geological data. Terra. Nova 17, 560–572. https://doi.org/10.1111/j.1365-3121.2005.00649.x.
Rutter, E.H., 1983. Pressure solution in nature, theory and experiment. J. Geol. Soc. 140, 725–740. https://doi.org/10.1144/gsjgs.140.5.0725.
Rutter, E.H., Hackston, A.J., Yeatman, E., Brodie, K.H., Mecklenburgh, J., May, S.E., 2013. Reduction of friction on geological faults by weak-phase smearing. J. Struct. Geol. 51, 52–60. https://doi.org/10.1016/j.jsg.2013.03.008.
Sibson, R.H., 2000. Fluid involvement in normal faulting. J. Geodyn. 29, 469–499. https://doi.org/10.1016/S0264-3707(99)00042-3.
Siman-Tov, S., Aharonov, E., Boneh, Y., Reches, Z., 2015. Fault mirrors along carbonate faults: formation and destruction during shear experiments. Earth Planet Sci. Lett. 430, 367–376. https://doi.org/10.1016/j.epsl.2015.08.031.
Speranza, F., 2003. Genesis and evolution of a curved mountain front: paleomagnetic and geological evidence from the Gran Sasso range (central Apennines, Italy). Tectonophysics 362, 183–197. https://doi.org/10.1016/S0040-1951(02)00637-6.
Storti, F., Billi, A., Salvini, F., 2003. Particle size distributions in natural carbonate fault rocks: insights for non-self-similar cataclasis. Earth Planet Sci. Lett. 206, 173–186. https://doi.org/10.1016/S0012-821X(02)01077-4.
Tarquini, S., Isola, I., Favalli, M., Mazzarini, F., Bisson, M., Pareschi, M.T., Boschi, E., 2007. TINITALY/01: a new triangular irregular network of Italy. Ann. Geophys. 50, 407–425. https://doi.org/10.4401/ag-4424.
Tarquini, S., Vinci, S., Favalli, M., Doumaz, F., Fornaciai, A., Nannipieri, L., 2012. Release of a 10-m-resolution DEM for the Italian territory: comparison with global-coverage DEMs and anaglyph-mode exploration via the web. Comput. Geosci. 38, 168–170. https://doi.org/10.1016/j.cageo.2011.04.018.
Tchalenko, J.S., 1970. Similarities between shear zones of different magnitudes. Bull. Geol. Soc. Am. 81, 1625–1640. https://doi.org/10.1130/0016-7606(1970)81[1625:SBSZOD]2.0.CO;2.
Tesei, T., Collettini, C., Barchi, M.R., Carpenter, B.M., Di Stefano, G., 2014. Heterogeneous strength and fault zone complexity of carbonate-bearing thrusts with possible implications for seismicity. Earth Planet Sci. Lett. 408, 307–318. https://doi.org/10.1016/j.epsl.2014.10.021.
Tesei, T., Collettini, C., Viti, C., Barchi, M.R., 2013. Fault architecture and deformation mechanisms in exhumed analogues of seismogenic carbonate-bearing thrusts. J. Struct. Geol. 55, 167–181. https://doi.org/10.1016/j.jsg.2013.07.007.
Valoroso, L., Chiaraluce, L., Piccinini, D., Di Stefano, R., Schaff, D., Waldhauser, F., 2013.

Radiography of a normal fault system by 64,000 high-precision earthquake locations: the 2009 L'Aquila (central Italy) case study. J. Geophys. Res.: Solid Earth 118, 1156–1176. https://doi.org/10.1002/jgrb.50130.
Van Konijnenburg, J.H., Bernoulli, D., Mutti, M., 1999. Stratigraphic architecture of a lower cretaceous - lower tertiary carbonate base-of-slope succession: gran sasso D'Italia (central apennines, Italy). SEPM (Soc. Sediment. Geol.) Spec. Publ. 63, 291–315.
Vezzani, L., Festa, A., Ghisetti, F.C., 2010. Geology and Tectonic Evolution of the Central-Southern Apennines, Italy. Geological Society of America, pp. 1–58. Geological Society of America Special Papers, Geological Society of America Special Papers. https://doi.org/10.1130/2010.2469.
Viti, C., Collettini, C., Tesei, T., 2014. Pressure solution seams in carbonatic fault rocks: mineralogy, micro/nanostructures and deformation mechanism. Contrib. Mineral. Petrol. 167, 970. https://doi.org/10.1007/s00410-014-0970-1.
Welch, M.J., Davies, R.K., Knipe, R.J., Tueckmantel, C., 2009. A dynamic model for fault nucleation and propagation in a mechanically layered section. Tectonophysics 474, 473–492. https://doi.org/10.1016/j.tecto.2009.04.025.
Wells, D.L., Coppersmith, K.J., 1994. New empirical relationships among magnitude, rupture length, rupture width, rupture area, and surface displacement. Bull. Seismol. Soc. Am. 84, 974–1002 https://doi.org/ < p > < /p > .
Wojtal, S., Mitra, G., 1986. Strain hardening and strain softening in fault zones from foreland thrusts. Geol. Soc. Am. Bull. 97, 674. https://doi.org/10.1130/0016-7606(1986)97 < 674:SHASSI > 2.0.CO;2.
Woodcock, N.H., Dickson, J.A.D., Tarasewicz, J.P.T., 2007. Transient permeability and reseal hardening in fault zones: evidence from dilation breccia textures. Geol. Soc. Lond. Spec. Publ. 270, 43–53. https://doi.org/10.1144/GSL.SP.2007.270.01.03.
Yasuhara, H., Marone, C., Elsworth, D., 2005. Fault zone restrengthening and frictional healing: the role of pressure solution. J. Geophys. Res. 110, B06310. https://doi.org/10.1029/2004JB003327.

5

SUBAERIAL OUT-OF-SEQUENCE THRUSTING AND LATE-STAGE EXTENSION IN THE GRAN SASSO MASSIF, CENTRAL APENNINES, ITALY

This chapter is presented in the form of a manuscript that is currently in preparation for submission to *Tectonics*. This manuscript describes the structural architecture of the Monte Camicia out-of-sequence Thrust Fault and the associated paleofluid evolution. In this study we describe the contractional fabric along the fault zone and how it has been exploited and reworked during Quaternary extensional deformation. Specifically, we show that out-of-sequence thrusting along the Monte Camicia fault zone occurred in subaerial conditions associated with meteoric fluids infiltration which promoted de-dolomitization.

ARTICLE IN PREPARATION

Lucca A., Balsamo F., Storti F., Clemenzi L., Fondriest M., Burgess R., Iacumin P., and Di Toro G.

Article in preparation for submission to *Tectonics*

Subaerial out-of-sequence thrusting and late-stage extension in the Gran Sasso Massif, Central Apennines, Italy

Alessio Lucca[1], Fabrizio Balsamo[1], Fabrizio Storti[1], Luca Clemenzi[1], Michele Fondriest[2], Raymond Burgess[2], Paola Iacumin[3] Giulio Di Toro[4,5]

[1]NEXT - Natural and Experimental Tectonics research group, Department of Chemistry, Life Sciences and Environmental Sustainability, University of Parma, I-43124 Parma, Italy

[2]School of Earth, Atmospheric and Environmental Sciences, University of Manchester, Williamson Building, Oxford Road, Manchester M13 9PL, UK

[3]Department of Chemistry, Life Sciences and Environmental Sustainability, University of Parma, I-43124 Parma, Italy

[4]Dipartimento di Geoscienze, Università degli Studi di Padova, Via Giovanni Gradenigo, 6, 35131 Padova, Italy

[5]Istituto Nazionale di Geofisica e Vulcanologia, Via di Vigna Murata, 605, 00143 Roma RM, Italy

*Corresponding Author Details

E-mail: alessio.lucca@studenti.unipr.it

Telephone number: +39 393 1323420

Abstract

Fault zone structural-diagenetic evolution is controlled by fluid-rock interactions that, in turn, result from the complex interplay between deformation mechanisms, lithology, environmental conditions of deformation, and fault permeability architecture. Understanding why fault zones act as preferential conduits for fluid infiltration or as seals that impede cross-fault fluid circulation has first-order implications in the characterization of hydrocarbon and groundwater reservoirs and in seismic hazard assessment. We studied the Camicia and Vado di Ferruccio out-of-sequence thrusts, exceptionally exposed in the Gran Sasso Massif, Central Apennines of Italy. These faults accommodated shortening in the Mesozoic carbonatic Adria passive margin sedimentary succession from Late Messinian to Early Pliocene times. Since Pleistocene times, extensional deformations started to affect the area, exploiting the structural inheritance from the contractional fault architecture. We used structural, petrographical and geochemical analyses, namely carbon, oxygen, strontium and noble gases isotopes, to constrain fault kinematics and the associated paleofluid evolution. We show that in the Vado di Ferruccio Thrust, pressure solution-mediated mass transfer promoted low-permeability conditions in the fault core that

led to a semi-closed fluid circulation, pore fluid overpressuring, and dolomite crystallization. On the other hand, in the Camicia Thrust, dominant cataclasis allowed meteoric fluid infiltration. Late-stage extensional deformations enhanced meteoric fluids circulation, particularly in the more permeable Camicia Thrust, where intense dolomite dissolution and calcitization occurred.

1. Introduction

It has long been recognized that fault zones exert a fundamental control on fluid circulation within the crust, behaving as preferential conduits or barriers mainly depending on lithological juxtaposition and deformation mechanisms (Sibson, 1977; Chester & Logan, 1986; Wojtal & Mitra, 1986; Wintsch et al., 1995; Caine et al., 1996; Storti et al., 2003; Faulkner et al., 2010; Hadizadeh et al., 2012; Solum and Huisman, 2016; Delle Piane et al., 2017). Pore fluid overpressuring favors fault slip by reducing the effective shear stress and lubricating master slip surfaces (Sibson, 1990; Byerlee, 1993; Faulkner & Rutter, 2001; Mittempergher et al., 2011). The fundamental role of fluids on rupture nucleation and propagation has been documented in many earthquakes (Miller et al., 2004, Chiarabba & Chiodini, 2013). As a consequence, a deep understanding of the interplay between faulting and fluid flow bears fundamental implications for seismic hazards mitigation and accumulation of both aquifers and hydrocarbon reservoirs in the subsurface (Sibson, 1981; Oliver, 1986; Moore & Vrolijk, 1992; Knipe & McCaig, 1994; Di Toro et al., 2011). For this purpose, exhumed field analogues have long been studied to investigate on interaction modalities between fault zone and paleofluid evolution (Ghisetti et al., 2001; Kirschner & Kennedy, 2001; Agosta & Kirschner, 2003; Bussolotto et al., 2007; Agosta et al., 2008; Breesch et al., 2009; Hausegger et al., 2010; Clemenzi et al., 2015; Smeraglia et al., 2016, 2018).

Syntectonic cements in exhumed fault zones provide information on environmental conditions of deformation in fault zones. Combining different geochemical analyses allows to better constrain the structural diagenetic evolution and to understand fluid-rock interaction processes, fluid migration pathways and fluid sources (Burkhard & Kerrich, 1988; Roure et al., 2005; Laubach & Ward, 2006; Vilasi et al., 2009; Wiltschko et al., 2009; Dewever et al., 2010; Cooley et al., 2011; Ferket et al., 2011). The oxygen stable isotopes ratios of cements depend mainly on compositions and precipitation temperatures of fluids while carbon stable isotope ratios depend on the sources of CO_2 in fluids (Friedman &

O'Neil, 1977; Hoefs, 1997). Therefore, carbon and oxygen stable isotope ratios are commonly used to identify the diagenetic environment of cements (Allan & Matthews, 1977; Hudson, 1977; Banner & Hanson, 1990; Nelson & Smith, 1996). Strontium geochemistry is specifically used in carbonate rocks stratigraphic and diagenetic studies as a proxy for age correlations and for fluid-rock interaction processes (Burke et al., 1982; Emery & Robinson, 1993). The strontium isotopes ratio of the cements directly records that of the cementing fluid (Banner, 1995; McArthur et al., 2012). Noble gases geochemistry, moreover, indicates whether volatile elements trapped in minerals derive from groundwaters saturated by atmospheric gases, from crustal fluids recording radiogenic decay or from magmatic fluids coming from the mantle (Ballentine et al., 2002a-b).

The Gran Sasso Massif, in the Central Apennines (Fig. 1), provides outstanding exposures of both thrusts and extensional fault zones affecting limestones and dolostones (e.g. Ghisetti and Vezzani, 1991; D'Agostino et al., 1998; Cardello and Doglioni, 2014; Pace and Calamita, 2015; Demurtas et al., 2016). Despite several structural studies, significant uncertainty still remains on the first-order structural architecture of the area, which includes Jurassic syn-rift structural inheritance, Messinian to Early Pliocene in-sequence and out-of-sequence thrusting, and Quaternary extensional faulting (e.g. Cardello & Doglioni, 2015). Among the matter of debates, the low-angle fault outcropping around Mt. Camicia (Fig. 2) has been interpreted as either a Mesozoic extensional fault passively rotated during folding and thrusting (Pace et al., 2014; Pace & Calamita, 2015), an Early Pliocene out-of-sequence thrust (Ghisetti & Vezzani, 1986, 1991; Ghisetti, 1987) or a Pleistocene postorogenic extensional fault (D'Agostino et al., 1998).

In this contribution, we present the results of a multidisciplinary study of the structural architecture and diagenetic evolution of the Camicia fault and the underlying Vado di Ferruccio Thrust (after Leah et al., 2018; or Upper Thrust after Cardello & Doglioni, 2015; Pace & Calamita, 2015). Structural analysis was combined with petrographical and geochemical analyses to understand the paleofluid evolution in the fault zones. Syntectonic cements were analyzed through optical and cold cathodoluminescence microscopy, carbon, oxygen, strontium and noble gases isotopes geochemistry. Our results support a thrust kinematics for the Camicia fault, then overprinted by late-stage extension, and indicate that the Camicia and Vado di Ferruccio thrust zones had a completely different structural diagenetic evolution, which was not

influenced by basement-derived fluids during thrust stacking and folding in the Gran Sasso Massif.

2. Geological Framework of the Central Apennines

The Central Apennines fold-and-thrust belt is a segment of the Alpine-Himalayan orogeny that grew in Neogene times due to westward subduction and rollback of the Adria microplate underneath the Eurasia plate (e.g. Principi and Treves, 1984; Malinverno and Ryan, 1986; Royden, 1988; Dewey et al., 1989; Patacca et al., 1990; Doglioni, 1991; Royden & Faccenna, 2018). The evolution of the Central Apennines thrust wedge has progressed by telescoping the Triassic to Cretaceous Adria passive margin carbonate sedimentary succession, which is characterized by important lateral facies variations between the Lazio-Abruzzi platform to the south, and the Umbria-Marche basin to the north (Fig. 1B, e.g., Colacicchi & Praturlon, 1965; Accordi & Carbone, 1986; Ciarapica & Passeri, 1998; Cosentino et al., 2010). In particular, the latter is characterized by thick Upper Triassic evaporites, which do not occur in the former, where poorly layered platform limestone dominates (Adamoli et al., 1990; Ciarapica, 1990; Ciarapica, 2007; Cosentino et al., 2010). Evidence for a Mesozoic complex syn-rift extensional tectono-sedimentary architecture is widespread in the Central Apennines and typically consists of horst-and-graben patterns generally sealed by the Upper Jurassic-Lower Cretaceous post-rift Maiolica formation (Centamore et al., 1975; Castellarin et al., 1978; Cosentino & Parotto, 1986; Santantonio, 1993; Pierantoni et al., 2013). The carbonatic succession exposed in the Gran Sasso massif preserves the paleogeographic transition between the Lazio-Abruzzi platform and the Umbria-Marche basin (Fig. 1B; Ciarapica, 1990; Ghisetti & Vezzani, 1991; Ciarapica & Passeri, 1998), including superb examples of Jurassic faulting (e.g., Cardello & Doglioni, 2015).

Synorogenic siliciclastic sediments constrain the onset of thrusting in the south-westward sector of the Central Apennines to the Late Tortonian, up to Early Pliocene times in the Gran Sasso Massif (Ghisetti & Vezzani, 1991; Ghisetti et al., 1993b; Cipollari & Cosentino, 1995; Cipollari et al., 1999; Centamore & Rossi, 2009). Thrust nucleation occurred in-sequence by overall north-eastward piggyback accretion, and was overprinted by out-of-sequence thrusting (Bally et al., 1986; Cavinato et al., 1994; Cipollari & Cosentino, 1995; Sani et al., 2004; Billi et al., 2006; Cosentino et al., 2010; Carminati et al., 2014), which is well evident in the Gran Sasso massif (Ghisetti & Vezzani, 1986,

1991), where the arc-shaped frontal thrust trending E-W in the western sector and N-S in the eastern one (Fig. 1B) resulted from the combined effects of both re-activation of the Mesozoic tectono-sedimentary extensional inheritance (Castellarin et al., 1978; Galluzzo & Santantonio, 2002; Scisciani et al., 2002; Calamita et al., 2003) and syn-orogenic block rotations about vertical axes (Dela Pierre et al., 1992; Mattei et al., 1995; Speranza et al., 2003; Satolli et al., 2005).

Intramontane basins started developing in the Central Apennines since Late Pliocene times, associated with NW-SE trending high-angle extensional faulting that dissected the previously formed contractional architecture (e.g. Cavinato & DeCelles, 1999; Ghisetti & Vezzani, 1999; D'Agostino et al., 2001; Cosentino et al., 2017). In particular, a major extensional pulse occurred at about 2 Ma and promoted uplift and widespread erosion, and the reorganization of the drainage systems (Bartolini et al., 2003; Centamore & Nisio, 2003; Galadini et al., 2003; Ascione et al., 2008; Cosentino et al., 2017).

The crustal structure of the Central Apennines is still a matter of debate and either thin- or thick-skinned tectonic styles have been proposed (Bally et al., 1986; Calamita e Deiana, 1988; Sage et al., 1991; Ghisetti et al., 1993a; Chiarabba and Amato, 1996; Barchi et al., 1998; Doglioni et al., 1998; Liotta et al., 1998; Patacca et al., 2008). According to Tozer et al. (2002), deformation rates obtained from balanced cross-sections where the crystalline basement is involved, provide more reasonable results compared to estimates from thin-skinned tectonic models. This adds to the Moho depth underneath the belt, which approaches 50 km (Tiberti et al., 2005; Mele et al., 2006; Di Luzio et al., 2009) thus suggesting thick-skin tectonics. However, the two contrasting models may not be alternative end-member solutions because the depth-to-décollement typically shallows forelandward in thrust wedges (Davis et al., 1983; Dahlen et al., 1984). The presence of the thick Triassic evaporites in basinal successions may have favoured mechanical decoupling between deformations affecting the overlying sedimentary successions and contraction in the basement (Davis & Engelder, 1985; Graveleau et al., 2012).

The environmental conditions of deformation in the Central Apennines have been constrained by vitrinite reflectance studies, apatite fission track thermochronology, fluid inclusion microthermometry and stable isotope geochemistry (Corrado, 1995; Ghisetti et al., 2001; Murgia et al., 2004; Rusciadelli et al., 2005; Agosta et al., 2008; Ronchi et al., 2010; Smeraglia et al., 2016). Thermochronological modelling suggests that maximum

burial of the exposed carbonate successions never exceeded 4 km, at temperatures lower than about 100 °C, indicating a geothermal gradient of about 20 °C/km, and that the burial history of the Adria passive margin successions is characterized by two burial and exhumation episodes, related to the passive margin and the foredeep stages, respectively (Rusciadelli et al., 2005).

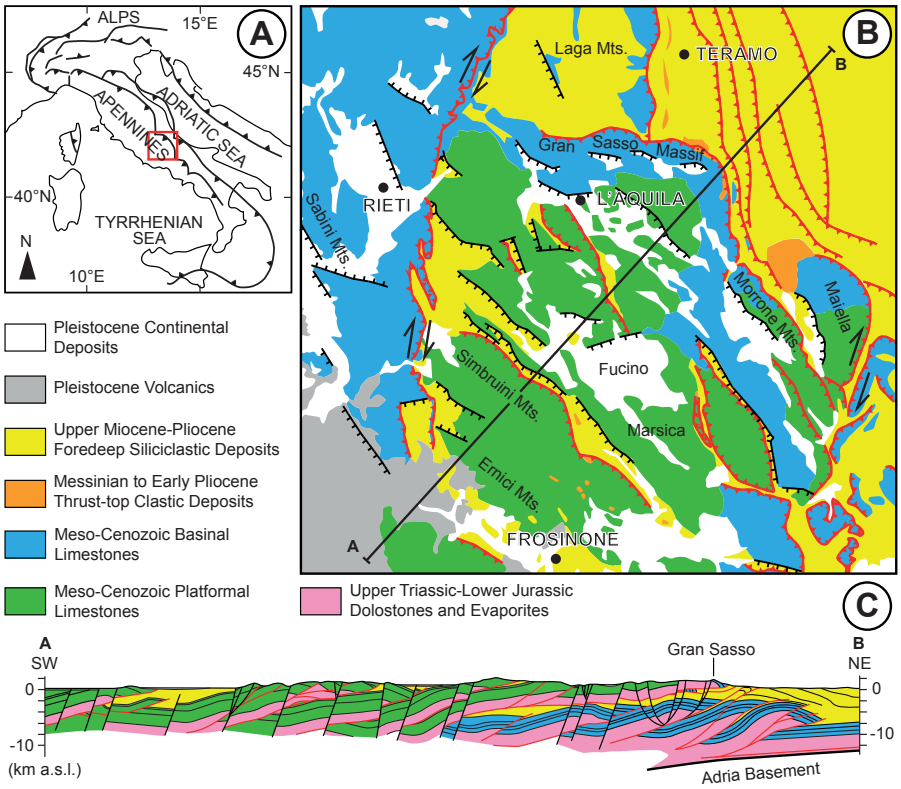


Figure 1. (A) Location of the study area, in the Central Apennines. (B) Tectonic sketch map of the Central Apennines showing the Gran Sasso Massif and other major thrust sheets overprinted by extensional faulting; arrows indicate transpressive lineaments and trace A-B refers to cross-section in C. (C) Cross section of the Central Apennines orogenic wedge, after Cosentino et al., 2010.

3. Structural Setting of the Study Area

The following summary description is largely based on geological mapping and structural analysis work performed in the area by F. Ghisetti & L. Vezzani (1986; 1991; 1997). The first-order structural architecture of the Gran Sasso massif consists of three vertically stacked thrust sheets, lying in the hanging wall of the Gran Sasso Frontal Thrust and separated by, from bottom to top, the Vado di Ferruccio and Monte Camicia thrusts, respectively (Figs. 2, 3). Overturned, E-W striking, anticlines and synclines involving the Lower Jurassic to Messinian sedimentary succession characterize the TS3 thrust sheet, directly overlying the Gran Sasso Frontal Thrust, and are decapitated by the out-of-sequence, convex-upward Vado di Ferruccio Thrust (Fig. 2C). The hanging wall of the latter consists of Upper Triassic bituminous dolostones to Miocene calcarenites, mostly arranged in a NNE-dipping monocline (TS2 in Figs. 2B, C). At the top of the stack, the hangingwall of the Monte Camicia thrust consists of 20° to 50° N-dipping Upper Triassic

dolostones to Paleogene marly limestones and marls (TS1 in Figs. 2B, C). This fault juxtaposed younger-on-older rocks, indicating again an out-of-sequence chronology, and is characterized by an array of subsidiary thrusts dissecting the overall monocline geometry.

The Campo Imperatore Fault (e.g. Demurtas et al., 2016) extensional fault system has an estimated maximum downthrow of about 2000 m (Servizio Geologico d'Italia, 1963) and consists of an array of E-W to NW-SE striking high-angle fault zones bounding to the north the Campo Imperatore intermontane basin (Figs. 2A, B; e.g. Ghisetti and Vezzani, 1986). The latter is filled by fluvio-glacial Quaternary deposits affected by well evident extensional deformations (Giraudi & Frezzotti, 1997; Galadini & Messina, 2004).

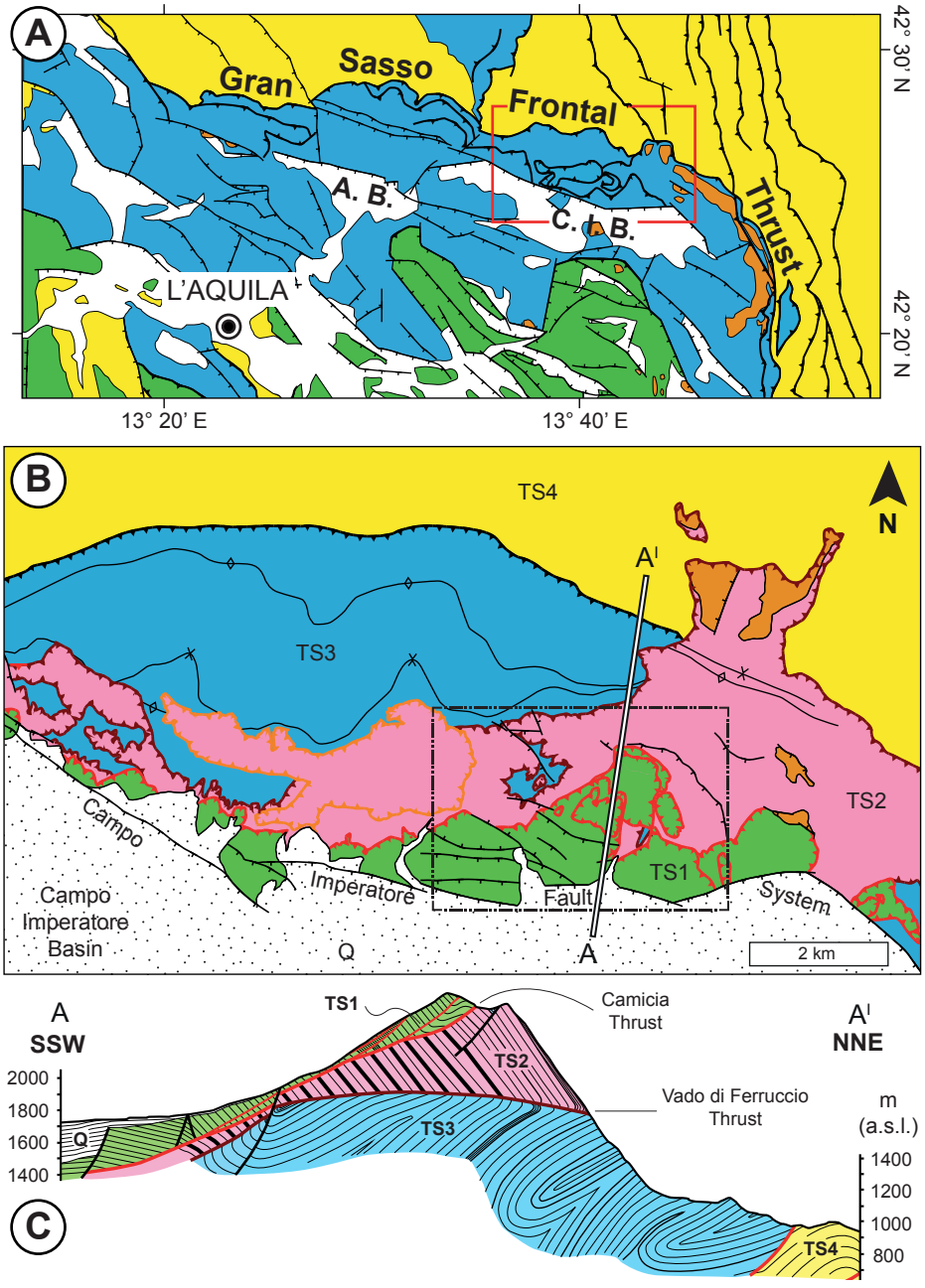


Figure 2. (A) Tectonic map of the Gran Sasso Massif showing the arc-shaped geometry of the Frontal Thrust and the extensional fault-bounded Campo Imperatore Basin (C.I.B.) and Assergi Basin (A.B.); red square indicates B; colors as in Fig.1. (B) Structural map showing the four thrust sheets (of which TS1 to TS3 belong to the blue lithostratigraphic unit of Figs. 1B and 2A) and the main faults and folds between Vado di Corno and the north-eastern apex of the massif; trace A-A' corresponds to the cross-section in C; dashed black rectangle represents the study area. (C) Cross-section passing through Mt Camicia (adapted from Ghisetti & Vezzani, 1986); colors as in B.

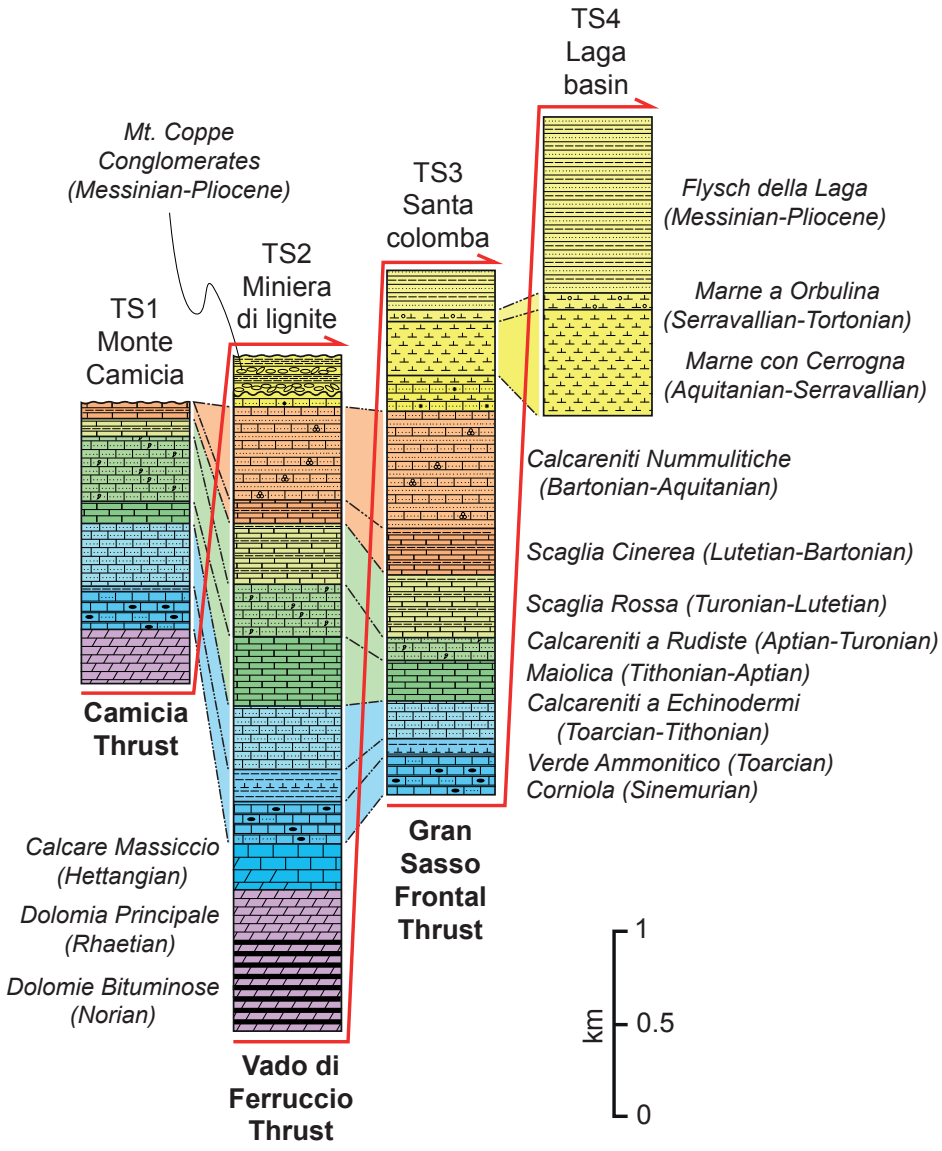


Figure 3. Stratigraphic sections, after Ghisetti & Vezzani (1991), showing variations in thickness of Jurassic, Cretaceous and Paleogenic formations in the four thrust sheets represented in Figs. 2B-C and the Camicia, Vado di Ferruccio and Gran Sasso Frontal Thrusts.

4. Methods

4.1 Structural analysis

A total of 1480 structural data were collected at thirty-nine structural sites, along the Camicia and Vado di Ferruccio thrust faults. Data from the latter are summarized from Leah et al. (2018). Structural data are reported according to the right-hand rule, and were analyzed by the Daisy3 software (Salvini, 2018), using Wulff and Schmidt nets for stereographic projections of planes, and pole to planes contouring, respectively.

4.2 Petrography

101 thin sections were cut from 61 rock specimens sampled in the fault cores and

damage zones of the Camicia and Vado di Ferruccio fault zones, respectively, and in the protoliths unaffected by faulting-related deformations. Each sample was cut in two slabs, one of which was stained with Alizarin Red S and potassium ferricyanide to discriminate the different carbonates such as calcite and dolomite and their iron-rich equivalents (Dickson, 1966). The remaining slab was used to obtain a 30 μm thick thin section. Petrographic optical analysis was performed by a Zeiss Axioplan 2 microscope. Moreover, cold cathodoluminescence (CL) microscopy was performed by a Technosyn 8200 Mark II cold CL stage, mounted on a LEICA DM2700P optical microscope, at 10 kV and 256 μA gun current. Qualitative compositional maps of the two studied fault zones were acquired on four thin sections with a Zeiss Gemini 500 Scanning Electron Microscope. Operating conditions were 20 kV and 1.2 nA, 60 μm aperture, 8 mm distance and a 300-600 s counting time.

4.3 Carbon and oxygen stable isotopes

Oxygen and carbon stable isotope ratios were measured on 94 selected samples of limestone and dolostone host rocks and cements after petrography and cathodoluminescence analyses. Stable isotope ratios are expressed in V-PDB (Vienna Pee Dee Belemnite). 73 sub-samples of veins and host rocks were drilled directly from thin sections with an ESI New Wave Research Micromill with sub-micron step resolution and a milling chuck speed ranging from 1200 rpm to 35000 rpm. 21 additional sub-samples were drilled from rock slabs using a dental drill with 500 μm of width drill bits. 150-200 μg of carbonate powder for each sample were loaded into a GasBenchII autosampler, interspaced with three different reference materials (NBS18, NBS19 and MAB99). After helium flushing, 100% orthophosphoric acid was added at 25 °C and reacted for 2 h at 72°C. Dolostone samples were corrected according to Rosenbaum and Sheppard, 1986). Resulting gases were analyzed automatically using a Thermo Finnigan Delta V+ mass spectrometer. A total of 40 peaks, in 10 steps, were measured for each sample. Each sample was analyzed twice. Data uncertainty is ±0.10‰ and ±0.15‰ for $\delta^{13}C$ and $\delta^{18}O$, respectively.

4.4 Strontium isotopes

Strontium isotope ratios were measured with a ThermoElectron Triton plus TIMS at Vrije Universiteit, Amsterdam. $^{87}Sr/^{86}Sr$ ratios were measured in 20 blocks of 10 cycles with an 8 s per cycle integration time. $^{87}Sr/^{86}Sr$ ratios were corrected for mass fractionation using Russell's exponential law with an $^{86}Sr/^{88}Sr$ ratio of 0.1194 (Steiger and Jager, 1977). NBS987 is the international standard used for $^{87}Sr/^{86}Sr$ ratio calibration. Analytical reproducibility was checked with load sizes of 10 ng and 100 ng of the international Sr standard NBS987 (N=58). Mean $^{87}Sr/^{86}Sr$ ratio for the 10 ng NBS987 loads measurements was 0.710245 ± 0.000022 while it was 0.710242 ± 0.000008 for the 100 ng loads (Font et al., 2012).

4.5 Noble gases isotopes

The abundances and isotopic composition of the noble gases were measured by in vacuo crushing release using a VG5400 noble gas mass spectrometer that has upgraded electronics and software (Isotopx NGX) to improve instrument stability during the measurements. Around 200 mg of 0.5-1 mm-sized sample fragments were washed in acetone followed by de-ionised water in an ultrasonic bath. The washed samples were dried under a heat lamp. The cleaned samples were placed in a stainless-steel screw-type crusher (Stuart et al., 1994) and baked under vacuum at ~150 °C for 12 hours to reduce adsorbed atmospheric gases. The crushing step involved screwing down the piston to crush the samples and release gases from fluid inclusions. After the crushing step, the released noble gases underwent purification using a hot SAES GP50 getter for 10 minutes to remove active gases. The heavy noble gases, Ar, Kr and Xe were trapped on a cold finger of activated charcoal, cooled by liquid nitrogen to 77K, whilst the light noble gases, He and Ne, were expanded into the mass spectrometer. Following He and Ne isotope determinations, Ar, Kr and Xe were released from the cold finger by heating to 250 K and admitted to the mass spectrometer. $^{3}He/^{4}He$ and $^{40}Ar/^{36}Ar$ ratios were determined together with abundances of ^{21}Ne, ^{84}Kr and ^{132}Xe. Blanks were obtained by using an identical procedure to sample analysis, but without operating the crushers and were carried-out after each sample loading. The noble gas blank level is <1% of a sample release of He, Ar and Kr and no higher than 3% for Ne and Xe. Data were acquired using either Faraday ^{4}He (Ar isotopes) or electron multiplier detectors measured over 20 cycles and regressed to inlet time. Calibration for instrument mass discrimination and sensitivity was determined using the HESJ standard for He ($^{3}He/^{4}He$ = R = 20.63 ± 0.01, R/Ra; Ra = atmospheric $^{3}He/^{4}He = 1.39 \times 10^{-6}$; Matsuda et al., 2002) and air for Ar, Kr and Xe. Calibrations were

analyzed at the start of each day.

5. Contractional Structural Architecture

The mapped fault pattern and contractional structural data are illustrated in Fig. 4.

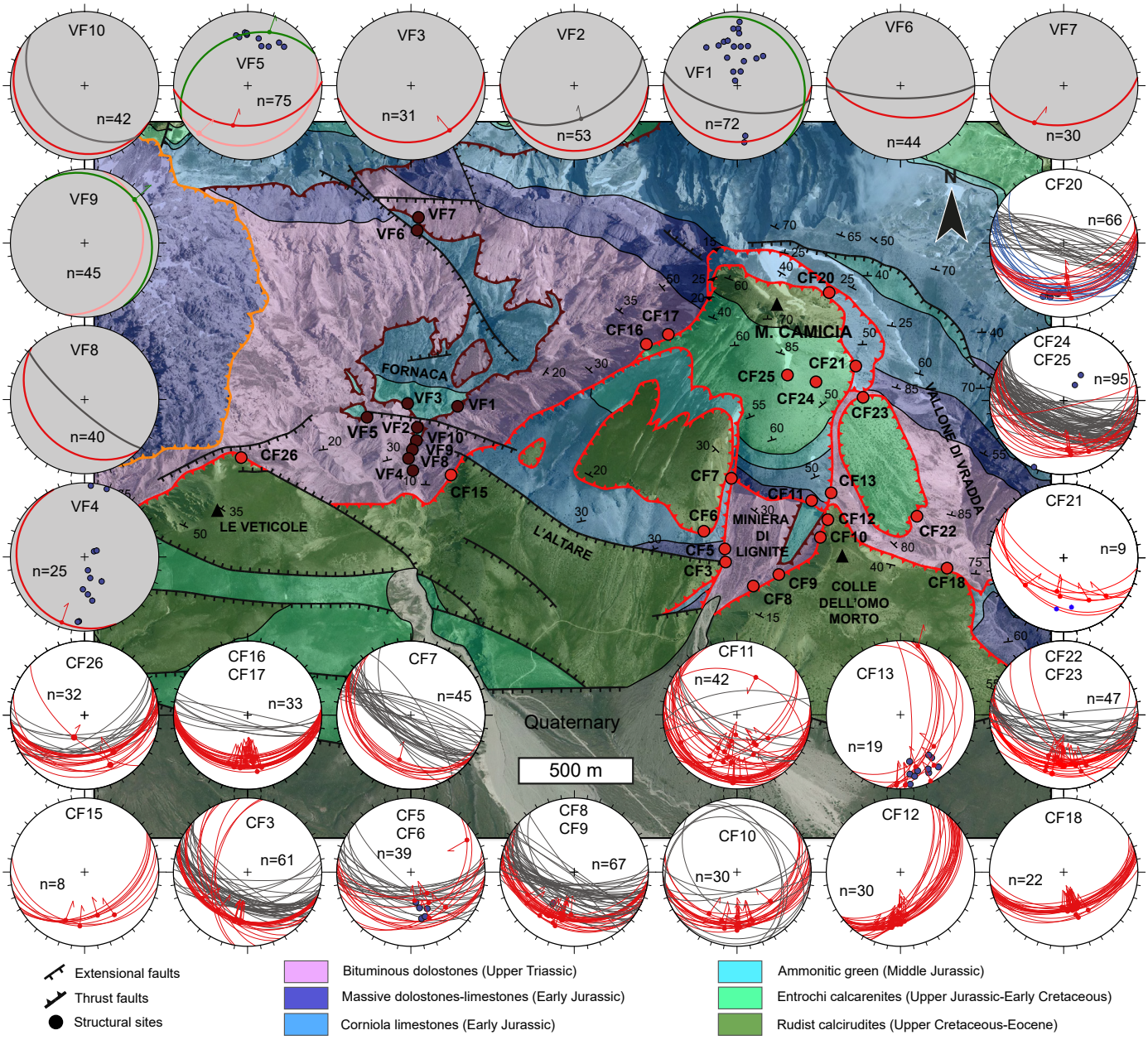


Figure 4. Aerial orthophoto showing lithostratigraphic units, thrusts, extensional faults and structural sites in the study area. Red for the Camicia Thrust, bordeaux for the Vado di Ferruccio Thrust and orange for the Prena splay Thrust. In the stereographic projections, great circles and slickenlines in red represent thrust surfaces and relative lineations, grey for tectonic stylolites, blue for bedding parallel stylolites, green for C' shear surfaces, pink for subsidiary thrust surfaces and blue dots correspond to poles to bedding. Stereonets with white background for the Camicia Thrust and grey background for the Vado di Ferruccio Thrust.

The map indicates that the Monte Camicia Thrust is a complex fault system consisting of a basal master slip surface (ϕ_1 to ϕ_4 in Ghisetti and Vezzani, 1986) mostly placing northward-dipping Jurassic to Cretaceous limestones onto northeastward-dipping Upper Triassic bituminous dolostones and Early Jurassic massive dolostones at the footwall. Two main splay thrusts (ϕ_3 and ϕ_2 in Ghisetti and Vezzani, 1986) emanate from the basal one, respectively near Mt. Camicia and to the south-west (Figs. 5A, B). Overall, this thrust array can be described as an out-of-sequence structure characterized by a strong lateral variability.

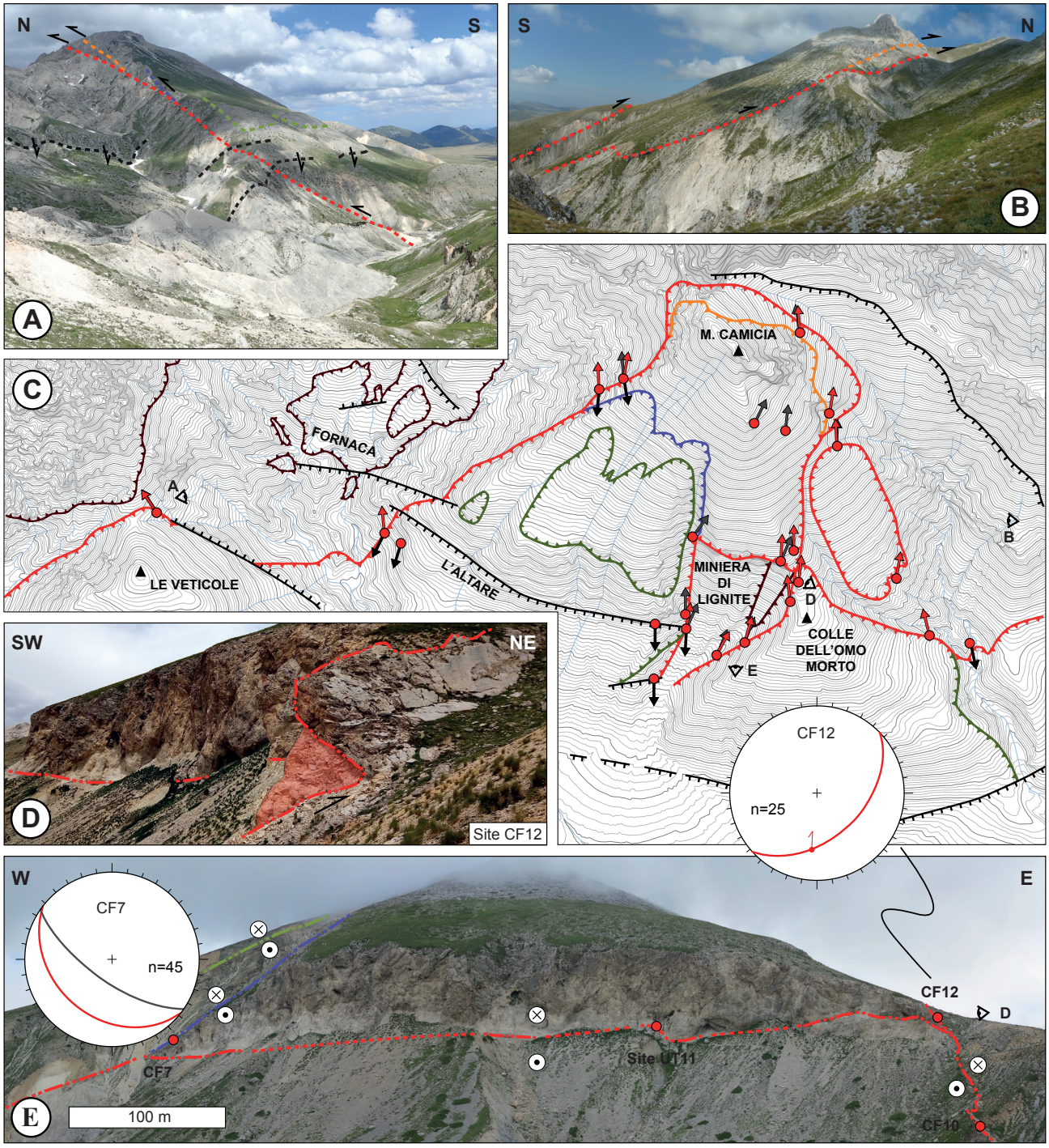


Figure 5. Pictures and line-drawings of the Camicia Thrust seen from the west (A) and from east (B). The master basal slip surface is in red, minor splays are in orange, green and purple while high-angle extensional faults are in black. Arrows indicate kinematics. (C) Architecture of the Camicia Thrust and mean directions of the kinematics measured in the structural sites. Red arrows represent slickenlines on thrusts, grey arrows are orthogonal to the intersection line between S and C planes of thrusts and black arrows for slickenlines on extensional faults. “Eye” symbols indicate where pictures were acquired. (D) Picture and drawing of Site CF12, where the Camicia Thrust shows transpressional kinematics. (E) Picture and linedrawing of the top of the Miniera di Lignite area, where the hanging wall acquires a lensoidal geometry. The splay thrust on the west, in Site CF7, shows southwest dipping planes while they are southeast dipping in the eastern part (Site CF12; D). Stereographic projections show average planes and slickenlines in the respective site. Grey for tectonic stylolites and red for thrust surfaces and slickenlines.

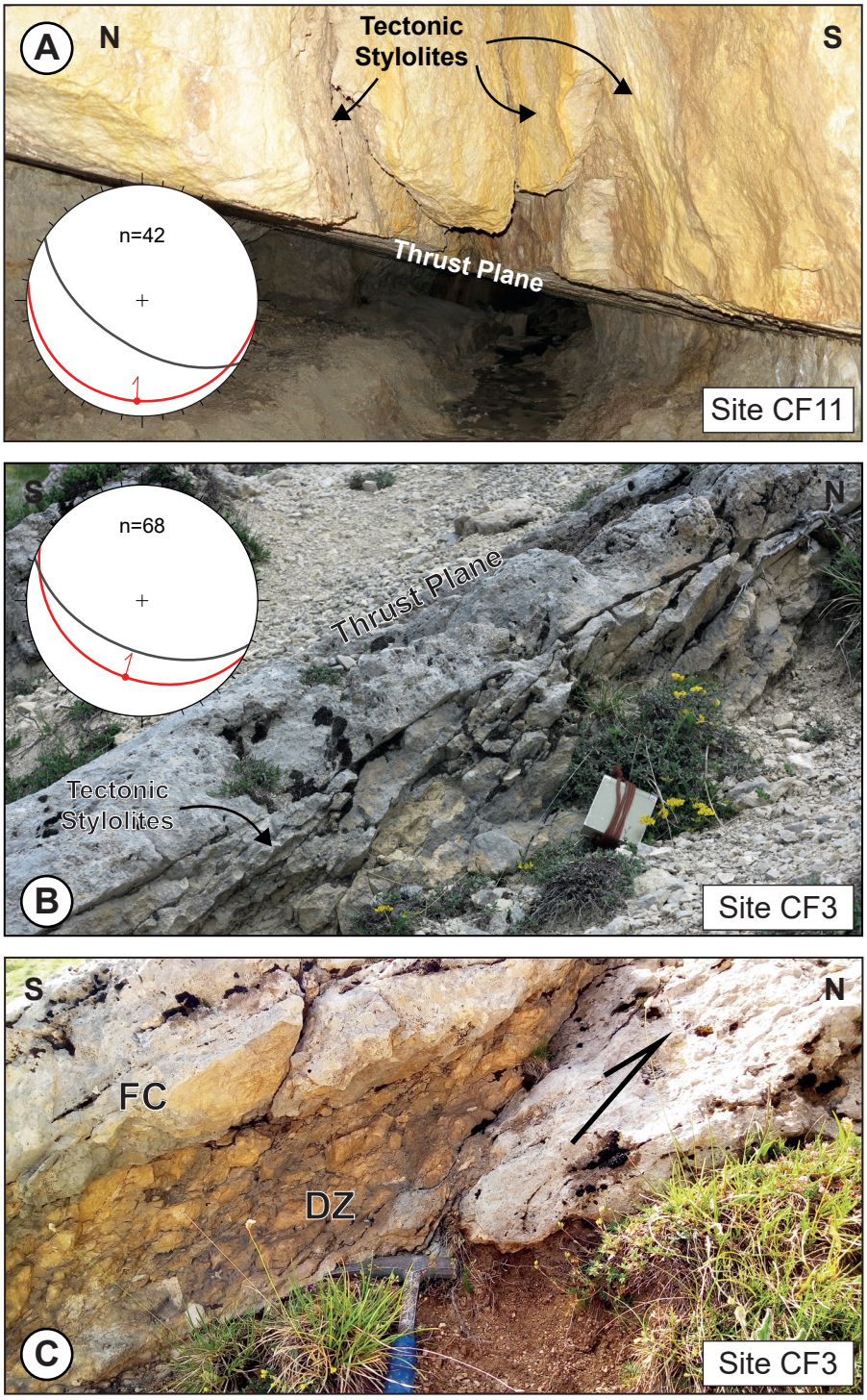


Figure 6. Pictures showing contractional structures of the Camicia Thrust. (A) Fonte Grotte cave, Site CF11, showing sharp south dipping thrust surface with top-to-the north kinematics and high-angle south-southwest dipping tectonic stylolites in the hanging wall damage zone. (B) Western side of the Miniera di Lignite area, Site CF3, showing karstified fault core and tectonic pressure solution planes in the footwall damage zone that dip south-southwest and have a top-to-the north-northeast transport direction. (C) Picture acquired in the same site of B showing a subsidiary thrust which causes duplexing of the Thrust zone. Stereographic projections show average planes and slickenlines in the respective site. Grey for tectonic stylolites and red for thrust surfaces and slickenlines.

The Monte Camicia Thrust basal master slip surface strikes WSW-ENE in the Le Veticole area to the west (sites CF26 and CF27), E-W near the summit of Mt. Camicia (sites CF16 and CF17) and in the klippe to the east (sites CF22 and CF23), and again WSW-ENE at the east of Colle dell'Omo Morto (site CF18; Fig. 4). Tectonic transport directions are typically to the north, provided by S-C like arrays of compactional and shear surfaces (Fig. 6). Only in Le Veticole area the tectonic transport direction is towards the north-west (Fig. 5C). In the Miniera di Lignite tectonic window, fault geometry shows a higher variability, from WNW-ESE strike (sites CF3, CF7, CF8 and CF9) to E-W (sites CF5 and CF11), up to WSW-ENE (site CF10), SW-NE (site CF12) and almost N-S (site CF13). Despite such a variability, tectonic transport directions are constantly to the north, apart from sites CF7, CF8 and CF9, where shear sense is towards NNE (Fig. 5C). This implies that NNE-SSW to N-S faults attain a left-lateral transpressional (site CF12) to almost strike-slip (site CF13) kinematics (Fig. 5D). As a consequence, the basal thrust sheet in this area pinches out towards the east and attains a lensoidal shape (Fig. 5E). Structural data on the splay thrust near the summit of Mt. Camicia (site CF20) indicate a northward transport direction (Fig. 5C).

Structural data of the Vado di Ferruccio Thrust are synthetically illustrated in Fig. 4 and show that the master slip surface strikes almost E-W and dips southward, apart from sites VF8 and VF10 where it attains a NW-SE strike and a south-westward dip. The fault zone is characterized by well-developed S-C-C' structural fabrics (Figs. 7A-D) indicating significant variability in the tectonic transport, ranging from top to the NW in the southwestern sector of the Fornaca tectonic window, up to top to the NE in the southeastern one. Folding in the footwall damage zone is common and poles to fold limbs describe N-S girdles (Leah et al., 2018).

To sum up, cumulative analysis of structural data collected along the Monte Camicia Thrust indicates that the mean strike of the master slip surface is 092° and the mean dip is 33° to the S. Slickenlines mean rake is 008° 35°, with a northward tectonic transport direction, as indicated by pressure solution surfaces in the thrust damage zones, which strike 109° and dip 68° southward (Fig. 8). Cumulative analysis of structural data collected along the Vado di Ferruccio Thrust show two main clusters oriented 083° 24° and 088° 48°, respectively. Slickenlines have a mean rake of 037° 39° and dip to the south. Pressure solution surfaces in the thrust damage zone have quite variable orientations, with three main maxima, at 138° 40°, 130° 80° and 090° 70°, respectively.

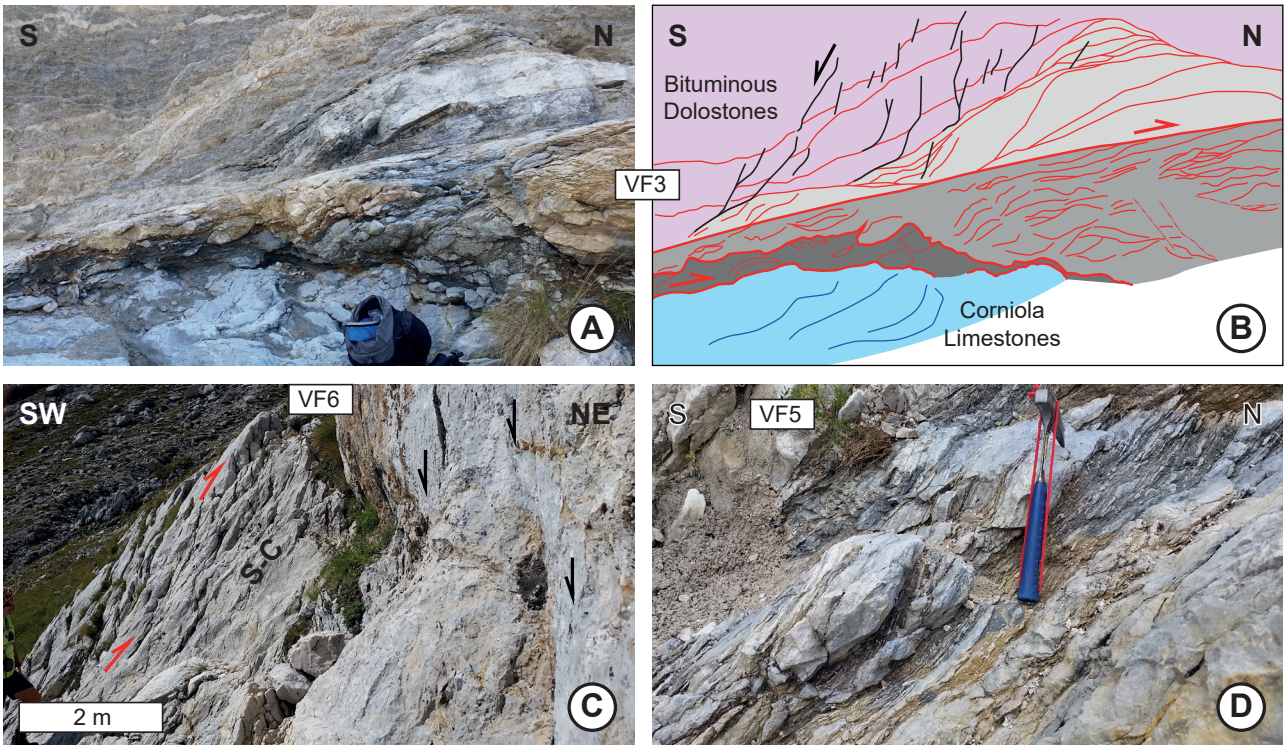


Figure 7. Picture (A) and linedrawing (B) of the Vado di Ferruccio Thrust. The footwall damage zone is composed of folded corniola limestones, the fault core has a sharp upper boundary and pressure solution increases towards the bottom and the hanging wall damage zone is made of a zone of minor duplexing near the fault core and a zone interested by extensional faults that sole down onto the fault core upper boundary. (C) NW-SE near vertical extensional fault cutting through the Vado di ferruccio Thrust. (D) The fault core is a foliated cataclasite. Here, in Site VF5, C' synthetic low-angle planes are well developed.

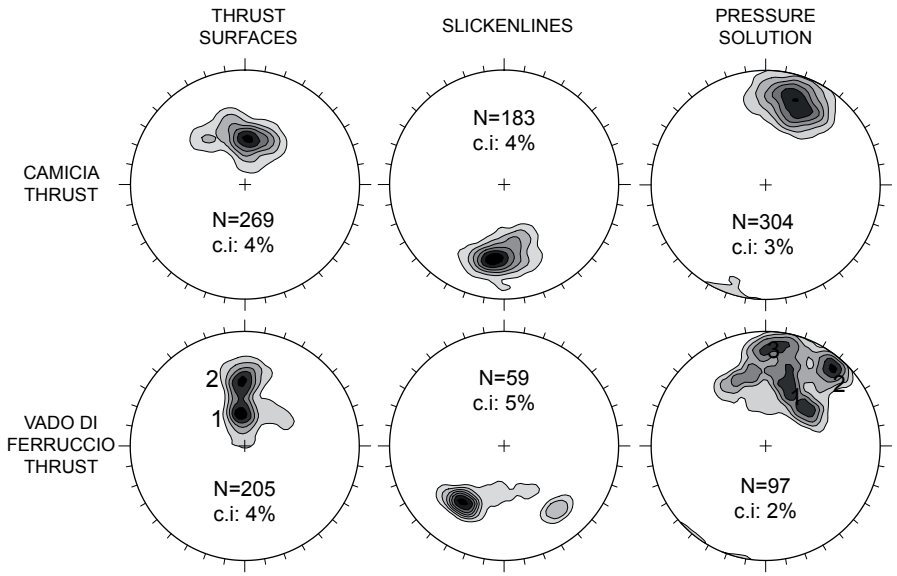


Figure 8. Stereographic projections of cumulative structural data of thrust surfaces, slickenlines and pressure solution planes collected along the Vado di Ferruccio and Camicia thrusts. N and c.i. indicate number of data and the contouring interval, respectively.

6. Extensional Structural Architecture

The extensional fault pattern is best expressed in the southern part of the study area and consist of E-W to NW-SE striking, high-angle fault zones dipping either northward or southward and overprinting the contractional pattern (Fig. 9). In the Fornaca

valley, the Vado di Ferruccio Thrust is dissected by two extensional fault zones striking WNW-ESE (site VF2) and NW-SE (site VF6; Fig. 7C), respectively. Structural data indicate dip-slip motion in both cases, as well as at other sites in the hanging wall (VF4, VF9 and VF10) and in the footwall (VF8) of the Vado di Ferruccio Thrust. At sites VF3 and VF5, low-displacement high-angle extensional faults sole down into the master slip surface of the Vado di Ferruccio Thrust (Figs. 7A, B).

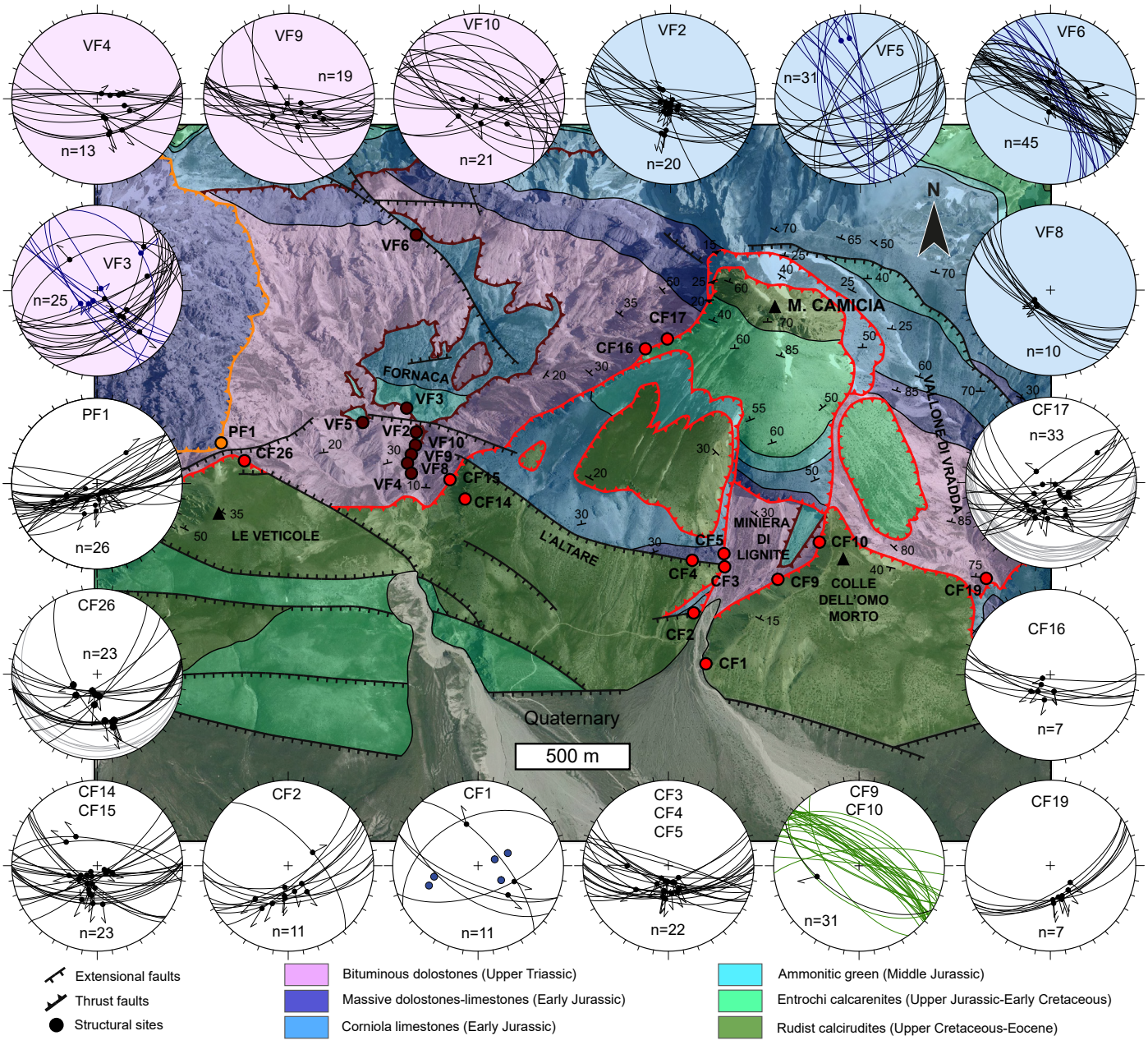


Figure 9. Aerial orthophoto showing lithostratigraphic units, thrusts, extensional faults and structural sites in the study area. Red for the Camicia Thrust, bordeaux for the Vado di Ferruccio Thrust and orange for the Prena splay thrust. In the sterographic projections, black great circles and slickenlines for extensional faults, blue for NW-SE strike-slip faults, grey for low-angle tectonic stylolites, green for extensional joints in the Camicia Thrust hanging wall damage zone and blue dots are poles to bedding planes. Stereographic projections with white background for Sites where extensional faults are in the hanging wall of the Camicia Thrust while orange where extensional faults cut through it. Pink and blue backgrounds for Sites where extensional faults sole down onto and cut through the Vado di Ferruccio Thrust, respectively.

Evidence for negative inversion of the contractional architecture is widespread along the Monte Camicia Thrust. Subsidiary extensional faults are abundant in the hanging wall of the basal master slip surface to the west of Mt. Camicia and flatten down into it.

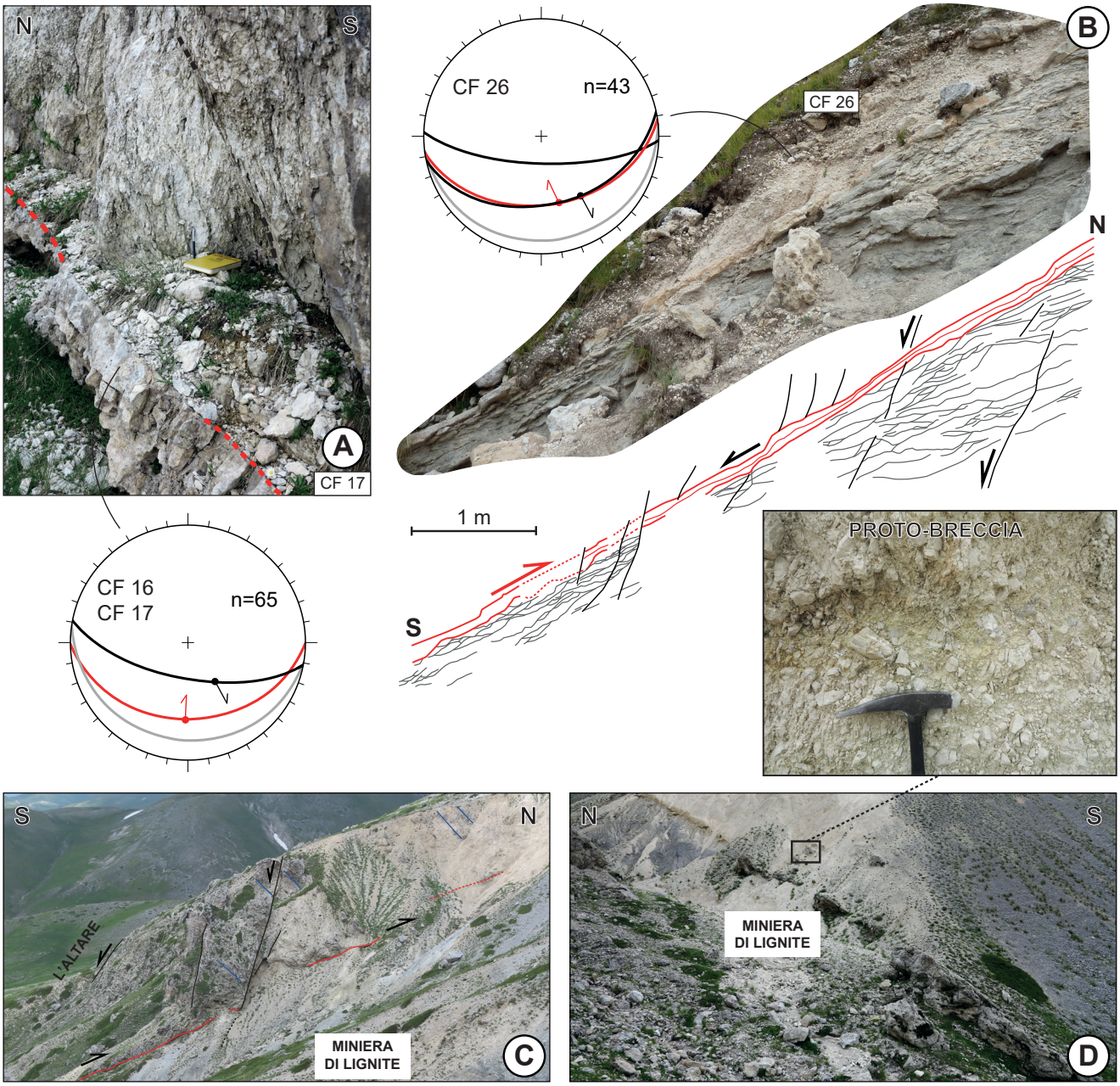


Figure 10. (A) Outcrop picture of south dipping extensional faults, shaded black lines, flattening down onto the Camicia Thrust, shaded red lines, in the calcarenites near the top of Mt. Camicia, in Site CF17. (B) Picture and linedrawing of the Camicia Thrust in Site CF26 where extensional reactivation is testified by extensional faults both falttening and cutting the thrust surface and by low-angle tectonic stylolites. (C) Picture showing the western side of the Miniera di Lignite area where an extensional fault zone with metric offset, black lines, dissects the Camicia Thrust, red lines. (D) Picture showing the eastern side of the Miniera di Lignite area. Here, as in the footwall of the extensional fault zone in C, the hanging wall of the Camicia Thrust is characterized by intense fracturing by high-angle joints causing proto-brecciation of the Calcarenites, as illustrated in the inset.

Near horizontal tectonic stylolites occur mainly in the footwall of the fault (site CF17; Fig. 10A). A similar geometric and kinematic array occurs along a subsidiary thrust splay, at site CF14, in the hanging wall (Fig 9). Near the westward boundary of the study area, negative inversion of the basal master slip surface produced abundant shallow dipping compactional surfaces in the footwall damage zone (Fig. 10B). Exposures of the Monte Camicia Thrust in the Miniera di Lignite tectonic window preserve evidence for both the negative inversion of the master slip surface (site CF10), and its offsetting by a high angle extensional fault zone (sites CF3, 4, 5). It is worth noting that intense jointing and proto-brecciation affects the rocks in the footwall of this fault zone (Fig. 10C). A similar fabric is well developed on the eastern side of the valley, in the hanging wall of the thrust master slip surface (Fig. 10D).

Summarizing, cumulative structural data analysis indicates that extensional fault zones flattening onto the Vado di Ferruccio Thrust have a mean orientation of 088° 80° with slickenlines oriented 199° 77°. On the other hand, extensional fault zones cutting through the thrust are oriented 121° 85° with a mean slickenline orientation of 202° 82° (Fig. 11). In the hanging wall of the Monte Camicia Thrust, extensional fault zones flattening onto the main basal slip surface are oriented 095° 74° with slickenline orientation of 200° 70°. In the southern part of the Miniera di Lignite area, extensional faults dissecting the thrust are oriented 086° 62° and show slickenlines with a mean orientation of 184° 67°.

7. Structural Diagenetic Features of the Monte Camicia and Vado di Ferruccio Thrust

7.1. Monte Camicia thrust zone

The Monte Camicia thrust zone is generally composed of a sharp and well-defined principal slip surface juxtaposing up to 5 meters thick shattered calcarenites in the hanging wall damage zone, onto a 2 to 3 meters thick footwall damage zone made of dolostones, which locally show vuggy porosity. Hanging wall Rudist Calcarenites (RCHR) are composed of bioclasts, carbonatic micrite and minor chert and are interested by bedding-parallel pressure solution surfaces, while Bituminous Dolostones (BDHR) in the footwall are made of fine crystalline idiotopic-S dolomite crystals (Gregg & Sibley, 1984), clays and organic material. The fault core consists of cataclasites and foliated cataclasites (Figs. 12A-B). The latter show an array of S-C planes made of micritic calcite (CFCalSB) separating lensoids of crackle-brecciated dolostones (Woodcock & Mort, 2008) and dolostones survivor clasts (CFDolCalSB; Fig. 12A; Site CF26), frequently overprinted by extensional shear fractures. Injection veins of finely crystalline dolomitic-calcareous matrix

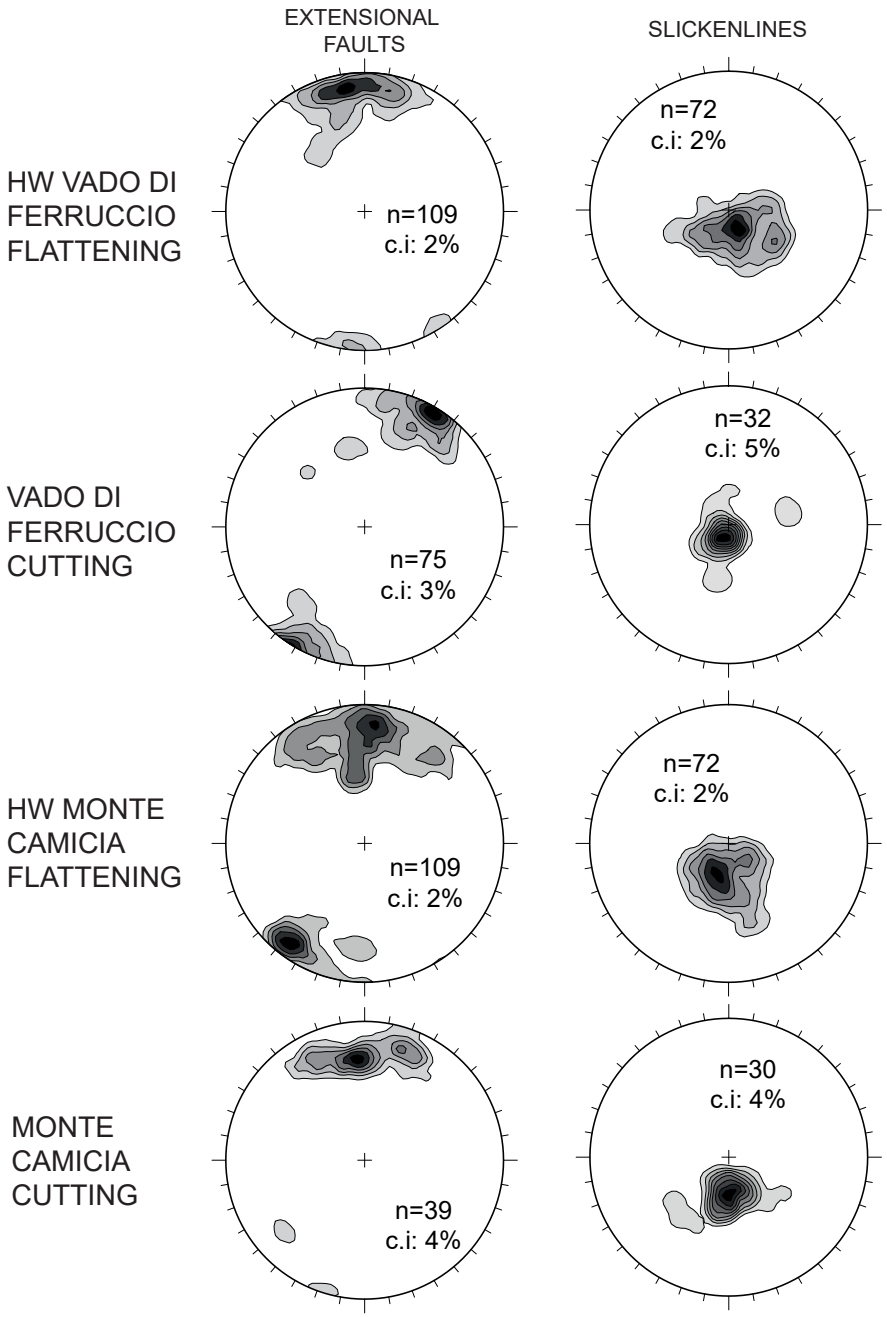


Figure 11. Stereographic projections of cumulative structural data of extensional fault planes and slickenlines flattening onto and cutting through the Vado di Ferruccio and the Camicia thrusts. N and c.i. indicate number of data and the contouring interval, respectively.

originated at the principal slip surface and propagated into the hanging-wall cataclastic material. The principal slip surface is typically dilated and cemented by a thin calcite vein (Fig. 12B). Some low-angle tectonic stylolites also affect the fault core rocks. In the Miniera di Lignite, the thrust zone is characterized by widespread karstification (Sites CF3, CF5-10) affecting cataclastic rocks both on the hanging wall and footwall sides. Karst porosity is cemented by non-ferroan dogtooth to equant calcite crystals (CFCalV) that typically have dimensions lower than about 100 μm and show alternating non-luminescent and yellow colours under cathodoluminescence (Figs. 12C-F). Calcite veins dipping gently to the north occur in the footwall of the southward-dipping principal slip surface. They are locally

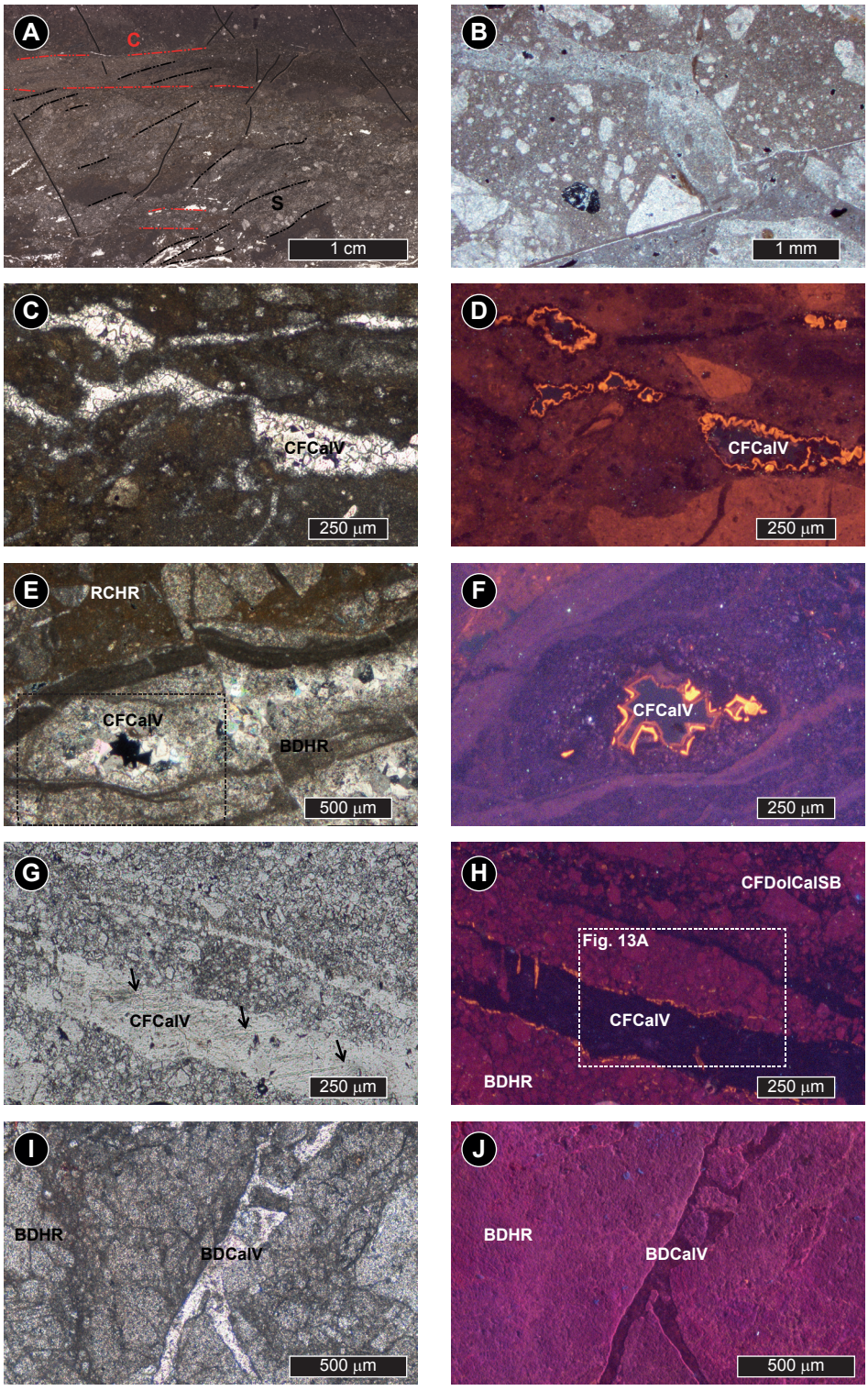


Figure 12. Petrography of the Camicia thrust zone. All images have top-to-the right shear sense. (A) Thin section scan of foliated cataclasite sampled in the fault core in Site CF26; line-drawing hgihlights the S-C surfaces overprinted by high-angle extensional shear planes. (B) XPL image showing injection of vein of cataclastic material into the hanging wall damage zone and low-angle vein along the main thrusting surface; sampled in Site CF22. (C) PPL and (D) CL images of calcarenites sampled in the fault core in Site CF10 where microfractures subparallel to the thrust are cemented with dogtooth, black-yellow-black zoned calcite. (E) PPL and (F) CL images showing dolostones interested by vuggy porosity below the fault core in Site CF9; vugs are cemented by dogtooth black-yellow-black zoned calcite. (G-I) PPL and (H-J) CL images illustrating the black-yellow-black CFCalV calcite low-angle vein (G-H) and the non-luminescent BDCalV calcite high-angle vein (I-J) in the footwall damage zone in Site CF3.

interested by Type I twinning of Burkhard (1993), and show the same alternating cathodoluminescence colours of cements infilling karst porosity (CFCalV; Figs. 12 G, H). High-angle, non-luminescent and non-ferroan calcite veins (BDCalV) occur in Bituminous Dolostones the footwall damage zone. Qualitative compositional maps highlights that, approaching the principal slip surface, discrete veining is replaced by diffuse stockwork

microcracking, cemented by calcite. Both dolostones clasts and calcite cements are affected by dissolution that creates vuggy porosity. The volume of voids increases in proximity of the principal slip surface (Figs. 13A-C).

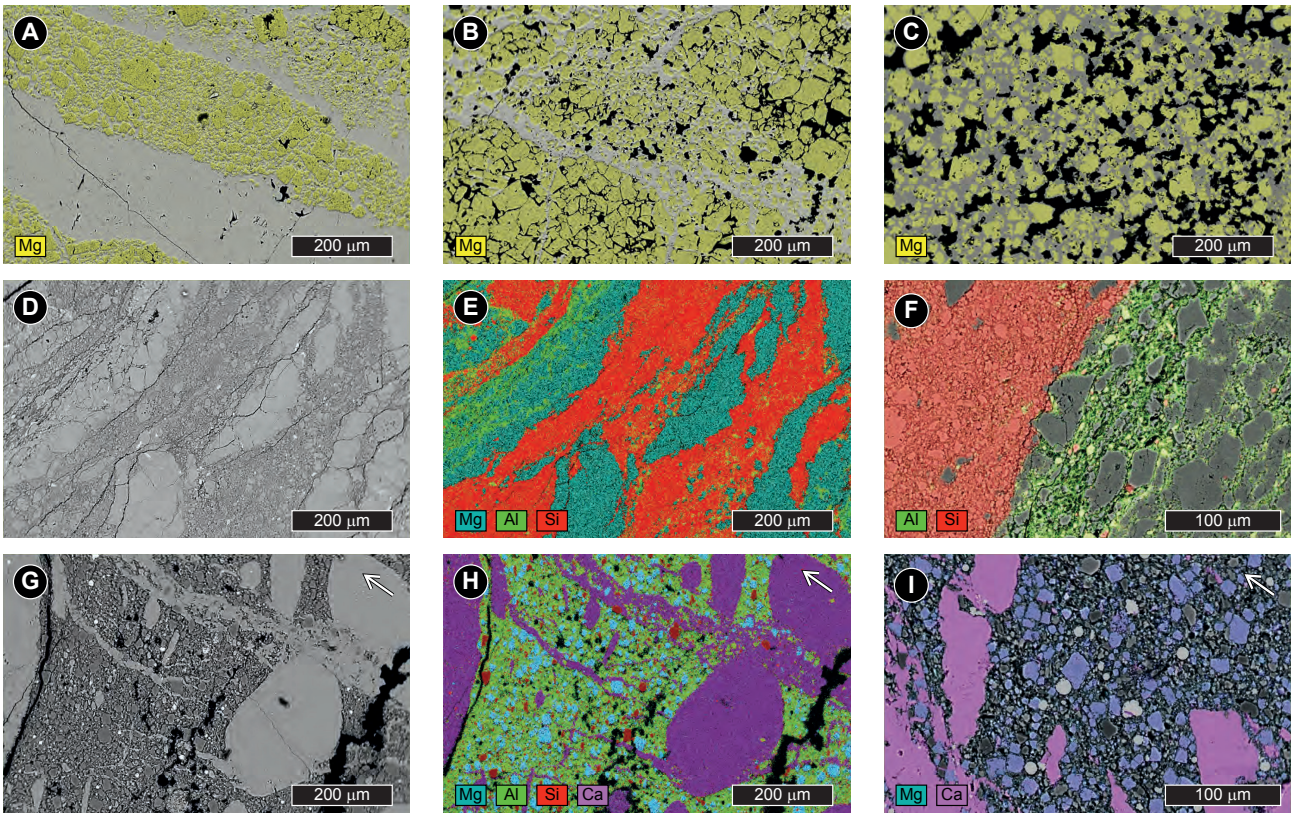


Figure 13. BSE images overlapped onto SEM-EDS qualitative compositional maps. (A-B-C) show calcite cement in the Bituminous Dolostones of the footwall damage zone (A-B) and in the fault core of the Camicia Thrust (C); fracturing increases towards the fault core causing disaggregation of dolostones; calcite, occurring in discrete microfractures in A, becomes interparticle cement in C; secondary porosity increases. BSE (D) and map (E) of micro-crystalline silica bands overprinting tectonic stylolites in the hanging wall damage zone of the Vado di Ferruccio Thrust in Site VF1. (F) Detail of (D-E) illustrating a silica band parallel to- and re-opening a pressure solution plane. BSE (G) and map (H) of tectonic stylolite in Corniola Limestones of the Vado di Ferruccio Thrust footwall damage zone in Site VF3 showing Cal1 vein cutting through the stylolite and affected by partial dissolution, and idiotopic-E dolomite crystals occurring in the stylolite only. (I) Detail of the stylolite in (G-H) illustrating the idiotopic-E dolomite, which occurs only in the stylolite and is unaffected by dissolution.

7.2. Vado di Ferruccio thrust zone

The Vado di Ferruccio thrust zone is composed of a 0.5 to 2 meters thick fault core juxtaposing Bituminous Dolostones Formation in the hanging wall, onto Corniola Formation in the footwall. The fault core is represented by a foliated cataclasite (VFCore), with S-C-C' structure and abundant pressure solution seams (Leah et al., 2018). Dolostones in the hanging wall damage zone show an up to 2 meters thick zone, characterized by a thrust parallel to low-angle oriented network of fault-veins (sensu

Woodcock & Mort, 2008). The latter are syntaxial and cemented by coarse dolomite crystals (BDDolFV), which display growth competition and become locally saddle-shaped (Xenotopic-C of Gregg & Sibley, 1984) towards the median line (Figs. 14A-B). In places, fault-veins are re-brecciated producing crackle to chaotic breccias (Woodcock & Mort, 2008; Figs. 14A and 14C). Dolomite crystals infilling veins have the same purple color of the host rock under cathodoluminescence, apart from some red colours that are locally observed in their outer parts (Fig. 14D). Dolomite crystals in both veins and host rock are non-ferroan. Where dolostones are clay-rich, pressure solution surfaces are well-developed and add to microcracks and fault-veins to accommodate deformation (Fig. 14A). In places, fault-veins and tectonic stylolites in the hanging wall damage zone are associated with microcrystalline silica, which is preferentially located in anastomosed

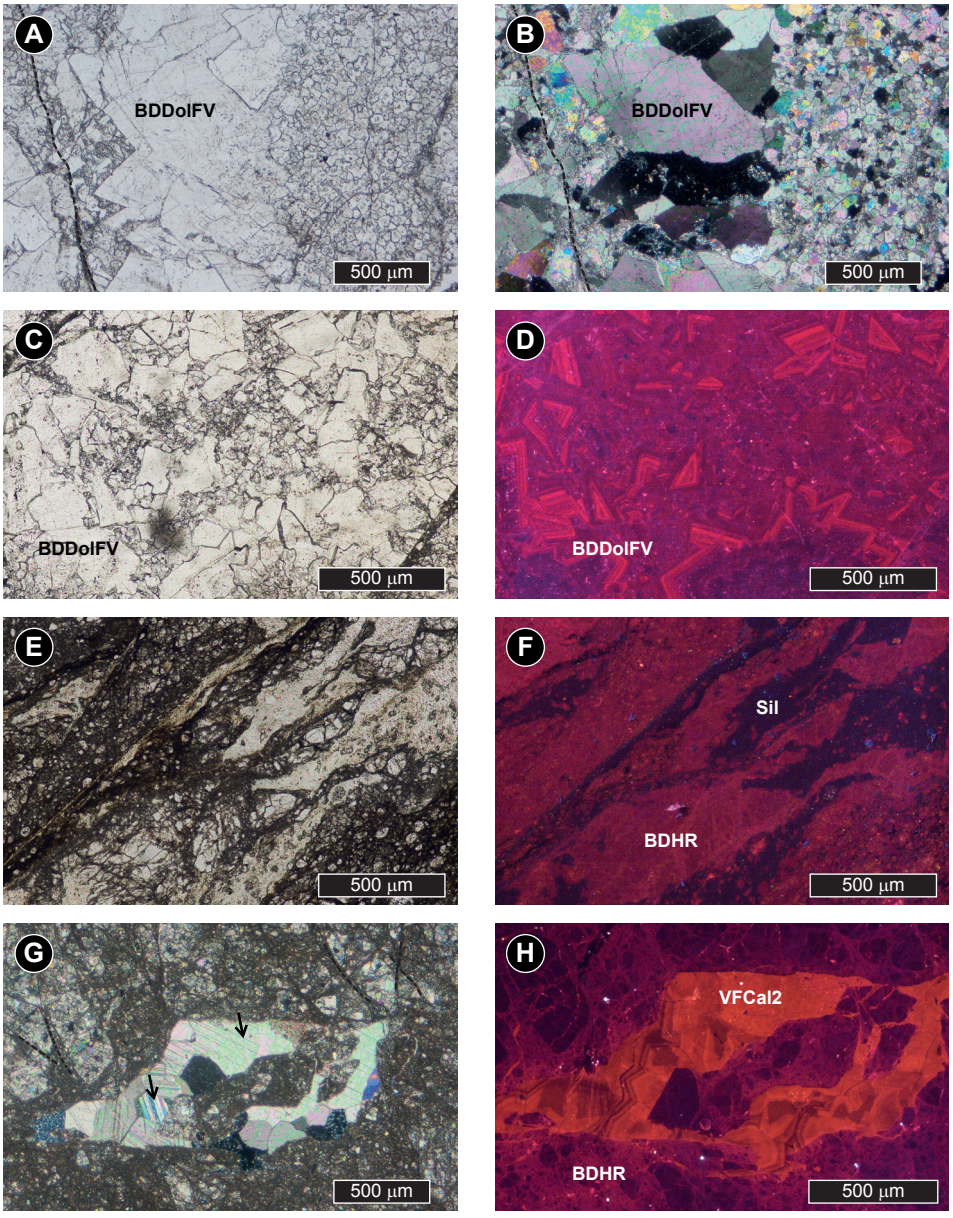


Figure 14. Petrography of the Bituminous Dolostones in the hanging wall of the Vado di Ferruccio Thrust. (A) PPL and (B) XPL images showing fault-veins composed of coarse dolomite crystals, sometimes saddle-shaped, and chaotic dolomite breccia towards the median line. (C) PPL and (D) CL images of chaotic breccia; both dolomite host rock and cement are purple colored, except for the outer growth zones which display a red color. (E) PPL and (F) CL images of silica cemented fractures overprinting tectonic stylolite. (G) XPL and (H) CL images of extensional dilation jog cemented by equant calcite with ornage-dull growth zones and interested by twinning.

bands, which are parallel to and re-open pressure solution surfaces. Silica crystal size is typically lower than about 50 μm (Figs 13D, F, 14F). High-angle extensional fractures and dilation jogs in dolostones overprint the contractional structures and are cemented by equant calcite showing Type I twinning of Burkhard (1993) and characterized by well-zoned orange to orange-dull colors under cathodoluminescence (Figs. 14G-H).

The footwall damage zone is composed of bioclastic limestones (CoHR) interested by a dense network of pressure solution surfaces, parallel and at low-angle to the fault core, and by abundant veins (Fig. 15). Stylolite abundance and thickness increases approaching the fault core. Crosscutting relationships and cathodoluminescence observations show that two equant, non-ferroan calcite cements occur in the veins. VFCal1 veins strike parallel to the principal slip surface, are perpendicular to pressure solution surfaces, and mutually crosscut with them, while VFCal2 veins are subvertical and always cut pressure solution seams. VFCal1 veins are characterized by dull luminescence, darker than the host rock, while VFCal2 ones display orange color in cathodoluminescence (Figs. 15A-D). Some residual porosity in Cal1 veins was sealed by overgrowths of calcite 2, which typically has lower twinning intensity (Figs. 15E, F). In the Corniola Formation limestones, bedding-perpendicular veins infilled by up to centimetric calcite crystals (CoCalV) showing Type I twinning of Burkhard (1993), predate both VFCal1 and VFCal2 veins.

Tectonic stylolites include idiotopic-E dolomite crystals (Gregg & Sibley, 1984) that, under cathodoluminescence, show red-purple cloudy cores and, red and yellow growth zones (Figs. 13I, 15G, H). This indicates that they pertain to a dolomite generation that is different from both the Bituminous Dolostones host rocks and dolomite infillings in fault-veins.

8. Geochemical data

8.1 Carbon and oxygen stable isotopes data

Results of carbon and oxygen stable isotopes ratios are illustrated in the $\delta^{13}C$ vs. $\delta^{18}O$ cumulative plot of Figure 16A and then separately shown as $\delta^{18}O$ and $\delta^{13}C$ vs. the corresponding thrust sheet, respectively (Figs. 16B, C). Rudist calcarenites (RCHR) in the hanging wall of the Monte Camicia Thrust have $\delta^{18}O$ values ranging from -1.76 ‰ to -0.30 ‰ and $\delta^{13}C$ values between 1.69 ‰ and 2.38 ‰. In the hanging wall damage zone, the calcareous matrix (CFCalSB) has $\delta^{18}O$ values ranging from -7.53 ‰ to -4.56 ‰ whereas $\delta^{13}C$ values are comprised between -2.88 ‰ and -0.40 ‰. Fault core rocks are shear

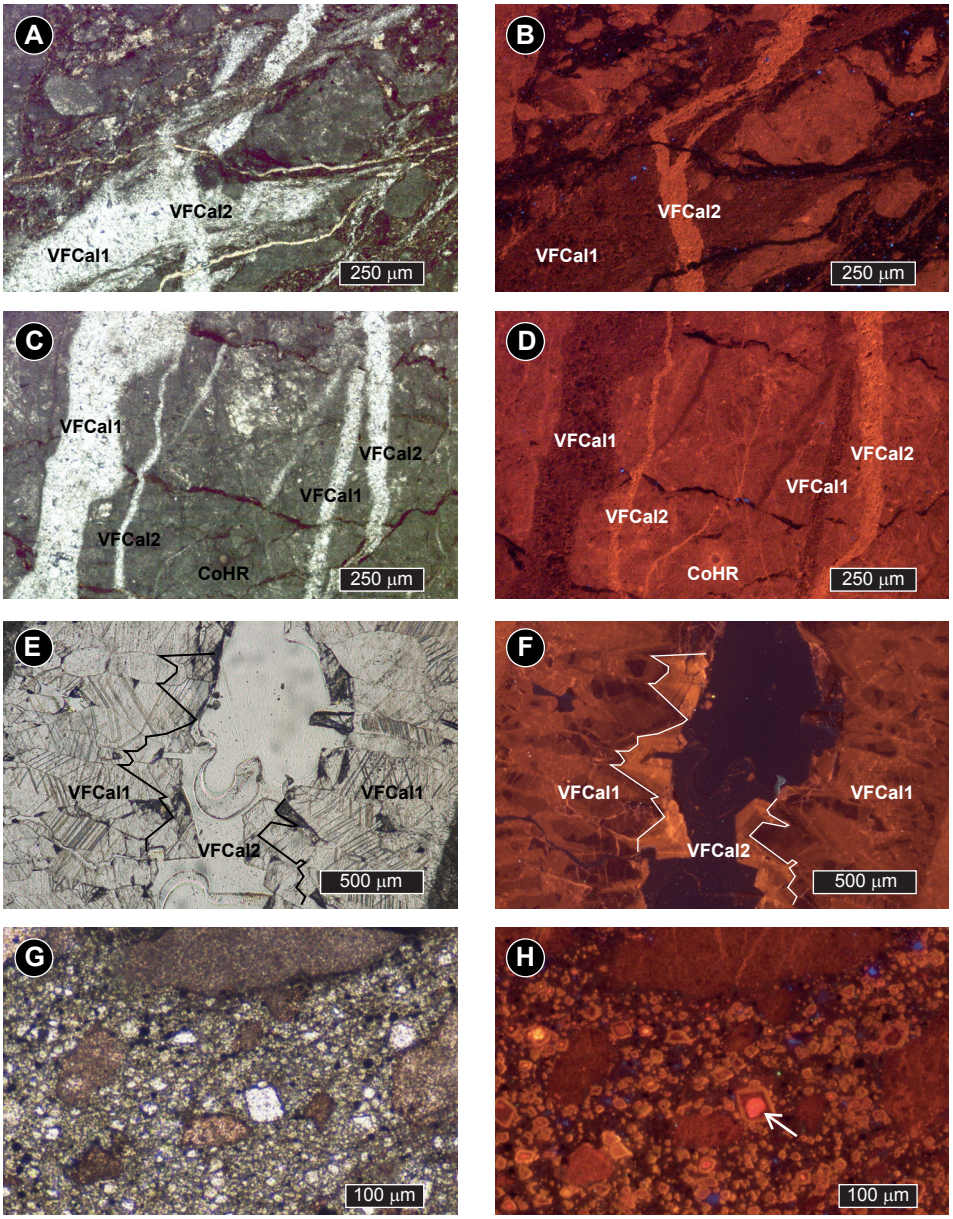


Figure 15. Petrography of the Corniola Limestones in the footwall damage zone of the Vado di Ferruccio Thrust. (A) PPL and (B) CL images of low-angle tectonic stylolites mutually crosscutting with VFCal1 veins and cut by VFCal2 veins. (C) PPL and (D) CL images showing high-angle, E-W striking veins cemented with VFCal1 and VFCal2 and crosscutting low-angle stylolites; Cal1 is dissolved where crosscut by the stylolites. PPL (E) and (F) CL images showing high-angle, N-S striking vein cemented with VFCal1 and VFCal2 in optical continuity; twinning is more intense in Cal1. (G) PPL and (H) CL images showing idiotopic-E dolomite crystals in tectonic stylolites, characterized by cloudy pink cores and red-yellow growth zones.

bands (CFDolCalSB) composed of a mixture of calcite and dolomite (their isotopic values have to be considered with caution). $\delta^{18}O$ values range between -2.71 ‰ and -0.38 ‰ and $\delta^{13}C$ values are comprised between -0.25 ‰ and 1.45 ‰. Calcite cement (CFCalV) filling veins and vugs in the fault zone shows both $\delta^{18}O$ and $\delta^{13}C$ depleted compared with the matrixes, with values ranging from -8.30 ‰ to -6.06 ‰ for oxygen and from -3.86 ‰ to 0.54 ‰ for carbon.

Bituminous Dolostones host rocks (BDHR) $\delta^{18}O$ values range from -0.09 ‰ to 2.20 ‰ and $\delta^{13}C$ shows values in the range 1.40 ‰ to 2.31 ‰. Only four samples collected at site CF3, have $\delta^{18}O$ values comprised between -2.22 ‰ and -1.05 ‰. Dolomite fault-veins in bituminous dolostones (BDDolFV) in the haging wall of the Vado di Ferruccio Thrust

have $\delta^{18}O$ and $\delta^{13}C$ values comprised between -0.48 ‰ and 0.83 ‰, and between 1.69 ‰ and 2.22 ‰, respectively. A fault-vein included in bitumen layers shows depleted values with a $\delta^{18}O$ value of -2.65 ‰ and a $\delta^{13}C$ value of -1.60 ‰. Calcite micro-veins in bituminous dolostones (BDCalV) show depleted values of $\delta^{18}O$ and $\delta^{13}C$ compared to the host and have values ranging from -6.86 ‰ to -2.93 ‰ and from -4.68 ‰ to 2.02 ‰, respectively. Dolostones host rocks sampled at site PF1 display heavier $\delta^{18}O$ values, comprised between 3.26 ‰ and 3.79 ‰, and the associated fault-veins show heavier $\delta^{13}C$ values, from 2.24 ‰ to 2.58 ‰, compared to the bulk of the samples.

In the Vado di Ferruccio fault core, like in the Monte Camicia Thrust, data were collected from a limestone-dolostone mixed material (VFCore). Isotopic values are comprised between -0.48 ‰ and 0.39 ‰ for $\delta^{18}O$, and from 1.55 ‰ to 2.13 ‰ for $\delta^{13}C$, respectively. Vein sets VFCal1 and VFCal2, in the footwall damage zone, have depleted $\delta^{18}O$ values, ranging from -5.82 ‰ to 0.13 ‰, respectively. Their $\delta^{13}C$ values range from -1.01 ‰ to 1.61 ‰. The marly limestones of the Corniola Fm. in the footwall of the thrust, show $\delta^{18}O$ values comprised between -1.15 ‰ and 0.00 ‰, and $\delta^{13}C$ values ranging between 1.62 ‰ and 2.65 ‰, respectively. Only at site VF1, two $\delta^{13}C$ values of 0.52 ‰ and 0.56 ‰ were obtained. Veins CoCalV typically have $\delta^{13}C$ values ranging from 1.98 ‰ to 2.55 ‰ and only at site VF1 they decrease to a range varying between 0.25 ‰ and 0.36 ‰. CoCalV show $\delta^{18}O$ values comprised between -1.43 ‰ and 0.22 ‰.

8.2. Strontium isotopes data

Eight samples were selected for strontium isotopes analysis, including two dolostone host rocks (BDHR), two dolomite fault-veins (BDDolFV), two limestone host rocks (RCHR and CoHR), a calcite vein (CoCalV), and a dolomitic-calcareous micritic matrix in the Monte Camicia Thrust fault core (CFDolCalSB). Results are illustrated in Fig. 17A, where host rock strontium isotope ratios are plotted vs. their depositional age (McArthur et al., 2012). Bituminous dolostones display $^{87/86}Sr$ values of 0.707968 and 0.707843, and show a good correlation with the seawater strontium ratio of their depositional ages. A similar feature occurs also for the Corniola sample, with a $^{87/86}Sr$ value of 0.707157, whereas Rudist Calcarenites show a $^{87/86}Sr$ value of 0.707035, which is depleted compared to the age of this formation. Plotting $^{87/86}Sr$ values versus the corresponding $\delta^{18}O$ values indicates that thrusting-related dolomite fault-veins have $^{87/86}Sr$ values of 0.707707 and 0.707500, which are depleted compared to their host rocks (Fig.

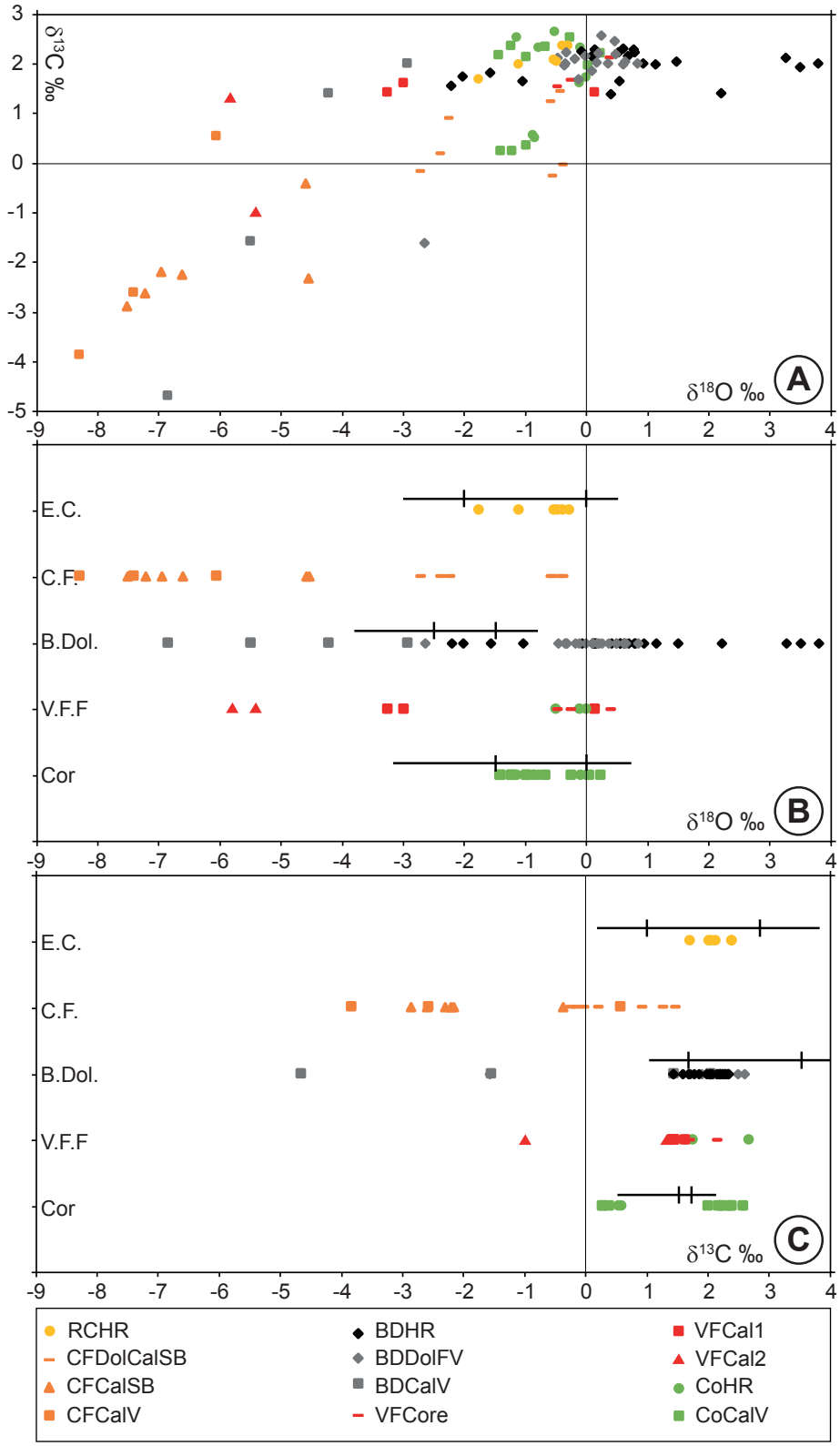


Figure 16. Oxygen and carbon stable isotopes data. (A) $\delta^{18}O$ vs. $\delta^{13}C$ plot; axes are in ‰ V-PDB. (B) $\delta^{18}O$ vs. structural unit plot; black ticks and lines are average $\delta^{18}O$ ‰ and ± 1σ values of the seawater for the structural unit host rock age. (C) $\delta^{13}C$ ‰ vs. structural unit plot; black ticks and lines are average $\delta^{13}C$ ‰ and ± 1σ values of the seawater for the structural unit host rock age; seawater reference values from Veizer et al., 1999.

17B). The $^{87/86}Sr$ value of the calcite vein CoCalV from Corniola is 0.707397, i.e. enriched compared to the host rock. The $^{87/86}Sr$ value from the Monte Camicia fault core is 0.707786.

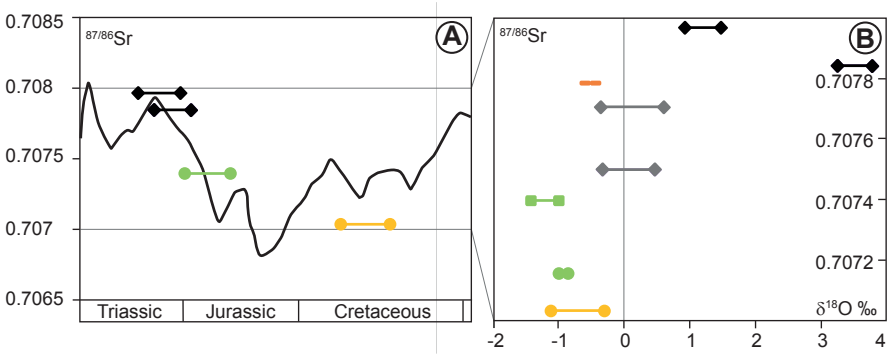


Figure 17. (A) Age vs. $^{87/86}$Sr plot of host rock samples; black line represents strontium isotopes ratio of seawater. (B) δ^{18}O vs. $^{87/86}$Sr plot; δ^{18}O in ‰ V-PDB. See legend in Fig. 16; seawater reference values from McArthur et al., 2012.

8.3. Noble gases isotopes data

Results of noble gas analyses are reported as ratios in Table 1. ^{3}He and ^{4}He were below instrumental detection limits in all samples. ^{40}Ar/^{36}Ar ratios range between 280.2 and 309.8, i.e. typical values of the atmosphere. Fig. 18 shows the measured heavy noble gas ^{84}Kr and ^{132}Xe data plotted as a function of ^{36}Ar values. ^{84}Kr/^{36}Ar are comprised between 0.0228 and 0.0347 and ^{132}Xe/^{36}Ar show values ranging from 0.00126 to 0.00378. Almost all samples lie on an ideal mixing trend whose end-members are represented by atmosphere (Air) and air-saturated water (ASW). The bituminous dolostone host rock sample deviates from this trend and shows a higher ^{132}Xe concentration, reaching a ^{132}Xe/^{36}Ar value of 0.01126. Massive dolostone samples provided ^{84}Kr/^{36}Ar values always lower than 0.0282, which are closer to the Air end-member. On the other hand, limestone and calcite cement samples have ^{84}Kr/^{36}Ar values always higher than 0.0279, closer to the ASW end-member.

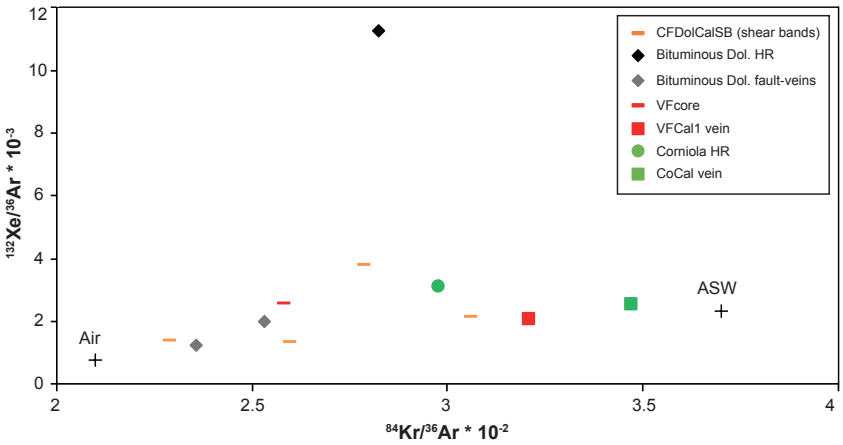


Figure 18. ^{84}Kr/^{36}Ar vs. ^{132}Xe/^{36}Ar plot of all analyzed samples; all samples excluding Bituminous Dolostones lie on a mixing trend between Air and ASW (Air Saturated Water).

9. Discussion

9.1 Host rock diagenetic framework

Corniola limestones show δ^{18}O and strontium isotope ratios values in the range of Lower Jurassic seawater and δ^{13}C values distributed in two clusters, slightly higher and

Table 1: Noble gases isotopes ratios of analyzed samples and reference ratios of natural reservoirs; Air-atmosphere; ASW-air saturated water

Sample	3He/4He	±	R/Ra	±	*21Ne/22Ne	±	40Ar/36Ar	±	84Kr/36Ar	±	132Xe/36Ar	±
CFCalDolSB	1,13E-06	1,43E-06	6,58E-01	8,33E-01	4,50E-02	4,36E-03	3,00E+02	1,45E+00	2,79E-02	1,51E-04	3,78E-03	3,28E-05
CFCalDolSB	5,46E-07	1,55E-06	3,18E-01	9,03E-01	2,82E-02	4,89E-03	3,00E+02	2,13E+00	2,29E-02	1,89E-04	1,40E-03	2,44E-05
CFCalDolSB	1,47E-07	1,22E-06	8,53E-02	7,08E-01	3,44E-02	6,00E-03	2,98E+02	6,52E-01	2,60E-02	7,95E-05	1,34E-03	1,24E-05
CFCalDolSB	-5,29E-07	-1,24E-06	-3,07E-01	-7,19E-01	2,31E-02	2,63E-02	3,09E+02	5,44E+00	3,06E-02	5,72E-04	2,15E-03	5,86E-05
Bit.Dol.HR	8,50E-07	1,11E-05	4,94E-01	6,45E+00	4,48E-02	3,66E-02	3,10E+02	3,17E+00	2,82E-02	3,15E-04	1,13E-02	1,41E-04
Bit.Dol.V	-9,43E-06	-4,77E-05	-5,48E+00	-2,77E+01	3,50E-02	6,43E-03	3,02E+02	1,41E+00	2,36E-02	1,26E-04	1,23E-03	1,78E-05
Bit.Dol.V	5,14E-06	4,36E-06	2,99E+00	2,53E+00	3,66E-02	3,90E-03	3,00E+02	1,13E+00	2,53E-02	1,11E-04	1,98E-03	1,99E-05
VFCore	7,54E-05	5,99E-05	4,38E+01	3,48E+01	3,00E-02	3,45E-03	2,87E-03	9,45E-02	2,58E-02	6,03E-04	2,56E-03	7,54E-05
VFCal1	-5,88E-06	-2,62E-05	-3,42E+00	-1,53E+01	2,14E-02	2,59E-03	2,98E+02	3,42E+00	3,21E-02	3,88E-04	2,07E-03	3,58E-05
VFCal2	3,06E-06	1,08E-05	1,78E+00	6,27E+00	2,91E-02	3,72E-03	-	-	-	-	-	-
CoHR	4,38E-06	3,98E-06	2,55E+00	2,31E+00	3,69E-02	5,71E-03	2,96E+02	1,15E+01	2,98E-02	1,18E-03	3,08E-03	1,39E-04
CoCalV	-1,09E-06	-1,28E-02	-6,36E-01	-7,45E+03	3,19E-02	3,15E-03	3,06E+02	3,09E-01	3,47E-02	1,49E-04	2,52E-03	2,61E-05
Reference Ratios												
Air			1		0,0291		298,5		0,021		0,000784	
ASW (25°C)					0,0291				0,037		0,002340	
Mantle			8		< 0.0291							
Crust			0.01-0.05		> 0.0291		>298.5					

lower than seawater values, respectively (Figs. 16A-B-C, 17A). This indicates that bacterially-mediated processes occurred during early-diagenesis in the bioclastic-rich Corniola Fm (Hoefs, 1997).

Bituminous Dolostones in the thrust sheet bounded by the Vado di Ferruccio and Monte Camicia thrust faults, respectively, have $\delta^{18}O$ values enriched by +2 to +3.5 ‰ compared to the Upper Triassic seawater ratio (Fig. 16B). $\delta^{18}O$ fractionation of +3 to +4 ‰ in dolomite compared to calcite at low temperature (Land, 1980), supports the hypothesis that seawater was likely the main fluid involved in early-diagenetic dolomite crystallization, despite recrystallization of the dolomite host during burial can't be excluded based on our stable isotopes data (Machel, 2004). Samples from site PF1, characterized by heavier $\delta^{18}O$ values, reasonably interacted with slightly evaporated seawater during early-diagenesis. This inference is supported by $\delta^{13}C$ values and also by the strontium isotope ratios (Figs. 16C-D, 17A). The high $^{132}Xe/^{36}Ar$ ratio is likely due to preferential adsorption of ^{132}Xe by organic matter (Fig. 18, Hohenberg et al., 2002).

Rudist Calcarenites in the hanging wall of the Monte Camicia thrust show $\delta^{18}O$ and $\delta^{13}C$ values that correspond to the mean ranges of the Lower Cretaceous seawater stable isotopic composition (Fig. 16B-C). However, their strontium isotopes ratio does not fit with this age (Fig. 17A). This feature could be due to the detrital origin of the Rudist Calcarenites.

9.2 Structural diagenesis

The older vein set exposed in the studied thrust sheet pile, CoCalV, is cut by all the studied deformation structures and, thus, predates out-of-sequence thrusting and is likely related to in-sequence thrusting-related folding.

CoCalV veins are characterized by mean $\delta^{18}O$ and $\delta^{13}C$ values comparable to the Corniola host rock (Figs. 16A-B-C, 17A) and their strontium isotope ratio is slightly higher than the host rock value (Fig. 17B). Such isotopic values, together with the same cathodoluminescence colours in the host rock, support crystallization from formational fluids in closed system conditions, at low water/rock ratios (Dietrich & McKenzie, 1983).

The mutual cross-cutting relationships between VFCal1 veins and tectonic stylolites in the footwall damage zone of the Vado di Ferruccio Thrust (Fig. 19A), indicate that the former are associated with out-of-sequence thrusting (e.g. Ramsay, 1980; Ghisetti, 1987). Their cathodoluminescence colours darker than the host rock, $\delta^{13}C$ values similar to both hanging wall and footwall host rocks, and $\delta^{18}O$ values from 0 ‰ to -3 ‰, suggest either (i)

heterogeneous fluid compositions resulting from different degrees of mixing between formational fluids circulating in the footwall and hanging wall damage zones, or (ii) precipitation from the same fluid at different temperatures (Friedman & O'Neil, 1977; Muchez et al., 1995).

Different cathodoluminescence colours of idiotopic-E-dolomite crystals in the Vado di Ferruccio fault core, compared to the host dolostones, suggest that they grew from dolomitizing fluids characterized by a different chemical signature with respect to those in the hanging wall damage zone, probably characterized by higher Mg^{2+}/Ca^{2+} ratios. However, stylolites have been documented to be characterized by different chemical properties with respect to the surrounding limestones, and could promote localized dolomitization (Warren, 2000; Evans & Elmore, 2006)

Moreover, fluids circulating in the fault core contained dissolved silica which precipitated in the hanging wall damage zone in microcrystalline bands re-opening tectonic stylolites and dolomite fault-veins (Fig. 19B). Considering that strontium isotopes do not record high $^{87}Sr/^{86}Sr$ ratios in dolomite fault-veins, typical of fluids which interacted with siliciclastic rocks, silica could have been locally sourced by local dissolution of chert nodules included in carbonatic rocks.

The abundance of thrust-parallel and low-angle crackle fault-veins (BDDolFV) affecting Bituminous Dolostones indicates that they formed at pore fluid overpressure conditions, possibly with fluid pressures higher than lithostatic (Sibson, 1981, 1990). Dolomite crystals in the veins display $\delta^{18}O$ and $\delta^{13}C$ values in the same range of the Bituminous Dolostones host rock (Fig. 16). Strontium isotopes ratios are slightly depleted compared to that of the host rocks, but still in the range of the analyzed Mesozoic host rocks (Fig. 17B). All this evidence and the same cathodoluminescence colours between dolomite fault-veins and dolostones host rocks, imply that the former crystallized during thrusting from fluids with isotopic and chemical compositions similar to their host rocks. This could be the result of fluid circulation in closed system conditions, or at low water/rock ratios during fluid-rock interaction, by fluids with marine affinity (Fig. 19B; Ghisetti et al., 2001; Kirschner & Kennedey, 2001).

Cataclastic shear bands in Bituminous Dolostones (CFDolCalSB) involved in the footwall damage zone of the Monte Camicia Thrust have $\delta^{18}O$ and $\delta^{13}C$ values that are intermediate between the isotopic composition of the host rock and that of the fine calcareous shear bands in the hanging wall damage zone (Figs. 16A-B-C). Their cathodoluminescence colours suggest infiltration by meteoric fluids during deformation.

Also shear bands (CFCalSB) and microveins (CFCalV) have cathodoluminescence colours and $\delta^{18}O$ and $\delta^{13}C$ values indicating interaction with infiltrating meteoric fluids during thrusting (Figs. 16A-B-C; e.g. Ghisetti et al., 2001; Agosta & Kirschner, 2003; Agosta et al., 2008; Smeraglia et al., 2016). The negative shift of by $\delta^{18}O$ values from samples collected in Site CF3 is caused by contamination of meteoric calcite, which occurs as micrite in these samples, likely associated with extensional faulting.

Summarizing, petrographic and geochemical evidence from veins and shear bands associated with contractional deformations, indicate that fluids involved in out-of-sequence thrusting along the Vado di Ferruccio Thrust are characterized by marine fluids signature, semi-closed system conditions and their migration pathways are likely restricted to the carbonatic Mesozoic succession while those that circulated during out-of-sequence thrusting at shallow depth in the Monte Camicia fault zone are of meteoric origin and infiltrated from the surface. Noble gases geochemistry indicates that volatiles dissolved in fluids are atmosphere-derived, allowing us to exclude external sources like the basement and the mantle (Ballentine et al., 2002a, 2002b).

Cathodoluminescence orange colours and moderately depleted oxygen and carbon stable isotope values of calcite cements from deformation features produced by extensional faulting affecting the Vado di Ferruccio Thrust (VFCal2) reasonably indicate calcite precipitated from meteoric fluids with different degrees of water-rock interaction. Also in extension-related cements associated with the negative inversion of the Monte Camicia Thrust (CFCalV), depleted oxygen and carbon values indicate that calcite precipitated from infiltrating meteoric fluids (Allan & Matthews, 1982; Agosta & Kirschner, 2003; Hausegger et al., 2010; Cooley et al., 2011; Smeraglia et al., 2018). Calcite precipitation from meteoric fluids after different degrees of water-rock interaction can be infererred also from geochemical and petrographic features of cements associated with the master extensional fault zones (BDCalV) that dissect both the Monte Camicia and Vado di Ferruccio Thrusts to the south, and bound the Campo Imperatore basin in this area. Similar environmental conditions during extensional faulting have been proposed by other authors in the Gran Sasso region and in the Central Apennines in general (Ghisetti et al., 2001; Ronchi et al., 2004; Bussolotto et al., 2007; Agosta et al., 2008; Dewever et al., 2010; Smeraglia et al., 2016). Noble gases data, as for the preceding stage, allow us to exclude any fluid contribution from the basement and the mantle into the paleofluid circulation of the area.

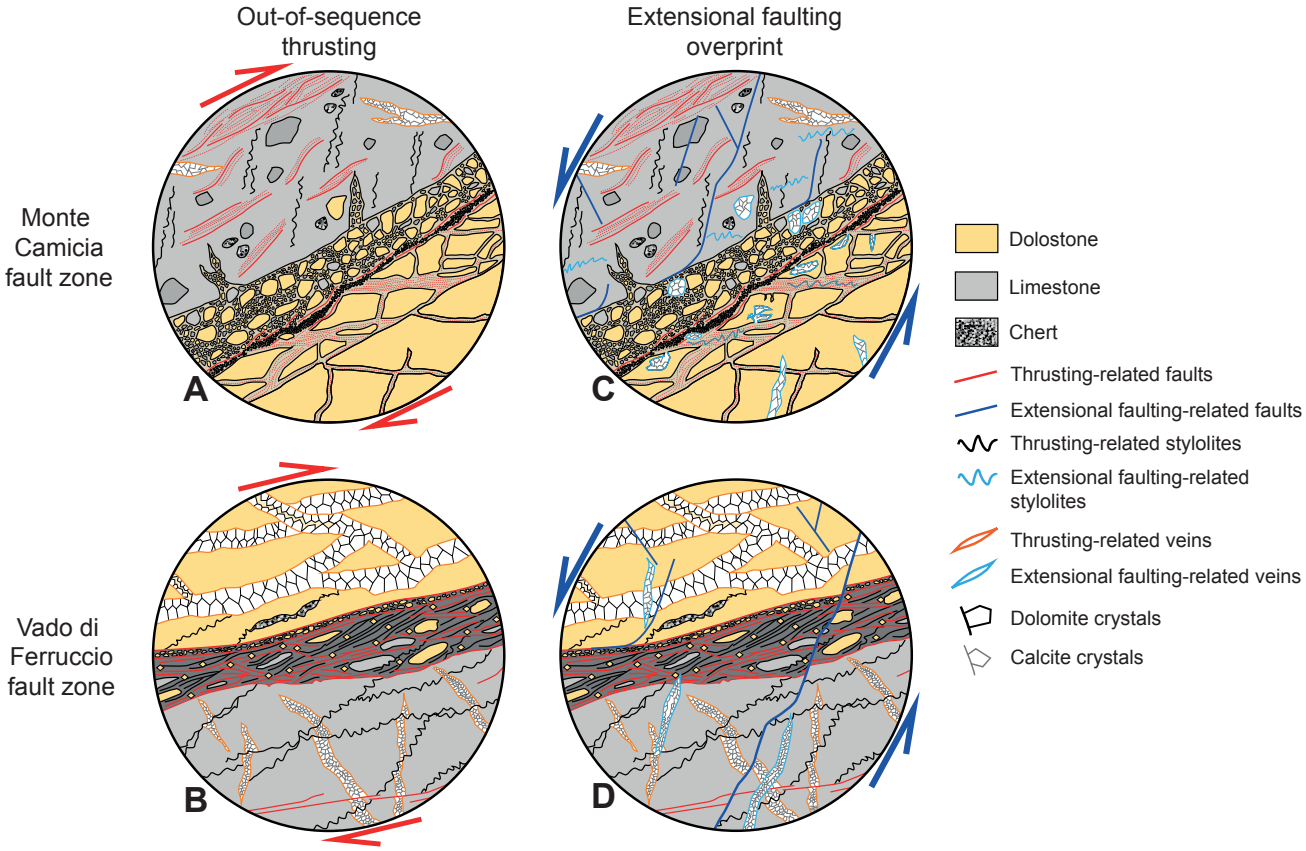


Figure 19. Conceptual structural diagenetic model of the studied fault zones. Fault zone architectures of the Monte Camicia (A) and Vado di Ferruccio (B) out-of-sequence thrusts during contractional deformation and their architectures after extensional deformation overprint in (C) and (D), respectively.

9.3 Evolutionary model

Structural analysis, petrography, and stable isotope geochemistry, allow us to propose a conceptual structural evolutionary model during out-of-sequence thrusting and extensional faulting of the Gran Sasso thrust sheet stack. Contractional deformations affected a complex paleogeography of fault-bounded carbonate platform blocks and the transition to the Umbria-Marche basinal domain (Fig. 20 A; e.g. Centamore et al., 1975; Cosentino & Parotto, 1986; Santantonio, 1993; Cardello & Doglioni, 2015). Thrusting along the Gran Sasso frontal thrust and associated folding started in Messinian times (Ghisetti & Vezzani, 1986, 1991; Cipollari & Cosentino, 1995; Centamore & Rossi, 2009) and caused the translation of the Gran Sasso carbonate thrust sheet onto Laga pre-evaporitic Messinian foredeep siliciclastic deposits, overlying the Mesozoic carbonate succession (Fig. 20B). To maintain the thrust wedge at the mechanical equilibrium between tectonic and gravitational forces, and account for the effects of surface processes (Davis et al., 1983), out-of-sequence thrusting affected the folded Mesozoic succession in the Gran Sasso thrust sheet, possibly triggered by abundant syntectonic sedimentation at the

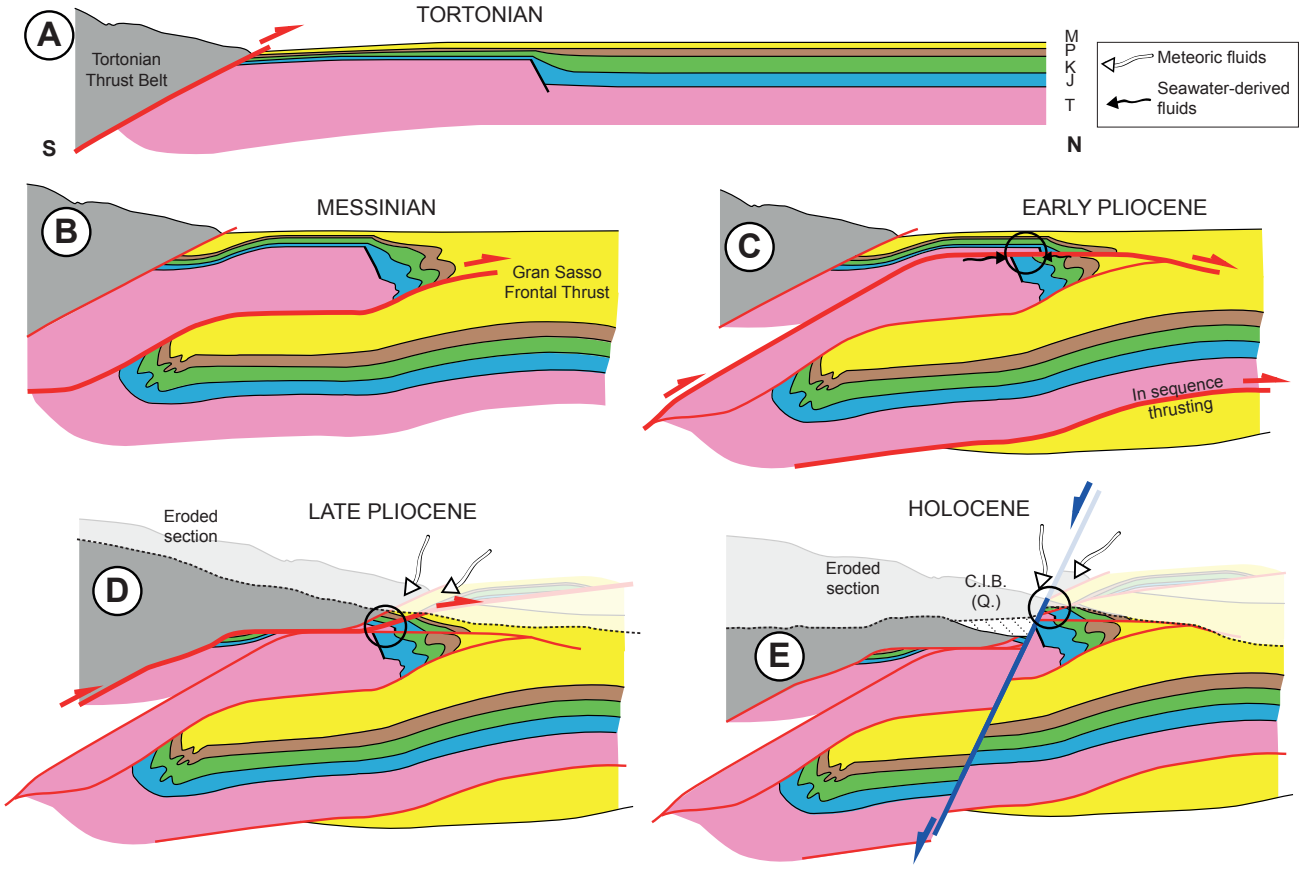


Figure 20. Conceptual evolutionary model of the studied part of the Gran Sasso Massif. Cross-sectional structural architecture of the Gran Sasso Massif in Tortonian (A), Messinian (B), Early Pliocene (C), Late Pliocene (D) and Holocene (E) times.

wedge toe (e.g. Storti & McClay, 1995). The Vado di Ferruccio Thrust formed at this stage, cutting the Gran Sasso Frontal Thrust and overthrusting the post-evaporitic to Early Pliocene Laga siliciclastics (Ghisetti & Vezzani 1986; Pace & Calamita, 2015; Leah et al., 2018). In the study area, the Vado di Ferruccio Thrust juxtaposed the folded Upper Triassic dolostones onto Lower Jurassic platform slope limestones, pertaining to the same anticlinal forelimb (Fig. 20C). Renewed out-of-sequence thrusting affected the Vado di Ferruccio thrust sheet during Pliocene times, when in sequence thrusting shifted further eastwards and erosion started to take place in the Gran Sasso Massif area (Centamore & Nisio, 2003; Centamore & Rossi, 2009). This tectonic event created the Monte Camicia Thrust, which juxtaposed younger on older rocks (Fig. 20D). The former were possibly located in the backlimb of the Gran Sasso anticline and then underwent further folding during forelandward translation.

Extensional tectonics in this region of the Central Apennines started in Quaternary times and created accommodation space for accumulation of continental deposits in fault-

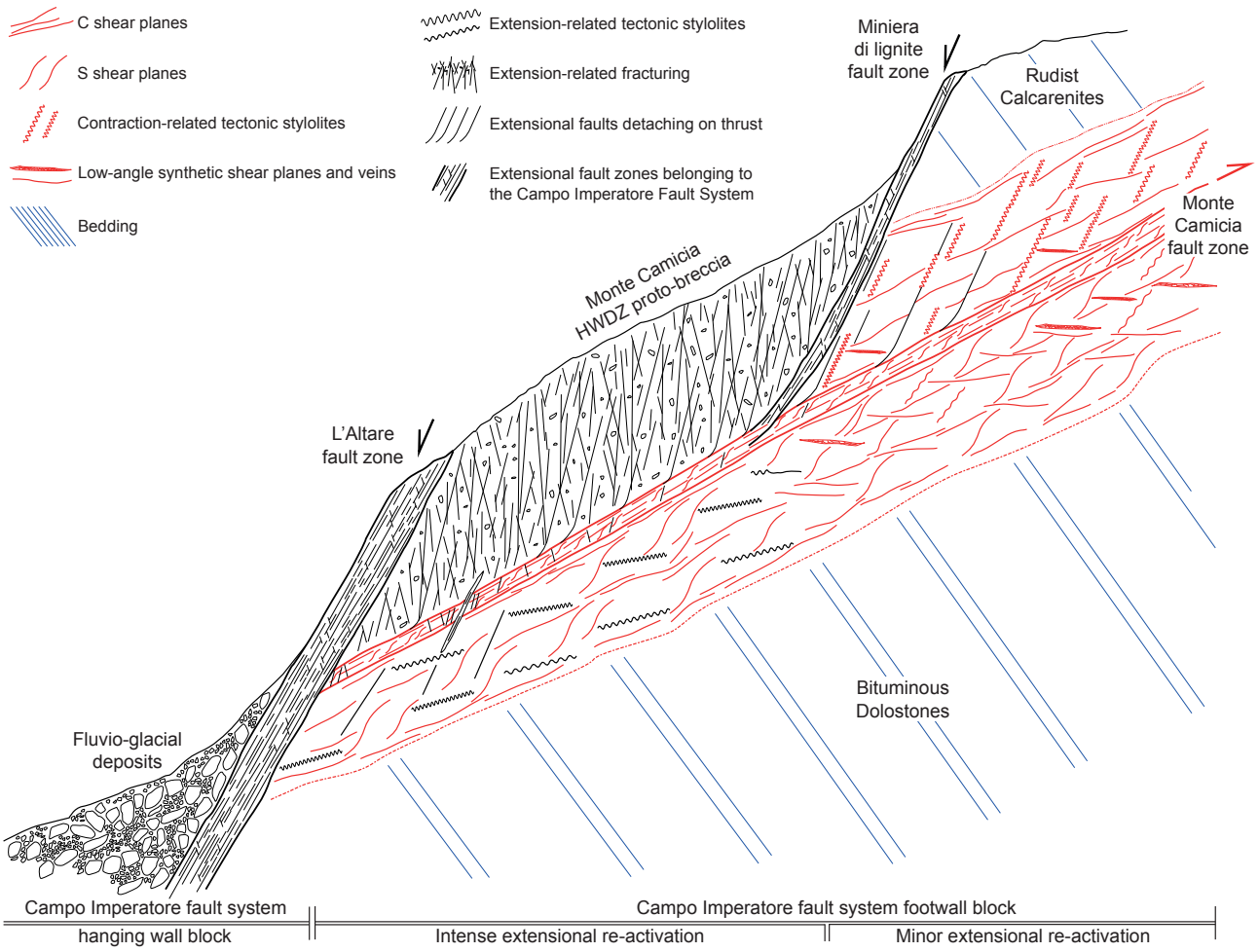


Figure 21. Conceptual structural sketch illustrating the Monte Camicia out-of-sequence thrust fault zone and the architectural modifications after extensional deformation overprint.

bounded intermontane basins (Cavinato & DeCelles, 1999; D'Agostino et al., 2001; Cosentino et al., 2017). The Campo Imperatore fluvio-glacial basin is the most external one in the region and is bounded northward by the SSW-dipping Campo Imperatore extensional fault system (Demurtas et al; 2016), developed by the partial contribution of negative inversion of the previously formed contractional architecture (Fig. 20E; e.g. Ghisetti & Vezzani, 1999; Cosentino et al., 2010), possibly during further thrust stacking at depth, as recently proposed for the Montagna dei Fiori Fault to the north (Storti et al., 2018). The extensional fault zone that cuts at high angle through the Vado di Ferruccio and Monte Camicia thrusts, at the southern termination of the study area, was triggered by development of the Campo Imperatore Fault and its evolution caused the progressive removal of the tectonic load on the Monte Camicia thrust, and consequent release of fault strength. Eventually, the Monte Camicia thrust ramp segment in the footwall of the Campo Imperatore Fault failed in extension, causing dilation of the contractional structural fabric in

the hanging wall damage zone and its transformation into a protobreccia zone (Fig. 21). Our interpretation of the Monte Camicia Thrust supports the contractional origin initially proposed by Ghisetti and Vezzani (1986) and not the extensional one suggested by Pace et al. (2014). Extensional activity along the Monte Camicia Thrust is limited, and is associated with Quaternary faulting (D'Agostino et al., 1998).

10. Conclusions

The Monte Camicia and Vado di Ferruccio thrusts accommodated internal shortening within the Gran Sasso thrust stack in Late Messinian and Early Pliocene times, in an out-of-sequence fashion. Starting in Pleistocene times, they were dissected by the high-angle Campo Imperatore extensional fault system and, in particular, the Monte Camicia Thrust underwent negative inversion. Our multidisciplinary study including structural, petrographical and geochemical analyses, allowed us to propose the following conclusive points, which shed new lights into the still debated tectonic evolution of the Gran Sasso region.

- The Monte Camicia Thrust activated after and crosscuts the Vado di Ferruccio Thrust; as a consequence, its younger-on-older relationships are produced by juxtaposition of Mesozoic rocks initially located in the backlimb of the Gran Sasso Anticline. Extensional kinematics is associated with low displacement, Quaternary negative inversion of the fault.
- Fluid-rock interaction during Early Pliocene out-of-sequence thrusting along the Camicia fault zone was characterized by open system conditions and meteoric fluids infiltrated from the surface along the fault zone, equilibrating at different degrees with formational fluids. This supports the subaerial activity of the thrust, which resulted in dolomite dissolution and calcitization processes along the fault
- Fluid-rock interaction during the Late Messinian out-of-sequence activity along the underlying Vado di Ferruccio Thrust was characterized by semi-closed system conditions and by the involvement of fluids with marine signature, as indicated by geochemical data. Pressure solution mediated mass transfer locally promoted ideal conditions for dolomite crystallization in the foliated and clay-rich material of the fault core.
- Quaternary extensional deformation overprinted the contractional structural architecture. Subsidiary extensional faults exploited the low-angle thrust surfaces as detachment levels. As a result, hanging wall damage zones of the studied thrusts

are intensely faulted and fractured. Specifically, the hanging wall damage zone of the Camicia thrust was mostly transformed in a decametric-wide zone of proto-brecciated calcarenites.

- Fluid-rock interaction during Quaternary extensional faulting is characterized by meteoric fluids circulation both in the Camicia and Vado di Ferruccio fault zones. Nevertheless, their fault core permeability architectures acquired during contractional deformation controlled the degree of fluid-rock interaction, promoting and impeding fluid circulation in the Camicia and Vado di Ferruccio fault zones, respectively.
- Noble gas geochemistry of vein cements rules out any significant contribution of deeply sourced fluids during both contractional and extensional faulting.

Acknowledgements

We are indebted with Andrea Comelli for thin section preparation, Enrico Selmo for providing carbon and oxygen stable isotopes data, Zita Kelemen for support with the micromilling equipment, and Paolo Gentile for help with SEM microscopy. Strontium isotopes data were provided by Gareth Davies, at Vrije Universiteit, Amsterdam. Fieldwork was partly funded by Shell Global Solutions International B.V., Amsterdam, The Netherlands. The “Ente Parco Nazionale del Gran Sasso e Monti della Laga” is thanked for permission to conduct fieldwork in the Campo Imperatore area. Author’s contributions: Alessio Lucca participated to some fieldwork, performed the microstructural, diagenetic and isotopic work, and wrote the manuscript; Fabrizio Storti conceived the research and, together with Fabrizio Balsamo, acquired most of the structural data and participated to the tectonic interpretation; Luca Clemenzi, Michele Fondriest and Giulio Di Toro participated to some fieldwork and contributed to discuss tectonic interpretations; Paola Iacumin participated to the interpretation of carbon and oxygen stable isotopes data in syntectonic cements; Raymond Burgess participated to the analyses and interpretation of noble gases isotopes data in syntectonic cements; all co-authors critically revised the manuscript.

Accordi, G., & Carbone, F. (1986). Lithofacies map of Latium-Abruzzi and neighbouring areas, scale 1:250.000, Progetto Finalizzato Geodinamica, *Consiglio Nazionale Ricerche Italy, Roma*.

Adamoli, L., Bigozzi, A., Ciarapica, G., Cirilli, S., Passeri, L., Romano, A., Duranti, F., & Venturi, F. (1990). Upper Triassic bituminous facies and hettangian pelagic facies in the Gran Sasso range: *Boll. Soc. Geol. It., 109,* 219-230.

Agosta, F., & Kirschner, D.L. (2003). Fluid conduits in carbonate-hosted seismogenic normal faults of Central Italy: *Journal of Geophysical Research, 108 (B4),* 2221, doi:10.1029/2002JB002013.

Agosta, F., Mulch, A., Chamberlain, P., & Aydin, A. (2008). Geochemical traces of CO2-rich fluid flow along normal faults in central Italy: *Geophys. J. Int., 174,* 758-770.

Allan, J.R., & Matthews, R.K. (1977). Carbon and oxygen isotopes as diagenetic and stratigraphic tools: surface and subsurface data, Barbados, West Indies: *Geology, 5,* 16-20.

Allan, J.R., & Matthews, R.K. (1982). Isotopic signatures associated with early meteoric diagenesis: *Sedimentology, 29,* 797-817.

Alvarez, W., Engelder, T., & Lowrie, W. (1976). Formation of spaced cleavage and folds in brittle limestone by dissolution: *Geology, 4,* 698-701.

Ascione, A., Cinque, A., Miccadei, E., & Villani, F. (2008). The Plio-Quaternary uplift of the Apennines Chain: new data from the analysis of topography and river valleys in Central Italy: *Geomorphology, 102,* 105–118. doi:10.1016/j.geomorph.2007.07.022.

Ballentine, C.I., Burgess, R., & Marty, B. (2002a). Tracing fluid origin, transport and interaction in the crust: *Rev. Mineral. Geochem., 47,* 539-614.

Ballentine, C.J., & Burnard, P.G. (2002b). Production, release and transport of noble gases in the continental crust: *Rev. Mineral. Geochem.,* 47, 481-538.

Bally, A.W., Burbi, L., Cooper, C., & Ghelardoni, R. (1986). Balanced sections and seismic reflection profiles across the central Apennines: *Memorie della Società Geologica Italiana, 35,* 257-310.

Banner, J.L., & Hanson, G.N. (1990). Calculation of simultaneous isotopic and trace element variations during water-rock interaction with applications to carbonate diagenesis: *Geochimica et Cosmochimica Acta, 54,* 3123-3137.

Banner, J.L. (1995). Applications of the trace element and isotope geochemisty of strontium to studies of carbonate diagenesis: *Sedimentology, 45 (2),* 805-824.

Barchi, M., Minelli, G. & Pialli, G. (1998). The CROP03 profile: a synthesis of result on deep structures of the Northern Apennines: *Mem. Soc. geol. It., 52,* 383-400.

Bartolini, C., D'Agostino, N., & Dramis, F. (2003). Topography, exhumation, and drainage network evolution of the Apennines: *Episodes, 23,* 212-217.

Billi, A., Tiberti, M.M., Cavinato, G.P., Cosentino, D., Di Luzio, E., Keller, J.V.A., Kluth, C., Orlando, L., Parotto, M., Praturlon, A., Romanelli, M., Storti, F., & Wardell, N. (2006). First results from the CROP-11 deep seismic profile, central Apennines, Italy: evidence of mid-crustal folding: *Journal of the Geological Society, London, 163,* 583-586.

Breesch, L., Swennen, R., & Vincent, B. (2009). Fluid flow reconstruction in hanging and footwall carbonates: compartmentalization by Cenozoic reverse faulting in the Northern Oman Mountains (UAE). *Mar. Pet. Geol., 26,* 113-128. http://dx.doi.org/10.1016/j.marpetgeo.2007.10.004.

Burke, W.H., Denison, R.E., Hetherington, E.A., Koepnick, R.B., Nelson, H.F., & Otto, J.B. (1982). Variation of seawater $^{87}Sr/^{86}Sr$ throughout Phanerozoic time: *Geology, 10,* 516-519.

Burkhard, M. (1993). Calcite twins, their geometry, appearance and significance as stress-strain markers and indicators of tectonic regime: a review. Journal of Structural Geology, 15, 351-368.

Burkhard, M., Kerrich, R. (1988). Fluid regimes in the deformation of the Helvetic nappes, Switzerland, as inferred from stable isotope data: Contrib. Mineral. Petrol., 99, 416-429.

Bussolotto, M., Benedicto, A., Invernizzi, C., Micarelli, L., Plagnes, V., & Deiana, G. (2007). Deformation features within an active normal fault zone in carbonate rocks: the Gubbio fault (Central Apennines, Italy): *Journal of Structural Geology, 29,* 2017-2037.

Byerlee, J. (1993). Model for episodic flow of high-pressure water in fault rocks before earthquakes: *Geology, 21,* 303-306.

Calamita, F., & Deiana, G. (1988). The arcuate shape of the Umbria-Marche-Sabina Apennines (Central Italy): *Tectonophysics, 146,* 139-147.

Calamita, F., Paltrinieri, W., Pelorosso, M., Scisciani, V., & Tavarnelli, E. (2003). Inherited Mesozoic architecture of the Adria continental paleomargin in the Neogene central Apennines orogenic system, Italy: *Boll. Soc. Geol. Ital., 122,* 307-318.

Cardello, G.L., & Doglioni, C. (2014). From Mesozoic rifting to Apennine orogeny: The

Gran Sasso range (Italy): *Gondwana Research,* http://dx.doi.org/10.1016/j.gr.2014.09.009.

Carminati, E., Corda, L., Mariotti, G., Scifoni, A., & Trippetta, F. (2013). Mesozoic syn- and postrifting evolution of the Central Apennines, Italy: the role of Triassic evaporites: *Journal of Geology, 121,* 327-354.

Carminati, E., Fabbi, S., & Santantonio, M. (2014). Slab bending, syn-subduction normal faulting, and out-of-sequence thrusting in the Central Apennines: *Tectonics, 33,* 530-551.

Castellarin, A., Colacicchi, R., & Praturlon, A. (1978). Fasi distensive, trascorrenze e sovrascorrimenti lungo la "Linea Ancona-Anzio," dal Lias medio al Pliocene: *Geologica Romana, 17,* 161-189.

Cavinato, G.P., Cosentino, D., De Rita, D., Funiciello, R., & Parotto, M. (1994). Tectonic-sedimentary evolution of intrapenninic basins and correlation with the volcano-tectonic activity of central Italy: *Memorie Descrittive Servizio Geologico Italiano, 39,* 44-59.

Cavinato, G.P., & De Celles, P.G. (1999). Extensional basins in the tectonically bimodal central Apennines fold-thrust belt, Italy: Response to corner flow above a subducting slab in retrograde motion: *Geology, 27,* 955-958.

Centamore, E., Jacobacci, A., Malferrari, N., Martelli, G., Pieruccini, U., & Valletta, M. (1975). Carta Geologica d'Italia alla scala 1:50.000, F291 Pergola: *Servizio Geologico D'Italia.*

Centamore, E., & Nisio, S. (2003). Effects of uplift and tilting in the Central-Northern Apennines, Italy: *Quat. Int., 101-102,* 93-101.

Centamore, E., & Rossi, D. (2009). Neogene-Quaternary tectonics and sedimentation in the Central Apennines: *Ital. J. Geosci. (Boll. Soc. Geol. It.), 128 (1),* 73-88.

Chiarabba, C., & Amato, A. (1996). Crustal velocity structure of the Apennines (Italy) from P-wave travel time tomography: *Ann. Geofis., 39,* 1133-1148.

Chiarabba C., & Chiodini G. (2013). Continental delamination and mantle dynamics drive topography, extension and fluid discharge in the Apennines: *Geology, 2013,* vol. 41 (6), 715-718.

Ciarapica, G. (1990). Central and Northern Apennines during the Triassic: a review: *Boll. Soc. Geol. It., 109 (1),* 39-50.

Ciarapica, G., & Passeri, L. (1998). Evoluzione paleogeografica degli Appennini: *Atti Ticinensi di Scienze della Terra, 40,* 233-290.

Ciarapica, G. (2007). Regional and global changes around the Triassic-Jurassic boundary reflected in the late Norian-Hettangian history of the Apennine basins: *Palaeogeography, Palaeoclimatology, Palaeoecology, 244,* 34-51.

Cipollari, P., Cosentino, D. & Parotto, M. (1995). Modello cinematico-strutturale dell'Italia centrale: *Studi Geologici Camerti, Vol. Spec. 1995/2,* 135-143.

Cipollari, P., Cosentino, D., Esu, D., Girotti, O., Gliozzi, E., & Praturlon, A. (1999). Thrust-top lacustrine–lagoonal basin development in accretionary wedges: late Messinian (Lago-Mare) episode in the central Apennines (Italy): *Palaeogeography, Palaeoclimatology, Palaeoecology, 151,* 149-166.

Colacicchi, M., & Praturlon, A. (1965). Stratigraphical and paleontological investigations on the Mesozoic shelf-edge facies in Eastern Marsica (Central Apennines, Italy): Geologica Romana, 4, 89-118.

Cooley, M.A., Price, R.A., Kyser, T.K., & Dixon, J.M. (2011). Stable-isotope geochemistry of syntectonic veins in Palaeozoic carbonate rocks in the Livingstone Range anticlinorium and their significance to the thermal and fluid evolution of the southern Canadian foreland thrust and fold belt: *AAPG Bull., 95,* 185-1882.

Corrado, S. (1995). Optical parameters of maturity of organic matter dispersed in sediments: first results from the central Apennines (Italy): *Terra Nova, 7,* 338-347.

Cosentino, D., & Parotto, M. (1986). Assetto strutturale dei Monti Lucretili settentrionali (Sabina): Nuovi dati e schema tettonico preliminare: *Geologica Romana, 8,* 73-90.

Cosentino, D., Cipollari, P., Marsili, P., & Scrocca, D. (2010). Geology of the Central Apennines: A regional review: in Beltrando, M., Peccerillo, A., Mattei, M., Conticelli, S., & Doglioni, C., eds., The Geology of Italy: *Journal of the Virtual Explorer (Electronic Edition), 36,* paper 11.

Cosentino, D., Asti, R., Nocentini, M., Gliozzi, E., Kotsakis, T., Mattei, M., Esu, D., Spadi, M., Tallini, M., Cifelli, F., Pennacchioni, M., Cavuoto, G., & Di Fiore, V. (2017). New insights into the onset and evolution of the central Apennine extensional intermontane basins based on the tectonically active L'Aquila Basin (central Italy): *GSA Bull., 129 (9/10),* 1314-1336.

D'Agostino, N., Chamot-Rooke, N., Funiciello, R., Jolivet, L., & Speranza, F. (1998). The role of pre-existing thrust faults and topography on the styles of extension in the Gran Sasso range (Italy): *Tectonophysics, 292,* 229-254.

D'Agostino, N., Jackson, J.A., Dramis, F., & Funiciello, R. (2001). Interactions between mantle upwelling, drainage evolution and active normal faulting: an example from the

central Apennines (Italy): *Geophys. J. Int., 147,* 475-497.

Dahlen, F.A., Suppe, J., & Davis, D. (1984). Mechanics of fold-and-thrust belts and accretionary wedges: Coiesive Coulomb theory: *Journal of Geophysical Research, 89,* 10,087-10,101.

Davis, D.M., Suppe, J., & Dahlen, F.A. (1983). Mechanics of foldand-thrust belts and accretionary wedges: *J. Geophys. Res., 88,* 1153-1172.

Davis, D.M., & Engelder, T. (1985). The role of salt in foldand-thrust Belts: *Tectonophysics, 119*, 67-88.

Dela Pierre, F., Ghisetti, F., Lanza, R., & Vezzani, L. (1992). Palaeomagnetic and structural evidence of Neogene tectonic rotation of the Gran Sasso range (central Apennines, Italy): *Tectonophysics, 215,* 335-348.

Delle Piane, C., Ben Clennell, M., Keller, J.V.A., Giwelli, A., & Luzin, V. (2017). Carbonate hosted fault rocks: A review of structural and microstructural characteristic with implications for seismicity in the upper crust: *Journal of Structural Geology, 103,* 17-36.

Demurtas, M., Fondriest, M., Balsamo, F., Clemenzi, L., Storti, F., Bistacchi, A., Di Toro, G. (2016). Structure of a normal seismogenic fault zone in carbonates: The Vado di Corno Fault, Central Apennines (Italy): *Journal of Structural Geology, 90,* 185-206.

Dewever, B., Berwouts, I., Swennen, R.L., Breesch, L., & Ellam, R. (2010). Fluid flow reconstruction in karstified Panormide platform limestones (north-central Sicily): Implications for hydrocarbon prospectivity in the Sicilian fold and thrust belt: *Marine and Petroleum Geology, 27,* (4), 939-958.

Dewey, J.F., Helman, M.L., Knott, S.D., Turco, E., & Hutton, D.H.W. (1989). Kinematics of the western Mediterranean, In: Coward M.P., Dietrich D., and Park R.G., eds., Alpine Tectonics: *Geological Society of London Special Publication, 45,* 265–283.

Di Luzio, E., Mele, G., Tiberti, M.M., Cavinato, G.P., & Parotto, M. (2009). Moho deepening and shallow upper crustal delamination beneath the central Apennines: *Earth and Planetary Science Letters, 280,* 1-12.

Di Toro, G., Han, R., Hirose, T., De Paola, N., Nielsen, S., Mizoguchi, K., Ferri, F., Cocco, M., & Shimamoto, T. (2011). Fault lubrication during earthquakes: *Nature, 471,* 494-498.

Dickson, J.A.D. (1966), Carbonate identification and genesis as revealed by staining. *Journal of Sedimentary Petrology, 32,* 491-505.

Dietrich, D., McKenzie, J.A., & Song, H. (1983). Origin of calcite in syntectonic veins as

determined from carbone-isotope ratios: *Geology, 11,* 547-551.

Doglioni, C. (1991). A proposal for the kinematic modelling of W-dipping subductions - Possible applications to the Tyrrhenian-Apennines system: *Terra Nova, 3 (4),* 423-434.

Doglioni, C., Mongelli, F., & Pialli, G. (1998). Boudinage of the Alpine belt in the Apenninic back-arc: *Mem. Soc. Geol. Ital., 52,* 457-468.

Emery, D., & Robinson, A.G. (1993). Inorganic Geochemistry: Applications to Petroleum Geology: *Blackwell, Oxford,* 254 pp.

Engelder, T. (1984). The role of pore water circulation during the deformation of foreland fold and thrust belts: *Journal of Geophysical Research, 89,* 4319-4325.

Evans, M.A., & Elmore, R.D. (2006). Fluid control of localized mineral domains in limestone pressure solution structures: *J. Struct. Geol., 28,* 284-301.

Faulkner, D.R., & Rutter, E.H. (2001). Can the maintenance of overpressured fluids in large strike-slip fault zones explain their apparent weakness*?: Geology, 29 (6),* 503-506.

Faulkner, D., Jackson, C., Lunn, R., Schlische, R., Shipton, Z., Wibberley, C., & Withjack, M. (2010). A review of recent developments concerning the structure, mechanics and fluid flow properties of fault zones: *J. Struct. Geol. 32,* 1557-1575. http://dx.doi.org/10.1016/j.jsg.2010.06.009.

Ferket, H., Guilhaumou, N., Roure, F., & Swennen, R. (2011). Insights from fluid inclusions, thermal and PVT modelling for paleo-burial and thermal reconstruction of the Córdoba petroleum system (NE Mexico): *Marine and Petroleum Geology, 28 (4),* 936-958.

Friedman, I., & O'Neil, J.R. (1977). Compilation of stable isotope fractionation factors of geochemical interest, In: *Fleisher, M., ed., Data of Geochemistry (6th ed.): U.S. Geological Survey Professional Paper 440-KK,* 117 p.

Galadini, F., Messina, P., Giacco, B. & Sposato, A. (2003). Early uplift history of the Abruzzi Apennines (Central Italy): available geomorphological constraints: *Quat. Int., 101-102,* 125-135.

Galadini, F., & Messina, P. (2004). Early-Middle Pleistocene eastward migration of the Abruzzi Apennine (central Italy) extensional domain: *J. Geodyn., 37,* 57-81.

Galluzzo, F., & Santantonio, M. (2002). The Sabina Plateau: a new element in the Mesozoic palaeogeography of Central Apennines: *Boll. Soc. Geol. It., vol. spec. n. 1,* 561-588.

Ghisetti, F. & Vezzani, L. (1986). Assetto geometrico ed evoluzione strutturale della catena del Gran Sasso tra Vado di Siella e Vado di Corno: *Boll. Soc. Geol. It., 105,* 131-171.

Ghisetti, F. (1987). Mechanisms of thrust faulting in the Gran Sasso chain, Central Apennines, Italy: *Journal of Structual Geology, 9,* 955-967.

Ghisetti, F. & Vezzani, L. (1991). Thrust belt development in the Central Apennines (Italy): northward polarity of thrusting and out-of-sequence deformations in the Gran Sasso chain: *Tectonics, 10,* 904-919.

Ghisetti F., Barchi M., Bally A.W., Moretti I., & Vezzani L. (1993). Conflicting balanced sections across the central Apennines: Problems and implications: In A.M. Spencer (ed.), Generation, accumulation, and production of Europe's hydrocarbons. *Special Publication of the European Association of Petroleum Geoscientists, 3*, 219-231.

Ghisetti, F., Vezzani, L., & Follador, U. (1993b). Transpressioni destre nelle zone esterne dell'Appennino centrale: *Geologica Romana, 29,* 73-95.

Ghisetti, F. & Vezzani, L. (1997). Interfering paths of deformation and development of arcs in the fold-and-thrust belt of the Central Apennines (Italy): *Tectonics, 16,* 523-536.

Ghisetti, F. & Vezzani, L. (1999). Depths and modes of Pliocene-Pleistocene crustal extension of the Apennines (Italy): *Terra Nova, 11,* 67-72.

Ghisetti, F., Kirschner, D.L., Vezzani, L., & Agosta, F. (2001). Stable isotope evidence for contrasting paleofluid circulation in thrust faults and normal faults of the central Apennines, Italy: *Journal of Geophysical Research, 106,* 8811-8825.

Giraudi, C. & Frezzotti, M. (1997). Late Pleistocene glacial events in the Central Apennines, Italy. *Quaternary Research, 48,* 280-290.

Graveleau, F., Malavieille, J., & Dominguez, S. (2012). Experimental modelling of orogenic wedges: a review: *Tectonophysics, 538–540,* 1–66.

Gregg, J.M., & Sibley, D.F. (1984). Epigenetic dolomitization and the origin of xenotopic dolomite texture: *J. Sediment. Petrol. 54,* 907-931.

Hadizadeh, J., Mittempergher, S., Gratier, J.P., Renard, F., Di Toro, G., Richard, J., & Babaie, H.A. (2012). A microstructural study of fault rocks from the SAFOD: implications for the deformation mechanisms and strength of the creeping segment of the San Andreas Fault: *J. Struct. Geol. 42,* 246-60.

Hausegger, S., Kurz, W., Rabitsch, R., Kiechl, E., & Brosch, F.J. (2010). Analysis of the internal structure of a carbonate damage zone: implications for the mechanisms of fault breccia formation and fluid flow: *J. Struct. Geol., 32 (9),* 1349-1362.

Hoefs, J. (1997). Stable Isotope Geochemistry: *Springer-Verlag, Berlin,* 200 p.

Hohenberg, C.M., Thonnard, N., & Meshik, A. (2002). Active capture and anomalous adsorption: new mechanisms for the incorporation of heavy noble gases. *Meteorit. Planet. Sci., 37,* 257–267.

Hudson, J.D. (1977). Stable isotopes and limestone lithification: *J. Geol. Soc. London, 133,* 637-660.

Land, L.S. (1980). The isotopic and trace element geochemistry of dolomite: the state of the art: *In: Zenger, D.H., Dunham, J.B., Ethington, R.L. Eds., Concepts and Models of Dolomitization. Spec. Publ.-SEPM, 28,* 87-110.

Laubach, S.E., & Ward, M.W. (2006). Diagenesis in porosity evolution of opening-mode fractures, Middle Triassic to Lower Jurassic la Boca Formation, NE Mexico: *Tectonophysics, 419,* 75–97.

Leah, H., Fondriest, M., Lucca, A., Storti, F., Balsamo, F., and Di Toro, G. (2018). Coseismic extension recorded within the damage zone of the Vado di Ferruccio Thrust Fault, Central Apennines, Italy. *Journal of Structural Geology, 114,* 121-138.

Lena, G., Barchi, M.R., Alvarez, W., Felici, F., & Minelli, G. (2015). Mesostructural analysis of S-C fabrics in a shallow shear zone of the Umbria-Marche Apennines (Central Italy): In, Faulkner, D.R., Mariani, E. & Mecklenburgh, J. Eds. Rock Deformation from Field, Experiments and Theory: A Volume in Honour of Ernie Rutter. *Geological Society, London, Special Publications, 409,* 149-166. http://dx.doi.org/10.1144/SP409.10.

Liotta, D., Cernobori, L., & Nicolich, R. (1998). Restricted rifting and its coexistence with compressional structures; results from the CROP 3 traverse (Northern Apennines, Italy): *Terra Nova, 10,* 16-20.

Kirschner, D.L., & Kennedy, L. (2001). Limited syntectonic flow in carbonate-hosted thrust faults of the Front Ranges, Canadian Rockies, inferred from stable isotope data and structures: *J. Geophys. Res., 106,* 8827-8840.

Knipe, R.J., McCaig A.M. (1994). Microstructural and microchemical consequences of fluid flow in deforming rocks: *In Parnell, J., ed, Geofluids: Origin, migration and evolution of fluids in sedimentary basins, Geological Society Special Publication No. 78,* 99-111.

Machel, H.G. (1985). Cathodoluminescence in calcite and dolomite and its chemical interpretation: *Geoscience Canada, 12,* 139-147.

Machel, H.G. (2004). Concepts and models of dolomitization - A critical reappraisal: *In C. Braithwaite, G. Rizzi, and G. Darke, eds., The geometry and petrogenesis of*

dolomite hydrocarbon reservoirs: Geological Society (London) Special Publication, 235, 7-63.

Malinverno, A., & Ryan, W.B.F. (1986). Extension in the Tyrrhenian Sea and shortening in the Apennines as result of arc migration driven by sinking of the lithosphere: *Tectonics, 5,* 227-245.

Matsuda, J., Matsumoto, T., Sumino, H., Nagao, K., Yamamoto, J., Miura, Y., Kaneoka, I., Takahata, N., & Sano, Y. (2002). The $^{3}He/^{4}He$ ratio of the new internal He standard of Japan (HESJ). *Geochemical Journal, 36,* 191-195.

Mattei, M., Funiciello, R., & Kissel, C. (1995). Paleomagnetic and structural evidence for Neogene block rotations in the Central Apennines, Italy: *Journal of Geophysical Research, 100,* 863-883

McArthur, J.M., Howarth, R.J., & Shields, G.A. (2012). Strontium isotope stratigraphy. In: Gradstein, F.M. (Ed.), *The Geologic Time Scale. Elsevier Science Limited*, pp. 127-144.

Mele, G., Sandvol, E., & Cavinato, G.P. (2006). Evidence of crustal thickening beneath the central Apennines (Italy) from teleseismic receiver functions: *Earth and Planetary Science Letters, 249,* 425-435.

Miller, S.A., Collettini, C., Chiaraluce, L., Cocco, M., Barchi, M., & Kaus, B.J.P. (2004). Aftershocks driven by a high-pressure CO_2 source at depth: *Nature, 427 (6976),* 724-727.

Mittempergher, S., Di Toro, G., Gratier, J.-P., Hadizadeh, J., Smith, S.A.F., & Spiess, R. (2011). Evidence of transient increases of fluid pressure in SAFOD phase III cores: *Geophysical Research Letters, 38,* LO3301.

Moore J.C., Vrolijk, P. (1992). Fluids in accretionary prisms: *Reviews of Geophysics, 30 (2),* 113-135.

Muchez, P., Slobodnik, M., Viaene, W.A., & Keppens, E. (1995). Geochemical constraints on the origin and migration of palaeofluids at the northern margin of the Variscan foreland, southern Belgium: *Sedimentary Geology, 96,* 191-200.

Murgia, M.V., Ronchi, P., & Ceriani, A. (2004). Dolomitization processes and their relationships with the evolution of an orogenic belt (Central Apennines and peri-Adriatic foreland, Italy): in Swennen, R., Roure, F., & Granath, J.W. eds., Deformation, fluid flow, and reservoir appraisal in foreland fold and thrust belts: *AAPG Hedberg Series, no. 1,* 277-294.

Nelson, C.S., & Smith, A.M. (1996). Stable oxygen and carbon isotope compositional fields

for skeletal and diagenetic components in New Zealand Cenozoic nontropical carbonate sediments and limestones: a synthesis and review: *New Zealand Journal of Geology and Geophysics, 39,* 93–107.

Oliver, J. (1986). Fluids expelled tectonically from orogenic belts: Their role in hydrocarbon migration and on geologic phenomena: *Geology, 14,* 99-102.

Pace, P., Di Domenica, A., & Calamita, F. (2014). Summit low-angle faults in the Central Apennines of Italy: Younger-on-older thrusts or rotated normal faults? Constraints for defining the tectonic style of thrust belts: *Tectonics, 33,* 756-785.

Pace, P., & Calamita, F. (2015). Coalescence of fault-bend and fault-propagation folding in curved thrust systems: an insight from the Central Apennines, Italy: *Terra Nova, 27,* 175-183.

Park, W.G., & Schott, E.H. (1968). Stylolites: Their nature and origin: *Journal of Sedimentary Petrology, 38,* 175-191.

Patacca, E., Sartori, R., & Scandone, P. (1990). Tyrrhenian Basin and Apenninic arc: Kinematic relations since late Tortonian times: *Mem. Soc. Geol. It., 45,* 425–451.

Patacca, E., Scandone, P., Di Luzio, E., Cavinato, G.P., & Parotto, M. (2008). Structural architecture of the central Apennines: interpretation of the CROP 11 seismic profile from the Adriatic coast to the orographic divide: *Tectonics, 27,* TC3006, doi:10.1029/2005TC001917.

Pierantoni, P., Deiana, G., & Galdenzi, S. 2013. Stratigraphic and structural features of the Sibillini Mountains (Umbria–Marche Apennines, Italy): *Ital. J. Geosci., 132 (3),* 497-520.

Principi, G., & Treves, B. (1984). Il sistema corso-appennino come prisma d'accrezione. Riflessi sul problema generale del limite Alpi-Appennino: *Mem. Soc. Geol. It., 28,* 529-576.

Ramsay, J.G. (1980). Shear zone geometry: a review: *J. Struct. Geol., 2,* 83-99.

Ronchi, P., Jadoul F. & Savino R. (2004). Quaternary dedolomitization along fracture systems in a Late Triassic dolomitized platform (western Southern Alps, Italy): *Carbonates and Evaporites, 19 (1),* 51-66.

Ronchi, P., Di Giulio, A., Ceriani, A., & Scotti, P. (2010). Contrasting fluid events giving rise to apparently similar diagenetic products; late-stage dolomite cements from the Southern Alps and Central Apennines, Italy: in, Van Buchem, F.S.P., Gerds, K.D., & Esteban, M. eds, Mesozoic and Cenozoic Carbonate Systems of the Mediterranean and the Middle East: Stratigraphic and Diagenetic Reference Models. *Geological*

Society, London, Special Publications, 329, 397-413.

Rosenbaum, J. & Sheppard, S.M.F. (1986). An isotopic study of siderites, dolomites and ankerites at high temperature. *Geochimica te Cosmochimica Acta, 50,* 1147-1150.

Roure, F., Swennen, R., Schneider, F., Faure, J.L., Ferket, H., Guilhaumou, N., Osadetz, K., Robion, P., & Vandeginste, V. (2005). Incidence and importance of tectonics and natural fluid migration on reservoir evolution in foreland fold-and-thrust belts: *In: Brosse, E. (Ed.), Oil and Gas Science and Technology, Oil and Gas Science and Technology. Revue de l'IFP 60,* 67–106.

Royden, L. (1988). Flexural behaviour of the continental lithosphere in Italy: Constraints imposed by gravity and deflection data: *Journal of Geophysical Research, 93,* 7747–7766.

Royden, L., & Faccenna, C. (2018). Subduction Orogeny and the Late Cenozoic Evolution of the Mediterranean Arcs: *Annu. Rev. Earth Planet. Sci., 46,* 261-89.

Rusciadelli, G., Viandante, M.G., Calamita, F., & Cook A.C. (2005). Burial-exhumation history of the central Apennines (Italy), from the foreland to the chain building: thermochronological and geological data: *Terra Nova, 17,* 560-572.

Sage, L., Mosconi, A., Moretti, I., Riva, E., & Roure, F. (1991). Cross section balancing in the central Apennines: An application of LOCACE: *AAPG, 75 (4),* 832-844.

Sani, F., Del Ventisette, C., Montanari, D., Coli, M., Nafissi, P., & Piazzini, A. (2004). Tectonic evolution of the internal sector of the Central Apennines, Italy: *Marine and Petroleum Geology, 21,* 1235-1254.

Santantonio, M. (1993). Facies associations and evolution of pelagic carbonate platform/basin systems: examples from the Italian Jurassic: *Sedimentology 40,* 1039-1067.

Satolli, S., Speranza, F., & Calamita F. (2005). Paleomagnetism of the Gran Sasso range salient (central apennines, Italy): Pattern of orogenic rotations due to translation of a massive carbonate indenter: *Tectonics, 24,* 1-22.

Scisciani, V., Tavarnelli, E., & Calamita, F. (2002). The interaction of extensional and contractional deformations in the outer zones of the Central Apennines, Italy: *Journal of Structural Geology, 24,* 1647-1658, doi: 10.1016/S0191-8141(01)00164-X.

Servizio Geologico d'Italia (1963). Carta geologica d'Italia, Foglio n. 140. Teramo, Roma.

Sibson, R.H. (1977). Fault rocks and fault mechanisms: *Geological Society of London Journal, 133,* 191-231.

Sibson, R.H. (1981). Fluid flow accompanying faulting: Field evidence and models: in

Simpson, D.W., and Richards, P.G., cds., Earthquake prediction-An international review: American (Gophysical Union Monograph, Maurice Ewing Series, 4, 593-603.

Sibson, R.H. (1990). Conditions for fault-valve behaviour: *In: Geological Society of London, Special Publication, 54,* 15-28.

Smeraglia, L., Berra, F., Billi, A., Boschi, C., & Carminati, E. (2016). Origin and role of fuids involved in the seismic cycle of extensional faults in carbonate rocks: *EPSL, 450,* 292-305.

Smeraglia, L., Bernasconi, S.M., Berra, F., Billi, A., Boschi, C., Caracausi, A., Carminati, E., Castorina, F., Doglioni, C., Italiano, F., Rizzo, A.L., Uysal, T., & Zhao, J.-x. (2018). Crustal-scale fluid circulation and co-seismic shallow comb-veining along the longest normal fault of the central Apennines, Italy: *EPSL, 498,* 152-168.

Solum, J.G., & Huisman, B.A.H. (2016). Toward the creation of models to predict static and dynamic fault-seal potential in carbonates: *Petroleum Geoscience, 23 (1),* 70-91.

Speranza, F., Adamoli, L., Maniscalco, R., & Florindo F. (2003). Genesis and evolution of a curved mountain front: paleomagnetic and geological evidence from the Gran Sasso range (central Apennines, Italy): *Tectonophysics, 362,* 183-197.

Steiger, R.H. & Jager, E. (1977). Subcommission on geochronology: Convention on the use of decay constants in geo- and cosmochronology. *Earth Planet. Sci. Lett., 36,* 359-362.

Storti, F., & McClay, K. (1995). Influence of syntectonic sedimentation on thrust wedges in analogue models: *Geology, 23,* 999-1002.

Storti, F., Billi, A., & Salvini, F. (2003). Particle size distributions in natural carbonate fault rocks: insights for non-self-similar cataclasis: *Earth and Planetary Science Letters, 206,* 173-186.

Storti, F., Balsamo, F., Mozafari, M., Koopman, A., Swennen, R., & Taberner, C. (2018). Syn-Contractional Overprinting Between Extension and Shortening Along the Montagna Dei Fiori Fault During Plio-Pleistocene Antiformal Stacking at the Central Apennines Thrust Wedge Toe: *Tectonics, first published online 20 September 2018,* https://doi.org/10.1029/2018TC005072.

Stuart, F., Turner, G. & Taylor, R. (1994). He-Ar isotope systematics of fluid inclusions: resolving mantle and crustal contributions to hydrothermal fluids. In: Matsuda, J. (Ed.), *Noble Gas Geochemistry and Cosmochemistry.* Terra Scientific Publishing Company, Tokyo.

Tesei, T., Collettini, C., Viti, C., & Barchi, M.R. (2013). Fault architecture and deformation

mechanisms in exhumed analogues of seismogenic carbonate-bearing thrusts: *Journal of Structural Geology, 55,* 167-181.

Tiberti, M.M., Orlando, L., Di Bucci, D., Bernabini, M., & Parotto, M. (2005). Regional gravity anomaly map and crustal model of the Central-Southern Apennines (Italy): *Journal of Geodynamics, 40,* 73-91.

Tozer, R.S.J., Butler R.W.H., & Corrado S. (2002). Comparing thin- and thick-skinned thrust tectonics models of the Central Apennines, Italy: in Continental Collision and the Tectono-Sedimentary Evolution of Forelands, *Stephan Mueller Spec. Publ. Ser., 1,* 181-194, Eur. Geosci. Union, Strasbourg, France.

Veizer, J., Ala, D., Azmy, K., Bruckschen, P., Buhl, D., Bruhn, F., Carden, G.A.F., Diener, A., Ebneth, S., Godderis, Y., Jasper, T., Korte, C., Pawellek, F., Podlaha, O.G. & Strauss, H. (1999) .87Sr/86Sr, $\delta^{13}C$ and $\delta^{18}O$ evolution of Phanerozoic seawater: *Chem. Geol., 161,* 59-88.

Vezzani, L., Festa, A., & Ghisetti, F.C. (2010). Geology and tectonic evolution of the Central-Southern Apennines, Italy: *Geological Society of America Special Paper 469,* 1-58.

Vilasi, N., Malandain, J., Barrier, L., Callot, J-P., Amrouch, K., Guilhaumou, N., Lacombe, O., Muska, K., Roure, F., and Swennen, R. (2009). From outcrop and petrographic studies to basin-scale fluid flow modelling: the use of the Albanian natural laboratory for carbonate reservoir characterisation: *Tectonophysics, 474 (1-2),* 367-392.

Warren, J. (2000). Dolomite: occurrence, evolution and economically important associations: *Earth Science Reviews, 52,* 1-81.

Wiltschko, D.V., Lambert, G.R., & Lamb, W. (2009). Conditions during syntectonic vein formation in the footwall of the Absaroka Thrust Fault, Idaho-Wyoming-Utah fold and thrust belt: *Journal of Structural Geology, 31,* 1039-1057.

Wintsch, R.P., Christoffersen, R., Kronenberg, A.K. (1995). Fluid-rock reaction weakening of fault zones: *Journal of Geophysical Research - Solid Earth, 100 (B7),* 13021-13032.

Wojtal, S., & Mitra, G. (1986). Strain hardening and strain softening in fault zones from foreland thrusts: *GSA Bull., 97,* 674-687.

Woodcock, N.H., & Mort, K. (2008). Classification of fault breccias and related fault rocks. *Geol. Mag., 145 (03),* 435-440.

Lucca et al., (Subaerial out-of-sequence thrusting and late-stage extension in the Gran Sasso Massif, Central Apennines, Italy), Data Repository

Table S1: Oxygen and carbon stable isotopes contents

Cement Type	Site	$\delta^{18}O$‰ (V-PDB)	$\delta^{13}C$‰ (V-PDB)
BDCalV	CF3	-4,23	1,42
BDCalV	CF3	-2,93	2,02
BDCalV	CF9	-6,86	-4,68
BDCalV	CF9	-5,50	-1,57
CFCalV	CF3	-6,06	0,54
CFCalV	CF3	-8,30	-3,86
CFCalV	CF3	-7,42	-2,59
VFCal1	VF3	0,13	1,42
VFCal1	VF5	-3,26	1,44
VFCal1	VF5	-3,00	1,61
VFCal2	VF3	-5,40	-1,01
VFCal2	VF5	-5,82	1,32
VFCore	VF5	-0,48	1,55
VFCore	VF5	0,39	2,13
VFCore	VF5	-0,25	1,68
CoCalV	VF1	-0,99	0,36
CoCalV	VF1	-1,23	0,26
CoCalV	VF1	-1,41	0,25
CoCalV	VF3	-1,43	2,19
CoCalV	VF3	-0,27	2,55
CoCalV	VF8	-1,24	2,37
CoCalV	VF8	0,22	2,22
CoCalV	VF8	-0,98	2,15
CoCalV	VF8	-0,68	2,35
CoCalV	VF8	0,03	1,98
CoHR	VF1	-0,85	0,52
CoHR	VF1	-0,88	0,56
CoHR	VF3	-1,15	2,55
CoHR	VF3	-0,51	2,65
CoHR	VF5	-0,11	1,62
CoHR	VF5	0,00	1,73
CoHR	VF8	-0,10	2,33
CoHR	VF8	-0,78	2,33
BDHR	CF3	0,93	2,01
BDHR	CF3	1,48	2,04
BDHR	CF3	0,13	2,20
BDHR	CF3	-1,05	1,67
BDHR	CF3	-2,03	1,75
BDHR	CF3	-1,58	1,82
BDHR	CF3	-2,22	1,55

BDHR	CF9	2,20	1,41
BDHR	CF9	0,40	1,40
BDHR	CF9	0,53	1,65
BDHR	CF9	0,13	2,30
BDHR	CF9	0,60	2,31
BDHR	CF9	0,68	2,17
BDHR	CF9	0,79	2,25
BDHR	CF18	0,08	2,16
BDHR	VF1	0,53	2,24
BDHR	VF1	1,13	1,99
BDHR	VF9	0,77	2,29
BDHR	VF9	0,10	2,16
BDHR	VF10	-0,09	2,26
BDHR	CF26	3,26	2,12
BDHR	CF26	3,49	1,95
BDHR	CF26	3,79	2,01
BDDolFV	CF3	0,60	2,00
BDDolFV	CF3	0,08	1,87
BDDolFV	CF3	-0,35	2,02
BDDolFV	CF9	-0,13	1,69
BDDolFV	CF9	-0,48	2,12
BDDolFV	CF9	-0,03	2,17
BDDolFV	CF9	-0,36	1,98
BDDolFV	CF9	-2,65	-1,60
BDDolFV	CF18	0,19	2,22
BDDolFV	CF18	0,16	2,04
BDDolFV	VF1	0,83	2,02
BDDolFV	VF1	0,63	2,06
BDDolFV	VF9	0,47	2,20
BDDolFV	VF9	0,35	2,02
BDDolFV	VF10	-0,20	2,10
BDDolFV	CF26	0,24	2,58
BDDolFV	CF26	-0,33	2,24
BDDolFV	CF26	0,47	2,46
CFCalSB	CF3	-7,22	-2,62
CFCalSB	CF10	-7,53	-2,88
CFCalSB	CF10	-6,96	-2,19
CFCalSB	CF10	-4,56	-2,32
CFCalSB	CF10	-4,60	-0,40
CFCalSB	CF15	-6,63	-2,24
CFCalDolSB	CF3	-2,24	0,90
CFCalDolSB	CF10	-2,39	0,20
CFCalDolSB	CF10	-2,71	-0,16
CFCalDolSB	CF15	-0,38	-0,04
CFCalDolSB	CF26	-0,58	1,25
CFCalDolSB	CF26	-0,43	1,45
CFCalDolSB	CF26	-0,56	-0,25

RCHR	CF9	-0,54	2,10
RCHR	CF9	-0,40	2,38
RCHR	CF9	-1,76	1,69
RCHR	CF9	-0,48	2,05
RCHR	CF9	-1,11	2,00

Table S2: Strontium isotope ratios and standard deviations of the analyzed samples

Cement Type	Site	$^{87/86}Sr$	Error
CoCalV	VF1	0,707397	0,000009
CoHR	VF1	0,707157	0,000009
Bit.Dol.V	CF3	0,707707	0,000009
Bit.Dol.HR	CF3	0,707968	0,000010
Bit.Dol.V	CF26	0,707500	0,000010
Bit.Dol.HR	CF26	0,707843	0,000010
CFDolCalSB	CF26	0,707786	0,000011
Rudist Cal. HR	CF9	0,707035	0.000009

Table S3: Noble gases contents of the analyzed samples

Sample	<125 µm (g)	>125 µm (g)	% crushed	3He	±	4He	±	21Ne	±	22Ne	±	CO2	±	40Ar	±	36Ar	±	84Kr	±	132Xe	±
CFCalDolSB	0,0587	0,2074	22,1	5,10E-02	1,45E-01	1,50E-03	2,39E-05	3,38E+01	7,31E+00	1,70E+03	4,24E+01	2,48E+04	3,90E+02	4,30E-01	1,03E-04	1,40E-03	9,96E-06	7,14E+03	2,96E+01	5,04E+02	8,00E+00
CFCalDolSB	0,0396	0,2461	13,9	1,70E-02	1,41E-01	1,86E-03	1,64E-05	6,56E+01	9,98E+00	2,61E+03	5,79E+01	3,53E+04	4,30E+02	1,59E+00	3,53E-04	5,20E-03	1,13E-05	3,00E+04	6,45E+01	1,78E+03	1,61E+01
CFCalDolSB	0,0551	0,2042	21,2	-5,30E-02	1,24E-01	1,61E-03	1,90E-05	8,00E+01	4,10E+00	1,28E+03	3,60E+01	4,68E+04	5,87E+02	1,77E-01	3,50E-05	5,58E-04	9,81E-06	3,80E+03	2,40E+01	3,08E+02	6,40E+00
CFCalDolSB	0,0358	0,2493	12,6	8,40E-02	1,06E-01	1,19E-03	2,11E-05	2,04E+01	4,76E+00	1,44E+03	4,97E+01	4,94E+04	6,11E+02	7,54E-01	1,07E-04	2,45E-03	1,18E-05	1,52E+04	3,82E+01	2,37E+03	1,71E+01
Bit.Dol.HR	0,0261	0,2130	10,9	1,77E-02	2,31E-01	3,34E-04	1,47E-05	2,80E+01	4,90E+00	1,85E+03	6,00E+01	6,13E+04	4,88E+02	3,07E-01	8,00E-05	9,67E-04	9,91E-06	6,07E+03	2,70E+01	2,79E+03	2,00E+01
Bit.Dol.V	x	0,118	x	-2,66E-02	1,34E-01	4,52E-05	2,14E-05	4,22E+01	9,35E+00	2,26E+03	5,12E+01	5,27E+04	6,50E+02	9,32E-01	2,00E-04	3,01E-03	1,40E-05	1,58E+04	4,20E+01	9,46E+02	1,30E+01
Bit.Dol.V	0,0902	0,119	43,1	3,21E-01	2,72E-01	1,00E-03	2,10E-05	4,77E+01	7,35E+00	3,59E+03	6,95E+01	1,14E+05	1,00E+03	1,08E+00	8,00E-04	3,50E-03	1,30E-05	1,97E+04	4,60E+01	1,78E+03	1,66E+01
VFCore	0,0232	0,2405	8,8	1,67E-01	9,80E-02	3,55E-05	1,90E-05	2,12E+01	5,04E+00	1,21E+03	4,44E+01	2,51E+04	2,72E+02	1,59E-06	5,23E-05	5,40E-04	1,20E-05	3,10E+03	2,19E+01	3,54E+02	6,86E+00
VFCal1	0,046	0,1449	24,1	-3,10E-02	1,38E-01	8,44E-05	2,05E-05	7,72E+00	4,28E+00	7,77E+02	3,56E+01	2,09E+04	2,16E+02	3,73E-01	1,30E-04	1,22E-03	1,40E-05	8,71E+03	3,30E+01	6,49E+02	8,36E+00
VFCal2	0,025	0,1736	12,6	4,80E-02	1,69E-01	2,51E-04	2,00E-05	3,21E+01	5,76E+00	1,69E+03	4,57E+01	2,93E+04	3,25E+02	x	x	x	x	x	x	x	x
CoHR	0,019	0,1681	10,2	1,98E-02	1,66E-02	7,25E-05	2,53E-05	2,10E+01	6,00E+00	1,44E+03	3,90E+01	4,35E+04	5,10E+02	1,01E-01	4,00E-05	3,32E-04	1,29E-05	2,20E+03	1,70E+01	2,62E+02	6,00E+00
CoCalV	0,0346	0,1533	18,4	-1,40E-02	1,64E+02	2,05E-04	1,90E-05	1,58E+01	4,40E+00	1,20E+03	4,50E+01	3,54E+04	4,52E+02	6,10E-01	3,00E-04	1,95E-03	1,72E-06	1,50E+04	6,30E+01	1,26E+03	1,30E+01

6

PORE TYPE EVOLUTION AND FLOW PROPERTIES OF CARBONATE FAULT ROCKS

This chapter is presented in the form of a manuscript that is currently being published by to the *Society for Sedimentary Geology*. This manuscript describes carbonatic and dolomitic fault rocks along the Campo Imperatore and Assergi Extensional Fault Systems and their petrophysical properties. In this study we document increasing comminution and decreasing pore size moving towards the fault cores, and we show that breccias and cataclasites are characterized by the highest and lowest permeability values, respectively. As a result, depending on structural position and architecture, fault zones can act as dynamic seals or as effective fluid conduits.

SUBMITTED ARTICLE

Cilona A., Solum J.G., Balsamo F., Lucca A., Storti F., and Taberner C.

Submitted to: *Society for Sedimentary Geology (SEPM)*

Date of Submission: 20 April 2018

Date of Acceptance: 16 January 2019

Pore type evolution and flow properties of carbonate fault rocks

A. Cilona[1], J.G. Solum[2], F. Balsamo[3], A. Lucca[3], F. Storti[3], C. Taberner[1]

[1]Carbonate Research Team, Shell Global Solutions International B.V., Grasweg 31, 1031 HW Amsterdam, The Netherlands.

[2]Structural Geology R&D Team, Shell International Exploration and Production, 3333 Hwy 6, Houston, TX 77082, USA

[3]NEXT - Natural and Experimental Tectonics research group, Department of Chemistry, Life Sciences and Environmental Sustainability, University of Parma, I-43124 Parma, Italy

Keywords: Porosity; Permeability; Fault Seal; Microstructures; Heterogeneity

Abstract

In carbonates, fault zone architecture, distribution of different types of fault rocks in fault cores (e.g., breccias, cataclasites), and the interplay between deformation and diagenesis must be considered to predict the flow properties of a fault zone. We present the results of an integrated structural and petrophysical study of two carbonate outcrops in central Italy, where faults are known to act as dynamic seals at depth causing ≈70m of hydraulic head drop in a karstified groundwater reservoir

The architecture of these fault zones is very well-exposed, allowing for detailed mapping of the along-strike distribution and continuity of fault cores and associated fault rocks over a distance of ≈8 km. More than 150 samples, comprising several fault architectural elements and carbonate host rocks, were collected in transects orthogonal to the fault zones. Fault rock porosity and permeability were measured on 1-inch plugs and then linked to characteristic microstructures and fault rock textures. This allowed us to obtain ranges of porosity, permeability for each type of fault rock.

A trend of increasing comminution and decreasing pore size was observed from the outer toward the inner portions of fault cores. Three types of breccias (crackle, mosaic and chaotic) and various types of cataclasites were identified. Crackle breccias reach the highest plug permeabilities (up to 100s of mD), whereas the ultra-cataclasites have the lowest plug permeability (down to 0.01 mD, which is roughly equivalent to unfractured host rock). These data are used to discuss the effect of various fault rocks on the host rock permeability and to display the permeability anisotropy of fault zones in carbonates.

1. INTRODUCTION

Methods and techniques to predict sealing behavior of faults in clastics are relatively well understood (see Yielding et al., 2010 and Freeman et al., 2010 for a full review), however similar methods and techniques are not yet available for faults in carbonates (cf. Solum and Huisman, 2017).

Permeability is controlled mainly by pore systems, which, in carbonates, depend on both depositional and diagenetic processes and tectonic overprinting. For instance, sedimentary

environment determines quantity of lime mud, grain size, and sorting, and therefore is a key depositional control on permeability (Loucks, 2002; Melim et al., 2001). Post-depositional processes are equally significant. Carbonates have a metastable mineralogical composition, which makes them prone to diagenesis and accompanying changes in rock texture. Such modifications result in drastic changes of the pore systems and, consequently, permeability (Flügel, 2013). In addition to the diagenetic overprint, tectonic stresses can cause rock deformation and fracturing and drastically alter the pore system and the permeability of the rock (e.g., Aydin, 2000; Arzilli et al., 2016; Tondi et al., 2016, Klimchouck et al., 2016).

Fault zones include very heterogeneous rock volumes/architectural elements (Fig. 1a), which are typically subdivided into damage zone and fault core (Caine et al., 1996). Caine et al. (1996) describe the damage zone as a network of subsidiary fault-related structures where fracture intensity is higher than in the host rock. Whereas, fault cores are the zones where most of the strain localized; consisting of single or multiple slip surfaces bounding various types of fault rocks (Storti et al., 2003; Agosta and Aydin. 2006).

The prevalent faulting mechanisms in carbonates depend on the host rock lithology and thus is strongly controlled by texture and porosity (Antonellini et al., 2008). In tight carbonates, fault zones nucleate and develop by shearing and linkage of preexisting discontinuities, such as joints, veins and stylolites (Fig. 1b-c; Agosta et al. 2009; Agosta et al., 2015). Conversely, in porous carbonates, fault nucleation and development take place through deformation bands (Fig. 1d; Tondi et al., 2006; Cilona et al., 2014). Because lithology controls the faulting mechanism, by knowing host rock lithology one can estimate whether faulting will tend to improve or reduce the porosity and permeability of the host rock (Fig. 1b-d; Bense et al., 2013). However, this rule of thumb is more difficult to apply to all types of faults in carbonates. To date, rules for predicting fault sealing capacity are not yet available for carbonates, although examples of faults in carbonates sealing over geological time scales do exist (Solum and Huisman, 2017). Understanding faulting processes and their fault core and damage zone geometry, composition, petrophysics, spatial distribution, as well the diagenesis is crucial for building realistic models of fault zone architecture and predicting fluid flow behavior in fractured carbonate reservoirs (Aydin, 2000; Agosta et al., 2007, Storti & Balsamo, 2010; Balsamo et al., 2016; Solum and Huisman, 2017).

In this paper, we present a new dataset of petrophysical properties from two large-displacement fault zones cropping out in the Gran Sasso Massif, Central Apennines (Italy). The architecture of these two fault zones is excellently exposed and allowed us to collect more than 150 samples from various fault architectural elements and carbonate host rocks. Fault cores with different types of fault rocks were systematically sampled and petrophysical properties (i.e., porosity, permeability) were measured and linked to characteristic fault rock microstructures, textures and pores. In addition, we used this dataset, to discuss the evidence for dynamic sealing displayed by one of the studied faults.

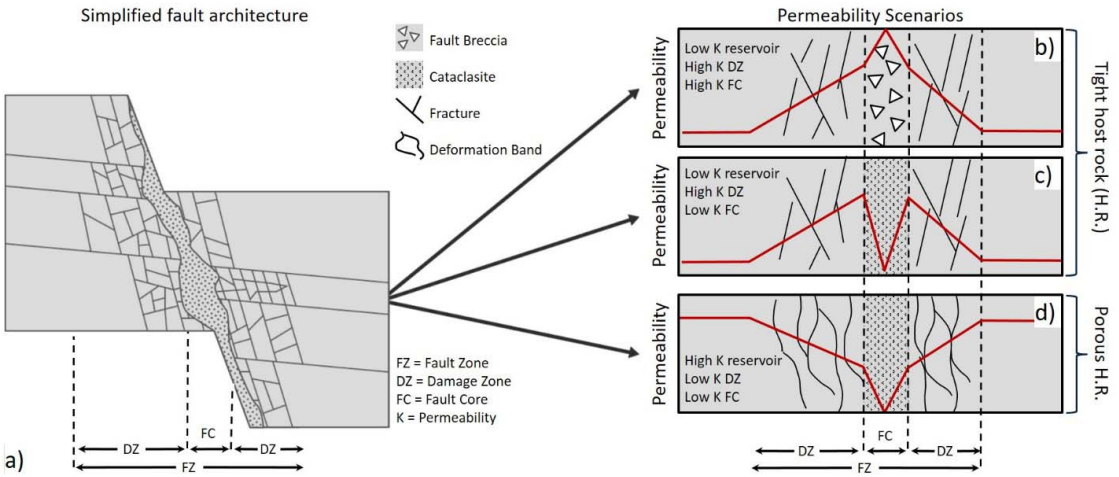


Figure 1: Fault zone architecture and permeability structure. a) Cross-section of a normal fault displaying main architectural elements: fractured damage zone, and fault core, modified after Solum and Huisman (2017); Qualitative representation of permeability profile across a fault zone: a-b in tight carbonates with fractured damage zone and breccias (b) or cataclasites (c) in the fault core, adapted after Agosta et al. (2007), and c) in porous carbonates with deformation bands in the damage zone and cataclasites in the fault core, adapted after Tondi et al (2016).

2. GEOLOGICAL SETTING

The Gran Sasso Massif (GSM) is one of the principal structural features of the Central Apennines and formed during Late Messinian, to Middle Pliocene orogenic contraction (Ghisetti and Vezzani, 1991). The main thrust and its related anticline, display an arcuate geometry consisting of two main segments striking ~E-W and N-S, respectively (Fig. 2a). The GSM consists of an array of six major thrust faults crosscutting each other in an out-of-sequence geometry (Ghisetti and Vezzani, 1991) with the uppermost thrust faults outcropping in the Vado di Corno area (i.e., the Omo Morto thrust fault; Ghisetti and Vezzani, 1991, Fig. 2a). The presence of a well-developed system of active extensional fault zones including the Vado di Corno Fault Zone (VCFZ), described by Demurtas et al. (2016), is the result of Early Pleistocene to Present extension in the GSM. In the study area, the VCFZ is mostly developed within the Calcare Massiccio Fm. (Lower Jurassic; e.g. Adamoli et al., 2012, Fig.2 b), which consists of a thick (≈600 m) sequence of whitish to brownish limestones with beds (5 to 50 cm thick) organized in 1 to 5 m thick bed sets. In the study area, these limestones are often dolomitized (Adamoli et al., 2003). Demurtas et al. (2016) interpreted the two observed dolostone lithofacies as result of different timing and intensity of dolomitization. The other lithologies cropping out along the fault zone are: i) the slope and basinal deposits of the Corniola (mudstone, Lower Jurassic), ii) Verde Ammonitico e Calcari e Marne a Posidonia (micritic limestone, Lower-Middle Jurassic), iii) Calcari Bioclastici Inferiori (breccias and megabreccias Middle- Upper Jurassic), and iv) Maiolica Detritica (micritic limestone, Upper Jurassic-Lower Cretaceous) formations (Adamoli et al., 2012).

Eastward respect to the study area, the Verde Ammonitico and Calcari e Marne a Posidonia formations are overthrusted by the Calcare Massiccio Fm. (e.g., Ghisetti and Vezzani, 1991; Adamoli et al., 2012). In the footwall of the VCFZ, Demurtas et al. (2016) documented occurrences of strongly dolomitized Verde Ammonitico Fm. and associated dark chert remnants. Demurtas et al. (2016) used this line of evidence to suggest that the stratigraphic stacking, cropping out to the east of the study area, is present also in the footwall of the VCFZ, where Verde Ammonitico and Calcare Massiccio formations were severely dolomitized prior to Quaternary extensional faulting. Small outcrops of the Maiolica Detritica Fm. are present in the hanging wall of VCFZ near Mt. Brancastello, whereas most of the Vado di Corno intramontane basin is filled by glacial, alluvial and colluvial deposits (Demurtas et al., 2016). The former is related to Late Pleistocene glacial events (Giraudi and Frezzotti, 1995, 1997; Adamoli et al., 2012); the latter are Holocene in age and derived from weathering of the exposed carbonate rocks. Most of the hanging wall exposures are of this Pleistocene/Holocene fill.

The VCFZ crops out for ca. 5 km delimiting northward the Campo Imperatore intramontane basin (Fig. 2a), this fault zone belongs to the Campo Imperatore Fault System, which runs for ca. 20 km in the GSM and is thought to have accommodated a cumulative throw of 2000-3000 m (Ghisetti and Vezzani, 1991, D'Agostino et al., 1998). Isotopic analysis suggested that the fault

zone was exhumed from ca. 1-2 km depth starting in the Early-Pleistocene (Agosta and Kirschner, 2003). Between Vado di Corno, Mt. Brancastello and Mt. Camicia, numerous creeks create a badland morphology and expose the footwall of the VCFZ allowing the characterization of the architecture of this fault block. Demurtas et al. (2016) describe the VCFZ as an array of NW-SE trending and mostly SW-dipping, extensional faults, which are continuous over distances of 20-30 m and comprise layers of cataclasite with thickness up to 30 cm (Demurtas et al. 2016). A large number of such faults crosscuts the outcrop resulting in significant cumulative cataclasite thicknesses (Demurtas et al., 2016). These faults bound different structural units both in the fault core and in the fractured damage zone (Demurtas et al., 2016). At the base of the badlands, a well-polished fault slip surface, interpreted as the master fault, juxtaposes the white cataclastic rocks against the Quaternary deposits in the hanging wall.

To the south from the VCFZ, the Assergi Fault Zone (AFZ) is exposed. This fault is more than 17 km long and has a maximum displacement of ca. 1000 m (Fig. 2a; Pizzi et al., 2002). Fault scarps can be followed in the field for several kilometers and represent the morphological expression of this active fault. In the area surrounding the Gran Sasso tunnel, the AFZ juxtaposes the dolomitized Calcare Massiccio Fm. against the Maiolica Detritica Fm (Adamoli et al., 2012). The architecture of this fault has been described by several authors, documenting the presence of a thick (3-15 m) cataclasite fault core flanked by fault breccias (e.g., Celico et al. 2005; Ortner et al., 2014). The fault core is flanked by a fractured damage zone with a width of several 10s of meters. Characterizing fracture intensity both in host rock and damage is beyond the scope of this work, however our qualitative observations suggest that the lithologies crosscut by the fault have a different response to fracturing.

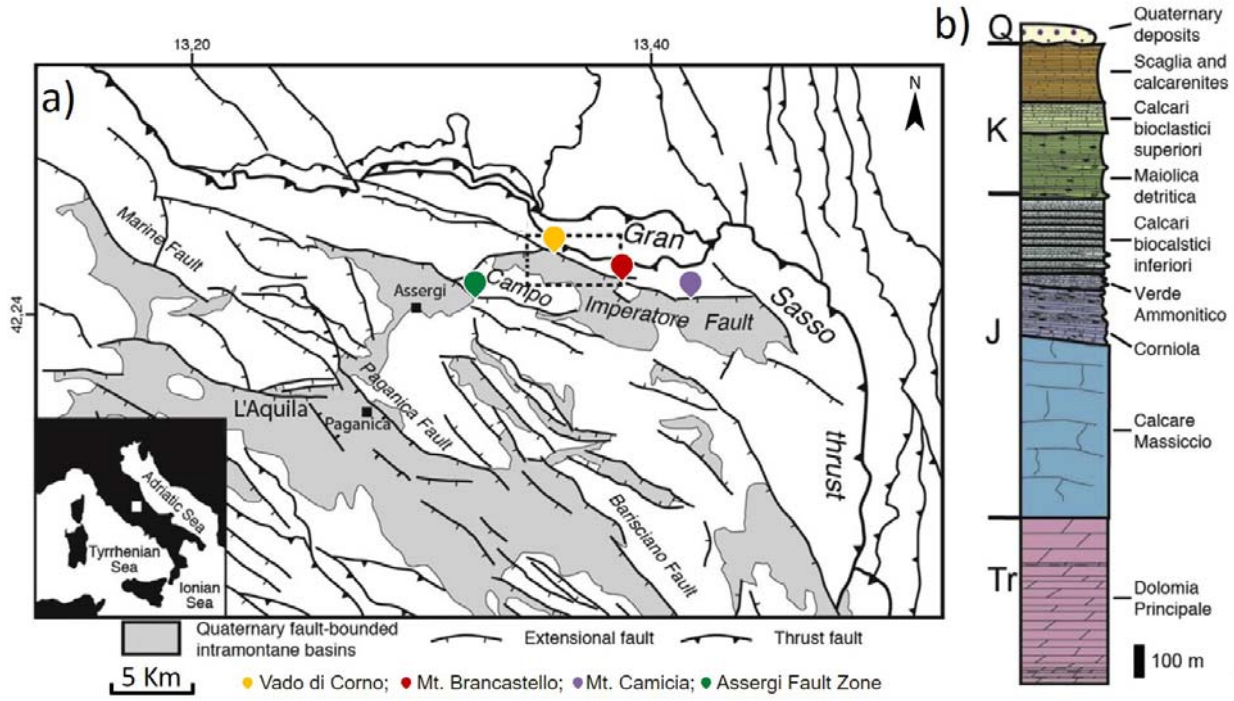


Figure 2: Geological setting of the Campo Imperatore area. a) Structural map of the Gran Sasso area (modified after Storti et al., 2013); (b) Stratigraphic column of the Campo Imperatore area (modified after Cardello and Doglioni, 2014).

3. METHODS

For this study, large samples (up to 50 cm in size) were collected from outcrops representative of fault architectural elements (i.e., host rock, fault damage zone, fault core). The spatial orientation of key features (e.g., bedding, fractures, veins, slip surfaces) was measured on the samples, and sampling location was recorded using a field GPS.

From each sample, three 2.5 cm diameter 5 cm-long plugs were cored in mutually perpendicular directions (i.e., normal to fault plane, parallel to strike and parallel to dip). Coring three plugs of 5 cm length was only possible in the largest samples. Depending on the sample availability, either plug trim ends or other portions of the sample were used for standard petrographic thin section preparation. The rock samples were impregnated with blue dye resin and stained with mixed solution of Alizarin Red S and potassium ferricyanide (see Dickson, 1965 for more details) . The blue resin was used to enhance pore visualization, whereas the dual staining of Alizarin Red S and potassium ferricyanide allowed the differentiation of calcite (pink or red stain) and dolomite, as well as ferroan carbonate minerals (ferroan calcite = blue, ferroan dolomite = turquoise). The stained surface was mounted on the glass and then, after reaching the standard thickness the thin sections were mirror-polished. The petrographic study was carried out using a Nikon Eclipse E600 transmitted light microscope and thin section photographs were acquired with a Nikon DS-Fi1 digital camera, using plane parallel and cross-polarized light. Thin sections were used for textural and microstructural analysis.

White light pictures of each plug were taken before performing petrophysical measurements. Plug density was calculated as follows: sample volume was obtained by submerging dry plugs (at least 48 hours under vacuum at 95°C) in mercury. The displacement of mercury in the container was used to measure the volume of the plug. Mercury-derived volumes were compared to volumes calculated from length and diameter measured with a caliper (0.01 mm precision). Dry plugs were weighed using a high-precision scale (precision: 0.001 gram), and then chloroform-saturated. The dry weight and chloroform-saturated weight measurement were used as input to calculate grain volume and grain density. Plug porosity was measured using sample bulk density (both caliper and mercury volume) and grain density as input (Equation 1). Where ρ is the sample density, □ is the porosity expressed in fraction, ρ_{fl} is the density of the fluid saturating the pores and ρ_g is the grain density.

Equation 1 $$\rho = \phi\rho_{fl} + (1-\phi)\rho_g$$

Permeability was measured with an AP-608 Automated Permeameter Porosimeter produced by CORETEST SYSTEMS INC. This apparatus measures permeability ≥0.001 mD and requires plugs with a regular geometry (cylinder shape) and with length ≥2 cm. Measurements were performed at three pressure steps: 3.5 MPa (500 psi), 13.5 MPa (2000 psi), and 45 MPa (6500 psi) to investigate the influence of stress on permeability. The permeabilities were then Klinkenberg (Klinkenberg, 1941) and turbulence corrected.

4. RESULTS

4.1. Fault Rocks

The two fault zones consist of multiple irregular geobodies juxtaposed against each other. Each geobody is made up of one or more fault architectural elements (*sensu* Caine et al., 1996) and various types of fault rocks.

In the field, we identified: i) fractured damage zones, ii) clast-supported breccias, iii) matrix supported breccias, and iv) cataclasites (Fig. 3). In addition to these classes, which are mainly based on fault rock textures, we considered whether the fault rock was loose or cohesive. In the study area, the fractured damage zones consist of few to several 10s of meters wide fractured carbonate rocks (i.e., limestone and/or dolostone) where stratigraphic markers (e.g., bedding, lamination) can be still identified (Fig. 3a-b). In these damage zones, the most pervasive deformation features are joints, stylolites, and shear fractures (small-scale faults, cf. Demurtas et al., 2016). The damage zones have different degrees of deformation, separated into low and high strain domains based on fracture intensity (Demurtas et al., 2016). This paper focuses on fault cores, more specifically on classification and sampling of the fault rock types present in the two study areas.

In grain-supported breccias (Fig. 3c-d), the clasts are in direct contact with each other, forming a continuous framework. Clast shape is very angular and with size ranging from several millimeters to a few centimeters. It is often possible to identify clasts that used to be attached due to offset markers (Woodcock and Mort, 2008). In matrix-supported breccias (Fig. 3f), most large clasts are not in direct contact with each other and float in a matrix of sub-millimetric grains. In these breccias, the clasts have a less angular shape with respect to clast-supported breccias, and clast size ranges from millimeter to cm scale. Commonly, each clast has lost any geometric fit to the adjacent clasts, indicating rotation and translation.

Cataclasites often have a lighter color with respect to protolith and their grain size can be as small as clay size (Fig. 3e-f). Outcrops of the AFZ expose white loose cataclasite, which can be easily dug out by hand (cf. Storti & Balsamo, 2010). The granular material is often crosscut by shear bands (*sensu* Aydin et al., 2006), which often are a more resistant to erosion than the surrounding rock (Fig. 3e). Along other outcrops, both the AFZ and the VCFZ expose white cohesive cataclasites. In the field, these fault rocks appear massive and when hammered they tend to break along preexisting discontinuities (Fig. 3f). Commonly, the discontinuities are shear fractures or shear bands with measurable offsets. The surface of these fractures is very smooth and shows very high light reflectivity (Fig. 3f). These slip surfaces are known in literature as mirror-like slip surfaces (Fondriest et al. 2013; Demurtas et al., 2016), and their high reflectivity is given by the ultra-fine grain size. Some authors interpret these features as the result of co-seismic slip (Fondriest et al. 2013).

4.2. Fault Core/ Fault Rock Microstructures

The fault rocks were grouped following the classification of Woodcock and Mort (2008). These authors classify fault rocks into cataclasites if less than 30% of clasts exceed 2 mm, and as a

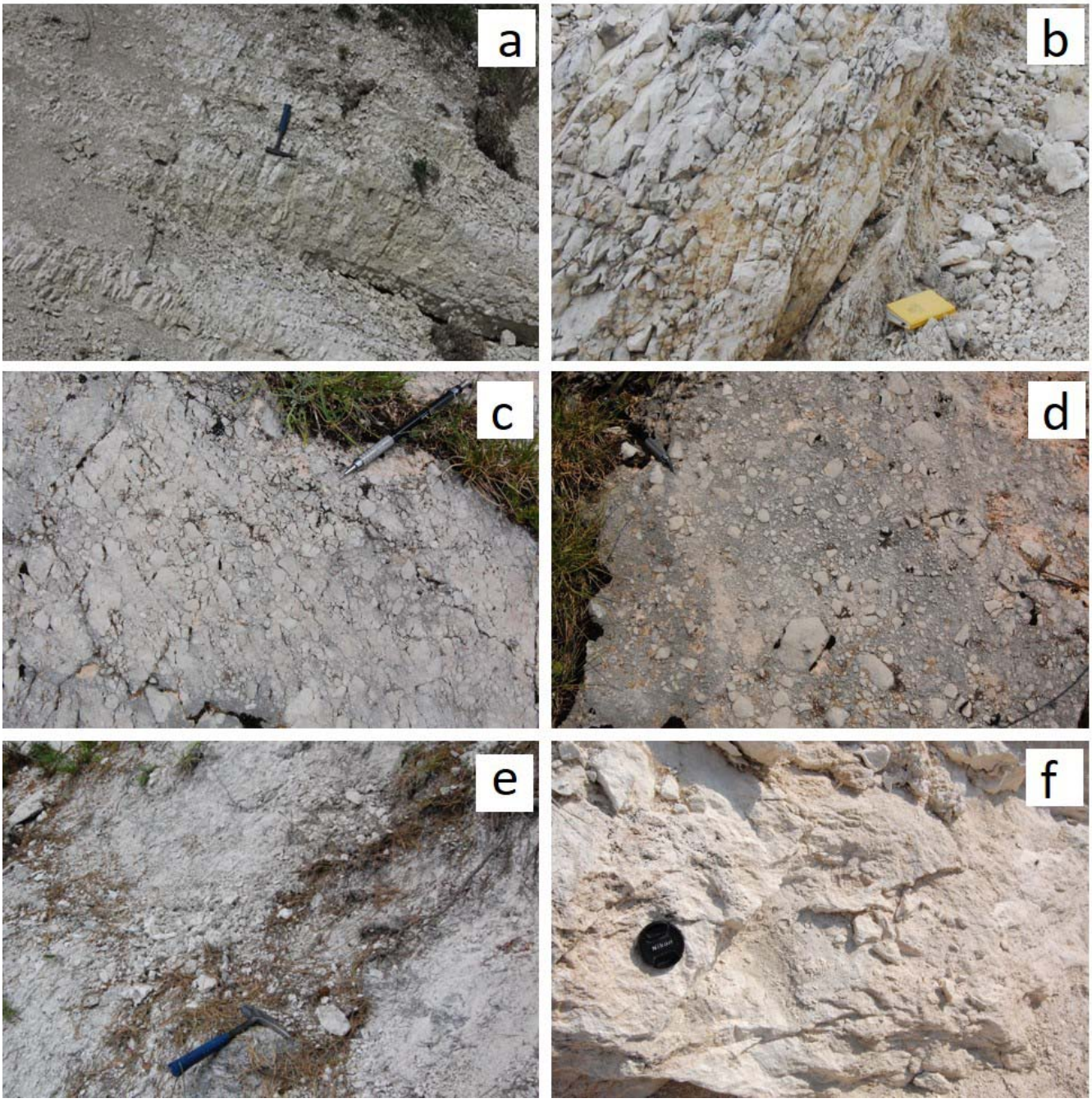


Figure 3: Field examples of architectural elements: Fractured damage zones of the Campo Imperatore Fault System at Mt. Brancastello (a) and Assergi Fault Zone (b). c) Clast-supported and d) matrix-supported breccias in the Assergi Fault Zone; e) Loose cataclasite from AFZ at Valle Fredda; f) Cohesive cataclasite and slip surfaces from the Campo Imperatore Fault System at Vado di Corno.

breccia if more than 30% of clasts exceed that threshold. Further, breccias are subdivided into crackle, mosaic or chaotic based on how well breccia clasts fit together (Woodcock and Mort, 2008).

Figure 4a-c presents a three photomicrographs of crackle breccias with both limestone and dolostone clast mineralogy. These breccia samples are characterized by pervasive fractures in multiple orientations. The clasts often show little-to-no sign of rotation (Fig. 4a-c). A large volume of these fractures is open, but portions are filled with cataclasite, or post-deformation calcite cement. Crackle breccias transition to other breccia types both at the scale of the outcrop as well as at sample scale. Typically, they transition to mosaic breccias approaching a

slip surface. In Figure 4d-f we show three photomicrographs of mosaic breccia images, which include both calcite and dolomite mineralogy. Mosaic breccias may resemble crackle breccias because they are crosscut by multiple fracture sets, which isolate rock fragments. However, different from crackle breccias, clasts in mosaic breccias often show evidence of rotation and have more rounded shapes (Fig. 4e-f). Despite being subject to rotation, mutual spatial relations between clasts are preserved allowing recognition of clasts that were adjacent before deformation. In mosaic breccias, the distance between clasts is larger than in crackle breccias, and also the amount of finer cataclastic material infilling fracture meshes is greater. We documented both cemented and not cemented mosaic breccias, calcite cement often postdates deformation. Commonly, larger fractures appear to be cemented but intergranular porosity is often preserved in pockets of fine-grained material (Fig. 4e).

In chaotic breccias, rock fragments are seldom bounded by open fractures. Instead, larger clasts "float" in a "matrix" of fine-grained fragments (Fig. 4g-i). Clasts have a rounded shape and mutual spatial relations are not preserved. The fine-grained material originates by comminution because of the greater magnitude of shearing (cf. Billi 2005). Chaotic breccias may sometimes show an incipient foliation. As with mosaic breccias, in this sample set larger fractures are often cemented by a post-deformation calcite cement, whereas the intragranular porosity between the finer-grained material is preserved. In dolomite breccias, the clasts show internal fragmentation (Fig. 4), which follows the crystalline fabric of the pristine dolomite. Crystal boundaries planes of weakness, indeed Figure 5(g-h) shows how these boundaries often represent point of nucleation/propagation of fractures.

Figure 5 shows a compilation of cataclasites from various locations along the studied fault zones. Cataclasites often represent the lateral transition from chaotic breccias towards the main slip surfaces. In addition to large (up to 10s of meters) cataclasite geobodies, which are present in both fault zones (Ortner et al., 2014; Demurtas et al., 2016). These fault rocks also occur in narrow (<10cm) slivers cutting across breccia bodies along secondary slip surfaces (Fig. 5a and c). Grain size can drastically vary in cataclasites with clasts ranging from one millimeter down to 10s of microns, or even less than the resolution of the optical microscope (Fig. 5h -i). Grain shape is mainly rounded, but sometimes elongated clasts with the long axis aligned parallel to the slip direction can be found (Fig. 5a, d). In dolomite cataclasites, larger grains are highly fragmented, and often these fragments are single dolomite crystals (Fig. 5d-e), which can be easily separated from the grain because of rotation and translation. Foliation is often present in the cataclasites (Figure 5e and h), and multiple slivers of finer grained material can be observed also at the scale of the thin section (Figure 5h and i). These slivers are deformation bands forming by strain localization in the granular cataclastic material, analogous to those commonly forming in sandstones (cf. Aydin et al., 2006). Within these bands both grainsize and pore size (down to few microns) are reduced even further with respect to the surrounding cataclasite (cf. Aydin et al., 2006). Despite most of the cataclasites have preserved some intergranular porosity, we documented examples of fully cemented cataclasite (Fig. 5d-f).

4.3. Porosity

Porosity measurements are displayed in Figure 6 on a box and whiskers plot. The porosities are grouped based on the fault architectural element (i.e., host rock in grey; breccia in green; cataclasite in brown; and damage zone in red). We measured a total of 92 samples, among which only two are damage zone samples, whereas the rest is from the host rock (n=40) and from the fault core cataclasites (n=28) and breccias (n=21). The reason why damage zone is poorly represented is because the plugs used for our measurements had a diameter of 2.5-cm and thus would not be able to include a representative fracture array, which is usually providing

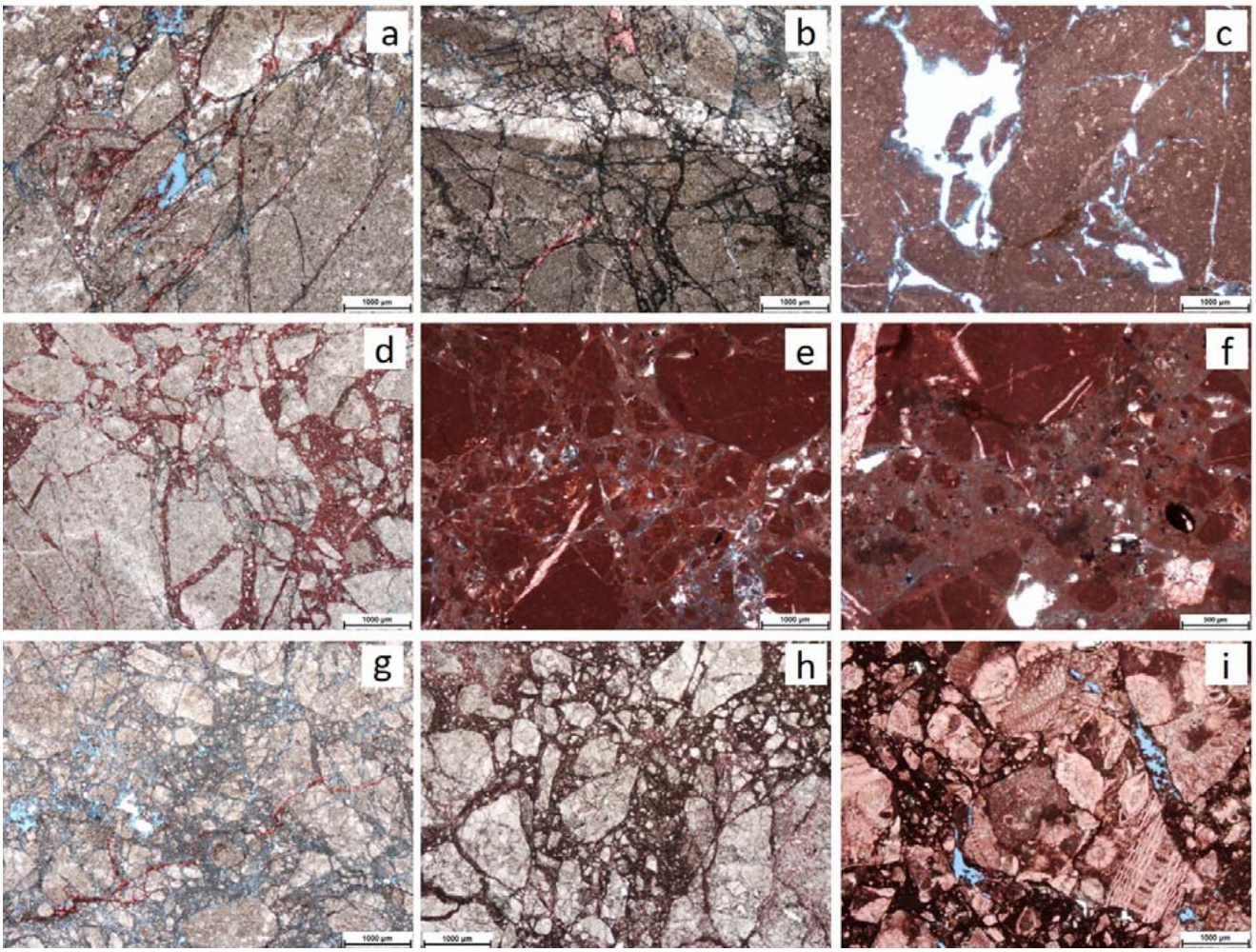


Figure 4: Collage of photomicrographs various types of breccias (blue indicates porosity, red indicates calcite). In a, b, c examples of crackle breccias; in d, e, f examples of mosaic breccias; in g, h, i examples of chaotic breccias.

the larger contribution to porosity and fracture permeability in tight rocks (Storti et al., 2003; Agosta et al., 2007).

The porosity of the host rock is quite low and ranges between 0.1 and 9.7 % (mean value 2.8%; mode 2.8%), however 38 out of 40 values are ≤6%. Among the 40 host rock samples 23 are limestones and 17 dolostones. The limestones have porosities comprised between 0.1% and 9.7% (Figure 6b), and a mean value of 2.5% (mode 0.1 %) whereas the dolostones have porosities ranging between 2% and 6.1%, with a mean value of 3.2% (mode 2.8%; Figure 6a).

The damage zone samples have a relatively high porosity: the limestone sample has a porosity of 19.1% (Fig. 6b) whereas the dolostone sample has a porosity of 11.2 % (Fig. 6a).

The breccias have porosities ranging between 2.2 and 13.1 % with a mean value of 7% (mode 8.1%). Among these samples, nine are dolostones (Figure 6a) and 12 are limestones (Figure 6b). The limestone breccias have porosities between 5.5% and 13.1% with a mean value of 8% (mode 4.6%), whereas the dolostone breccias have porosities ranging between 3.6% and 10.8%, with a mean value of 5% (2.2%). Breccias have higher porosities than host rocks.

The porosity of cataclasites ranges from 3.1 to 15.4 % with a mean value of 8.8% (mode 10.2%). Among these samples, 18 are dolostones (Figure 6a) and 10 are limestones (Figure 6b). The limestone cataclasites have porosities between 3.1% and 12% with a mean value of 6.3% (mode 3.6%), whereas the dolostone cataclasites have porosities ranging between 3.2% and 15.4%, with a mean value of 10.2% (mode 10.2%). Dolostones have a wider range of porosity variation than the limestones and their mean porosity is higher than the limestone cataclasites by a factor of almost two (Figure 6). Cataclasite porosity is greater than host rock porosity.

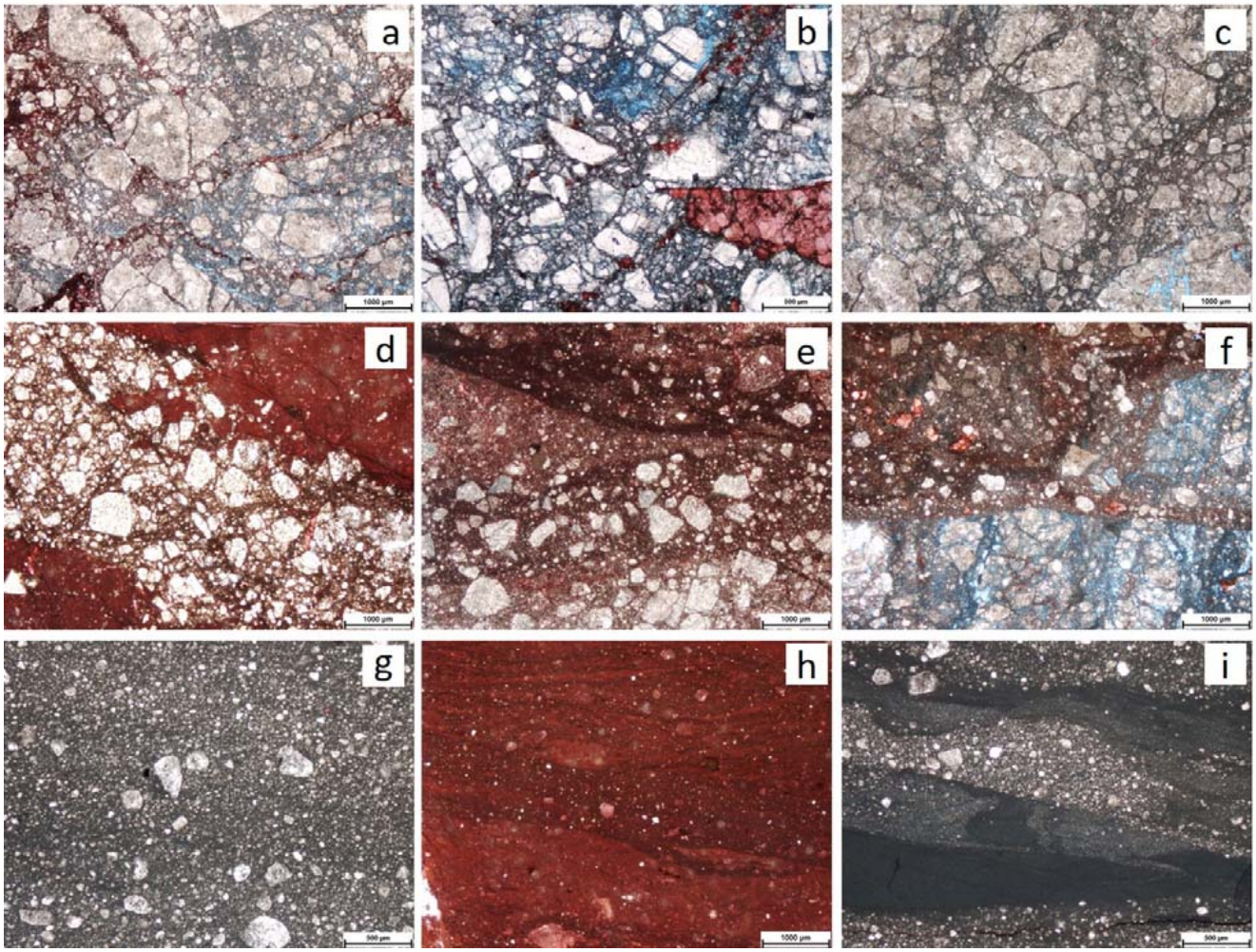


Figure 5: Collage of photomicrographs various types of cataclasites (blue indicates porosity, red indicates calcite). In a, b, c examples of proto-cataclasites; in d, e, f examples of cataclasites; in g, h, i examples of ultra-cataclasites.

4.4. Permeability

We measured 60 samples in total including 25 host rock samples (15 dolostones, 10 limestones), 15 breccia samples (6 dolostones, 9 limestones), 20 cataclasite samples (12 dolostones, 8 limestones), and one damage zone sample (Fig. 7). In addition to these categories, the measurements were divided by fault zone: blue diamonds for the Campo Imperatore Fault System (VCFZ, Mt. Brancastello, Mt. Camicia), and yellow diamonds for the Assergi Fault Zone. The permeability of the host rock ranges between 0.001 (minimum resolution of the apparatus) and 598 mD, with an average value of 24.1 mD. Among the host rock samples, limestone permeability ranges between 0.002 and 598mD (mean 59.8 mD) and dolostone permeability

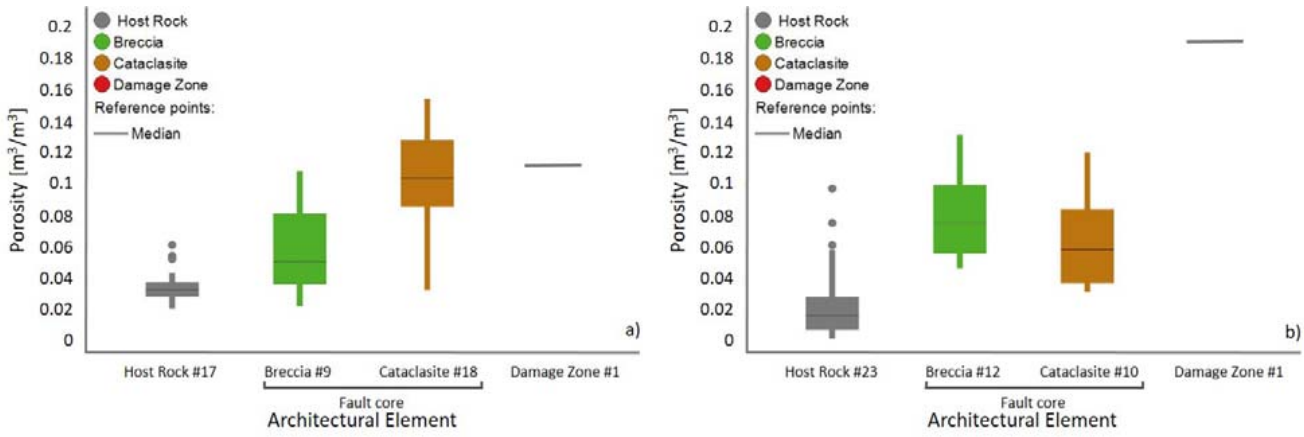


Figure 6: Box and whiskers plots of porosity of architectural elements: i.e., host rock (grey), breccias (green), cataclasites (brown), damage zones (red). In a) dolostone and in b) limestone data.

ranges 0.001 and 2.73 mD (mean 0.30 mD). The only measurement of damage zone permeability is for a limestone and has a value of 0.32 mD.

Breccias have a permeability ranging between 0.003 to 558 mD, with an average value of 59.2 mD. Among the breccia samples, the limestones have a permeability ranging between 0.003 and 558 mD (mean 96.7 mD), whereas the dolostone permeability varies between 0.17 and 14.7 mD (mean 2.9 mD).

Cataclasite permeability ranges between 0.002 and 1.5 mD, with an average of 0.3mD. Among the cataclasite sample, limestones have a permeability varying from 0.002 and 1.47 mD (mean 0.18 mD), whereas for the dolostone samples the range goes from 0.008 to 1.5 mD (mean 0.34 mD).

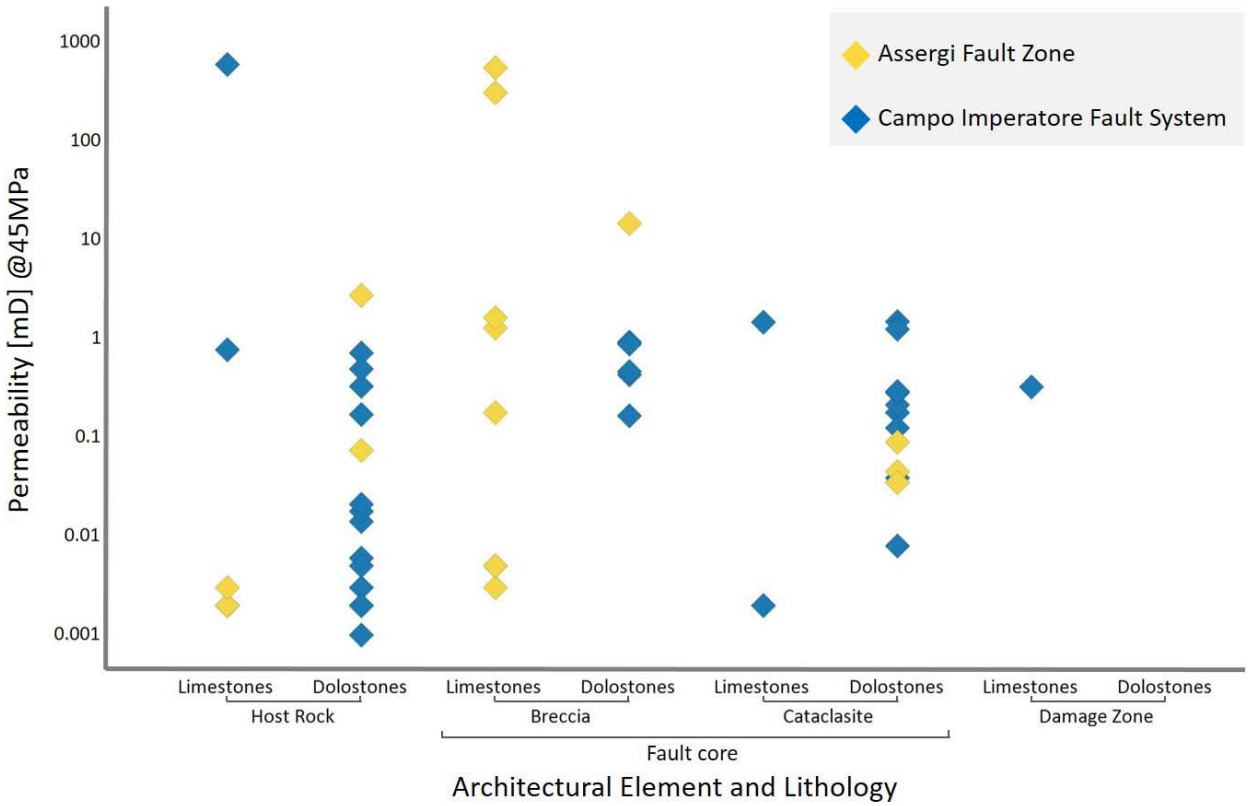


Figure 7: Permeability data grouped by architectural elements, and split based on sample mineralogy (limestones left column, and dolostones right column). Yellow diamond for data from the AFZ, blue diamond for data from the Campo Imperatore Fault System.

5. DISCUSSION

5.1. Fault Core Rocks and Fault Displacement

This study presents data from two regional scale fault zones (Campo Imperatore Fault System and Assergi Fault Zone) located in central Italy. These faults have been studied by previous authors who characterized fault architectures, seismic activity and their effect on the local hydrogeological system (e.g., Bella et al., 1998; Demurtas et al., 2016). In the recent past, many authors (e.g., Agosta et al., 2007; Storti et al., 2007; Matonti et al. 2012; Tondi et al. 2016; Balsamo et al., 2016; Michie et al., 2018) have mapped, sampled and measured various petrophysical properties of fault rocks in carbonates. In this study we systematically measured porosity, permeability and combined them with microstructural analysis of thin sections. The progressive stages of deformation, responsible for strain accumulation and transition from host rock to damage zone and eventually to the full spectrum of fault rocks (*sensu* Sibson, 1977; Woodcock and Mort, 2008) have been thoroughly documented in literature (Billi et al. 2003; Storti et al., 2003; Agosta and Krishner 2003; Agosta and Aydin, 2006; Michie & Haines, 2016; Demurtas et al. 2016; Ferraro et al., 2018). This process begins with fracturing of the host rock, which evolves to brecciation till a point beyond which cataclastic flow is favored. Eventually, progressive comminution is responsible for the production of cataclasite. This process is linked to the increased magnitude of rotation and translation of the clasts, which results into grain crushing, comminution and smoothing (Billi et al., 2003, Storti et al., 2007). As shown in figures 4 and 5, the microstructures of same type of fault rocks derived from host rock with different mineralogy (limestone vs. dolostones) do not differ significantly. This suggests that mechanical processes responsible for the development of the fault rocks are the same in these two lithologies. Overall, this dataset includes a larger number of limestone breccias (n=12) than dolostone breccias (n=9), and smaller number limestone cataclasites (n=10) than dolostone cataclasites (n=18), which might suggest that the transition from breccia to cataclasite is faster in dolostones than in limestones. The hypothesis of a faster transition in dolomite respect to calcite mineralogy would be in line with our microstructural observations. In particular, we postulate that it might be related to the crystalline texture of dolostones, which provides an intricate network of pre-existing discontinuities. For example, figures 4 and 5 show how even namely intact clasts are internally fragmented along crystal boundaries. We suggest that these weaker planes may promote fracture nucleation (Figs. 4 and 5), rock fragmentation, and grain size reduction down-to-the scale of single dolomite crystals. Dolomite crystals can be separated from the clast more easily than lithic fragments in a limestone, this makes them more prone to rotation and translation and thus may promote the cataclastic flow.

5.2. Petrophysical Properties

The porosity and permeability, measured for various fault rock and the surrounding host rocks, shows a wide range of variation. The porosity ranges between 1 and 20%, with the lowest porosities being measured in the limestone host rocks and the highest porosity being measured in the damage zone. Permeability spans across six orders of magnitude with the lowest permeabilities recorded in the dolostone host rocks and the highest in limestone breccias and host rocks (porosity <10%). Our microstructural observation and the presence of samples with relatively low porosity and high permeability are consistent with the fact that permeability of host rocks and breccias is likely controlled by the fractures. Consequently, measurements performed on 1-inch plugs will tend to underestimate permeability because do not fully incorporate the contribution of meso-scale fractures. Fracture contribution to permeability could be very relevant both in the host rocks and the damage zones of faults in tight carbonates, and it is commonly quantified using discrete fracture network models (e.g.,

Korneva et al., 2015).

The scatter plot in Figure 8 shows porosity vs. permeability data obtained in this study. Fault architectural elements are represented with different colors (host rock in grey; breccia in green; cataclasite in brown; and damage zone in red), and sample mineralogy is displayed with marker shapes (limestones=boxes, and dolostones=circles). Two main data clusters can be identified within the point cloud: i) including host rock and breccia samples; and ii) with cataclasite samples. The first cluster has a correlation coefficient of 0.41, whereas the second has a correlation coefficient of 0.57. These clusters have different porosity-permeability relationships; indeed, same increase of porosity in the cluster "Host rocks and breccias" corresponds to a much higher increase of the permeability than in cluster "Cataclasites". The microstructural and petrographic analyses allowed us to interpret the two responses. In breccias and host rock most of the pore volume is provided by a well-connected network of fractures; thus, higher porosity results in higher permeability. Conversely, cataclasites have much smaller grain size (sand-to-clay size) with respect to breccias (gravel-to-sand size) and their porosity is mainly intergranular, thus even with porosities larger than 10%, the samples have low permeability due to low pore connectivity and supposedly higher capillary entry pressure.

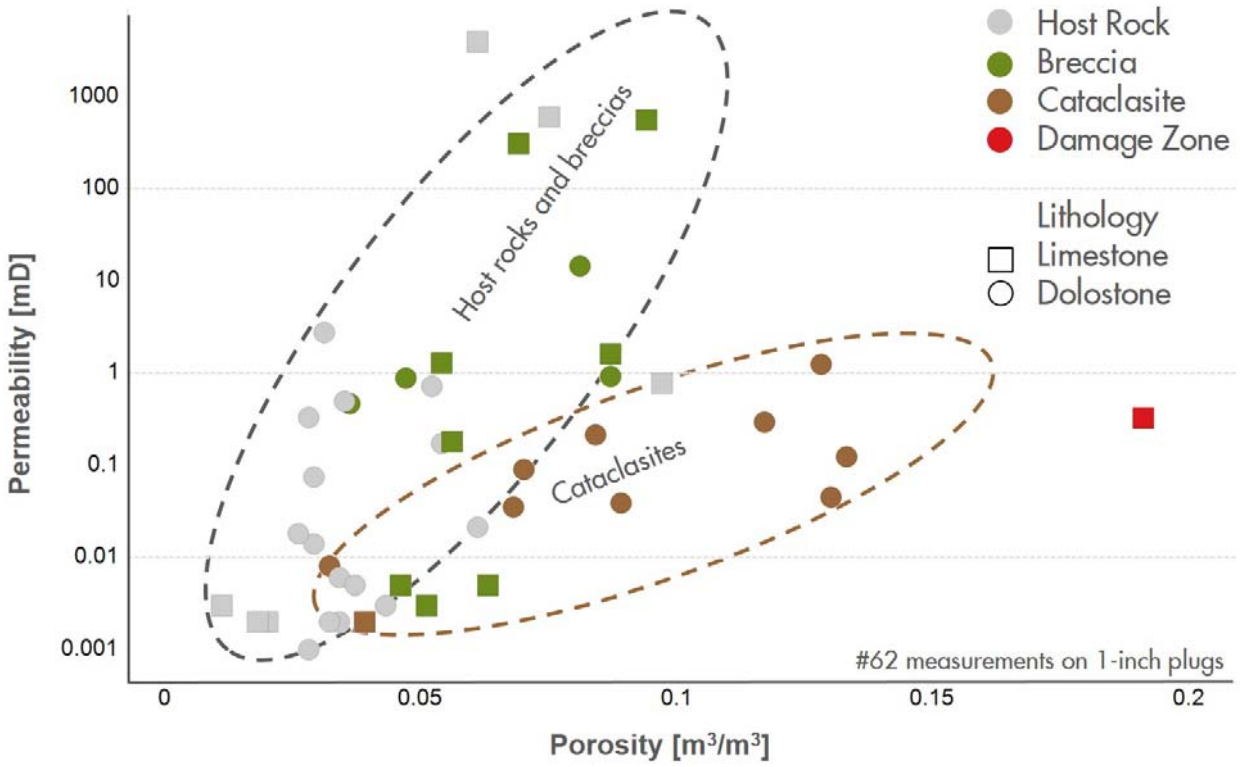


Figure 8: Scatter plot of porosity vs. permeability of host rocks (grey), breccias (green), cataclasites (brown), and damage zones (red). Symbol shapes indicate the mineralogy of the samples boxes for limestones and circles for dolostones. Dashed ellipses encompass the two data clouds, grey ellipse for host rocks and breccias, brown ellipse for cataclasites.

Consistently with previous studies (Billi et al., 2003; Storti et al., 2003; Agosta et al., 2007; Storti & Balsamo, 2010; Matonti et al., 2012; Haines et al., 2016; Michie & Haines, 2016; Ferraro et al., 2018), field, laboratory (i.e., microstructural and petrophysical), and statistical data presented in this manuscript highlighted the complex architecture of faults in carbonates and the marked heterogeneity of permeability distribution along and across strike. Figure 9 shows the conceptual model of a normal fault, which integrates and summarizes all the fault rock data presented in this study, and includes four cross-sections intersecting different architectural elements likely developed during progressive fault slip

(Billi et al., 2003): i) damage zone (A-A'); ii) damage zone and crackle breccia (B-B'); iii) damage zone, crackle and chaotic breccias (C-C'); iv) damage zone, crackle and chaotic breccias, and cataclasite (D-D'). On each section, we superimposed the ranges of permeability measured (on 1-inch plugs), for both limestones (blue empty box) and dolostones (red full boxes). This conceptual model resembles field-based schematic cross-sections presented in previous studies and showing the distribution of fault rock types along and across a fault zone (Matonti et al., 2012; Woodcock et al., 2014; Demurtas et al., 2016; Ferraro et al., 2018). Because our model displays also the fault rock permeabilities, it can be used as a guide for estimating ranges of permeability along and across a fault zone in tight carbonates.

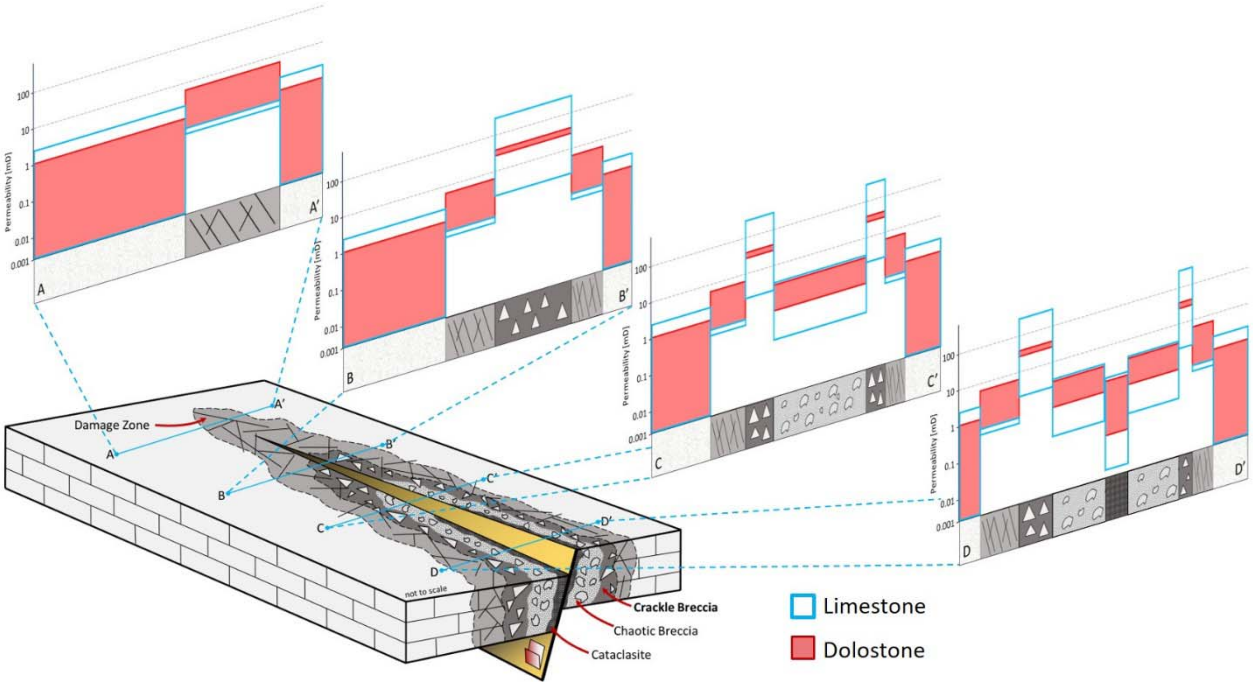


Figure 9: Fault zone (normal kinematics) conceptual model, showing fault-dependent geobodies. Four cross-sections display the ranges of permeability measured within each architectural element. Blue empty boxes represent the permeability of limestone samples, full red boxes the permeability of dolostone samples.

5.3. Implications for Fault Seal

Solum and Huisman (2017) paved the way for establishing rules to predict when faults can act as seals in carbonates. These authors compiled a list of literature data presenting evidence of dynamic and potentially static fault seal in carbonate reservoirs and aquifers. Their paper reports values of fault core permeability ranging from 0.0001 mD and 100 mD (Fig. 10a), which are comparable to the fault core permeability we documented in this study (Figs. 8 and 10a). Also in carbonate, if the permeability of a fault is sufficiently low, then faults may act as a production timescale baffle/barrier (cf. Solum and Huisman, 2017). This could cause compartmentalization or create infill drilling targets if the time required for re-equilibration of production-induced pressure depletion is sufficiently long. These authors presented a simple model of two reservoir blocks separated by a fault, where one block has been depleted during production. Using a certain number of assumptions (i.e., 2.5 × 2.5 km fault blocks; reservoir thickness of 50 m; fault throw 25 m; water saturation 0.1; porosity 0.25, compressibility of 1.45 × 10^{-9} Pa^{-1}; viscosity of 0.002 Pa S, and a fault core thickness of 7 m) the model by Solum and Huisman (2017) allows predicting the time needed to re-equilibrate the pressure difference across the two fault blocks. Using the permeability range measured in this study we get re-equilibration times ranging between 0.1 and 300 years (red shading), where the longer time correspond to cataclasite fault cores (Fig. 10b). These results suggest that fault with continuous cataclasites in the fault cores can act as dynamic seals.

The lines of evidence to prove large-scale sealing potential of the Assergi Fault are provided by Celico et al. (2005). These authors characterized how this fault impacts the groundwater system in the Gran Sasso

Massif, and quantified the aquifer water discharge in the highway tunnel crossing the Gran Sasso Massif. Indeed, before building the tunnel, the groundwater level in the footwall of the Assergi Fault was ≈70 meters higher than in its hangingwall (ANAS-COGEFAR, 1980; Fig. 11d). Because of the hydraulic head difference across the fault, when the structure was penetrated a huge volume of water and cataclasite slurry spilled over into the tunnel causing three fatalities (ANAS-COGEFAR, 1980; Fig. 11a-c). The hydraulic head difference was a consequence of the permeability contrast between the karst aquifer, which according to Bella et al. (1998) has a bulk permeability of up-to 100 mD and the fault cataclasite where we measured permeabilities comprised between 0.01 and 0.1 mD. Note that despite having sampled loose cataclasite along the Assergi Fault, it was not possible to perform permeability measurements on these fault rocks. The Assergi Fault is a clear example of a dynamically sealing fault on carbonate/carbonate juxtaposition, and its displacement of ≈1000 m at the tunnel location (Adamoli et al., 2012), is consistent with the presence of a laterally continuous cataclasite layer able to sustain a water column of several 10s of meters. To test the lateral continuity of the cataclasites, we sampled the fault core of the Assergi Fault, at several locations also close to its NW termination (UTM 33T, 366530E, 4702646N). At this location, where according to the geological map (Adamoli et al., 2012) the Assergi Fault has a minimum offset of ≈500 m, we documented cataclasites and chaotic breccias; however, it is expected that as the fault displacement will decrease toward the fault tip (not cropping out) also the likelihood of having a continuous cataclasite layer will decrease.

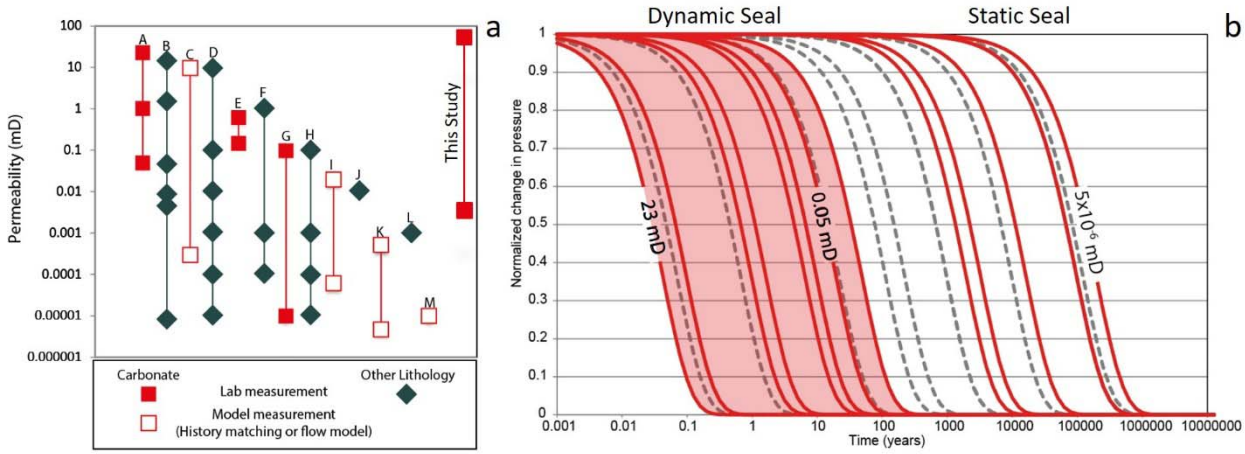


Figure 10: a) Compilation of permeabilities for fracture-based fault zones with reduced permeability fault cores (Solum and Huisman, 2017). Carbonates are represented by black squares and other fractured lithologies (dominated by crystalline rocks) are represented by grey diamonds. Samples from other fractured lithologies are included with the carbonate samples to enable fault core permeability in conduit–barrier fault systems to be compared with in carbonates to conduit–barrier fault systems in other lithologies. Solid symbols represent laboratory measurements and open symbols represent calculations derived from models (aquifer flow models or back-calculated from reported fault transmissibility multipliers). The measurements are arranged on the horizontal axis in order of datasets, with the greatest permeability to the least. Data are from a: Ran et al. (2014; plug measurements of fault core); b: Tsutsumi et al. (2004; gouge, breccia and fractured breccia); c: Meddaugh et al. (2007; back-calculated from reported FTMs); d: Uehara & Shimamoto (2004; cemented cataclasite, sandy and clay gouges); e: Micarelli et al. (2006a; cataclasite in continuous and discontinuous core); f: Wibberley & Shimamoto (2003; cataclasite, ultracataclasite and foliated gouge); g: Bauer et al. (2016; matrix-supported cataclasites); h: Sutherland et al. (2012; cataclasite and gouge); i: Agosta et al. (2007; cemented and uncemented fault core); j: Kitamura et al. (2014; fault rock); k: Hussain (1993; back-calculated from reported FTMs); l: Lockner et al. (2009; fault core); m: Meddaugh et al. (2007; back-calculated from reported FTMs); n: Micarelli et al. (2006b; fault core). b) Normalized change in pressure across a fault plotted against time, assuming a depleted and a pristine reservoir block are separated by a low permeability fault as described in the text. Each curve is calculated using one of the permeability values given in “a”. Solid red lines are for faults in carbonates and dashed grey lines are for faults in other fractured lithologies, red shading represents the range or permeabilities from this study.

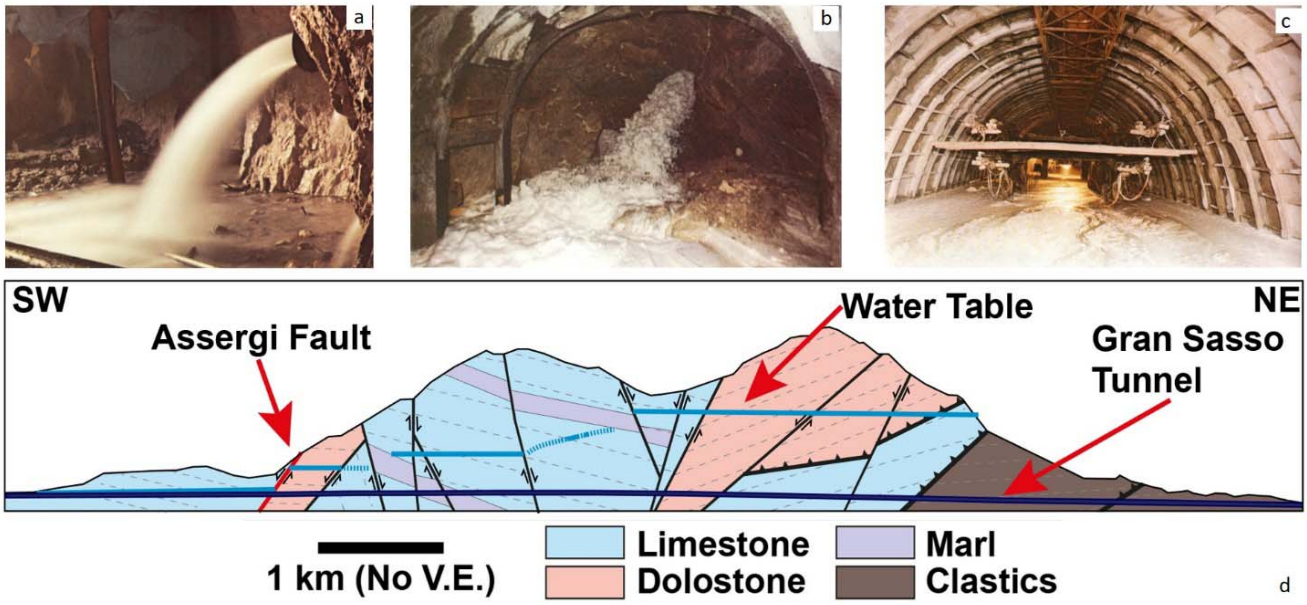


Figure 11: The Gran Sasso Tunnel: a to c images of water and cataclasite slurry flooding the tunnel during the excavation operations (ANAS-COGEFAR, 1980); d) Geological cross-section of the GSM, showing a drop of the water table across the Assergi Fault Zone, modified after Celico et al. (2005).

6. CONCLUSIONS

The outcomes of this paper can be summarized as follows:

- We consistently documented increasing comminution and decreasing pore size from the outer toward the inner portions of fault cores (Figures 3 and 8). Three types of breccias (crackle, mosaic and chaotic) and various types of cataclasites were identified (Figures 4 and 5).
- We postulated that the crystalline texture of dolostones promotes a faster transition from breccia to cataclasite compared to limestones. If all other factors are held constant, greater displacement is required to form a cataclasite in a limestone than in a dolostone.
- We measured porosity and permeability ranges (not including meso-scale fractures) of each architectural element (Figures 6 and 7). Crackle breccias reach the highest permeability (up to 100s of mD), whereas the ultra-cataclasites have the lowest permeability (down to 0.01 mD), which is roughly equivalent to unfractured host rock (Figures 8 and 9). These data highlight how breccias can enhance the host rock permeability up to several orders of magnitude, while cataclasites can represent a permeability barrier since their permeabilites approach that of unfractured host rock.
- The pore networks of different types of fault rocks vary significantly: fault breccias have larger pores heterogeneous in size, whereas and cataclasites have smaller pores with homogeneous (Figs. 4-5). This suggests that carbonate cataclasites can cause dynamic sealing potential, which can impact exploration of hydrocarbon reservoirs in settings for which the studied faults might be good analogues (Fig. 10).
- Fault zone architecture and properties vary in 3D as functions of lithology and displacement (Caine et al., 1996; Billi, 2003; Demurtas et al., 2016). Along-strike variations of displacement result in a varying permeability and occurrence of fault rock types along the fault (Figs. 9 and 11).

Acknowledgements

The authors would like to thank Shell Global Solutions International B.V. for funding the research and allowing the publication of these data. We are grateful to Dr. S. Saleh, who encouraged us to publish the results of this research. We have benefitted of fruitful discussions with Dr. Steven Naruk, Dr. Pascal Richard and Dr. Bastiaan Huisman.

7. Refereces

Adamoli, L., Calamita, F., Pelorosso, M. (2003). Itinerario No 2-Gran Sasso d'Italia: dai Prati di Tivo ai Prati di Tivo attraverso il ghiacciaio del Calderone, il Corno Grande, Campo Pericoli e la Val Maone. In: Guide Geologiche Regionali, Abruzzo: 102e112, BE-MA ed., Lodi (MI)

Adamoli, L., Calamita, F., Pizzi, A. (2012). Note Illustrative del Foglio 349 "G. Sasso" della Carta Geologica d'Italia alla scala 1: 50.000. ISPRA, Roma.

Agosta, F., & Aydin, A. (2006). Architecture and deformation mechanism of a basin-bounding normal fault in Mesozoic platform carbonates, central Italy. *Journal of Structural Geology*, *28*(8), 1445-1467.

Agosta, F., Alessandroni, M., Tondi, E., & Aydin, A. (2009). Oblique normal faulting along the northern edge of the Majella anticline, central Italy: Inferences on hydrocarbon migration and accumulation. Journal of Structural Geology, 31(7), 674-690.

Agosta, F., Kirschner, D. (2003). Fluid conduits in carbonate-hosted seismogenic normal faults of central Italy. J. Geophys. Res. 108 (B4), 2221. http://dx.doi.org/10.1029/2002JB002013.

Agosta, F., Prasad, M., & Aydin, A. (2007). Physical properties of carbonate fault rocks, fucino basin (Central Italy): implications for fault seal in platform carbonates. *Geofluids*, *7*(1), 19-32.

Agosta, F., Wilson, C., & Aydin, A. (2015). The role of mechanical stratigraphy on normal fault growth across a Cretaceous carbonate multi-layer, central Texas (USA). Italian Journal of Geosciences, 134(3), 423-441.

ANAS-COGEFAR (1980) - Gran Sasso, il traforo autostradale. Ed. Grafiche Sefra, Milano.

Antonellini, M., Tondi, E., Agosta, F., Aydin, A., & Cello, G. (2008). Failure modes in deep-water carbonates and their impact for fault development: Majella Mountain, Central Apennines, Italy. *Marine and Petroleum Geology*, *25*(10), 1074-1096.

Arzilli, F., Cilona, A., Mancini, L., & Tondi, E. (2016). Using synchrotron X-ray microtomography to characterize the pore network of reservoir rocks: A case study on carbonates. *Advances in water resources*, *95*, 254-263.

Aydin, A. (2000). Fractures, faults, and hydrocarbon entrapment, migration and flow. *Marine and petroleum geology*, *17*(7), 797-814.

Aydin, A., Borja, R. I., & Eichhubl, P. (2006). Geological and mathematical framework for failure modes in granular rock. *Journal of Structural Geology*, *28*(1), 83-98.

Balsamo, F., Clemenzi, L., Storti, F., Mozafari, M., Solum, J., Swennen, R., Taberner, C., Tueckmantel, C., (2016). Anatomy and paleofluid evolution of laterally-restricted extensional fault zones in the Jabal Qusaybah anticline, Salakh Arc, Oman. Geological Society of America Bulletin, v. 128, p. 957–972, doi: 10.1130/B31317.1

Bauer, H., Schröckenfuchs, T.C. & Decker, K. (2016). Hydrogeological properties of fault zones in a karstified carbonate aquifer (Northern Calcareous Alps, Austria). Hydrogeology Journal, no volume, 1–24.

Bella, F., Biagi, P. F., Caputo, M., Cozzi, E., Della Monica, G., Ermini, A., Plastino, & Sgrigna, V. (1998). Aquifer-induced seismicity in the Central Apennines (Italy). In *Seismicity Caused by Mines, Fluid Injections, Reservoirs, and Oil Extraction* (pp. 179-194). Birkhäuser, Basel.

Bense, V. F., Gleeson, T., Loveless, S. E., Bour, O., & Scibek, J. (2013). Fault zone hydrogeology. *Earth-Science Reviews*, *127*, 171-192.

Billi, A. (2005). Grain size distribution and thickness of breccia and gouge zones from thin (< 1 m) strike-slip fault cores in limestone. *Journal of Structural Geology*, *27*(10), 1823-1837.

Billi, A., Salvini, F., & Storti, F. (2003). The damage zone-fault core transition in carbonate rocks: implications for fault growth, structure and permeability. *Journal of Structural geology*, *25*(11), 1779-1794.

Caine, J. S., Evans, J. P., & Forster, C. B. (1996). Fault zone architecture and permeability structure. Geology, 24(11), 1025-1028.

Cardello, G., Doglioni, C. (2014). From mesozoic rifting to Apennine orogeny: the Gran Sasso Range (Italy). Gondwana Res.

Celico, P., Fabbrocino, S., Petitta, M., & Tallini, M. (2005). Hydrogeological impact of the Gran Sasso motor-way tunnels (Central Italy). Giornale di Geologia Applicata, 1, 157-165.

Cilona, A., Faulkner, D. R., Tondi, E., Agosta, F., Mancini, L., Rustichelli, A., Baud, P., & Vinciguerra, S. (2014). The effects of rock heterogeneity on compaction localization in porous carbonates. *Journal of Structural Geology*, *67*, 75-93.

D'Agostino, N., Chamot-Rooke, N., Funiciello, R., Jolivet, L., Speranza, F. (1998). The role of pre-existing thrust faults and topography on the styles of extension in the Gran Sasso range (central Italy). Tectonophysics 292, 229-254.

Delle Piane, C., Clennell, M. B., Keller, J. V., Giwelli, A., & Luzin, V. (2017). Carbonate hosted fault rocks: A review of structural and microstructural characteristic with implications for seismicity in the upper crust. Journal of Structural Geology.

Demurtas, M., Fondriest, M., Balsamo, F., Clemenzi, L., Storti, F., Bistacchi, A., & Di Toro, G. (2016). Structure of a normal seismogenic fault zone in carbonates: the Vado di Corno Fault, Campo Imperatore, Central Apennines (Italy). Journal of Structural Geology, 90, 185-206.

Dickson, J. A. D. (1965) A modified staining technique for carbonates in thin section. Nature 205.4971: 587-587.

Faulkner, D. R., Jackson, C. A. L., Lunn, R. J., Schlische, R. W., Shipton, Z. K., Wibberley, C. A. J., & Withjack, M. O. (2010). A review of recent developments concerning the structure, mechanics and fluid flow properties of fault zones. Journal of Structural Geology, 32(11), 1557-1575.

Ferraro, F., Griego, D.S., Agosta, F. & Prosser, G. (2018). Space-time evolution of cataclasis in carbonate fault zones. Journal of Structural Geology, 110, 45-64

Flügel, E. (2013). Microfacies of carbonate rocks: analysis, interpretation and application. Springer Science & Business Media.

Fondriest, M., Smith, S. A., Candela, T., Nielsen, S. B., Mair, K., & Di Toro, G. (2013). Mirror-like faults and power dissipation during earthquakes. Geology, 41(11), 1175-1178.

Freeman, S. R., Harris, S. D., & Knipe, R. J. (2010). Cross-fault sealing, baffling and fluid flow in 3D geological models: tools for analysis, visualization and interpretation. Geological Society, London, Special Publications, 347(1), 257-282.

Ghisetti, F., Vezzani, L. (1991). Thrust belt development in the Central Apennines (Italy): northward polarity of thrusting and out-of-sequence deformations in the Gran Sasso Chain. Tectonics 10, 904e919.

Giraudi, C., Frezzotti, M. (1995). Palaeoseismicity in the gran Sasso Massif (Abruzzo, central Italy). Quat. Int. 25, 81-93.

Giraudi, C., Frezzotti, M. (1997). Late Pleistocene glacial events in the Central Apennines. Italy. Quat. Res. 48 (3), 280e290.

Haines, T. J., Michie, E. A., Neilson, J. E., & Healy, D. (2016). Permeability evolution across carbonate hosted normal fault zones. Marine and Petroleum Geology, 72, 62-82.

Hussain, A. (1993). Dukhan Field (Onshore Qatar) Uwainat Reservoir Optimum Development Scheme. Paper SPE-25530-MS, http://doi.org/10.2118/25530-MS

Kitamura, M., Mukoyoshi, H. & Hirose, T. (2014). The relationship between displacement and thickness of faults in the Shimanto accretionary complex. Journal of the Geological Society of Japan, 120, 11–21.

Klimchouk, A., Auler, A. S., Bezerra, F. H., Cazarin, C. L., Balsamo, F., & Dublyansky, Y. (2016). Hypogenic origin, geologic controls and functional organization of a giant cave system in Precambrian carbonates, Brazil. Geomorphology, 253, 385-405.

Klinkenberg, L.J. (1941) The permeability of porous media to liquids and gases, Drilling and Production Practice, American Petroleum Inst., pp. 200–213.

Korneva, I., Cilona, A., Tondi, E., Agosta, F., Giorgioni, M. (2015). Characterisation of the permeability anisotropy of Cretaceous platform carbonates by using 3D fracture modeling: the case study of Agri Valley fault zones (southern Italy). Italian Journal of Geosciences; 134 (3): 396–408.

Lockner, D.A., Tanaka, H., Ito, H., Ikeda, R., Omura, K. & Naka, H. (2009). Geometry of the Nojima Fault at Nojima-Hirabayahi, Japan - I. A simple damage structure inferred from borehole core permeability. Pure and Applied Geophysics, 166, 1649–1667.

Loucks, R.G., (2002). Controls on Reservoir Quality in Platform-Interior Limestones Around the Gulf of Mexico: Example from the Lower Cretaceous Pearsall Formation in South Texas Depositional Setting and Systems of the Pearsall Formation. Gulf Coast Assoc. Geol. Soc. Trans. 52, 659–672.

Matonti, C., Lamarche, J., Guglielmi, Y., & Marié, L. (2012). Structural and petrophysical characterization of mixed conduit/seal fault zones in carbonates: example from the Castellas fault (SE France). Journal of Structural Geology, 39, 103-121.

Meddaugh, W.S., Barge, D., Todd, W.W. & Griest, S. (2007). The Jurassic-age Marrat Reservoir at Humma Field, Partitioned Neutral Zone (PNZ) Saudi Arabia and Kuwait—Utilization of a probabilistic, two stage design of experiments workflow for reservoir characterization and management. IPTC 11219, presented at the International Petroleum Technology Conference, 4–6 December 2007 Dubai, U.A.E.

Melim, L.A., Anselmetti, F.S., Eberli, G.P., (2001). The Importance of Pore Type on Permeability of Neogene Carbonates, Great Bahama Bank, in: Subsurface Geology of a Prograding Carbonate Platform Margin Great Bahama Bank Results of the Bahamas Drilling Project. SEPM Special Publication, pp. 217–238.

Micarelli, L., Benedicto, A., & Wibberley, C. A. J. (2006)a. Structural evolution and permeability of normal fault zones in highly porous carbonate rocks. *Journal of Structural Geology*, *28*(7), 1214-1227.

Micarelli, L., Moretti, I., Jaubert, M. & Moulouel, H. (2006)b. Fracture analysis in the south-western Corinth rift (Greece) and implications on fault hydraulic behavior. Tectonophysics, 426, 31–59.

Michie, E. A. H., & Haines, T. J. (2016). Variability and heterogeneity of the petrophysical properties of extensional carbonate fault rocks, Malta. Petroleum Geoscience, 22(2), 136-152.

Michie, E. A. H., Yielding, G., & Fisher, Q. J. (2018). Predicting transmissibilities of carbonate-hosted fault zones. Geological Society, London, Special Publications, 459(1), 121-137.

Ortner, H., Pomella, H., & Sanders, D. (2014). Formation of cataclasites in shallow-subsurface settings-meteoric diagenetic processes control fault rock formation at seismogenic faults in the Abruzzi Apennines, Italy. In EGU General Assembly Conference Abstracts (Vol. 16).

Pizzi, A., Calamita, F., Coltorti, M. , & Pieruccini, P. (2002). Quaternary normal faults, intramontane basins and seismicity in the Umbria-Marche-Abruzzi Apennine Ridge (Italy): contribution of neotectonic analysis to seismic hazard assessment. Boll. Soc. Geol. It., Spec. Publ, 1(31), 923-929.

Purcell, W. R. (1949). Capillary pressures—their measurement using mercury and the calculation of permeability: Transaction AIME, v. 186, p. 39-48.

Ran, G., Eyal, S., Yoseph, Y., Amir, S. & Noam, W. 2014. The permeability of fault zones: a case study of the Dead Sea rift (Middle East). Hydrogeology Journal, 22, 425–440.

Sibson, R. H. (1977). Fault rocks and fault mechanisms. Journal of the Geological Society, 133(3), 191-213.

Solum, J. G., & Huisman, B. A. H. (2017). Toward the creation of models to predict static and dynamic fault-seal potential in carbonates. Petroleum Geoscience, 23(1), 70-91.

Storti F.& Balsamo F (2010). Impact of ephemeral cataclastic fabrics on laser diffraction particle size distribution analysis in loose carbonate fault breccia. Journal of Structural Geology, v. 32, p. 507-522. DOI: 10.1016/j.jsg.2010.02.006

Storti F., Balsamo F., Salvini F. (2007). Particle shape evolution in natural carbonate granular wear material. Terra Nova, 19, 344-352.

Storti, F., Aldega, L., Balsamo, F., Corrado, S., Del Monaco, F., Di Paolo, L., Mastalerz, M., Monaco, P., Tallini, M. (2013). Evidence for strong middle Pleistocene earthquakes in the epicentral area of the 6 April 2009 L'Aquila seismic event from sediment paleofluidization and overconsolidation. J. Geophys. Res. 118 (7), 3767-3784.

Storti, F., Billi, A., & Salvini, F. (2003). Particle size distributions in natural carbonate fault rocks: insights for non-self-similar cataclasis. Earth and Planetary Science Letters, 206(1-2), 173-186.

Sutherland, R., Toy, V.G. et al. (2012). Drilling reveals fluid control on architecture and rupture of the Alpine fault, New Zealand. Geology, 40, 1143–1146.

Tondi, E. (2007). Nucleation, development and petrophysical properties of faults in carbonate grainstones: evidence from the San Vito Lo Capo peninsula (Sicily, Italy). Journal of Structural Geology, 29(4), 614-628.

Tondi, E., Antonellini, M., Aydin, A., Marchegiani, L., & Cello, G. (2006). The role of deformation bands, stylolites and sheared stylolites in fault development in carbonate grainstones of Majella Mountain, Italy. *Journal of structural geology*, *28*(3), 376-391.

Tondi, E., Cilona, A., Agosta, F., Aydin, A., Rustichelli, A., Renda, P., & Giunta, G. (2012). Growth processes, dimensional parameters and scaling relationships of two conjugate sets of compactive shear bands in porous carbonate grainstones, Favignana Island, Italy. *Journal of Structural Geology*, *37*, 53-64.

Tondi, E., Rustichelli, A., Cilona, A., Balsamo, F., Storti, F., Napoli, G., Agosta, F., Renda, P., & Giorgioni, M. (2016). Hydraulic properties of fault zones in porous carbonates, examples from central and southern Italy. *Italian Journal of Geosciences*, *135*(1), 68-79.

Tsutsumi, A., Nishino, S. et al. (2004). Principal fault zone width and permeability of the active Neodani fault, Nobi fault system, Southwest Japan. Tectonophysics, 379, 93–108.

Uehara, S.-I. & Shimamoto, T. (2004). Gas permeability evolution of cataclasite and fault gouge in triaxial compression and implications for changes in fault zone permeability structure throughout the earthquake cycle. Tectonophysics, 378, 183–195.

Wibberley, C.A.J. & Shimamoto, T. (2003). Internal structure and permeability of major strike-slip fault zones: the Median Tectonic Line in Mie Prefecture, Southwest Japan. Journal of Structural Geology, 25, 59–78.

Woodcock, N. H., & Mort, K. (2008). Classification of fault breccias and related fault rocks. Geological Magazine, 145(3), 435-440.

Woodcock, N. H., Miller, A. V. M., & Woodhouse, C. D. (2014). Chaotic breccia zones on the Pembroke Peninsula, south Wales: Evidence for collapse into voids along dilational faults. Journal of Structural Geology, 69, 91-107.

Yielding, G., Bretan, P., & Freeman, B. (2010). Fault seal calibration: a brief review. Geological Society, London, Special Publications, 347(1), 243-255.

7

GENERAL CONCLUSIONS

The structural architecture and paleofluid evolution of regional-scale fault systems have been studied through a multidisciplinary approach including detailed field investigations and multi-scale structural analyses, coupled with geochemical and thermobarometrical analyses of host rocks and syntectonic cements.

The selected fault systems dissect ramp anticlines and are potential seismogenetic sources. Although characterized by first-order structural analogies, the study areas have been chosen in different sectors of the Apennines orogenic wedge that show distinct geometries at the crustal scale. In fact, the Northern Lunigiana region is situated in the inner part of the Northern Apennines while the Gran Sasso Massif is in the axial zone of the Central Apennines thrust belt.

The Northern Lunigiana extensional fault system case study offered the possibility to analyse deformation structures that formed progressively during upward fault propagation and breakthrough. Our results indicate that the wall damage zone fracture pattern superimposed on the tip damage zone one, which in the footwall is formed by conjugate extensional fractures striking subparallel to the fault zone and characterized by acute angle bisectors oriented normal to bedding regardless of bedding dip. Most of syntectonic cement crystallization in the footwall, characterized by a prehnite, quartz and calcite assemblage, occurred during the tip damage zone stage from hydrothermal fluids, likely constituted by a mix of metamorphic and diagenetic fluids. Their precipitation started at temperatures 60-90 °C higher than the host rock temperature at peak burial and proceeded at lower temperatures during upward fault tip propagation and footwall block uplift. Microtextures indicate that crystallization events happened cyclically and episodically and was accompanied by fluid pressure variations from hydrostatic to suprahydrostatic that could relate to seismic ruptures. Subsidiary high-angle fault zones related to the wall damage zone stage are few compared to the tip damage zone pattern and testify for deformation localization during fault evolution. Fault zone displacement vs. width fits with scaling laws if we consider the fault distribution related to the wall damage zone stage. The tip damage zone shear fracture pattern in the footwall, which was quantitatively analysed, has a cross-sectional width twice that of the corresponding wall damage zone. Shear fracture pattern quantification data shows that fracture intensity increases logarithmically towards the fault core and that the network is

efficiently connected up to 0.9 km from the fault core due to a high proportion of crossing and abutting relationships.

The Gran Sasso Massif includes outstanding exposures of fault zones that allowed us to study many aspects of the contractional and extensional deformation history. Detailed structural analysis along the Monte Camicia out-of-sequence thrust zone allowed us to document the fault-related structures and kinematics, which indicate a top to the north transport direction. This thrust formed after the underlying Vado di Ferruccio out-of-sequence thrust zone. The two thrusts have contrasting permeability architectures that are the result of different deformation mechanisms, characterized by dominant cataclasis in the Monte Camicia, and by pressure solution-mediated mass transfer in the Vado di Ferruccio thrust zone. In turn, the timing of fault zone activation and its permeability architecture controlled the fluids circulating in the out-of-sequence thrust zones: they have marine origin in the Vado di Ferruccio thrust, where they promoted dolomitization, and meteoric origin in the Monte Camicia thrust, where de-dolomitization occurred. Quaternary extensional deformations partially exploited the previously acquired contractional architecture. In particular, the hanging wall damage zones of the two studied thrusts show a high frequency of high-angle faults and extensional fractures that exploit the thrusts fault core upper boundaries as detachment levels. The hanging wall damage zone of the Vado di Ferruccio thrust displays mirror-like high-angle subsidiary extensional faults interpreted to be coseismically activated. Instead, the hanging wall damage zone of the Monte Camicia thrust is interested by a dense network of extensional fractures that result in proto-brecciation in a decametric wide zone. High-angle extensional faulting is associated with further meteoric fluids infiltration, whose intensity in the area is controlled by the permeability architectures that the two thrust zone acquired during contractional deformation. Moreover, paleofluid circulation during deformation was restricted to very shallow depths without contributions from the basement and the mantle. The petrophysical characterization of the Campo Imperatore and Assergi fault systems shows a high variability of fault rock textures depending on fault displacement along strike. However, increasing comminution and decreasing pore size are documented approaching the fault core. Breccias are characterized by higher permeability compared to the protolith and can act as preferential fluid conduits. Conversely, cataclasites, which display the lowest permeability values, act as dynamic seals to fluid flow.

As a general conclusion, our multidisciplinary approach allowed us to: i) understand the cause-effect relationships between the structure and the paleofluid evolution; ii) identify and characterize the complexity of the structural-diagenetic processes; iii) comprehend the permeability architecture of the studied fault zones and their control on fluid circulation in the upper crust; (iv) trace fluid origin and migration at shallow crustal depths; (v) determine the conditions of deformation. Evidences for seismogenetic potential have been documented in the extensional fault

system of both study areas. The paleofluid flow patterns in the studied extensional faults are markedly distinct. The Lunigiana fault system was dominated by hot fluids that migrated upward from the metamorphic basement while fault zones in the Gran Sasso show syntectonic cements which precipitated from meteoric fluids infiltrated at the surface. These outcomes well agree with the crustal heat flow and shed light on the different driving mechanism of extensional faulting in the Apennines orogenic wedge. Specifically, extension in the study area of the Northern Apennines can be associated with the opening of the Tyrrhenian Sea back-arc. On the other hand, extension in the Gran Sasso area is likely related to gravity re-equilibration triggered by underthrusting at depth.